Acoustic emission-based indicators of shear failure of reinforced concrete structures without shear reinforcement

Zhang, F.

DOI
10.4233/uuid:9220a0c2-f4c1-46e6-a0a9-0069e4662730

Publication date
2022

Document Version
Final published version

Citation (APA)
Zhang, F. (2022). *Acoustic emission-based indicators of shear failure of reinforced concrete structures without shear reinforcement*. [Dissertation (TU Delft), Delft University of Technology]. https://doi.org/10.4233/uuid:9220a0c2-f4c1-46e6-a0a9-0069e4662730

Acoustic emission-based indicators of shear failure of reinforced concrete structures without shear reinforcement

Fengqiao ZHANG

Acoustic emission-based indicators of shear failure of reinforced concrete structures without shear reinforcement

Dissertation

for the purpose of obtaining the degree of doctor

at Delft University of Technology

by the authority of the Rector Magnificus, Prof.dr.ir. T.H.J.J. van der Hagen,

chair of the Board for Doctorates

to be defended publicly on

Wednesday 21, September 2022 at 12:30 o'clock

by

Fengqiao ZHANG

Master of Science in Civil Engineering,

Delft University of Technology, the Netherlands

born in Tangshan, China

This dissertation has been approved by the promotors.

Composition of the doctoral committee:

Rector Magnificus,	chairperson
Prof.dr.ir. M.A.N. Hendriks	Delft University of Technology Norwegian University of Science and Technology, Norway, promotor
Dr.ir. Y.Yang	Delft University of Technology, copromotor

Independent members:

Prof.dr. A.V. Metrikine	Delft University of Technology
Prof. T. Shiotani, Ph.D.	Kyoto University, Japan
Prof.dr.ir. E. Verstrynge	Katholieke Universiteit Leuven, Belgium
Prof.dr.ir. E.O.L. Lantsoght	Universidad San Francisco de Quito, Ecuador
Dr.ir. S.A.A.M. Fennis	Rijkswaterstaat
Prof.dr.ir. J.G. Rots	Delft University of Technology, reserve member

Prof.dr.ir. D.A. Hordijk has contributed greatly to the preparation of this dissertation.

This research was partly sponsored by Rijkswaterstaat, Ministry of Infrastructure and Water Management.

Printed by: IPSKAMP printing

ISBN: 978-94-6421-844-2

Email: zfq9393@gmail.com

To my dear parents

献给我亲爱的父母

Summary

The safety of existing concrete structures is important to the society. Many concrete bridges have been used for decades. The material degrades with time but the traffic load increases, which increases the risk of structural failure, impacting the citizen's safety and daily life.

To prevent the structural failure, reconstructing/repairing all the bridges that are suspected to have low reliability is not practical nor efficient. A solution is to first more accurately assess the structural bearing capacity. Based on the assessment, the asset managers can take more efficient interventions.

This dissertation provides methods to assess the structural bearing capacity of a typical concrete structural type – reinforced concrete beam/slab without shear reinforcement. This type of structure can have a critical failure mode of shear, which is catastrophic and with limited or no sign before it occurs.

To assess the structural performance against shear, this dissertation starts with literature reviews in the two relevant fields. One is on the shear failure mechanisms of reinforced concrete structures (Chapter 2). The review helps us understand the shear failure mechanisms and inspires a potential indicator for shear failure at structural level. The other review is on the monitoring techniques (Chapter 3). From the review, the acoustic emission (AE) technique stands out from the others. The unique benefits are that AE can detect the internal damages remotely and in real time, and AE is very sensitive to concrete cracking at an early stage. We find the potential of using AE to indicate shear failure.

However, many challenges are present in AE. According to a detailed review of AE in Chapter 4, AE monitoring is influenced by many uncertainties in the process, leading to inaccurate results. AE can detect concrete cracking but could not be well related to the crack width of a structure which is important for evaluating structural performance. Moreover, referring to upscaling to the structural level, no method is devised to interpret AE results as a failure indicator.

This dissertation addresses these knowledge gaps and develops AE-based failure indicators for reinforced concrete structures without shear reinforcements. The development is based on the observation in a series of shear failure tests on reinforced concrete beams and slabs. Chapter 5 summarizes the test setups, measurements and an overview of the results. These tests are used in the following chapters.

Firstly new AE methods are developed in Chapter 6 and 7. Chapter 6 develops an AE method, i.e. probability density field of AE events, to identify damage locations considering various uncertainties during the localization process. This method estimates the

probability of the location of AE events. Chapter 7 develops a method on source classification, to distinguish signals from tensile cracking and friction. The classification of AE source type is important for understanding the structural behaviour. The new classification method uses the signal parameters peak frequency and partial power, which are reliable and efficient to apply. The two new AE methods developed in Chapters 6 and 7 are used in the following chapters.

Chapter 8 closely studies the relationship between AE events and crack width at local positions. The relationships during loading and unloading are studied separately because different mechanisms are expected in the two processes. The relationship between AE and cracking has been explained physically. This provides a better understanding of AE events from crack opening and closure.

Based on all the former work (including literature review, experiments, two new AE methods on source localization and classification, relationships between AE and crack width), Chapter 9 develops AE-based failure indicators for reinforced concrete structures without shear reinforcement. A 'traffic light system' is proposed, where the green-light, yellow-light and red-light criteria show different damage levels of the structure. The system is evaluated to be robust within the available tests. In the end of this dissertation, general guidance is provided on implementing the AE-based indicators in a load test of a concrete structure.

As a general summary, this dissertation contributes to the field of AE monitoring of concrete structures in the following aspects:

- Developing an AE method which identifies the location of AE sources (local damage) in concrete, considering various uncertainties in the localization process (Chapter 6),
- Developing a source classification criterion based on signal parameters which is reliable and efficient (Chapter 7),
- Revealing the relationship between AE events and crack kinematics with a physical background (Chapter 8),
- Developing a set of AE-based failure indicators for reinforced concrete structures without shear reinforcement, with theoretical background and practical relevance (Chapter 9),
- Proposing general guidance on implementing the indicators (Chapter 10).

Samenvatting

De veiligheid van bestaande betonconstructies is belangrijk voor de samenleving. Veel betonnen bruggen zijn al tientallen jaren in gebruik. Het materiaal verslechtert met de tijd, maar de verkeersbelasting neemt toe, wat kan leiden tot structurele schade, met gevolgen voor zowel de veiligheid van de burger als voor het dagelijks leven.

Om structureel falen te voorkomen, is het verbouwen/verstellen van alle bruggen waarvan wordt vermoed dat ze defect zijn, niet praktisch en ook niet efficiënt. Een oplossing is om eerst het draagvermogen van de constructie te beoordelen. Op basis van de beoordeling kunnen assetmanagers passende interventies ondernemen.

Dit proefschrift biedt methoden om het draagvermogen van een typische betonconstructie zonder dwarskrachtwapening te beoordelen. Dit type constructie heeft een kritieke bezwijkmodus van afschuiving, een bros bezwijkmechanisme dat moet worden voorkomen.

Om de constructieve veiligheid voor afschuiving te beoordelen, begint dit proefschrift met literatuuronderzoeken in de twee relevante gebieden. Het eerste deel is over de afschuif bezwijkmechanismen van constructies van gewapend beton (hoofdstuk 2). De studie helpt ons de afschuif bezwijkmechanismen te begrijpen en inspireert de ontwikkeling van een mogelijke indicator voor afschuif bezwijken. Het bewaken van deze indicator kan afschuiving helpen voorkomen. De tweede review gaat over de monitoringtechnieken (Hoofdstuk 3), gericht op geschikte technieken voor dit proefschrift. Uit de review onderscheidt de akoestische emissie (AE)-techniek zich van de andere, omdat deze interne schade op afstand en in realtime kan detecteren. Bovendien is AE in een vroeg stadium erg gevoelig voor betonscheuren.

Er zijn echter veel uitdagingen bij het gebruik van AE. Volgens een gedetailleerd overzicht van AE in hoofdstuk 4, wordt AE-monitoring beïnvloed door veel onzekerheden in het proces, wat leidt tot onnauwkeurige resultaten. Verder kan AE betonscheuren detecteren, maar het is onduidelijk hoe de scheurbreedte te kwantificeren, wat belangrijk is voor het evalueren van constructieve veiligheid. Voor opschaling naar constructie niveau was geen methode om AE-resultaten als faalindicator te interpreteren voorhanden.

Dit proefschrift pakt deze kennislacunes aan en ontwikkelt AE-gebaseerde faalindicatoren voor gewapende betonconstructies zonder dwarskrachtwapening. De ontwikkeling is gebaseerd op een reeks bezwijkproeven op balken en platen van gewapend beton. Hoofdstuk 5 beschrijft de testopstellingen, metingen en algemene resultaten. Deze proeven worden in de volgende hoofdstukken gebruikt.

Ten eerste worden in hoofdstuk 6 en 7 nieuwe AE-methoden ontwikkeld. Hoofdstuk 6 presenteert een nieuwe AE-methode, het zogenoemde kansdichtheidsveld van AE-ge-

beurtenissen om schadelocaties te identificeren, rekening houdend met verschillende onzekerheden tijdens het lokalisatieproces. Deze methode schat de waarschijnlijkheid van de locatie van AE-gebeurtenissen. In Hoofdstuk 7 is een andere nieuwe methode ontwikkeld voor de bronclassificatie, om signalen van trekscheuren en wrijving te onderscheiden. Deze informatie is belangrijk voor het begrijpen van constructie gedrag. De nieuwe classificatiemethode maakt gebruik van signaalparameters piekfrequentie en gedeeltelijk vermogen, die betrouwbaar en efficiënt kunnen worden toegepast. De twee nieuwe AE-methoden die in de hoofdstukken 6 en 7 zijn ontwikkeld, worden in de volgende hoofdstukken gebruikt.

Hoofdstuk 8 bevat een analyse van de relatie tussen AE-events en scheurwijdte op lokale posities. Vanwege verschillende mechanismen worden de relaties tijdens laden en ontladen afzonderlijk bestudeerd. De relatie tussen AE en scheurwijdte is fysiek verklaard. Dit zorgt voor een beter begrip van AE-gebeurtenissen van het openen en sluiten van scheuren.

Gebaseerd op al het eerdere werk, inclusief het literatuuronderzoek, de experimenten, twee nieuwe AE-methoden, de gevonden relaties tussen AE en scheurwijdte, warden in hoofdstuk 9 AE-gebaseerde faalindicatoren voor gewapende betonconstructies zonder dwarskrachtwapening ontwikkeld. Er is een ‘verkeerslichtsysteem’ voorgesteld, waarbij het groen/geel/rood-lichtcriterium verschillende schadeniveaus van de constructie laat zien. Het systeem is binnen de beschikbare proeven robuust. Aan het einde van dit proefschrift wordt een leidraad gegeven voor het implementeren van de op AE gebaseerde indicatoren in proefbelastingen op betonconstructies.

Als algemene samenvatting draagt dit proefschrift bij aan het gebied van AE-monitoring van betonconstructies op de volgende aspecten:

- Het ontwikkelen van een AE-methode die de plaats van de schade in beton identificeert, rekening houdend met verschillende onzekerheden in het lokalisatieproces (hoofdstuk 6).
- Het ontwikkelen van een bronclassificatiecriterium op basis van signaalparameters dat betrouwbaar en efficiënt is toe te passen (hoofdstuk 7).
- Het inzichtelijk maken van de relatie tussen AE-gebeurtenissen en scheurbreedte door middel van een fysieke verklaring (hoofdstuk 8).
- Het ontwikkelen van op AE-gebaseerde faalindicatoren voor constructies van gewapend beton zonder dwarskrachtwapening, met een theoretische achtergrond (hoofdstuk 9).
- Het geven van voorstellen voor algemene richtlijnen voor de implementatie van de indicatoren (hoofdstuk 10).

Table of Contents

Chapter 1 Introduction

1.1 Structural assessment of existing concrete bridges

The safety of existing concrete bridges draws attention to the society in the Netherlands. For a total of around 3500 bridges in the road network, around 60% of bridges were built before 1975 (Lantsoght, van der Veen et al. 2013). The past design codes may not meet the requirements of the current design in terms of the bearing capacity and the traffic load. Moreover, the aging of the material over time may lead to further degradation of the structural bearing capacity. The outdated design details, aging materials and increasing load reduce the structural safety and may lead to structural failure.

To prevent structural failure, a method is to repair or replace the bridges that have reduced structural safety in a short period of time. However, this method is neither practical nor efficient. Firstly it is not practical to intervene at once all the bridges that are suspected to failure. This will occupy a lot of resources, which may influence other projects. And closing many bridges for intervention causes traffic blocks at a large scale, which influences the citizens' daily life or even the economy. Moreover, some bridges are observed damaged but may actually have enough bearing capacity after repair or even without the need of repair. Replacing or reconstructing a bridge that has enough bearing capacity is unnecessary and harms the environment.

Therefore, a wiser approach is to firstly assess the structural bearing capacity. Based on the assessment, interventions can be prioritized that the most critical bridges first get repaired or demolished. And the solutions can be tailored to every bridge according to its current load bearing capacity.

To assess the structural bearing capacity, proof load testing is considered an accurate method. The bridge is loaded until a desired load level, and if the structural performance does not violate the predefined stop criteria, the bridge is proved to the corresponding capacity (AASHTO 2018). In this process, monitoring the structural performance is vital. To indicate the structural performance, many conventional methods measure parameters at predefined locations, like crack width, shear displacement and deformation (Deutscher Ausschuss für Stahlbeton 2000). However, these parameters are mostly measured from the structural surface, and could not represent the internal damages which have been found critical for some types of structural failure (Muttoni and Fernández Ruiz 2008, Tue, Theiler et al. 2014). Therefore, we need to find a proper technique that can measure the internal damage.

Acoustic emission (AE) technique stands out from the others on measuring internal damages. Sudden changes in concrete like cracking will release energy and generate waves. The waves will propagate from the source to the AE sensors and be converted into electrical signals. By processing the obtained signals, AE can estimate the location of the source (which is called source localization) (Kundu 2014), classify the source type (which is called source classification) (Ohtsu 2010), and assess the structural integrity (Ohtsu

2010). These calculations are time-efficient, thus can provide real-time monitoring during load testing when damage evolution is rapid. Moreover, AE is very sensitive to minor changes in concrete even micro cracking. A previous study has found that AE can detect cracking earlier than the traditional displacement measurement (Zhang, Zarate Garnica et al. 2020). AE can also remotely detect the damages, which covers a larger measuring zone. All these favourable features make AE an ideal technique to indicate structural performance against failure.

Though AE shows favourable features, many knowledge gaps are present between the current state of research and the use of AE to indicate the structural failure. Firstly AE monitoring of concrete structures is influenced by various uncertainties in the monitoring and analysis process such as presence of crack between source and receiver. The influence of the uncertainties on the AE results needs to be evaluated. And considering the uncertainties, AE technique needs to be improved. For example, the estimated source location may not be the actual one, leading to source localization error. The error properties and its influence on identifying the location of cracking are not well studied. Considering the errors, the localization method needs to be improved. Secondly it has been generally recognized that the number of AE events is linked to concrete cracking. However, no quantitative relationship between crack width and the amount of AE events is available, which limits the usage of AE in crack detection. This gap lies at the local/material level. Then at the structural level, we miss a method to interpret the locally obtained AE events into the global performance of the structure.

1.2 Research goal and questions

The scope of this dissertation is limited to assessing the shear capacity of reinforced concrete structures without shear reinforcement during load testing. For this type of structure, one of the critical failure modes is shear failure, which is catastrophic with limited or no sign before it occurs. AE, with many favourable features as mentioned above, is expected to be able to indicate the shear failure beforehand. The goal of this research is to develop an AE system to indicate shear failure of reinforced concrete structures without shear reinforcement.

The main research question is: how can we use AE to indicate the shear failure of reinforced concrete structural members without shear reinforcement?

This main question can be broken down into sub-research questions, with the corresponding knowledge gaps.

The first discussed objective of AE is source localization. Due to uncertainties in the localization process, the estimated source location inevitably includes the localization errors compared to the actual one. Therefore, the first question is: (Q1) what are the properties of source localization error, considering various uncertainties in the localization

process? Then based on the error study, the next question is: (Q2) how can we improve the AE source localization results, considering the localization error?

Another important objective of AE is source classification, which distinguishes different types of AE sources in concrete cracking. We need to figure out: (Q3) how can we classify the types of AE sources in concrete cracking in an efficient and reliable way?

With the improved AE technique, we need to relate the results to the mechanical behaviour of concrete. Most available studies in literature state that AE events are related to crack opening in concrete in a qualitative way. But the relationship between AE events and crack width is not quantified. Therefore, we need to clarify: (Q4) what is the relationship between AE events and crack width?

At structural level, we need to find the relationship between AE events and structural behaviour. The question is: (Q5) how can we indicate possible shear failure of concrete member at early stage using AE? And considering the implementation, one following-up question is: (Q6) how can we apply the AE-based indicators of shear failure in load testing of concrete structures?

The six sub-questions form three parts of work. Part 1 includes questions Q1-Q3, to improve the AE technique. Part 2 focuses on Q4, to locally relate AE events and crack width. Part 3 includes Q5 and Q6, to upscale to the structural level to develop an AE system to indicate shear failure of reinforced concrete structures.

1.3 Research methodology

Following the logics of the research questions, we start with Part 1 (Q1-Q3) to improve the AE techniques. Then we work on Part 2 (Q4) to relate AE events and cracking behaviour of concrete locally. Finally we approach Part 3 (Q5 and Q6) to develop an AE system to indicate structural failure of reinforced concrete members.

Having access to experimental data is vital for this research. The experiments that are included in this dissertation are shear tests of reinforced concrete beams and slabs. The specimens are of large scale, without shear reinforcement, loaded till failure and monitored by various techniques including AE. Therefore, the experiments are adequate for developing AE-based shear failure indicators for reinforced concrete structures without shear reinforcement. These experiments are involved in the following methodology.

Methodology for Part 1 (Q1-Q3): To improve the AE source localization, we will first evaluate the properties of source localization error (Q1). A reliable evaluation requires a large amount of test data. In need of test data, we will use simulations to generate sufficient number of tests. The simulation is validated using experimental data to check the influence of uncertainties, which are the presence of crack and the arrival time picking error.

In the next step, we will use the error properties to obtain a probability density function of the location of an AE source (Q2). This function estimates the probability of an AE event located at any location in the field. The new method makes use of the error to estimate source location, and will be implemented in the whole dissertation. The detailed methods can be found in Chapter 6.

To improve the AE source classification (Q3), we will first evaluate the performance of various signal parameters on source classification using data obtained from experiments. In the experiments, AE signals are collected from different regions of a concrete member where the cracking type can be determined by other measurement method. Because the locations of the signals with respect to the sensors are random, the influence of wave propagation with respect to the wave travelling distances can be studied. By comparing the properties of AE signal from different sources and travelled through different distance, we will develop a new source classification criterion. The detailed methods can be found in Chapter 7.

Methodology for Part 2 (Q4): To relate AE events and crack kinematics locally, we will compare the probability density function of AE sources proposed in Part 1 with the whole crack kinematics measured by digital image correlation (DIC). We will compare the results of AE and DIC to obtain and explain the relationships between the AE events and crack kinematics. Due to different mechanisms, the relationships during crack formation and closure will be studied separately. The detailed methods can be found in Chapter 8.

Methodology for Part 3 (Q5 and Q6): To develop the AE-based failure indicators for concrete members (Q5), we will use the theoretical models of shear failure from the literature and the knowledge on the relationship between concrete cracking and AE. We will propose a set of AE-based indicators that closely relates to the theoretical models of shear failure. Then we will validate the indicators using shear tests on concrete beams and slabs presented in this dissertation. The detailed methods can be found in Chapter 9.

To implement the AE-based failure indicators in practice (Q6), we will consider the whole procedure from the system design to the execution and decision-making. The knowledge on execution in this dissertation mainly comes from the experiences of the lab experiments on AE and proof load tests of existing bridges and buildings. The merge of the previous experiences and the additional insights in this dissertation leads to a guidance on every step for the users in Chapter 10.

1.4 Outline

This dissertation includes 11 chapters. The main contents (excluding introduction and conclusion) answer the three parts of research questions described in Section 1.2. A schematic representation of the interaction between chapters is presented in Figure 1.1. The

brief contents of each chapter are listed below in the order of appearance in this dissertation.

- Chapter 1 introduces the research.
- Chapter 2 reviews the shear failure mechanisms of reinforced concrete structure, which inspires possible shear failure indicators.
- Chapter 3 reviews various non-destructive techniques for concrete monitoring. The review shows the reasons of using AE instead of others in this dissertation.
- Chapter 4 reviews AE technique including basic principles and application in concrete. The review motivates the further development of AE methods.
- Chapter 5 summarizes the experiments used in this dissertation including failure tests of reinforced concrete beams and slabs. This chapter serves as a reference for the following chapters when the tests are used.

Development of new AE methods, for research questions Part 1 (Q1-Q3)

- Chapter 6 develops a new AE source localization method. This method quantifies the spatial distribution of AE events, considering various uncertainties in the localization process. (Q1-Q2)
- Chapter 7 develops a new source classification criterion. The new criterion is reliable and efficient to apply. (Q3)

Reveal of relationship between AE and crack width, for research questions Part 2 (Q4)

- Chapter 8 reveals the relationship between AE events and local crack kinematics. The physical background behind the relationships is explained. (Q4)

Development of AE system to indicate shear failure, for research questions Part 3 (Q5-Q6)

- Chapter 9 develops AE-based failure indicators for reinforced concrete structures without shear reinforcement. The indicators are evaluated robust and extended from beams to slabs. The results provide a solid method to indicate structural failure using AE. (Q5)
- Chapter 10 provides a guidance on implementing the AE-based indicators in load testing. Discussions are given to the preliminary survey, load design, sensor layout design, execution and real-time data analysis and decision making. (Q6)
- Chapter 11 concludes the research and proposes the future research topics.

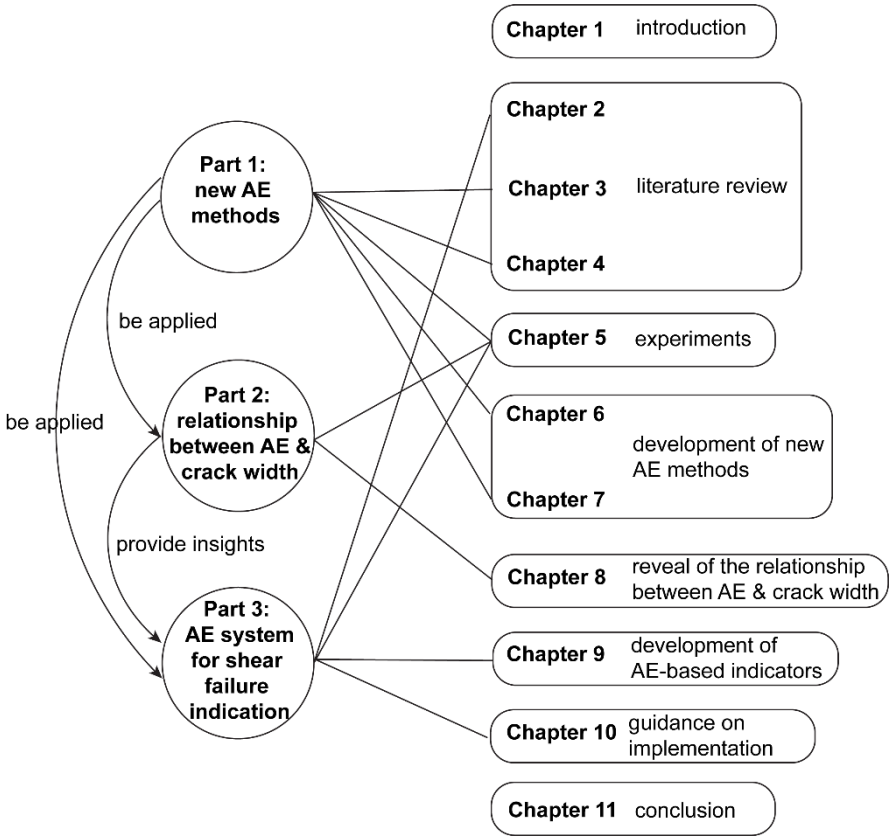

Figure 1.1 Outline of this dissertation

Chapter 2 Shear failure of reinforced concrete members without shear reinforcement

2.1 Introduction

Shear failure is a critical failure mode for reinforced concrete structures without shear reinforcement. It is a brittle failure mode that does not have an obvious warning beforehand. Moreover, shear failure often means a total loss of the structural bearing capacity. Therefore, this brittle and hazardous failure mode can lead to a catastrophe, losing lives and properties.

Due to the criticality, a large amount of studies have been carried out on the shear behaviour of reinforced concrete structures without shear reinforcement. They looked into the shear transfer mechanisms and proposed several shear failure models with rational background. From the literature, we can better understand the shear failure process and propose possible shear failure stop criteria for proof load testing.

This chapter first reviews shear transfer mechanisms in reinforced concrete structures without shear reinforcements. Then several shear failure models are described. Based on these, a discussion is presented on shear failure stop criteria for proof load testing.

2.2 Two types of cracks in reinforced concrete members

In reinforced concrete structures without shear reinforcement, with increasing load, two types of cracks develop in sequence, i.e. flexural cracks and flexural shear cracks.

Flexural cracks first form at the cross section of maximum bending moment (Figure 2.1a). The flexural crack is initiated when the tensile stress at the farthest location from the neutral axis reaches the concrete tensile strength. Since these tensile stresses are parallel to the longitudinal axis of the specimen, the flexural crack starts vertically. Shortly after initiating, the crack develops to its full height and stabilizes. The stabilized crack height s_{cr} can be calculated from the force equilibrium at cross section (Yang 2014)

$$s_{\mathrm{cr}} = \left(1 + \rho_{\mathrm{s}} n_{\mathrm{e}} - \sqrt{2\rho_{\mathrm{s}} n_{\mathrm{e}} + \left(\rho_{\mathrm{s}} n_{\mathrm{e}}\right)^2}\right) d_{\mathrm{e}} \tag{2.1}$$

where ρ_{s} is the reinforcement ratio, n_{e} is the elastic modulus ratio between steel and concrete, and d_{e} is the effective cross section height.

The spacing of flexural crack l_{cr} is related to the stabilized crack height

$$l_{cr} = s_{cr} / k_c \tag{2.2}$$

where k_{c} is the inclination of stress line which can be estimated to be 1.28 (Yang 2014).

Next to the primary flexural cracks, secondary cracks open at a certain distance (Figure 2.1a). This distance is related to the force transfer length at reinforcement determined by the bond-slip relationship between reinforcement and concrete.

With increasing load, flexural cracks also initiate in the bottom of the cross section in shear span. They start more or less vertically and then bend over toward the loading point (MacGregor, Sozen et al. 1960). This type of crack is called flexural shear crack (Figure 2.1a). The shape of flexural shear crack can be determined analytically and numerically (Slobbe, Hendriks et al. 2014, Classen 2020). But these calculations usually are complicated and time-consuming. Many studies simplify the shape into two branches to estimate the shear capacity (Zararis and Papadakis 2001, Yang, den Uijl et al. 2016): the first branch is the initiating flexural crack, and the second branch is the inclined crack from the tip of the first branch to the loading point. In Section 2.3.2, reference will also be made to Figure 2.1b.

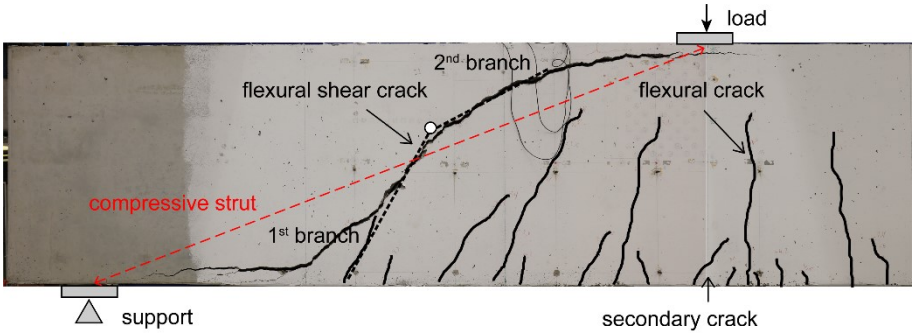

(a) I123A

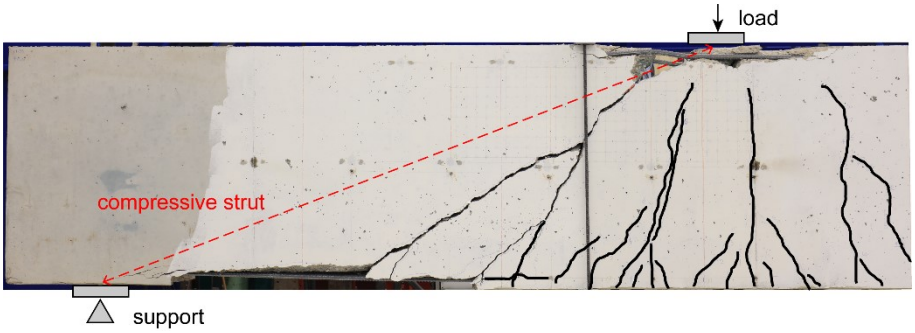

(b) H603A

Figure 2.1 Crack pattern at: (a) flexural shear failure of test I123A and (b) shear compression failure of test H603A (taken from test series described in Chapter 5).

2.3 Shear transfer mechanisms

2.3.1 Along flexural shear crack

A flexural shear crack can carry shear forces through three mechanisms, i.e. residual tensile stress at crack tip, aggregate interlock at crack faces and dowel action at the longitudinal bars (ACI-ASCE Committee 426 1973, ACI-ASCE Committee 445 1998). These

shear transfer mechanisms are illustrated in Figure 2.2, considering a free body diagram cut along the crack cross section.

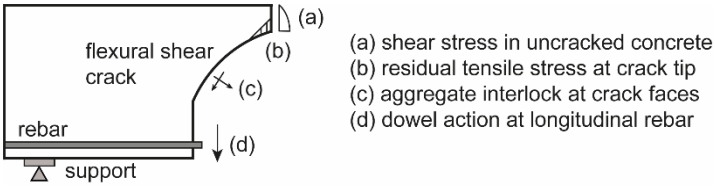

Figure 2.2 Part of a reinforced concrete member (free body) cut along a flexural shear crack.

At the free body diagram, shear force can also be transferred in the uncracked concrete. The shear stress distribution is usually simplified as a parabolic curve, which is shown in Figure 2.2 mechanism (a). Details of shear transfer in the uncracked concrete will not be further introduced and can be found in Mörsch (1909).

Residual tensile stress at crack tip

At crack tip, there is a zone consisting of microcracks. Tensile stress can still be transferred, even though the strain exceeds the cracking strain. This zone is called fracture zone or tension-softening zone (Pruijssers 1986). Figure 2.3 illustrates the stress distribution at the crack tip and a commonly-used relationship between tensile stress and crack width (Hordijk 1992). In the example, the critical crack width, over which limited tensile stress can be transferred, is 0.1 mm. In literatures, the critical crack width has been reported to vary from 0.09 mm to 0.25 mm (Hordijk 1993). Figure 2.2 mechanism (b) illustrates the residual tensile stress distribution at the tip of a flexural shear crack.

Since the residual tensile stress is mostly activated in a small zone at the crack tip, the contribution to the shear capacity is more pronounced in small specimens than in large ones (Reineck 1991).

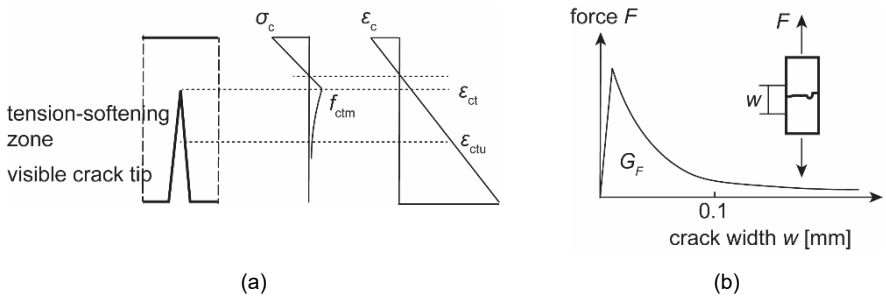

Figure 2.3 (a) Residual tensile stress at crack tip, reproduced from Pruijssers (1986), (b) tension-softening behaviour, reproduced from Hordijk (1992).

Aggregate interlock at crack faces

For normal strength concrete, cracks typically initiate along the interface between cement matrix and aggregates. The resulting rough crack faces can transfer shear stresses by aggregate interlock. The allowable shear stress can be calculated from the tangential/shear displacement (Δ) and normal displacement (w) of crack faces. Many theories have been developed to calculate shear resistance (Gambarova 1981, Li and Maekawa 1987). Among them, a widely-recognized model was developed by Walraven (Walraven 1980). In his model, aggregates are assumed to be rigid spheres with random diameter and location. With shear and normal displacements, the cement matrix crushes on contact with aggregates. Slip and crushing at the contact area generate shear and normal stresses (Figure 2.4).

The shear resistance from aggregate interlock is often larger than other mechanisms along a flexural shear crack. Especially for cracks with large shear displacement, experiments have shown that the contribution from aggregate interlock can reach 90% of the shear capacity (Huber, Huber et al. 2016, Zarate Garnica 2018).

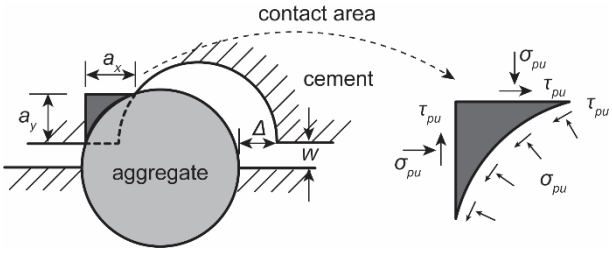

Figure 2.4 Model for aggregate interlock, reproduced from Walraven (1980).

Dowel action of longitudinal rebars

The longitudinal rebars crossing the flexural shear crack can resist shear force. The differential shear displacement between the two crack faces will result in bending, shear or kinking of the bars (Paulay, Park et al. 1974). With increasing shear force, dowel action usually fails in splitting of concrete at the level of rebars for reinforced concrete structures without shear reinforcement (Tassios and Vintzileou 1986), as illustrated in Figure 2.5.

The shear resistance of dowel action is related to the tensile strength of concrete cover, which is often low. Often the propagation of a dowel crack was found to trigger the final failure (Chana 1987, Yang, den Uijl et al. 2016). This opens a new view to explain shear failure which is further discussed in Section 2.4.3.

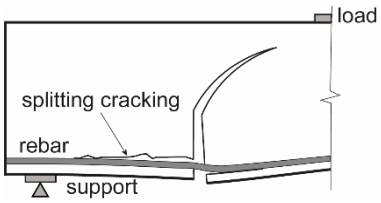

Figure 2.5 Splitting of concrete cover at the level reinforcement, reproduced from Yang (2014).

2.3.2 By compressive strut

After the formation of flexural shear cracks, an alternative shear transfer mechanism is direct force transfer through a compressive strut between the load and the support. The strut represents the compression stress-field between the load and the support. When the concrete in the strut crushes, the structure fails. A famous series of tests carried out by Leonhardt and Walther showed that for beams of a same shear span to depth ratio, compressive struts can offer twice the capacity of flexural shear cracks (Leonhardt and Walther 1962).

But the mechanism of compressive strut does not always act, depending on whether flexural shear cracks propagate into the region of compressive strut. When the compressive strut has been damaged by flexural shear cracks, the 'cracked' compressive strut could not provide additional shear capacity. The structure fails at flexural shear cracking, which is called flexural shear failure. When the compressive strut is not damaged by flexural shear cracks, the 'uncracked' compressive strut transfers shear force until concrete crushing. This failure mode is called shear compression failure. Figure 2.1 shows the two typical failure modes with the compressive strut marked. The examples are taken from a series of tests which are introduced in Chapter 5.

Many other literatures describe the condition of 'a cracked compressive strut' as 'a compressive strut that cannot form', and 'an uncracked compressive strut' as 'a compressive strut that can form'. They have the same physical background. This dissertation uses the term 'a cracked/uncracked compressive strut'.

2.4 Triggers of shear failure according to the theoretical models

Many theoretical models have been developed to predict shear failure in beams and one-way slabs to describe the loss of shear transfer mechanisms. However, these models consider the trigger of shear failure differently, which could be breakage of concrete tooth, loss of aggregate interlock, propagation of dowel crack or cracking in compressive field. This section reviews various triggers of shear failure according to the available models in literature. The discussion is based on the corresponding theoretical models.

2.4.1 Breakage of concrete tooth

Kani's tooth model is one of the first rational models to explain shear failure (Kani 1964). In his model, flexural cracks shape the beam into a comb-like structure (Figure 2.6). The flexural cracks create vertical concrete teeth. Each concrete tooth works like a cantilever beam, with one end loaded by the reinforcement in the tensile zone, and the other end fixed at the compressive zone. For beams with large shear span ratio, the structure fails at breaking-off of the tooth on the fixed end.

When the shear span ratio is small, after breaking-off of the concrete teeth, the concrete compressive strut takes over. Shear failure is then caused by crushing of the strut. Kani calculated the resistance by assuming a prismatic strut from load to support.

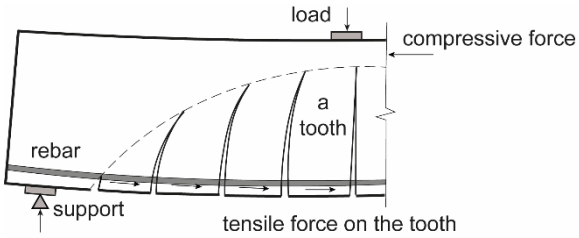

Figure 2.6 Kani's tooth model, reproduced from Kani (1964).

Kani's model has a limitation that, when calculating the resistance of a concrete tooth, only the resistance at crack tip is considered. The contributions from aggregate interlock and dowel action are not included (Kani 1964). Therefore, the shear capacity is underestimated.

2.4.2 Loss of aggregate interlock

As an improvement to Kani's tooth model, Reineck included the contributions of aggregate interlock, dowel action and shear in the compression zone to shear capacity (Reineck 1991). Reineck found that the main contributor of the shear capacity is aggregate interlock. Since a larger crack width results in less aggregate interlock, Reineck defined the critical crack width at a specific location which will lead to shear failure. Reineck's tooth model reflects that loss of aggregate interlock is the trigger of shear failure.

Another widely-applied model is the critical shear crack theory (CSCT) (Muttoni and Fernández Ruiz 2008). Muttoni et al. demonstrated the influence of crack location and width on shear capacity. When the compressive strut is damaged by the flexural shear crack, the shear capacity is significantly reduced. The opening and roughness of the flexural shear crack would determine the shear capacity. Muttoni et al. propose to calculate the shear capacity based on crack width at the pre-defined critical location.

The modified compression field theory (MCFT) reflects the importance of aggregate interlock in a different approach (Vecchio and Collins 1986). MCFT originates from compression field theory (Collins 1978), which simplifies the cracked concrete as a new material with its own stress and strain characteristics. Stress-strain relationships are expressed in terms of average stresses and strains. But the compression field theory does not include stresses at cracks due to aggregate interlock. MCFT adds the contribution from aggregate interlock according to Walraven's theory (Walraven 1980). The contribution from aggregate interlock is calculated using the average crack width in MCFT, which is the product of principle tensile strain and crack spacing.

2.4.3 Propagation of dowel crack

Chana first showed experimentally that formation of a dowel crack initiated the flexural shear crack (Chana 1987). This observation opens another view to explain the shear failure. Since then, many other studies have been carried out, and a most thoroughly researched method is the critical shear displacement theory (CSDT) developed by Yang (Yang 2014).

Yang explained the shear failure process as: dowel cracking detaches the reinforcement from concrete, lowering the stiffness of the tensile zone; this results in a larger flexural crack width; in the meantime, the crack branch in the compression zone further propagates, also leading to larger crack width; consequently, at aggregate interlock, a larger shear displacement is needed to reach the same shear stress; this larger shear displacement will further open the dowel cracks and the crack branch in the compression zone; under this loop, the crack width keeps increasing, which ends up as the collapse of the whole structure. He defined a critical shear displacement which triggers the unstable failure process.

CSDT calculates the shear capacity considering different shear transfer mechanisms including shear stress in uncracked concrete, aggregate interlock and dowel action. CSDT also suggests to verify the bearing capacity of the compressive strut as alternative shear transfer mechanism. Once a stable compressive strut can form after the flexural shear crack, a larger shear capacity is expected according to the model.

2.4.4 Cracking in compressive field

Shear failure usually comes along with an inclined crack initiated from the tip of flexural crack to the loading point. Based on this phenomenon, several models have been developed to calculate shear capacity.

Zararis and Papadakis considered that the shear failure is initiated by splitting of the compressive strut (Zararis and Papadakis 2001). They used the simplification that a flexural crack includes two branches: initiating flexural crack and inclined crack (Figure 2.7a). The second branch is considered as splitting crack under compression force in the strut.

Therefore, they calculated the shear capacity based on the splitting tensile strength of concrete.

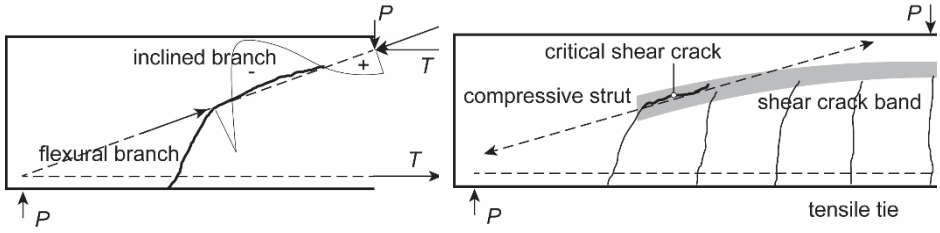

Figure 2.7 Models based on inclined cracking in compressive strut: (a) by Zararis and Papadakis, reproduced from Zararis and Papadakis (2001) and (b) by Tue et al., reproduced from Tue, Theiler et al. (2014).

Mari et al. also considered that the shear failure occurs when reaching the capacity of the compression chord (Mari, Cladera et al. 2014). The compression chord is under multi-axial loading and the principle stresses are calculated. The structural shear capacity is calculated as the sum of shear transferred by the compression chord, along the crack, by the stirrups and longitudinal reinforcement.

Tue et al. proposed a model which also relies on cracking in the compressive field (Tue, Theiler et al. 2014). By calculating the stress distribution, they defined the zones around the flexural crack tips as the shear crack band (Figure 2.7b), which is in the compressive field. When the principal tensile stress in the band reaches the concrete tensile strength, inclined cracks develop. They also found that cracking at one point in the band does not necessarily cause a shear failure. Instead, the inclined crack had to reach a certain length. Therefore, they proposed an indicator based on the presence and length of the inclined crack.

2.5 Understanding of shear failure process

Though the reviewed theoretical models reflect different triggers for shear failure, we can still learn from the models to conclude a general shear failure process for members without shear reinforcement.

The shear failure starts with formation of flexural cracks. When shear force increases, the inclination of the flexural cracks increases, and the dowel crack start to open from the bottom of the existing flexural crack (Figure 2.8). At this stage, due to larger crack width, contribution from aggregate interlock reduces. With increasing shear force, the inclined crack and the dowel crack further propagate. At a certain shear force, a flexural shear crack forms. Then depending on whether the flexural shear crack damages the compressive strut or not, the shear capacity of the structure varies. For an uncracked compressive strut, the shear capacity is often larger, determined by concrete compressive strength

(shear compression failure). For a cracked compressive strut, the capacity is lower, determined by shear transfer mechanisms along the flexural shear crack (flexural shear failure). The shear failure process reflects the importance of integrity of the compressive strut on the shear capacity.

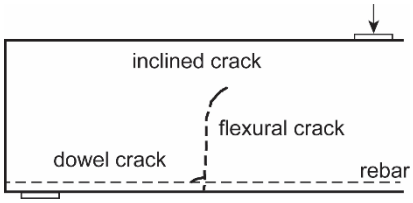

Figure 2.8 Formation of the inclined crack and the dowel crack from the flexural crack.

2.6 Shear failure stop criteria during proof load testing

An effective method to evaluate the structural shear capacity is proof load testing. The structure is loaded until a desired load level, and if the structural behaviour does not violate the predefined stop criteria, the structure has demonstrated its ability to carry the code prescribed load (ACI Committee 437 2013).

In literature, most stop criteria are developed for flexural failure, which could be concrete strain, steel strain, crack width and maximum deflection (Deutscher Ausschuss für Stahlbeton 2000, ACI Committee 437 2013). For shear failure, the stop criteria could be concrete strain and crack width at the critical cross section (Lantsoght 2017, Benitez, Lantsoght et al. 2018). These shear failure stop criteria are developed based on critical shear displacement theory (CSDT).

In Section 2.5 it was pointed out that the integrity of the compressive strut would influence the shear capacity. Therefore, another possible shear failure stop criterion could be related to the integrity of the compressive strut. The integrity of the compressive strut can be evaluated in terms of crack location and width. But only based on current literature, it is hard to conclude a specific shear failure stop criterion from the integrity of the compressive strut.

Chapter 3 Techniques for monitoring shear behaviour of reinforced concrete structures

3.1 Introduction

To monitor shear behaviour of reinforced concrete structures, many techniques are available. This chapter first lists the requirements on a proper monitoring technique during load testing. Then based on the requirements, various techniques are reviewed and compared.

3.2 Requirements on a proper monitoring technique during load testing

From the previous study, to monitor shear behaviour of reinforced concrete structures without shear reinforcement, crack location and width are of special interest. To measure these parameters, the ideal technique should meet a few requirements:

1. The technique should be sensitive to concrete cracking, in terms of the location and preferably the crack width.
2. The technique should be able to cover the whole interesting zone (a so-called full-field measurement), since the crack location is not always predictable.
3. The sensors should be easy to be mounted both in lab and on site.
4. The technique can provide a real-time monitoring so that proper interventions can be taken in time. Here, small time delay (e.g., tens of seconds) is still acceptable in a real-time monitoring, influenced by the data processing time and the data acquisition rate.

These requirements are listed for monitoring shear behaviour during load testing. For long-term monitoring under the service load, an additional requirement is the durability of the sensor under the environmental effect like change of temperature and humidity. Selecting a technique for long-term monitoring is out of the scope of this dissertation.

3.3 Overview of techniques

For a long time, most common monitoring methods are visual inspection (including using rulers) and core drilling. But, these methods are not sufficient because visual inspection could not detect the internal damages, and core drilling could not represent the whole structure.

Nowadays, various techniques have been applied which can provide more information. This section reviews the techniques in terms of their measuring capacity, working principle, pros and cons.

Linear variable differential transformer (LVDT)

An LVDT measures the change of distance between two points. The sensor consists of a movable core, surrounded by coils (Figure 3.1a). When the core moves, due to the elec-

tromagnetic induction, the output voltage increases linearly (fib 2003). In monitoring concrete structures, LVDTs are normally installed between two fixed nodes on the structural surface and measures the crack opening/closure in between (Figure 3.1b).

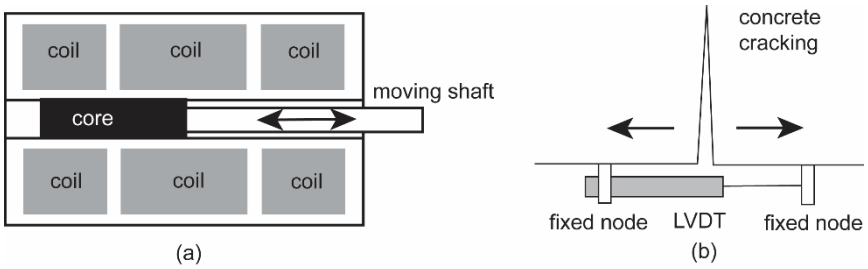

Figure 3.1 Schematic of an LVDT.

LVDTs are robust and sensitive, with accuracy in range of 10-100 μm (Zarate Garnica, Lantsoght et al. 2022). They can be applied both on lab and onsite, as long as the structural surface is not accessible. However, one LVDT can only measure the change of distance between two fixed points. A full-field monitoring is not possible. Moreover, an LVDT cannot distinguish multiple cracks between the nodes. To measure one crack only, the node spacing needs to be sufficiently small compared to the crack spacing.

Electrical resistance strain gauge

An electrical resistance strain gauge measures the strain and temperature change using electrical resistance (Hoffmann 1989). The strain gauge consists of a long thin piece of metal which folds zig zags (Figure 3.2). When the material expands or contracts, the metal gets longer or shorter, changing the resistance of the metal. The resistance change leads to the output voltage change through a Wheatstone bridge circuit.

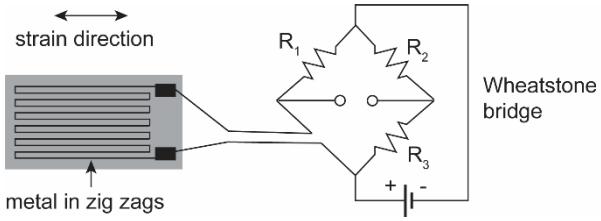

Figure 3.2 Schematic of working principle of an electrical resistance strain gauge.

Temperature variance will influence the measurement of strain. To remove the temperature effect, one can place a strain gauge orthogonal to the direction of the desired strain. The orthogonal one is expected to expand and contract mostly due to temperature change. In this way, the temperature effect can be measured and removed (Christenson 2019). The accuracy of strain gauge is in range of 1-10 με (Zarate Garnica, Lantsoght et al. 2022). However, the installation is hard, requiring smooth surface, strong adhesives and good

protection of the sensor after attachments (Hoffmann 1979). This adds difficulty for on-site monitoring. Moreover, a gauge can only measure the strain at a specific location, which is hard to provide a full-field monitoring. And one gauge can only be used once which is not environmentally friendly.

Optical fibre

Optical fibres measure the strain and temperature change. An optical fibre consists of a core surrounded by a cladding layer with a lower index of refraction (Figure 3.3a). Light can transfer in the core by total internal reflection. The light wavelength (frequency) will change with strain and temperature.

Many types of sensors have been developed using optical fibres, including interferometry sensors, intensity sensors, fibre Bragg grating, optical time domain reflectometry and distributed fibre optic sensors. Detailed descriptions can be found in literature (Chang and Liu 2003, Deng and Cai 2007, Lee, Kim et al. 2012, Soga and Luo 2018). Among them, fibre Bragg grating is one of the most-applied technique. Bragg gratings are pre-fabricated in the fibre, which can reflect the light with a wavelength corresponding to the grating spacing. When strain or temperature changes at the position of gratings, the grating space changes, causing a shift in the reflected wavelength (Figure 3.3b).

Optical fibres are robust and sensitive, with accuracy reaching 1 με and 0.1 °C. But the sensor could not discriminate the strain change and temperature change (Deng and Cai 2007). To detect concrete cracking, the temperature needs to be controlled during a test, especially for on-site measurements. Moreover, the sensor can only measure at discrete points. To overcome this drawback, distributed fibre optic sensors are developed which measures at any given point along the fibre (Guo, Xiao et al. 2011). Another way of achieving distributed sensing is to multiplex various discrete sensors in a fibre, for example every 5 cm in a total length of 10 km (Soga and Luo 2018). Fibre optic sensors can serve for real-time monitoring by constant sending and receiving lights.

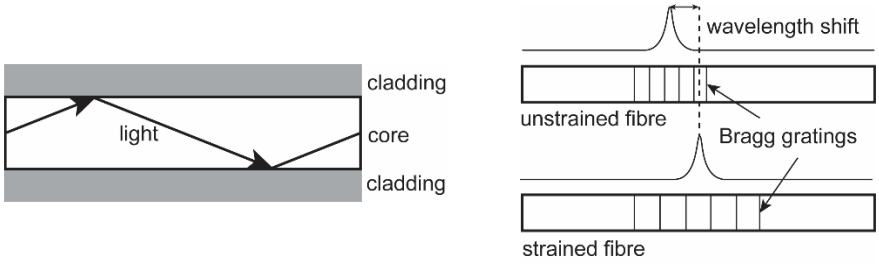

Figure 3.3 Schematic of fibre optic sensors: (a) the core and cladding, (b) working principle of fibre Bragg gratings

Digital image correlation (DIC)

DIC measures the displacements of any point in the measuring zone. The structural surface is painted with a random speckle pattern, which can be a natural texture or made by applying white and black paint (Figure 3.2). Photos of the structural surface at different statuses are used in a DIC measurement. The movement of the patterns in the photos in pixels can be transformed into a displacement field of the measurement area (Jones 2015). From the displacement field, crack opening in both normal and tangential direction to the crack trajectory can be calculated (Zarate Garnica 2018).

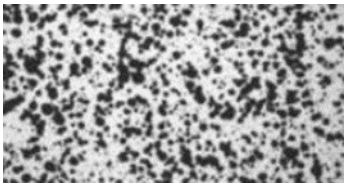

Figure 3.4 Random speckle pattern.

DIC can provide full-field displacements at any point in the measuring zone and in any direction. The accuracy of DIC measurement depends on the pattern quality, the lighting condition, the camera resolution and the resolution of the lens, which can reach 0.1 mm or even smaller. Due to the high requirement on the lighting condition, applying DIC on site is challenging. Real-time monitoring using DIC requires frequent photo-shooting. Considering the image processing time, a delay of a few minutes can occur when high resolution is required.

Ground penetration radar (GPR)

GPR uses radio waves to detect the subsurface reinforcements and cracks in concrete structures. A transmitter antenna sends radio pulses that penetrate through the material. When the pulse meets a discontinuity (which should have different electrical properties and can be cracks or reinforcements in concrete material), part of the energy is reflected to a receiver antenna. The flight time and velocity of the radio pulse signals provide the depth of the discontinuity.

The resolution of GPR can reach a few cm (McCann and Forde 2001). There is a compromise between resolution and penetration depth, depending on the frequency of the antenna. For higher frequencies, the resolution is better, but the penetration depth is lower. The antennas can have central frequencies between some MHz and some GHz (Soutsos, Denys et al. 2012). GPR are most used to detect cracks and reinforcements in parallel with the measuring surface. But crack width cannot be measured. GPR can detect multiple objects in the penetration depth, unless the reflections from the objects do not add together. Antennas do not need to be in contact with the structural surface. They are often mounted on a truck (150-500 mm away from the surface) (Kashif Ur Rehman, Ibrahim et al. 2016).

In this way, the testing is fast and does not influence the traffic. Real-time monitoring is possible by constant scanning (Wang, Zhao et al. 2019). For onsite measurement, the influence of moisture on the accuracy of measurement should be considered. With the increase of moisture, the dielectric permittivity of the material increases, resulting in decrease of wave velocity, which will influence the measurement accuracy (Soutsos, Bungey et al. 2001).

Infrared thermography (IR)

IR uses the infrared light to measure cracks in concrete structures. Two types of infrared thermography are currently applied (Soutsos, Denys et al. 2012, Kashif Ur Rehman, Ibrahim et al. 2016). The first type is passive measurement. The structural surface emits infrared energy and received by infrared sensors (cameras). The output can be converted to temperature. At the location of cracks, the temperature is higher. The second type is active measurement. The structural surface is heated by a radiation source. After switching off the heating source, the cooling down behaviour is recorded with infrared cameras. At the location of cracks, the heat flow will accelerate. From the relative temperature difference between the inside and outline of a crack, Su tried to quantify the crack width using IR (Su 2020). But no consistent relationship has been found. IR is only applicable to measure cracks in shallow depth which is limited by the thermal excitation frequency. In a day-night cycle, the thermal excitation frequency is approximately 1.16×10^{-5} Hz, resulting in only cracks within around 30 cm deep from the surface can be detected in concrete (Soutsos, Denys et al. 2012).

IR allows measuring a large surface area in a short time (Kashif Ur Rehman, Ibrahim et al. 2016). Therefore, this technique is suitable for monitoring large concrete structures (Clark, McCann et al. 2003). It is a compromise between measuring area and spatial resolution, depending on the location of the camera. For a camera at a farther distance, the measuring area is larger, but the resolution is reduced. The accuracy of IR is also influenced by the environmental conditions including wind, solar radiation, and humidity, which needs to be considered especially for on-site measurements.

Radiography

Radiography uses X-rays or gamma rays to detect the reinforcements and cracks in concrete structures. The radiographic energy source is on one side of an object, and a sensitive film is on the other side. Radiation travels through the object and exposes the film. The amount of energy passing through the object is influenced by the local density. At reinforcements, less energy passes through, resulting in lighter grey colour on the film. At cracks, more energy passes through, giving darker grey colour on the film. Radiography can also estimate the crack width, but the accuracy is limited by the image resolution (Chateau, Gélébart et al. 2011).

Compared to other techniques, radiography can provide a direct picture of the internal structure of concrete. But, due to the high attenuation, gamma rays and X-rays can only penetrate 60 cm and 120 cm into concrete, respectively (Soutsos, Denys et al. 2012). Regarding to the application, two faces of the structure must be accessible. Moreover, protections against radiation are needed (McCann and Forde 2001, Kashif Ur Rehman, Ibrahim et al. 2016). This adds difficulties especially for on-site measurements.

Ultrasonic pulse velocity (UPV)

UPV is an active elastic wave-based method which can measure concrete material quality change like presence of cracks or concrete hydration. In a typical UPV measurement, one transducer sends signals into concrete and the others receive the responses. A ray path is built between the two transducers. From wave propagation distance and time, UPV calculates the apparent wave velocity in the ray path. During concrete hydration, the elastic modulus increases, resulting in a higher wave velocity (Cheng, Zhang et al. 2022). And the presence of crack delays the wave travel time, resulting in a lower wave velocity (Pahlavan, Zhang et al. 2018). Moreover, the presence of a crack will also reduce the signal amplitude. An amplitude drop of 10-50 dB was found when a partially-closed crack presents in the ray path (Pahlavan, Zhang et al. 2018). Therefore, some studies use the amplitude drop to find the existing cracks (Chai, Momoki et al. 2011).

Based on UPV, some advanced methods have been developed including elastic wave tomography and AE tomography. The basic principle of these advanced methods is to increase the number of ray paths which can cover a multi-dimensional measuring zone. Detailed explanations can be found in literatures (Schubert 2004, Shiotani, Osawa et al. 2015, Hashimoto, Shiotani et al. 2017, Choi, Palacios et al. 2018).

The resolution of UPV is limited by sensor spacing. When two cracks present between the transducers, UPV is not able to distinguish them. Even in the advanced methods of tomography, the resolution is not much improved. In AE tomography of a reinforced concrete beam, the resolution can only reach half the sensor spacing (Zhang, Yang et al. 2018). To apply UPV on site, sensors need to be protected against moisture (e.g. rain) and collision (e.g. from traffic). One solution can be using embedded sensors in concrete (Song, Gu et al. 2008). In this way, the sensor is protected by the concrete.

Impact echo (IE)

IE measures the depth of cracks, which is also an active elastic wave-based method. A short pulse is sent into a structure by a hammer hitting on the surface. The waves are reflected by cracks and picked up by the transducer next to the hammer hitting point. Then, the waves are reflected into the structure and the cycles begin again. Therefore, the waves have multiple reflections between the two surfaces in a certain frequency. This

frequency is related to the wave speed and depth of cracks, and measured by transforming the received signal into frequency domain (Soutsos, Denys et al. 2012).

IE has the advantage that it only needs access to one structural surface. The results can be influenced by reflections at multiple boundaries, especially for small structures, and scatterings at aggregates (Martin and Forde 1995). Similar to GPR, IE can only locate the cracks that are parallel to the structural surface, and cannot measure crack width.

Acoustic emission (AE)

AE is a passive elastic wave-based method which detects concrete cracking. Unlike the active methods, AE does not send signals into the medium but only receives signals from concrete cracking. Cracking releases energy and generate waves. The waves propagate to the structural surface and are received by sensors. By processing the received waves, AE can identify the crack location (Kundu 2014), crack type (Ohtsu 2010), and determine the structural integrity in terms of crack width (Ohtsu, Uchida et al. 2002).

AE is very sensitive and suitable for crack detection at an early stage (Otsuka and Date 2000, Zhang, Zarate Garnica et al. 2020). Moreover, AE can monitor in real time with a high sampling rate e.g. 40 MHz in Vallen system (VALLEN 2021). To apply AE on site, sensors need to be protected against moisture (e.g. rain) and collision (e.g. from traffic). The drawbacks of AE are: the accuracy of AE is influenced by wave propagation, and quantification of the damage is difficult. A detailed review on the working principle and application is reported in Chapter 4.

3.4 Evaluation of techniques

Table 3.1 evaluates the reviewed techniques according to the requirements in Section 3.2. By comparing, AE is a promising technique which can estimate crack location, provide a full-field measurement, be easily installed, and monitor in real time. Only difficulty for now is measuring the crack width, which deserves further study (Chapter 8).

DIC can measure crack width accurately in full field. In this dissertation, DIC is used as a tool to calibrate AE results and provide crack width information when AE is studied to quantify crack width in Chapter 8.

IR also meets the requirements well but is not applied in this dissertation due to limited time and resources. Other techniques do not meet at least one requirement.

Table 3.1. Summary of available techniques

Technique	Parameter	Requirements of this dissertation				
		1		2	3	4
		Crack location	Crack width	Full-field	Easy installation	Real-time
LVDT	Change of distance	Yes	Yes	No	Yes	Yes
Strain gauge	Strain, temperature	Yes	Yes	No	No	Yes
Fibre optic sensors	Strain, temperature	Yes	Yes	No	Yes	Possible (by constantly sending lights)
DIC	Displacement	Yes	Yes	Yes	Yes	Possible (by constantly scanning)
GPR	Rebar, crack	Yes	No	No	Yes	Possible (by constantly scanning)
IR	Crack	Yes	Possible, but needs further quantification	Yes	Yes	Yes
Radiography	Rebar, crack	Yes	Possible with limited accuracy	Yes	No	Possible (by constantly scanning)
UPV	Crack, hydration degree	Yes	Possible, but needs further quantification	No	Yes	Possible (by constantly scanning)
IE	Crack	Yes	No	No	Yes	Possible (by constantly scanning)
AE	Crack	Yes	Possible, but needs further quantification	Yes	Yes	Yes

Chapter 4 Acoustic emission monitoring of concrete structures

4.1 Introduction

Acoustic emission (AE) is a promising technique for monitoring concrete structures. This chapter reviews the basics of the acoustic emission technique, and its application in concrete structures. In the end, a discussion is given on the promises and challenges of AE techniques, which motivates the further studies in this dissertation.

4.2 Basics of acoustic emission technique

Figure 4.1 illustrates the basic working principle of AE technique. Sudden changes in concrete, like cracking, will release energy and generate elastic waves. Waves propagate to sensors and change into electric signals. These electric signals go through a preamplifier, cables, and come into the data acquisition system. There the signals are filtered, amplified, and then converted into digital signals. After processing of the digital signals, the data can be used by various algorithms, which brings the specific information.

This section describes the whole working principle step by step, including the nature of the AE source (Section 4.2.1), wave propagation in a concrete medium (Section 4.2.2), instruments (Section 4.2.34.2.2), digital signal processing (Section 4.2.4) and AE algorithms (Section 4.2.5). Among these, focus is given to wave propagation in a concrete medium, digital signal processing and AE algorithms.

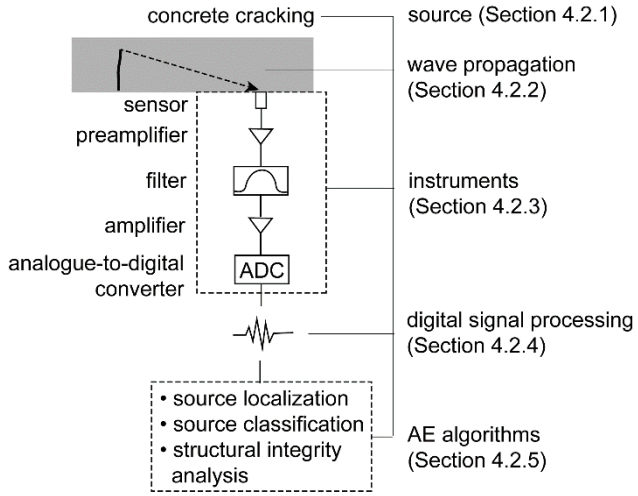

Figure 4.1 Schematic of working principle of AE technique

4.2.1 Acoustic emission source: concrete cracking

From energy balance, the total amount of mechanical energy that is applied to the structure is transferred into internal energy, surface energy, dissipated energy and kinetic energy (Schreurs 2012), where internal energy is the elastically stored energy, surface en-

ergy is used to break intermolecular bonds and generate free surface (Griffith 1921), dissipated energy is mostly due to friction or plastic deformation and results in temperature change, and kinetic energy is related to vibrations and generates AE.

Carpinteri et al. claimed that the amount of AE energy is related to local snapback instability (Figure 4.2) (Carpinteri, Corrado et al. 2013, Carpinteri, Lacidogna et al. 2016). Under displacement control, a sudden drop of load is obtained. 'E' represents the kinetic energy for vibration (AE). Even in a globally stable cracking process, multiple local snapbacks occur.

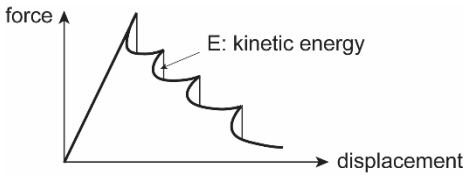

Figure 4.2 Multiple local snapback instabilities at a global stable behaviour, reproduced from Carpinteri, Lacidogna et al. (2016).

This opinion has been proven by various experiments. Aggelis et al. performed bending tests on plain concrete and steel fibre reinforced concrete beams under displacement control (Aggelis, Soulioti et al. 2013). Most AE were observed at local snapback instability, which confirmed the possible relationship. Lacidogna et al. tested several gypsum samples under compression (Lacidogna, Accornero et al. 2019). They considered the global compressive stress interacted with local areas which were in tension and cracked. The tests have been controlled in two ways: through axial displacement or circumferential elongation. For the tests controlled by axial displacement, a clear increase of cumulative AE hits appeared with sudden drop of load in the load-deflection curve. For the tests controlled by circumferential elongation, the decrease of axial displacement at local snapback can be captured experimentally. Therefore, no surplus energy E (denoted in Figure 4.2) was present, and no AE burst was detected. Their experimental results clearly proved a close relationship between AE and kinetic energy at local snapback instability.

Some earlier work related AE energy to fracture energy (Landis and Baillon 2002) (Prasad and Sagar 2008). Fracture energy is calculated as the area under stress-crack width curve (Hillerborg, Modéer et al. 1976). But this possible relationship between AE energy and fracture energy could not be confirmed by experiments.

Therefore, for now, it is more likely that AE is related to the kinetic energy at local snapback instability. To confirm this relationship, further studies are needed but will not be part of this dissertation.

4.2.2 From source to sensors: wave propagation in concrete

Waves propagate from the source to the sensors through the concrete medium. In sound concrete, the wave travelling paths from the source to the sensors are assumed to be straight. If the wavelength is sufficiently larger than the size of the aggregates, concrete can be assumed as a homogeneous medium.

In concrete, waves propagate in forms of body waves and surface waves. Body waves travel through the interior of concrete structures. Two types of body waves are primary waves (P-waves) and secondary waves (S-waves). In P-waves, particles move in parallel to the direction of travel. In S-waves, particles move perpendicularly to the direction of travel. The velocities of P-waves and S-waves can be determined by the classic wave theories (Bedford and Drumheller 1994):

$$c_{\mathrm{P}} = \sqrt{\frac{E(1-\upsilon)}{\rho(1+\upsilon)(1-2\upsilon)}} \tag{4.1}$$

$$c_{\mathrm{S}} = \sqrt{\frac{E}{2\rho(1+\upsilon)}} \tag{4.2}$$

where c_{P} and c_{S} represent the wave speed of P-waves and S-waves, E is the dynamic elastic modulus, υ is the dynamic Poisson's ratio, and ρ is the mass density.

Surface waves travel along the structural surface. In concrete, surface waves are mainly Rayleigh waves (R-waves), where particle movements can be parallel or perpendicular to the travel direction. The calculation of R-wave velocity is complicated, and is often approximated as (Achenbach 2012):

$$c_R = \frac{0.87+1.12\upsilon}{1+\upsilon} c_S \tag{4.3}$$

Supposing a dynamic elastic modulus of 37500 N/mm^2, a dynamic Poisson's ratio of 0.25, and concrete density of 2324 kg/m^3, the wave speeds are 4400 m/s, 2541 m/s and 2336 m/s for P-waves, S-waves and R-waves respectively. With the wave speed, we can estimate wave travel distance from wave travel time or vice versa.

During wave propagation, the signal amplitude reduces, which is called wave attenuation. In sound concrete, wave attenuation mainly comes from geometric spreading loss and material attenuation.

For the geometric spreading loss, P-waves and S-waves follow spherical spreading loss. R-waves follow cylindrical spread loss (Bormann, Engdahl et al. 2012). The expressions in decibel value are:

$$\Delta A_{1,\mathrm{PS}} = -20\log_{10}\left(\frac{r}{d}\right) \tag{4.4}$$

$$\Delta A_{1,\mathrm{R}} = -10\log_{10}\left(\frac{r}{d}\right) \tag{4.5}$$

where r is the source sphere radius, d is the wave travel distance from source to receiver.

Material attenuation includes intrinsic attenuation and scattering attenuation (Owino and Jacobs 1999). Intrinsic attenuation comes from the internal friction between particles. Higher frequency components have larger intrinsic attenuation due to more cycles of particle movements (Bormann, Engdahl et al. 2012). Moreover, S-waves have larger intrinsic attenuation than P-waves due to more friction in the particle motion of S-waves. Scattering attenuation is related to the wavelength (frequency) and scatters in the medium (Gaydecki, Burdekin et al. 1992). In concrete, the scatters could be aggregates or bubbles. Since scattering attenuation is hard to be distinguished from intrinsic attenuation (Owino and Jacobs 1999, Philippidis and Aggelis 2005), they are often described together using a frequency-dependent parameter called material attenuation factor α:

$$\Delta A_2 = \alpha \cdot d \tag{4.6}$$

where the material attenuation factor α is in decibels per length, depending on the implemented frequency and wave modes (Bormann, Engdahl et al. 2012).

When a crack lies between the AE source and the sensor, the wave propagation paths are more complicated. Waves are diffracted by the contact points along the crack and the crack tip (Ogilvy and Temple 1983). Pahlavan et al. tested on several relaxed cracks (the load was removed) with surface openings in the range of [0.05, 3] mm (Pahlavan, Zhang et al. 2018). They found that the amplitude reduced by 10-50 dB depending on the crack opening, and the arrival time delayed by 5-20 μs, possibly related to the angle between the wave propagating direction and the crack.

4.2.3 Instrumentation

This section briefly introduces AE instruments which convert the arrival waves into electric signals and modulates the signals for the later processing.

AE sensors

AE sensors convert the arrival waves into electric signals using piezoelectric ceramic or crystal (Ono 1997). Figure 4.3a shows the schematic drawings of two typical AE sensors, with piezoelectric element in a protection housing.

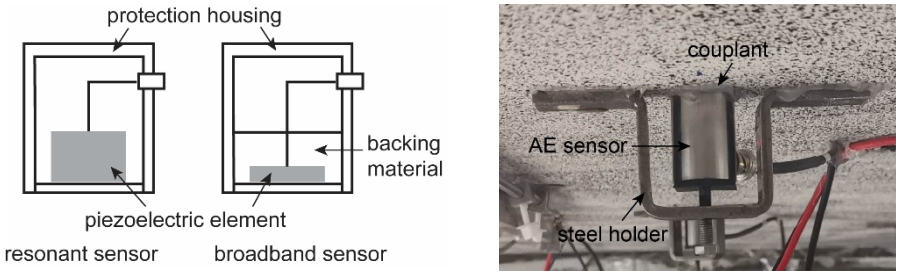

Figure 4.3 (a) Schematic of AE sensors of resonant and broadband type and (b) AE sensor on a concrete specimen fixed with a steel holder.

Two types of sensors are normally used for AE measurements, namely, wideband sensors and resonant sensors. Wideband sensors broaden the frequency response using a backing material behind the piezoelectric element (marked in Figure 4.3a) (Ono 1997). The bandwidth of a wideband sensor can be 1 MHz, while that of a resonant sensor is around 0.1 MHz (MISTRAS 2008). However, wideband sensors are usually less sensitive to waves (Ono 1997, Grosse and Ohtsu 2008): around 50 dB less sensitive than typical resonant sensors (MISTRAS 2008). Therefore, wideband sensors are only preferred when the AE sources type is unknown before the test or the AE signals have a large frequency range.

In concrete, the typical frequency range is from several kHz to 100 kHz (Ono 1997), which is not wideband. Therefore, resonant sensors are normally used. A typical commercial AE sensor is the R6I sensor from Mistras, which has an operating frequency range of 40-100 kHz and resonant frequency at 55 kHz (MISTRAS 2008). Figure 4.4 shows the frequency response of R6I. Here the frequency response is calibrated using two different methods: one is called absolute calibration (the blue line) for burst signals; the other is face-to-face calibration (the red line) for continuous signals (MISTRAS 2010). The detailed descriptions of the two calibration methods can be found in the standards (ASTM E1106-86 1997, ASTM E976-15 2015). Burst signals come from distinct events of energy release such as cracking. Continuous signals are often observed in plastic deformation of metals and leaks of liquid or gas (Ono 1997). In concrete, we mainly have burst signals from cracking and should refer to the absolute calibration.

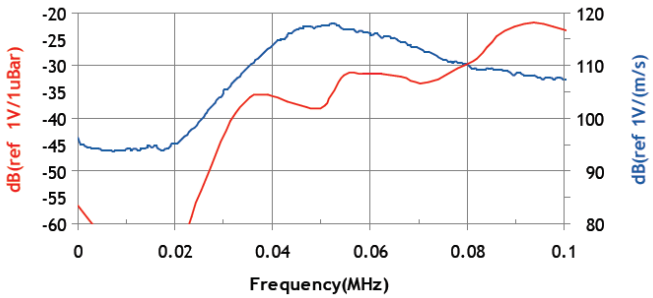

Figure 4.4 Frequency response of R6I from Mistras (MISTRAS 2008), where the blue line is from absolute calibration and the red line is from face-to-face calibration.

Most AE sensors are contact sensors which require a good coupling to the concrete surface. Proper couplants should fill the gaps between sensor surface and rough concrete surface with a layer preferred to be thin. The commonly-applied couplants are vacuum greases, propylene glycol or electrical compound (Theobald, Zeqiri et al. 2008). In addition, no movement between the sensor and the specimen should occur during the loading process. Therefore, a holding device is normally used, such as tapes, elastic bands, or steel holders (Soutsos, Denys et al. 2012). Figure 4.3b shows the installation of a sensor, with sensor, couplant and steel holder marked.

Preamplifiers

Preamplifiers are often used right after the AE sensors to magnify the signals (Grosse and Ohtsu 2008). This is for the purpose to minimize the electromagnetic noise in the cables to the data acquisition system.

The preamplifiers can be outside or inside the sensor. Sensors with internal preamplifiers are of larger size, with only one option of gain (normally 40 dB (MISTRAS 2010)). Sensors with external preamplifiers can be smaller and have different choices of gain (normally 20 dB, 40 dB and 60 dB (MISTRAS 2010)). Using external preamplifiers adds complexity to the installation, especially for on-site measurements.

Data acquisition system

When AE signals come into the data acquisition system, they are firstly filtered and amplified. We can set up different filters and gains. Then the analog signals are digitized by analog-to-digital converters. Further processing of the digital signals will be discussed in the next subsection.

4.2.4 Digital signal processing

Digital signal processing generally has two main objectives: filtering out noises and deriving signal parameters for further analysis using AE algorithms.

Noise Filtering

The received AE signals are not always burst signals from cracking, but also include mechanical noise from environment which are normally continuous signals (Van Steen, Pahlavan et al. 2019). An example is shown in Figure 4.5. A method to filter out this type of noise is dividing the signals into several time windows. For the signal segments in each window, the peak or the root mean square of the amplitude (MISTRAS 2011) is calculated. Signals that have comparable values in different windows are distinguished as noise.

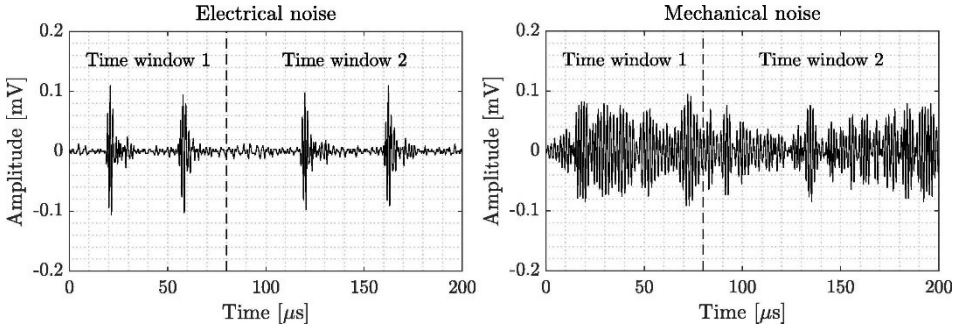

Figure 4.5 Examples of electrical and mechanical noise (Van Steen, Pahlavan et al. 2019).

Another type of noise is electrical noise (Figure 4.5). A same filtering method as mechanical noise can be used (Van Steen, Pahlavan et al. 2019). Moreover, since this type of noise is usually lying outside the informative range of frequencies (Barat, Borodin et al. 2010). Therefore, this noise can also be filtered out by a frequency filter.

Parameters extraction

An AE event can be detected by different sensors. The signal received by a sensor is called an AE hit. The feature of a hit can be described by signal parameters. Signal parameters are used particularly in the conditions that (1) we do not have enough computational time or data storage capacity to deal with the whole waveform, or (2) we only care about some specific signal features.

Various signal parameters are proposed in literature from the waveform in time domain and the frequency spectrum. From the waveform, signal parameters include first arrival, peak amplitude, duration, counts, rise time, counts to peak and energy (Ohtsu 2010, Ohtsu 2010, MISTRAS 2011). Based on these basic parameters, we can further calculate other parameters, such as RA value, average frequency, initiation frequency and reverberation frequency (MISTRAS 2011). From the frequency spectrum, the signal parameters are peak frequency, frequency centroid and partial power (Ono 1997). The definitions of these parameters are given below, and are illustrated in Figure 4.6.

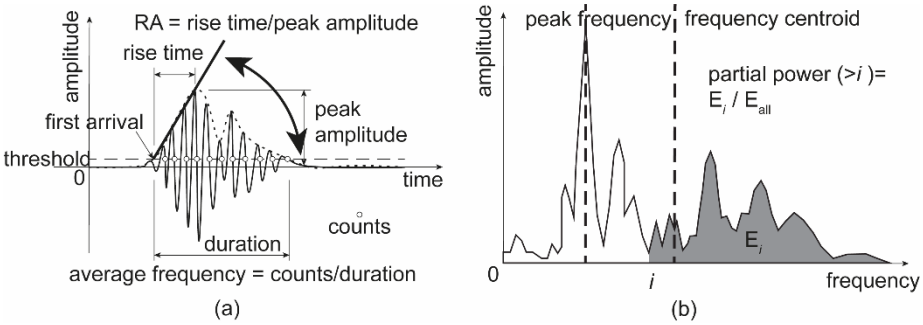

Figure 4.6 Illustration of signal parameters from: (a) waveform in time domain and (b) frequency spectrum.

Definitions of Parameters from waveform in time domain

- First arrival is the first point that crosses the threshold, when threshold arrival time picking method is used. The typical unit is s.
- Peak amplitude is the largest amplitude of the signal envelope. The typical unit is V.
- Duration measures the time duration from the first arrival to the point when the signal envelope decays to the threshold level. The typical unit is s.
- Counts is number of times the signal amplitude exceeds the threshold.
- Rise time is a duration time from the first arrival to the peak amplitude. The typical unit is s.
- Counts to peak is number of times the signal amplitude exceeds the threshold from the first arrival to the peak amplitude.
- Energy is integral of the signal envelop over the duration. The typical unit is Vs.
- RA value is the ratio between rise time and amplitude, which describes the shape of the waveform. The typical unit is s/V.
- Average frequency is defined as counts divided by duration. The typical unit is Hz.
- Initiation frequency is counts to peak divided by rise time. It can be considered as rise time frequency, describing the average frequency from the first arrival to the peak amplitude. The typical unit is Hz.
- Reverberation frequency can be considered as average frequency after the peak amplitude. It is calculated as (counts-counts to peak)/(duration-rise time). The

typical unit is Hz. Average frequency, initiation frequency, reverberation frequency are frequency-related parameters, though calculated in time domain.

Definitions of Parameters from frequency spectrum

- Peak frequency is the point where the frequency spectrum has the maximum amplitude. The typical unit is Hz.
- Frequency centroid is the centre of the mass of the frequency spectrum. The typical unit is Hz.
- Partial power is the percentage, calculated by summing the frequency spectrum in a specified range of frequencies and dividing it by the total energy of all frequencies.

4.2.5 Acoustic Emission algorithms

After data processing, the signals or parameters are ready for various algorithms. These algorithms can estimate the source location, classify source types or determine the structural integrity. Some commonly used algorithms are introduced below.

Source localization

Source localization algorithms estimate the location of an AE event. The commonly used method is based on the arrival times of the signals (Kundu 2014). Inputs are arrival times, sensor locations and wave speed. The basic rule is that the estimated wave propagation distance from the source to the receiver should meet with the measured wave propagation distance:

$$\left\|\mathbf{x}_{\mathrm{r},i}-\mathbf{x}_{\mathrm{S}}\right\| = c_{\mathrm{P}} \cdot \left(t_{\mathrm{r},i}-t_{\mathrm{S}}\right), \forall i \in \left\{1,2,\cdots,N_{\mathrm{r}}\right\} \tag{4.7}$$

where $\mathbf{x}_{\mathrm{S}}$ is the source location, $\mathbf{x}_{\mathrm{r},i}$ is the location of sensor i, c_{P} is the wave speed, $t_{\mathrm{r},i}$ is the arrival time at sensor i, t_{S} is the source time, and N_{r} is the total number of sensors.

In the equation, the left-hand side is the estimated wave propagation distance, and the right-hand side is the measured wave propagation distance.

In Equation (4.7), the sensor location $\mathbf{x}_{\mathrm{r},i}$ is known, the arrival time $t_{\mathrm{r},i}$ can be measured, and the wave speed c_{P} is assumed constant. Therefore, the unknowns are source location $\mathbf{x}_{\mathrm{S}}$ and source time t_{S}. To eliminate the unknown source time t_{S}, Equation (4.7) from two arbitrary sensors are combined, resulting in the differential distance of two arbitrary sensors:

$$\left\|\mathbf{x}_{\mathrm{S}}-\mathbf{x}_{\mathrm{r},i}\right\| - \left\|\mathbf{x}_{\mathrm{S}}-\mathbf{x}_{\mathrm{r},j}\right\| = c_{\mathrm{P}} \cdot \left(t_{\mathrm{r},i}-t_{\mathrm{r},j}\right), \forall i,j \in \left\{1,2,\cdots,N_{\mathrm{r}}\right\} \tag{4.8}$$

where j indicates the second sensor. Now the left-hand side is the estimated differential distance, and the right-hand side is the measured differential distance.

For k-dimensional source localization, the source location $\mathbf{x}_S$ contains k components in x, y and z directions, giving k unknowns. Therefore, at least k instances of Equation (4.8) with $k+1$ sensors at different locations are required. The source location can be calculated analytically by solving the equations.

Apart from the analytical approach, grid search method can also be used by searching the grid point that best fits the requirement (Grosse and Ohtsu 2008). In this method, the measuring zone is discretized by a particular grid. The distance between each grid point to the sensors can be calculated. The best-fitted grid point should meet the requirement that the residual r between calculated and measured differential distance is the minimum:

$$r(\mathbf{x}_{g,p}) = \sum_{i=1}^{N_r-1} \sum_{j=i+1}^{N_r} \left(\left\| \mathbf{x}_{g,p} - \mathbf{x}_{r,i} \right\| - \left\| \mathbf{x}_{g,p} - \mathbf{x}_{r,j} \right\| - c_P \cdot \left(t_{r,i} - t_{r,j} \right) \right)^2, p \in \left\{ 1, 2, \cdots, P_g \right\} \quad (4.9)$$

where $\mathbf{x}_{g,p}$ is the location of grid point p, among a total number of P_g grid points.

Uncertainties during the localization process may generate errors (Zhang, Pahlavan et al. 2020). The uncertainties can come from the arrival time picking error and wave propagation in concrete including the presence of cracks between source and sensors, and large sensor spacing which may fail receiving some signals. With grid search methods, the layout of the grid points can also introduce errors in source localization: as the measuring area is discretized, the sources can only be assigned to the grid points, which may not be the real location.

The source localization accuracy can be improved by reducing these uncertainties, like using advanced arrival time picking algorithm to reduce the arrival time picking error (Schechinger and Vogel 2007), adopting variable wave speed models to include the influence of cracks on wave propagation (Pahlavan, Paulissen et al. 2014, Gollob 2017), measuring the wave attenuation property in a preliminary test (Pahlavan, Zhang et al. 2018) to arrange a proper sensor spacing, or discretizing the measuring area into a dense grid to reduce the error from the grid search method. But these solutions usually take longer computational time and the uncertainties cannot be entirely removed.

Source classification

Source classification distinguishes signals from different types of sources, i.e. tensile cracking and friction in concrete. Tensile cracking occurs when the maximum principal stress exceeds concrete strength and the two crack faces move away from each other. Friction occurs when the two crack faces slide against each other, due to a protruding aggregate. In literature, the source type ‘friction’ is sometimes mentioned as ‘shear cracking’. But the actual phenomenon of shear cracking is: tensile cracking mixed with friction

between crack faces (Yang 2014). Therefore, this dissertation uses a more specific description 'friction', instead of 'shear cracking' to describe the real source of AE signal.

Generally, two types of methods are used: parameter-based and signal-based methods.

Parameter-based method

The RILEM technical committee recommends to use signal parameters RA value and average frequency to distinguish signals from tensile cracking and friction (Figure 4.7) (Ohtsu 2010). Signals from tensile cracking normally have a smaller RA value and a higher average frequency (Aggelis 2011, Livitsanos, Shetty et al. 2020, Zhang, Zarate Garnica et al. 2020). However, RILEM does not specify clear and consistent boundaries to distinguish the two types of sources. The boundaries may change with different experiments.

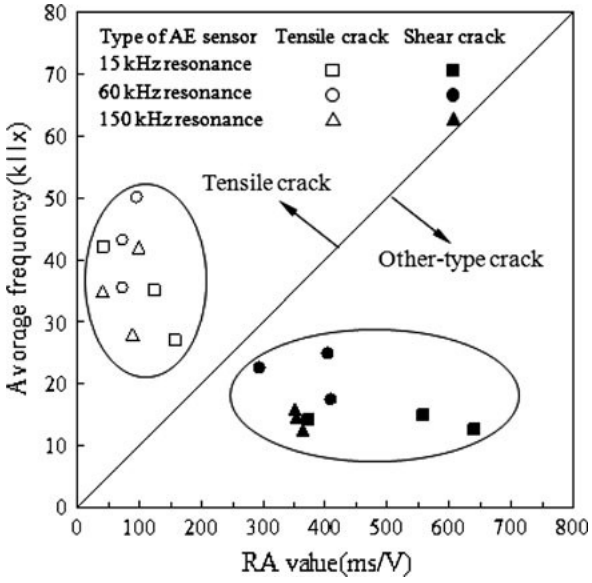

Figure 4.7 Source classification using RA value and average frequency (Ohtsu 2010)

Signal-based method

Signal-based method takes the advantage of the full information of a waveform including wave modes and reflections. In literature, two signal-based methods are present: one uses correlation of the whole signal (either the waveform in time domain or the frequency spectrum); the other uses the P-waves and S-waves of the signal in a moment tensor inversion.

The first method compares two signals using the coherence functions (Carter and Ferrie 1979, Grosse and Ohtsu 2008). The similarity of the signals is used as a measure of virtual distance between them. Signals from the same type of source are similar with shorter

virtual distance. Based on the correlation, van Steen et al. proposed a hierarchical clustering approach (Van Steen, Pahlavan et al. 2019).

The approach has been applied both to the waveform in time domain (Van Steen, Pahlavan et al. 2019) and the frequency spectrum (Srivastava 2020). For the waveform, a cross-correlation calculation is needed, requiring sliding along the time axis, as two signals may arrive at different times. This takes extra computational time. For the frequency spectrum, a simple correlation is sufficient (Carter and Ferrie 1979). Srivastava compared the clustering in time and frequency domain, and found that with the same amount of data (220 AE events), clustering in frequency domain was 4 times faster than that in time domain, presenting comparable results (74% AE events had same results) (Srivastava 2020).

The second method is moment tensor analysis (Jost and Herrmann 1989). It uses P-waves and S-waves of the received signal to quantify the crack mechanism including tensile mode, friction mode and mixed mode. Then Ohtsu proposed a simplified procedure only using P-waves to determine the crack type (Ohtsu, Shigeishi et al. 1991, Ohtsu, Okamoto et al. 1998, Shigeishi and Ohtsu 2001). The detailed description of the moment tensor analysis is not presented here.

Structural integrity analysis

Structural integrity analysis determines the damage level of the structure using AE. Two main strategies are reported in literature. One is load ratio-calm ratio. The other strategy is based on statistical analysis of AE signal strength/amplitude, including methods of intensity analysis and *b*-value analysis. The principles of these methods are introduced below.

Load ratio-calm ratio

Under cyclic loading, load ratio is defined as the ratio between the load level when AE occurs in the subsequent loading and the previous maximum load. And calm ratio is the number of AE hits in unloading divided by the total AE hits in the load cycle (Ohtsu, Uchida et al. 2002).

$$\text{load ratio} = \frac{\text{load when AE occurs in the subsequent loading}}{\text{maximum previous load}} \tag{4.10}$$

$$\text{calm ratio} = \frac{\text{number of AE events during unloading}}{\text{total AE events in the load cycle}} \tag{4.11}$$

The physical meaning of load ratio can be explained by the Kaiser effect. The Kaiser effect describes an AE phenomenon that AE occurs only after the previously applied stress level is exceeded (Kaiser 1950). With Kaiser effect, the load ratio is over 1.0. This

is often the case when concrete is uncracked. After cracking, Nagataki et al. reported that the Kaiser effect disappears (which means AE occurs before reaching the previous maximum stress) when the crack width is over 0.2 mm (Nagataki, Okamoto et al. 1991). The value of crack width when the Kaiser effect disappears varied among other researches (Ohtsu, Uchida et al. 2002, Barbara, Grzegorz et al. 2012).

Calm ratio describes the phenomenon that the number of AE hits during unloading is limited when the structure is statically stable (Ohtsu, Uchida et al. 2002).

Based on load ratio and calm ratio, Ohtsu et al. proposed criteria for different damage levels, i.e. minor damage, intermediate damage and heavy damage (Figure 4.8) (Ohtsu, Uchida et al. 2002). The damage level is severer when a smaller load ratio and a larger calm ratio are measured. However, the boundaries of load ratio and calm ratio to separate the damage levels were not consistent among tests in various literature (Colombo, Forde et al. 2005, Tsangouri, Remy et al. 2019). For concrete bridges, RILEM suggests a load ratio boundary of 0.3-0.45, and a calm ratio boundary of 0.6 (Ohtsu 2010). This threshold was based on tests of concrete beams with only 2-3 m span. A real bridge may have more than 10 times larger span. Yang et al. tested a reinforced concrete slab bridge (Zijlweg bridge, the Netherlands) with a span of 10.32 m (Yang, Hordijk et al. 2016). Most AE sensors showed load ratios over 0.5 and calm ratios lower than 0.4. They considered the damage level as intermediate.

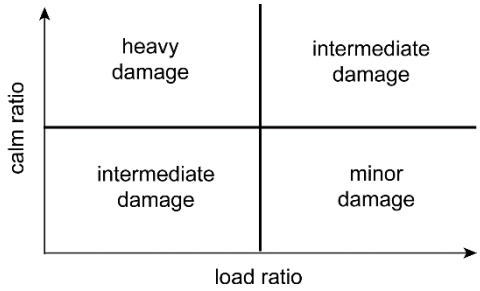

Figure 4.8 Damage assessment by load ratio and calm ratio, reproduced from Ohtsu (2010).

Other parameters have also been developed with the similar background. Ridge and Ziehl developed peak cumulative signal strength (PCSS) ratio, which required at least two repeated load cycles and each need to be hold for a while before unloading (Ridge and Ziehl 2006). The PCSS ratio was the PCSS in the reload hold period divided by the PCSS in the initial load hold period. Significant damage led to PCSS ratios larger than 0.4. Colombo et al. proposed another parameter, i.e. relaxation ratio, which was the average AE energy during unloading divided by the average AE energy during loading (Colombo, Forde et al. 2005). When the structure is damaged, AE during unloading increased, resulting in a larger relaxation ratio. This parameter has a similar background as calm ratio.

Application of these parameters can be found in Abdelrahman's dissertation (Abdelrahman 2013).

Intensity analysis

Intensity analysis uses two statistical parameters, i.e. historic index and severity index to determine the damage level (Fowler 1986). Historic index describes the change of average signal strength compared to history.

$$H(t) = \frac{\sum_{i=K+1}^{N_h} S_{O,i} / (N_h - K)}{\sum_{i=1}^{N_h} S_{O,i} / N_h} \tag{4.12}$$

where N_h is the number of AE hits up to time t, $S_{O,i}$ is the signal strength of the hit i, and K is an empirical constant depending on material and value of N_h (Nair and Cai 2010).

Severity index is the average of the J largest signal strength.

$$S_r = \sum_{i=1}^{J} S_{O,i} / J \tag{4.13}$$

where $S_{O,i}$ is the signal strength of the hit i, given i is sorted in a descending order based on the magnitude of the signal strength. J is an empirical constant depending on material. A value of 50 is normally used for concrete (Golaski, Gebski et al. 2002, Benedetti and Nanni 2014).

Figure 4.9 shows the intensity chart determined by historic index and severity index (CARP 1987). This chart can distinguish damage levels from 'insignificant' to 'major'. The damage level is heavier with larger values of historic index and severity index. The boundaries of historic index and severity index were experimentally derived for fibre-reinforced plastic vessels (Fowler 1986, Fowler, Blessing et al. 1989). Golaski et al. showed that the boundaries can be applied for prestressed concrete beams in lab (Golaski, Gebski et al. 2002). But, in on-site measurements, the historic index did not always provide proper and reliable results (Golaski, Gebski et al. 2002). Benedetti and Nanni tested on a reinforced concrete slab in a three-story building (Benedetti and Nanni 2014). They used boundaries not in line with the intensity chart provided by Fowler.

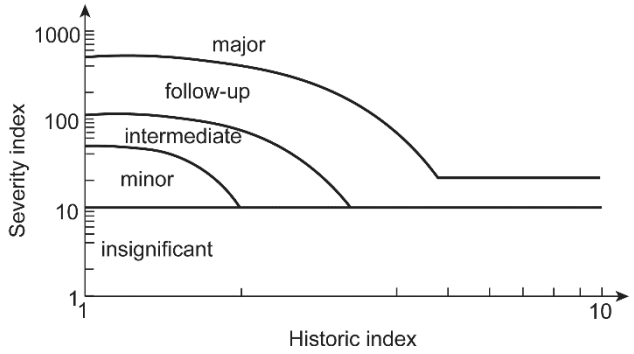

Figure 4.9 Intensity chart for fibre-reinforced plastic, reproduced from CARP (1987)

The applicability of intensity analysis is limited by the empirical constants both in historic and severity indices. Besides, the severity index is based on the absolute value of signal strength which depends on the wave propagation medium and AE instruments.

b-value analysis

b-value analysis originated from seismology, where earthquakes of larger magnitude occurred less frequently than those of smaller magnitude (Gutenberg and Ritcher 1954). For AE, an adopted equation was proposed by Sammonds et al. (Sammonds, Meredith et al. 1994):

$$\log_{10} N_e = a - b\left(\frac{A_{dB}}{20}\right) \tag{4.14}$$

where A_{dB} is the peak amplitude of AE events in decibels, N_e is the number of AE events within an amplitude range ($A_{dB} \pm \Delta A_{dB}$), a and b are both empirical constants determined from linear curve fitting, b is the so-called b-value.

Typically, the b-value decreases from microcracking to macrocracking (Colombo, Main et al. 2003, Schumacher, Higgins et al. 2011). However, the value normally had a large fluctuation, especially for on-site monitoring (Farhidzadeh, Salamone et al. 2013). Farhidzadeh et al. claimed that the large fluctuation could come from the environmental noise. They used a Gaussian filter to smooth the b-value (Farhidzadeh, Dehghan-Niri et al. 2013). Shiotani et al. improved the b-value analysis by considering the statistical distribution of AE amplitude (Shiotani, Fujii et al. 1994). Improved b-value analysis was applied in monitoring a reinforced concrete pier (Shiotani, Luo et al. 2007), and was shown to be more stable compared to the b-value. Nevertheless, it is still hard to set a criterion to distinguish microcracking from macrocracking.

4.3 Application of acoustic emission in concrete structures

In 1959, Rüsch first studied AE phenomena in concrete and found the Kaiser effect in concrete when reaching 75% of the failure load (Rüsch 1959). Since then, AE in concrete structures has drawn a great deal of attention, including lab tests and onsite measurements.

Different from lab tests, onsite measurements have the challenges of large noise, complex loading (e.g. ambient traffic load), environmental conditions like temperature changes, and lack of information especially for existing concrete structures.

This section reviews the onsite applications of AE in concrete structures, including existing concrete structures and new concrete structures. A few typical examples are described.

4.3.1 Monitoring existing concrete structures

Depending on the purpose, existing concrete structures can be monitored under only traffic and environmental load or during load testing. The former one is to continuously monitor the structural behaviour in service condition which usually takes longer time. The latter one is to quickly determine the structural condition by applying a relatively large load.

Under traffic and environment load

Bayane et al. monitored a reinforced concrete bridge deck slab for one year (Bayane and Brühwiler 2020). The deck slab at a span is instrumented by AE sensors, associated with strain gauges and thermocouples. They observed that AE parameters are related to temperature changes during the year. They also found that sensors near slab-girder connection and supports received more AE activities, which could be due to the friction. This application proved the robustness and feasibility of using AE in a long-term monitoring.

Van Steen et al. monitored a heavily-corroded column of an existing building (Van Steen, Zhang et al. 2018). Corrosion has led to concrete cover delamination, which required interventions (Figure 4.10a). Six AE sensors were installed around the delamination zone in a column. With only service and environment load applied, the monitoring took in total 18 hours (3 days with 6 hours/day). The localization results showed that all AE events were located next to the delamination zone in the height direction (Figure 4.10b). Since the delamination zone was observed from outside, AE events next to it could indicate further delaminating inside. Longer monitoring time is needed to find relationship with environmental changes like temperature.

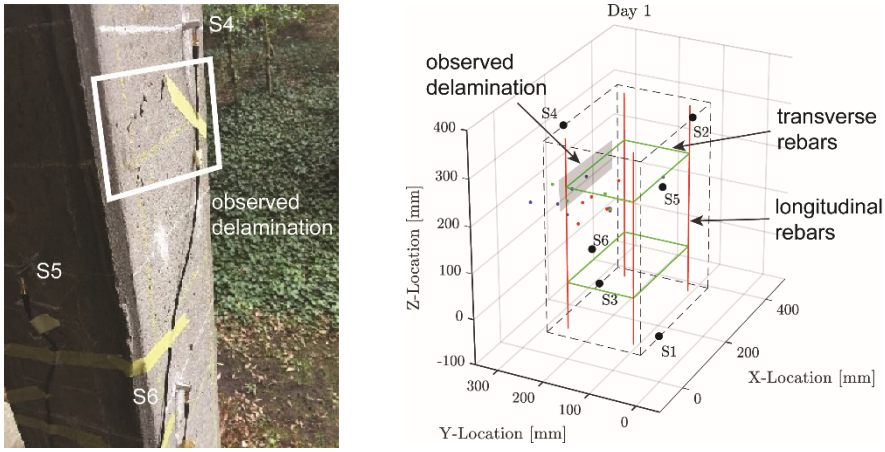

Figure 4.10 AE monitoring of corroded reinforced concrete column in Camilo Torres: (a) observed delamination, (b) sensor layout (S1-6) and localization results in Day 1, reproduced from Van Steen, Zhang et al. (2018)

During load testing

A typical example is the AE monitoring of a 45-m concrete bridge reported by Shiotani et al. (Shiotani, Aggelis et al. 2009). A total of 28 AE sensors were installed on the bottom surface of the bridge, and in the longitudinal direction with a spacing of 1.5 m. A load truck of 20 ton passed over the bridge. Figure 4.11 illustrates the sensor layout and the passing load truck. The results showed that sensor 10 received the most AE hits (around 15 m to the left support). Thus, more damages were expected there than at other locations. Afterwards, a detailed check was performed at the weak location around sensor 10 (which is referred as velocity examination in Figure 4.11).

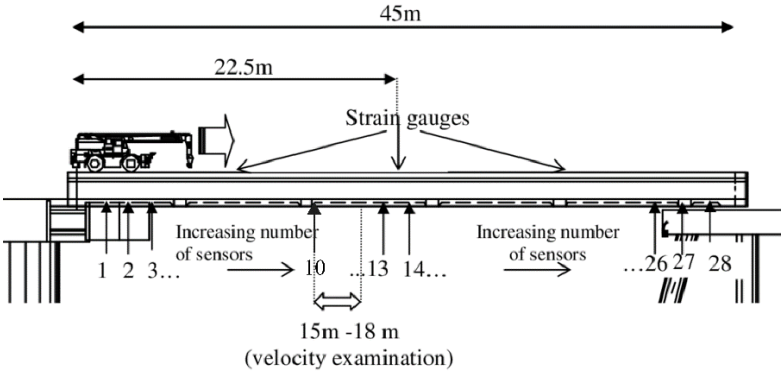

Figure 4.11 AE monitoring of a 45-m concrete bridge, reproduced from Shiotani, Aggelis et al. (2009).

Yang et al. applied AE in proof load testing of a reinforced concrete slab bridge (the Zijlweg bridge in the Netherlands) (Yang, Hordijk et al. 2016). Due to Alkali-Silica Reaction (ASR), the bridge was rated low for shear capacity. The bridge was proof loaded to assess the residual capacity. If the capacity is proved to be sufficient, the bridge could remain in service.

A total of 15 AE sensors were installed on the bottom of one bridge span. Two axle loads were applied, with the load magnitude corresponding to the Eurocode traffic load model 1 (CEN 2003). Figure 4.12 shows the location of load and sensors. Structural integrity analysis using load ratio and calm ratio was carried out. They found that the most damaged part was around AE06, where the damage level was still below the moderate level. This indicated that the bridge was safe under the desired load, which was in line with the conventional displacement measurements (Lantsoght, Koekkoek et al. 2018).

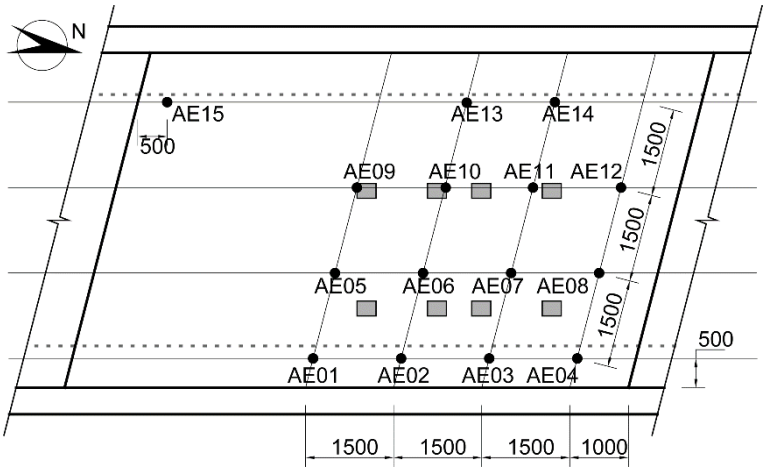

Figure 4.12 AE monitoring of Zijlweg bridge: sensor layout (AE01-15) and loading position (the gray wheel prints), reproduced from Yang, Hordijk et al. (2016)

4.3.2 Monitoring new concrete structures

New concrete structures also require monitoring in the condition that damages may occur during fabrication and transport of precast members, or during load testing prior to service.

During fabrication and transport of precast members

Huston et al. uses AE to detect the cracks that may form during fabrication and transport of the precast members (Figure 4.13a) (Dryver R. Huston and Mauricio 2021). During fabrication, eight AE sensors were installed in the end zone (Figure 4.13b). During detensioning the prestressing strand, a large number of AE events were detected (Figure 4.13b). These AE events could indicate formation of horizontal web cracks, but the localization results were not accurate enough.

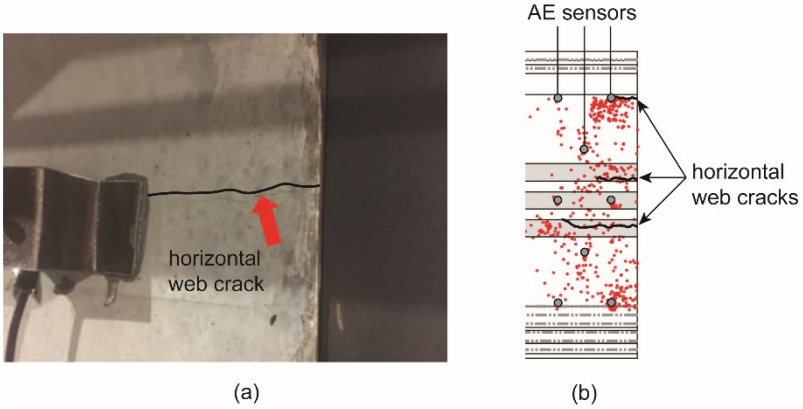

Figure 4.13 AE monitoring of horizontal web cracks during detensioning: (a) horizontal web crack, (b) sensor layout in the end zone and the AE source locations, reproduced from Dryver R. Huston and Mauricio (2021)

During transport from the factory to the bridge site, the sensors were installed in the mid-span. AE events were observed when the vehicle movement tended to bend the girder at tight turns. AE results provided insights into concrete cracking before in use, which was valuable for the future structural assessment.

During load testing of new concrete structures

Load testing can also be carried out on new structures, to prove the structural capacity prior to opening. AE can be applied during load testing of new structures.

Golaski et al. tested a new prestressed concrete bridge using AE (Golaski, Gebski et al. 2002). The bridge was loaded until the load level specified by the design code. This was the first time that the bridge was loaded. The AE method of severity and historic index was used to study the structural integrity. According to the intensity chart (Figure 4.9), all data fell into region of 'insignificant damages'. This proved that the concrete bridge was safe to open. Moreover, many investigators and supervisors found a great need to evaluate a new structure using AE. For a bridge that was graded 'insignificant damages' according to the intensity chart, a so-called 'AE Certificate' was provided.

4.4 Promises and challenges of acoustic emission technique

Literature has shown great promises of AE: by nature, AE is closely related to concrete cracking; through wave propagation, the internal cracking can be detected from outside; the AE instruments allow a real time monitoring with a very high sampling rate; and with various algorithms, AE can provide valuable information on crack location, crack type, and structural integrity in terms of crack width.

However, AE has not been fully devised. For example, the source localization result is not accurate, due to uncertainties in the process. And the source classification is strongly

influenced by wave propagation, leading to wrong results. Moreover, even though AE is closely related to cracking, it is difficult to quantify crack width using AE. And for the scope of this dissertation to indicate structural shear failure, very few applications can be found in the literature that link AE phenomena with shear failure processes.

According to the promises and challenges of AE, this dissertation attempts to further develop the technique by properly interpreting the erroneous source localization results (Chapter 6) and improving the source classification method (Chapter 7). With the new algorithms, the dissertation expects to better understand the relationship between AE phenomena and crack kinematics (Chapter 8), and develop an AE-based indicator for shear failure of reinforced concrete structures without shear reinforcement (Chapter 9).

Chapter 5 Experiments

5.1 Introduction

As stated in Chapter 1, experimental study is an important methodology to reach the goal of this dissertation, which is to develop AE-based failure indicators for reinforced concrete structures without shear reinforcement. The experiments should be representative of the target type of structure and monitored by AE until failure.

This dissertation uses series of tests on reinforced concrete beams and slabs that were performed in the Stevin Laboratory of Delft University of Technology (Figure 5.1). They can be used for the purpose of this dissertation, since (1) the specimens have no shear reinforcement, (2) the specimens are at scale of real structural elements, (3) the specimens are loaded to failure and (4) the structural behaviour has been monitored by various techniques including acoustic emission (AE).

(a) (b)

Figure 5.1 Photos of the tests on (a) reinforced concrete beams and (b) reinforced concrete slabs.

A note is that these tests were not specifically designed for the purpose of this dissertation. This chapter only describes the relevant parts. The original tests and additional information can be found in the reports on beam tests (Yang 2020) and slab tests (Zarate Garnica 2021).

Section 5.2 and Section 5.3 introduce the beam tests and slab tests respectively, including test setup, measurements, and an summary of results. Section 5.4 introduces the setup of the AE system and initial AE monitoring results.

5.2 Reinforced concrete beam tests

Six failure tests are taken from a series of tests on shear behaviour of reinforced concrete beams without shear reinforcement (Yang 2020). In the series, the tests are named as H601A, H602A, H603A, H604A, H851A and I123A.

5.2.1 Test setup

The dimensions of the beams are 10000 mm × 300 mm × 1200 mm. The concrete class is C65. The reinforcement layout is shown in Figure 5.2. I123A has plain rebars, and the rest have ribbed rebars. The tested end has no shear reinforcement.

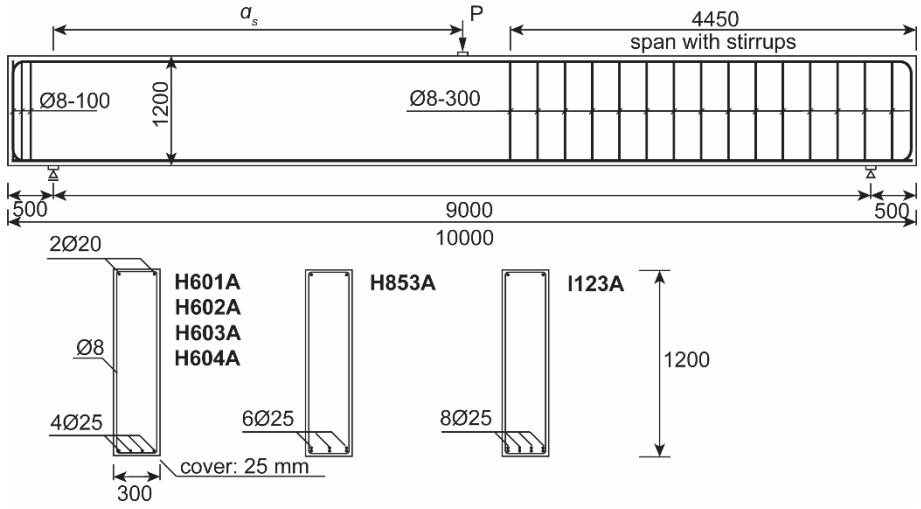

Figure 5.2 A sketch of beam configuration including beam dimension, reinforcement layout and locations of supports and load.

The beams were simply supported and loaded by a single point load. The distance between the centre of the point load and the closer support (defined as shear span) was a main variable, which was between 3000 mm and 4500 mm. The load was applied through a hydraulic jack in a displacement-controlled manner. The loading speed was 0.02 mm/s, except for some load cycles in H603A. There various loading speeds from 0.02 mm/s to 0.64 mm/s were taken, to evaluate the influence of loading speed on AE measurements (discussed in Chapter 8). Figure 5.3 is a photo of the test setup including frame, support, and hydraulic jack.

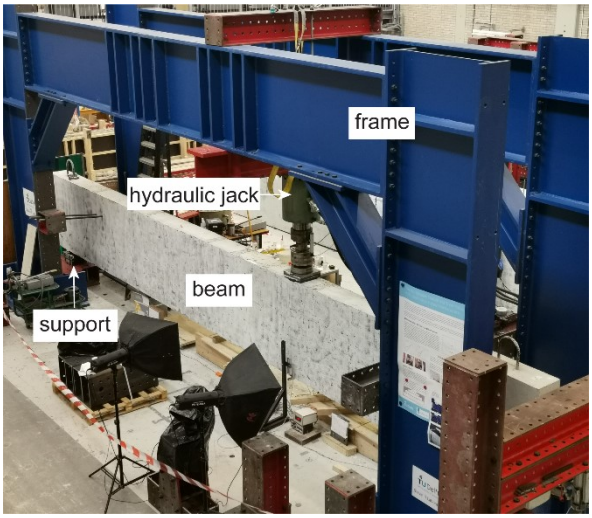

Figure 5.3 Photo of test setup including frame, support and hydraulic jack.

The loading histories of each beam test are given in Figure 5.4. When the beam was cyclically loaded, generally 2-4 load cycles were applied per load level. The first cycle was used to gradually load to the maximum in steps, and the others were used to check whether the structure behaviour is stable. In H601A and H603A, more load cycles were applied (47 and 75 respectively), to evaluate the influence of the number of cycles on AE measurements (discussed in Chapter 8).

Table 5.1 lists the test configurations, including concrete cubic compressive strength ($f_{c,cube}$) at a certain age, rebar configuration, rebar characteristic yield strength (f_{yk}), reinforcement ratio (ρ_s), shear span (a_s), effective depth (d_e), shear span ratio (a_s/d_e) and load type.

Table 5.1 Test configurations

Test no.	H601A	H602A	H603A	H604A	H853A	I123A
$f_{c.cube}$ [MPa]	86.40	86.08	86.08	86.08	82.99	78.24
Age [d]	31	38	46	66	86	85
Rebar Config.	4Ø25 Ribbed	4Ø25 Ribbed	4Ø25 Ribbed	4Ø25 Ribbed	6Ø25 Ribbed	8Ø25 Plain
f_{yk} [MPa]	500	500	500	500	500	240
ρ_s [%]	0.57	0.57	0.57	0.57	0.85	1.14
a_s [mm]	4500	4500	3000	3500	3000	3000
d_e [mm]	1158	1158	1158	1158	1150	1150
a_s/d_e [-]	3.89	3.89	2.59	3.02	2.61	2.61
Load type	Cyclic	Monotonic	Cyclic	Cyclic	Cyclic	Cyclic

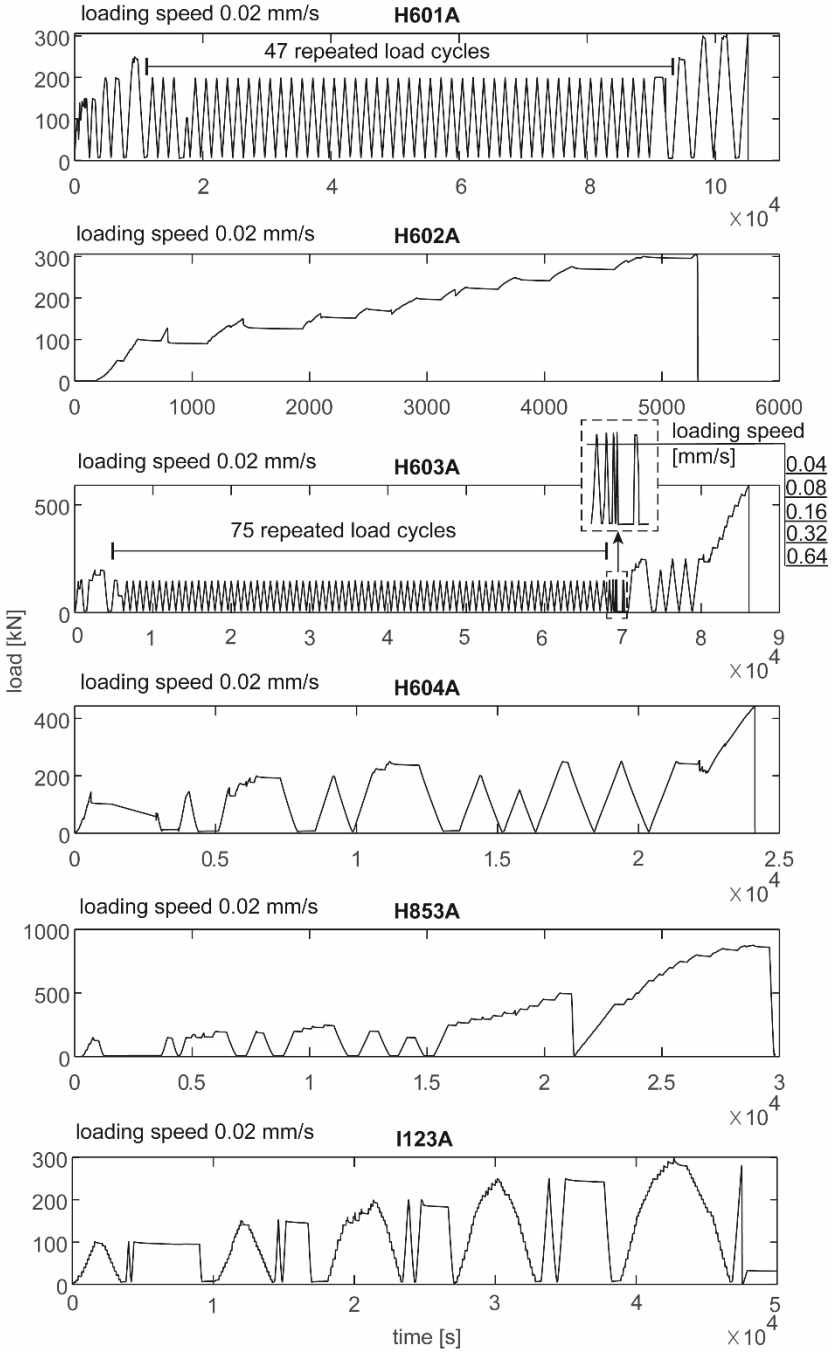

Figure 5.4 Loading history of the beam tests.

5.2.2 Measurements

The measurements during the tests included sensors for load measurement (load cell), displacement measurement (linear variable differential transformer (LVDTs), laser triangulation displacement sensors (lasers), digital image correlation (DIC)), and acoustic emission (AE) measurement (AE sensors). Figure 5.5 shows all the applied sensors (photos taken from test H601A). This section does not include AE measurements which will be detailed described in Section 5.4.

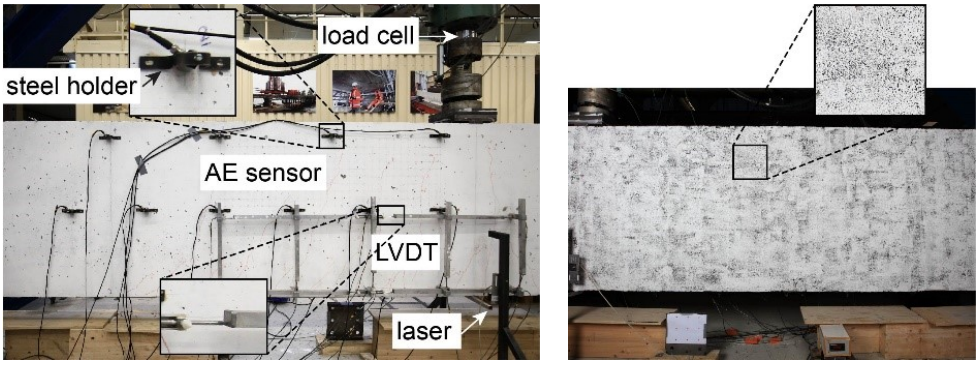

(a) (b)

Figure 5.5 Applied sensors in beam tests: (a) load cell, LVDTs, laser, AE sensors on one side and (b) DIC pattern on the other side (photos taken from test H601A).

Load measurement

A load cell was placed under the hydraulic jack to measure the applied load (Figure 5.5a).

Displacement measurement

LVDTs were used to measure the surface deformation such as opening of cracks between two fixed points. LVDTs were installed in a grid covering the lower half of the beam to measure the crack opening. A typical LVDT grid is given in Figure 5.5a, which included four horizontal ones at mid height, four horizontal ones at level of reinforcements, and five vertical ones in between.

A pair of lasers were installed under the loading point, at both sides of the specimen, to measure the vertical deflection. Figure 5.5a shows one laser at one side.

DIC was applied on the other side than LVDTs and AEs, to measure the crack pattern (Figure 5.5b). Detailed setups were reported by Zarate Garnica (2018). The direct output of DIC analysis was the displacement field of the photo. The displacement field was then converted into the principal strain distribution. The obtained strain field reflected the crack pattern. The DIC analysis used a publicly available Matlab code (Jones 2015). With

the crack pattern known, we further used the displacement field from DIC to calculate the local crack kinematics (Zarate Garnica 2018).

5.2.3 Summary of test results

This section summarises the experimental results that are relevant to the study of this research. That includes the load level at critical structural behaviour, failure mode and crack patterns.

Table 5.2 lists the load level when the first flexural crack opens (P_{CR1}), the load level when the critical flexural shear crack opens (P_u), the maximum load (P_m) and the failure mode of the tests. The load level when a certain crack opens (the first flexural crack or the critical flexural shear crack) was obtained from the real-time monitoring of crack opening using LVDT, DIC and AE. The technique that earliest detected the cracking determined when the crack first opened.

The failure mode includes flexural shear failure (FS) and shear compression failure (SC). The definitions of these failure modes have been introduced in Chapter 2. In a flexural shear failure, the specimen failed at formation of a critical flexural shear crack ($P_m = P_u$). For shear compression failure, after formation of critical flexural shear crack, compressive strut carried additional force, leading to larger failure load ($P_m > P_u$).

Table 5.2 Cracking load and failure mode

Test no.	P_{CR1} (kN)	P_u (kN)	P_m (kN)	Failure mode*
H601A	145	306	306	FS
H602A	125	306	306	FS
H603A	150	271	589	SC
H604A	150	251	445	SC
H853A	175	273	500	SC
I123A	170	300	300	FS

* FS represents flexural shear failure, SC represents shear compression failure.

Figure 5.6 shows the crack patterns after failure, observed from one side of the beams. The locations of load, support, AE sensors and LVDTs are also marked. The major cracks are numbered from CR1 to CRn according to their opening sequence. Generally, cracks first appeared at the cross section with the largest bending moments; thus the crack number increased from right (load side) to left (support side). Cracks that were outside the AE measuring zone are not numbered. They were mostly at the other span which is not interesting for this study.

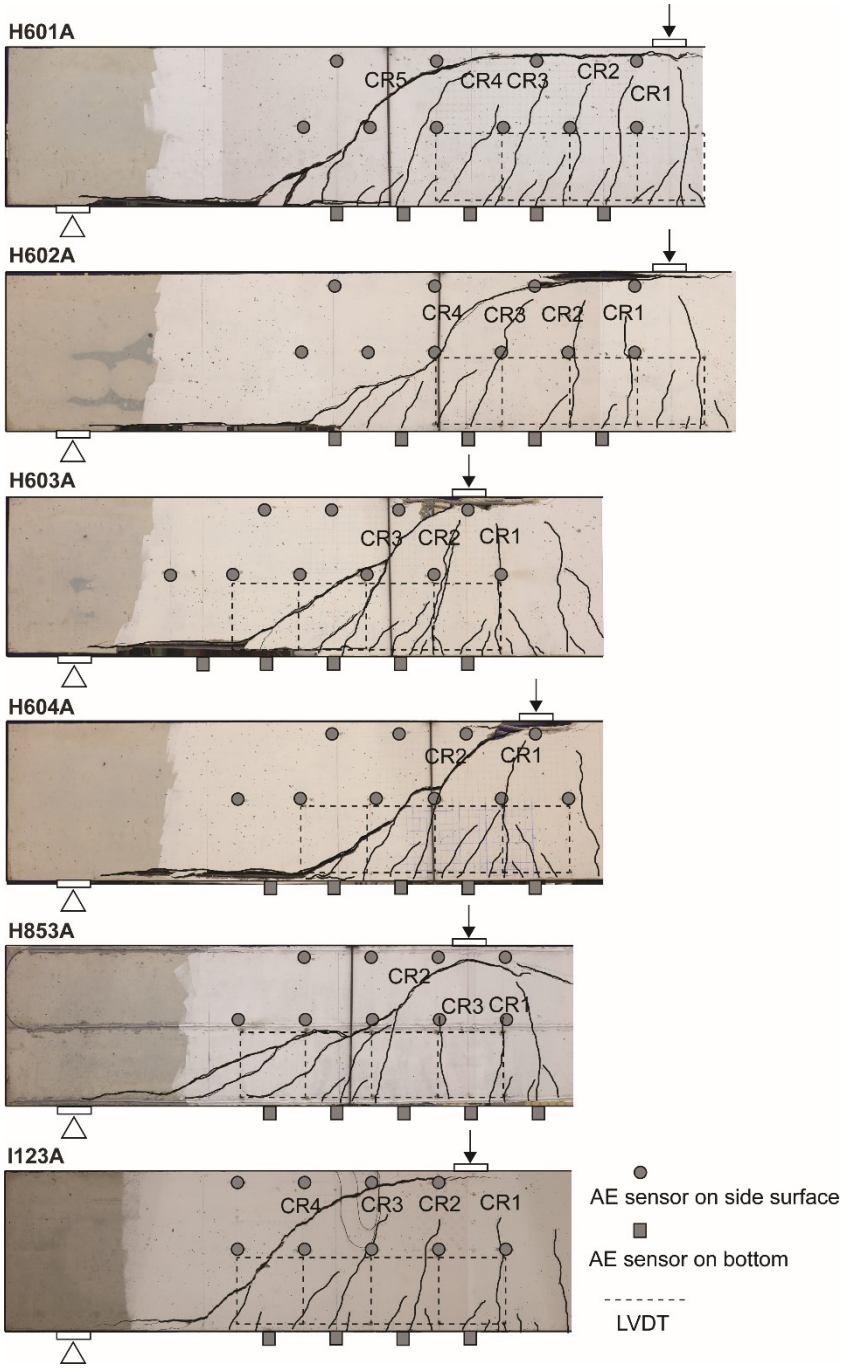

Figure 5.6 Observed crack patterns after failure of the beam tests.

The crack patterns can also reflect the failure mode. Figure 5.7 shows the relative location between the observed crack patterns and estimated compressive strut. We can find that the compressive strut was not damaged by flexural shear cracks in tests under shear compression failure (H603A, H604A and H853A). This meets with the expectation in Chapter 2 that the integrity of compressive strut influences the shear capacity.

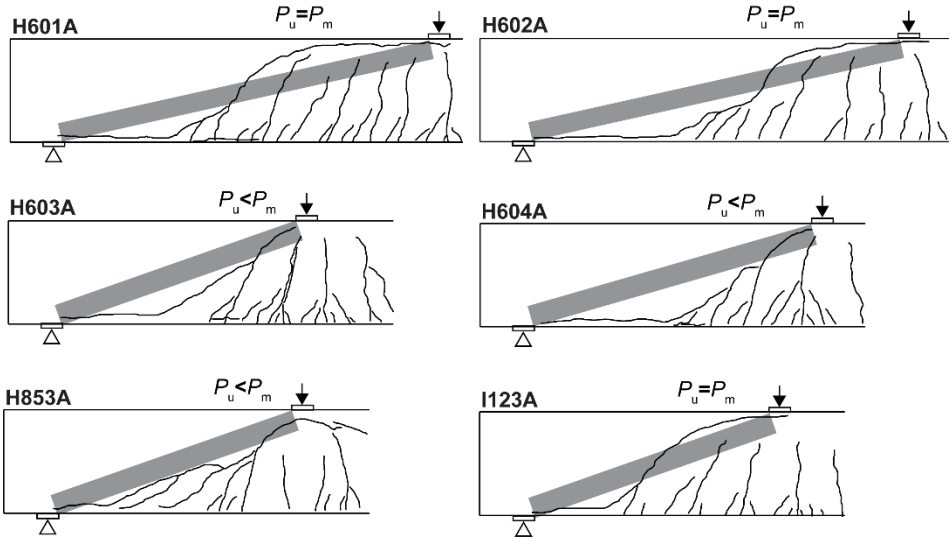

Figure 5.7 Relative location between observed crack patterns and estimated compressive strut in beam tests.

Figure 5.8 exemplifies the DIC results at 300 kN (right before failure) of test I123A. Plot a shows the crack pattern. Plot b and c show the normal and tangential displacements at selected points along CR2-4 respectively. The normal displacement is perpendicular to the local crack profile and the tangential displacement is parallel to the local crack profile. For clarity, only the maximum and minimum values along a crack are labelled. The normal and tangential displacements at local positions along the cracks with increasing load are listed in Appendix A.

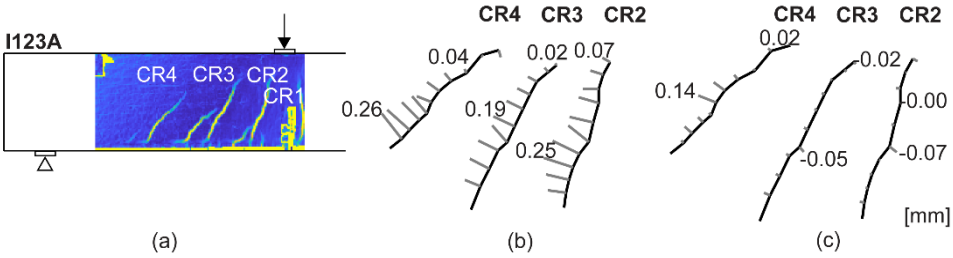

Figure 5.8 DIC results at 300 kN (before failure) of test I123A (a) crack pattern, (b) normal displacement and (c) tangential displacement.

5.3 Reinforced concrete slab tests

Three tests are taken from the series of failure tests on half-scale reinforced concrete slabs (Zarate Garnica 2021). In the series, the tests are named as SR1M1, SR2M1, and SR3M1.

5.3.1 Test setup

The dimensions of the reinforced concrete slab specimens are 5000 mm × 2500 mm × 300 mm. The concrete class is C35. The reinforcement layout is given in Figure 5.9.

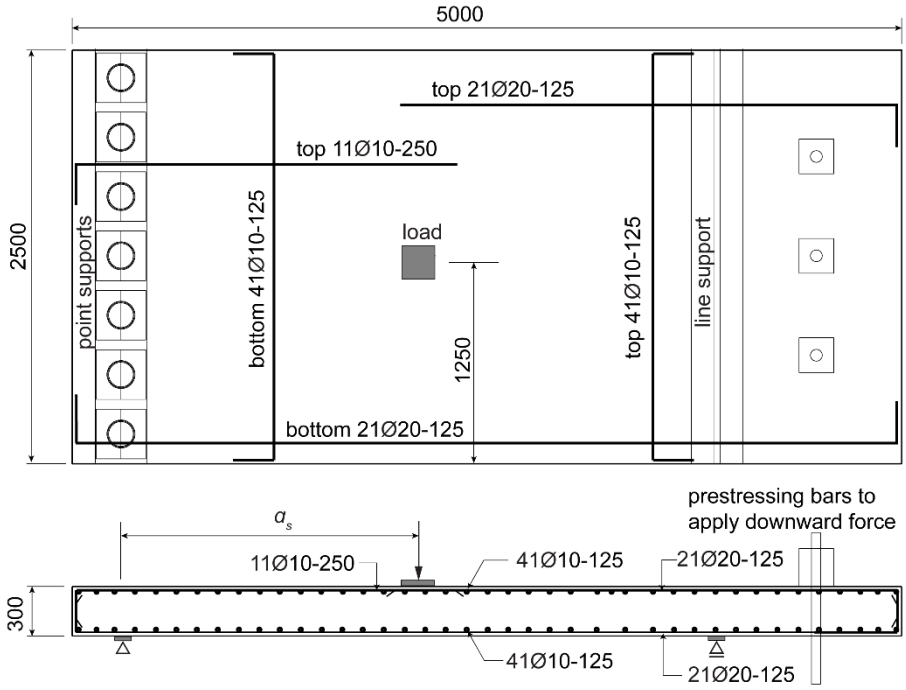

Figure 5.9 A sketch of slab configuration including slab dimension, reinforcement layout and locations of supports and load.

The slab was supported at one end by seven separate bearings, and at the other by a line support with a cantilever of 1 m (Figure 5.10). At the end of the cantilever, a downward force of 45 kN was applied by three prestressing bars (15 kN each), to simulate the clamping moment at the intermediate support of a continuous slab.

The slab was loaded by a single point load, with shear span of 1800 mm in SR1M1 & SR2M1 and 800 mm in SR3M1. The load was applied through the hydraulic jack in a displacement-controlled manner. The loading speed was 0.04 mm/s.

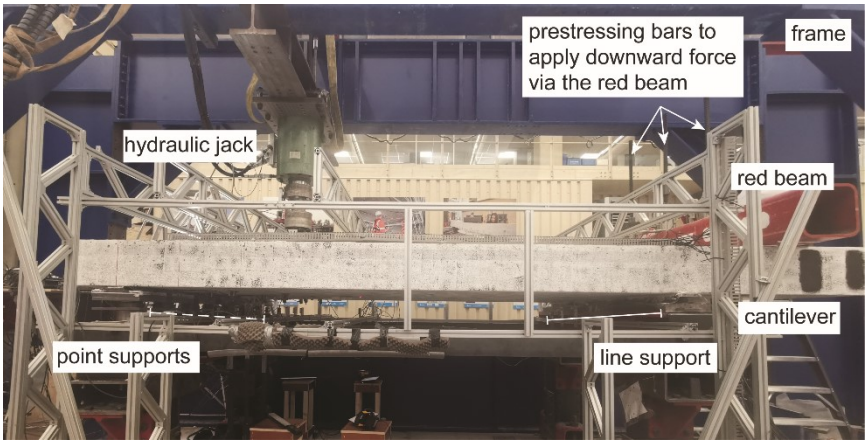

Figure 5.10 Photo of test setup including frame, supports and hydraulic jack.

Figure 5.11 shows the loading history. The loading protocol can be divided into two parts. The first part was carried out as a proof load test. The detailed considerations for the proof load test part have been reported by Zarate Garnica (2021). The second part included some load cycles of higher load level, then loaded the slab until failure. For every load level, generally 3-4 load cycles were applied.

Table 5.3 lists the test configurations, including concrete cubic compressive strength ($f_{c,cube}$) on 28th day after casting, rebar configuration, rebar characteristic yield strength (f_{yk}), reinforcement ratio (ρ_s), shear span (a_s), effective depth (d_c), shear span ratio (a_s/d_c) and load type.

Table 5.3 Test configurations

Test no.	SR1M1	SR2M1	SR3M1
$f_{c.cube}$ [MPa]	51.74	51.74	55.45
Age [d]	28	28	28
Rebar Config.	41Ø10 (trans.) 21Ø20 (long.) Ribbed	41Ø10 (trans.) 21Ø20 (long.) Ribbed	41Ø10 (trans.) 21Ø20 (long.) Ribbed
f_{yk} [MPa]	500	500	500
ρ_s [%]	0.996	0.996	0.996
a_s [mm]	1800	1800	800
d_c [mm]	265	265	265
a_s/d_c [-]	6.79	6.79	3.02
Load type	Cyclic	Cyclic	Cyclic

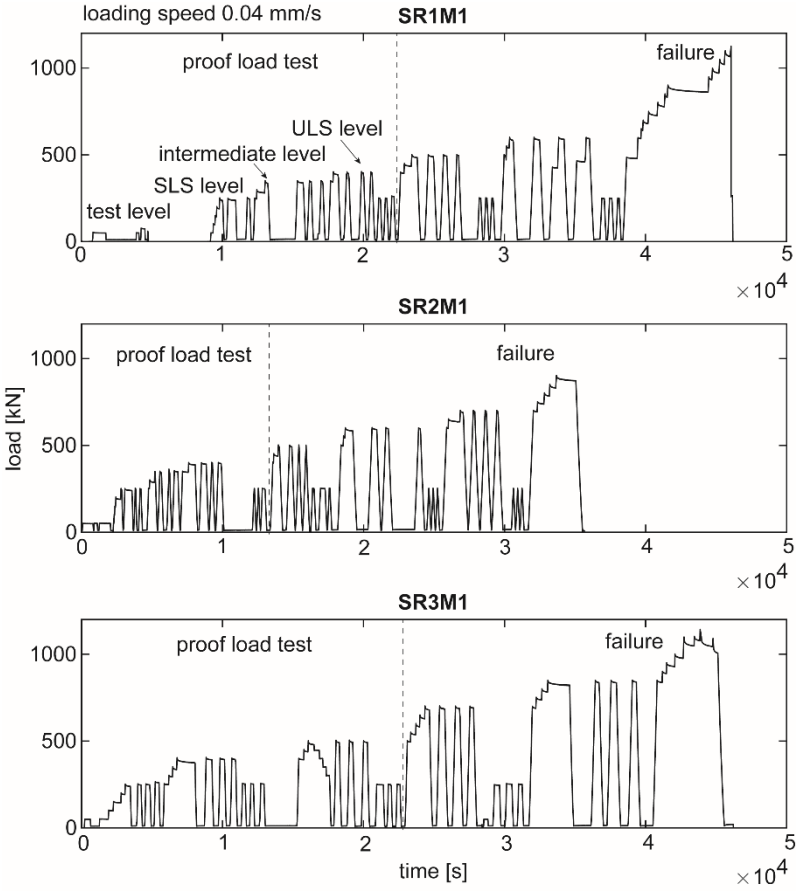

Figure 5.11 Loading history of the slab tests.

5.3.2 Measurements

The measurements during the test included load measurement (load cell), displacement measurement (LVDTs, lasers, and DIC), and AE measurement. Figure 5.12 shows the applied sensors (photos are taken from test SR2M1). Detailed setups were reported by Zarate Garnica (2021).

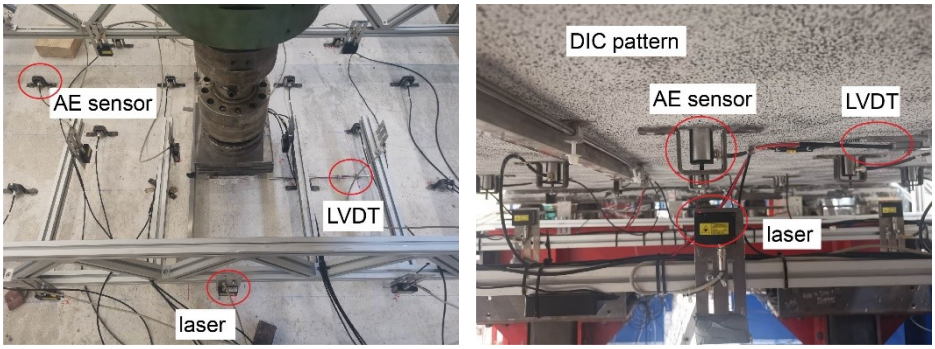

(a) (b)

Figure 5.12 Applied sensors in slab tests: (a) on the top surface and (b) on the bottom surface (photos from test SR2M1).

5.3.3 Summary of test results

This section summarises the experimental results that are relevant to the study of this research. That includes the load level at critical structural behaviour, failure mode and crack patterns.

Table 5.4 lists the load level when the first crack opens (P_{CR1}), the maximum load (P_m) and the failure mode. SR1M1 failed in flexure-induced punching, SR2M1 failed in flexure at yielding of reinforcements and SR3M1 failed in shear.

Table 5.4 Cracking load and failure mode

Test No.	F_{CR1} (kN)	P_m (kN)	Failure mode*
SR1M1	150	1125	Flexure-induced punching failure
SR2M1	150	900	Flexural failure
SR3M1	100	1143	Shear failure

Figure 5.13 shows the crack patterns measured by DIC after failure of test SR1M1. The AE measuring area is marked. Due to the complex moment distribution in the slab, the measured crack pattern on the surface cannot reflect the internal crack distribution. AE turned out to be the only method that can detect internal cracks in real time.

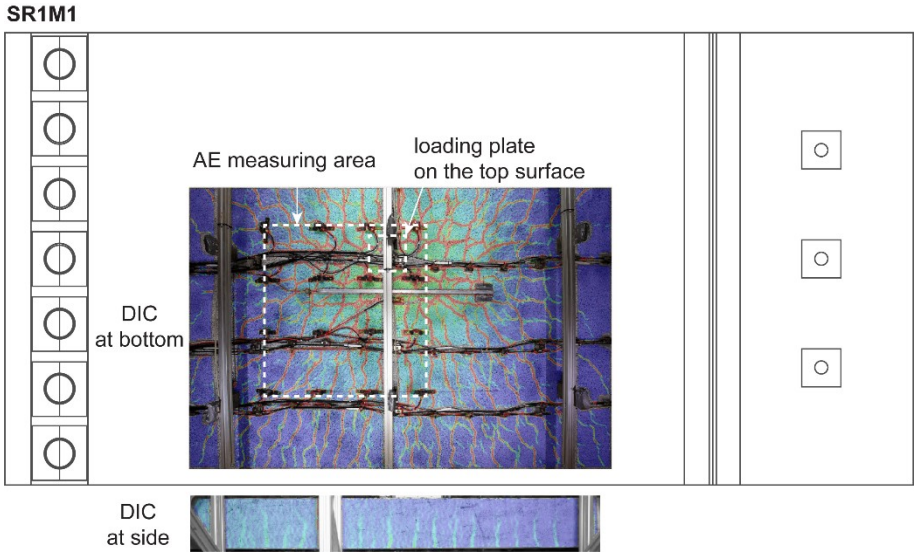

Figure 5.13 Crack patterns measured by DIC after failure of test SR1M1.

5.4 Acoustic emission measurements

5.4.1 Instrumentation

AE sensors of type R6I from MISTRAS (MISTRAS 2008) were used. The central frequency is 60 kHz. The sensor was fixed to the specimen by a steel holder. Grease-like material from MOLYKOTE (MOLYKOTE 2018) was used as couplant between the sensor surface and structural surface. A picture of installed sensors can be found in Figure 5.5 or Figure 5.12. Firstly the concrete surface was cleaned and smoothed; then the steel holder was glued to the surface; then the sensor was installed with couplant applied between the sensor and concrete surface; at the end, to ensure good contact, some pressure was kept by fastening the screw.

After installation, pencil lead break tests were carried out next to the sensor to prove sufficient coupling effect. Pencil lead with grade 2H and diameter 0.3 mm was used. The coupling was verified when the peak amplitude of the received signal was higher than 90 dB.

The data acquisition systems that we used throughout the research were 16-channel MISTRAS Sensor Highway II (in the beam tests) and 32-channel MISTRAS Express-8 (in the slab tests). Except for the number of channels, the two systems used the same data acquisition boards, thus had the same responses to given signals.

5.4.2 Data acquisition setup

The setups of data acquisition were similar among all the tests. Table 5.5 lists the parameters in the setup, including threshold, sample rate, hit length and pre-trigger.

- Threshold includes threshold for hit (thr_h) and waveform (thr_w). The former one indicates the minimum hit amplitude that the signal parameters are recorded by the channel, and the latter one indicates the minimum hit amplitude that the whole waveform is recorded. In the post processing, we unified the thr_h to be 45 dB and the thr_w to be 80 dB for all the tests.
- Sample rate counts the times that the data acquisition system measures the waveform in a second. A sample rate of 1 MSPS (Million Samples Per Second) means that the data acquisition system measures the wave every μs.
- Hit length: this determines the size (number of data points) of a waveform record. At a 4 MSPS sample rate, a hit length of 1 k will allow up to 256 μs.
- Pre-trigger: this value indicates the length of the signal in μs before the trigger point (the point at which the threshold for a hit is exceeded).

The detailed definitions can be found in the manual of AEwin software (MISTRAS 2011).

Table 5.5 Acoustic emission data acquisition setup

Parameters	Beam tests						Slab tests		
	H601A	H602A	H603A	H604A	H853A	I123A	SR1M1	SR2M1	SR3M1
thr_h [dB]	45	45	45	45	45	40	40	40	40
thr_w [dB]	75	75	75	75	80	70	75	75	75
Sample rate [MSPS]	5	5	5	5	5	1	5	5	1
Hit length	8k	8k	8k	8k	8k	4k	8k	8k	8k
Pre-trigger [μs]	256	256	256	256	256	256	256	256	256

5.4.3 Preliminary measurement of wave propagation properties

Before the actual test, the wave propagation properties in concrete medium was measured. The relevant properties for this dissertation are wave speed and attenuation factor.

The wave propagation properties are related to the mechanical properties of the material. We assume that concrete with same mixture design shares the same mechanical properties, thus the same wave propagation properties. Since all the beams use a same type of mixture and all the slabs use another type, preliminary tests were carried on one beam (I123A) and one slab (SR1M1).

In a typical wave preliminary measurement, fourteen sensors were installed in a line in the uncracked area (Figure 5.14a). The sensor spacing was 40 mm. The first transducer was used as a source, excited with a rectangular-shape pulse of 20 μs duration and 10 V

amplitude. The induced source in the medium was therefore considered as the convolution of the pulse with the transfer function of the transducer and the coupling. This induced source was received by other sensors after propagation. The sensor closest source was selected as the reference sensor. The arrival time and peak amplitude of the signals received by every sensor were calculated and compared to those from the reference sensor. In this way we obtained the travel time and amplitude drop from the reference.

Figure 5.14b and c show the travel time and amplitude drop from the reference against the wave travel distance measured on a beam specimen. The travel time was determined by the P-waves which arrived first. By diving the travel distance by the travel time, the wave speed was estimated to be around 4100 m/s. The amplitude drop mainly came from two sources: material attenuation and geometric spreading loss. For geometric spreading loss, we took the cylindrical loss since it was the surface waves that more influenced the peak amplitude. Therefore, the two sources of attenuation were estimated using Equations (4.6) and (4.5) respectively. We found an overall attenuation curve (the dashed line in Figure 5.14c) which included material attenuation with factor α = 20 dB/m and cylindrical spreading loss.

Assuming that P-wave and surface wave have a same material attenuation factor, Figure 5.14d shows their attenuations. After 1 m, P-wave attenuated around 55 dB and surface wave only 40 dB. This means that for a source signal of 100 dB and sensor threshold of 45 dB, after 1 m, P-waves could not be detected. Instead, other wave modes or reflections would be received as first arrivals, which could influence source localization (which will be further discussed in Chapter 6). To allow P-waves to be received, the sensor spacing should be within 1 m in the beam tests. The maximum sensor spacing needs to be adjusted according to the actual source amplitude. For a smaller source amplitude, the maximum sensor spacing needs to be reduced. As the distribution of the actual source amplitudes from concrete cracking is unknown, we assume the source amplitude to be 100 dB (which is the maximum value that the system can measure), resulting in a maximum sensor spacing of 1 m.

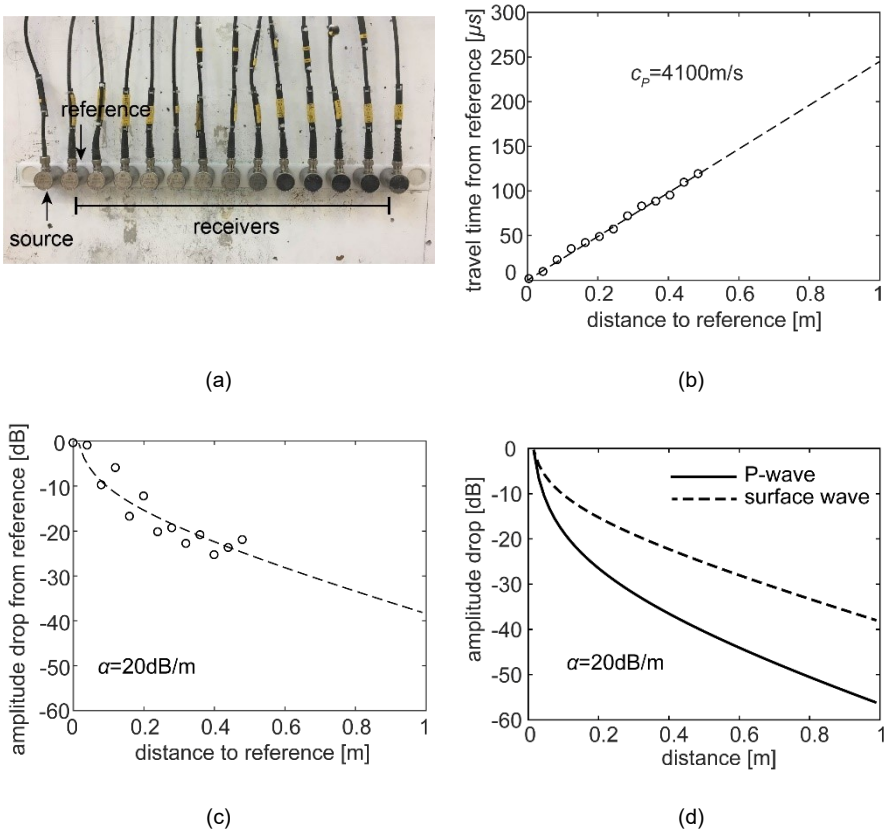

Figure 5.14 Preliminary test on wave propagation properties: (a) test setup, (b) estimation of wave speed of P-wave, (c) estimation of wave attenuation of surface wave, (d) estimation of wave attenuation of P-wave.

On a slab specimen, different wave propagation properties were found on the top and bottom surfaces. On the top surface, the measured wave speed was around 3000 m/s, but on the bottom surface around 4000 m/s. The material attenuation factor on the top and bottom was around 35 dB/m and 15 dB/m respectively. The wave properties on the top surface had lower wave speed and higher attenuation. This could be due to the rougher top surface or more air bubbles near the top surface. We did not consider the effect of variant wave propagation property, using the wave speed measured from bottom surface (4000 m/s) for the whole slab, since the top surface with low speed was shallow compared to the whole slab depth. For the material attenuation factor, which determines the maximum allowable sensor spacing, we used the largest value 35 dB/m measured from top surface. In this way, we overestimated the wave attenuation, resulting in a conservative allowable sensor spacing. Using the same analysis method as in the beam tests, the sensor spacing should be within 0.65 m in slab tests.

5.4.4 Acoustic emission sensor layout

Figure 5.15 shows the AE sensor layout of the beam tests. They were installed on a side surface (marked in circles) and the bottom surface (marked in rectangles). The ones on the bottom surface were in the middle line of the width direction. The sensor spacing in the length and height directions were around 0.5 m, with minimum 0.45 m and maximum 0.75 m. This met the requirement of sensor spacing to be within 1 m for beam tests (Section 5.4.3).

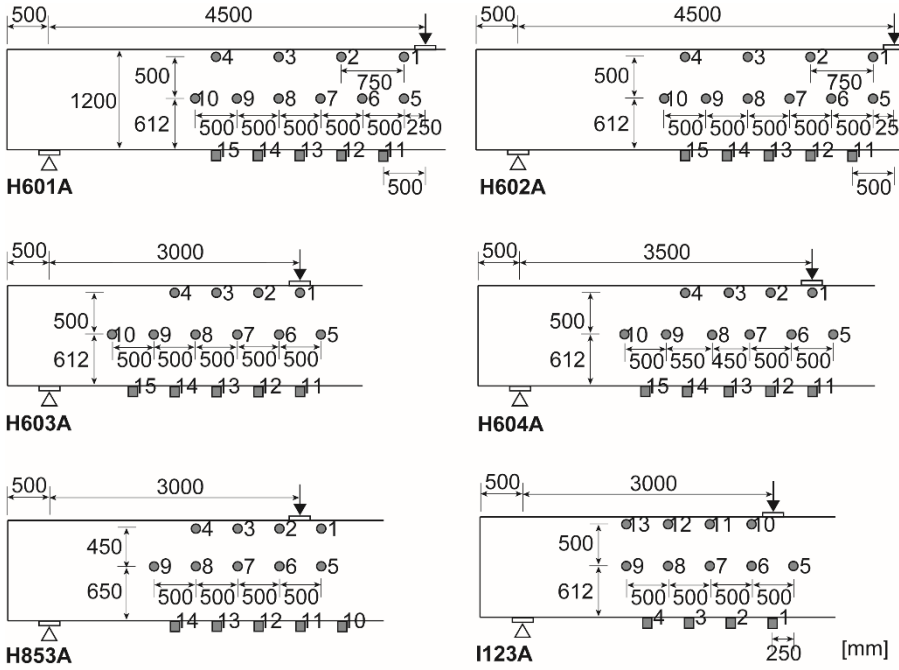

Figure 5.15 AE sensor layout in the tests.

Figure 5.16 shows the AE sensor layout of the slab tests. Sensors were installed both on the top and bottom surfaces. The sensor spacing in each direction was around 0.3 m, with minimum 0.25 m and maximum 0.425 m. This met the requirement of sensor spacing to be within 0.65 m for slab tests (Section 5.4.3).

When designing the sensor layout, the first test SR1M1 was used as a trial, where we found a more efficient sensor layout could be reached by setting a mismatch between the sensor positions on the top and bottom surfaces. In SR2M1 and SR3M1, the mismatch enabled a larger measuring zone using a similar amount of sensors.

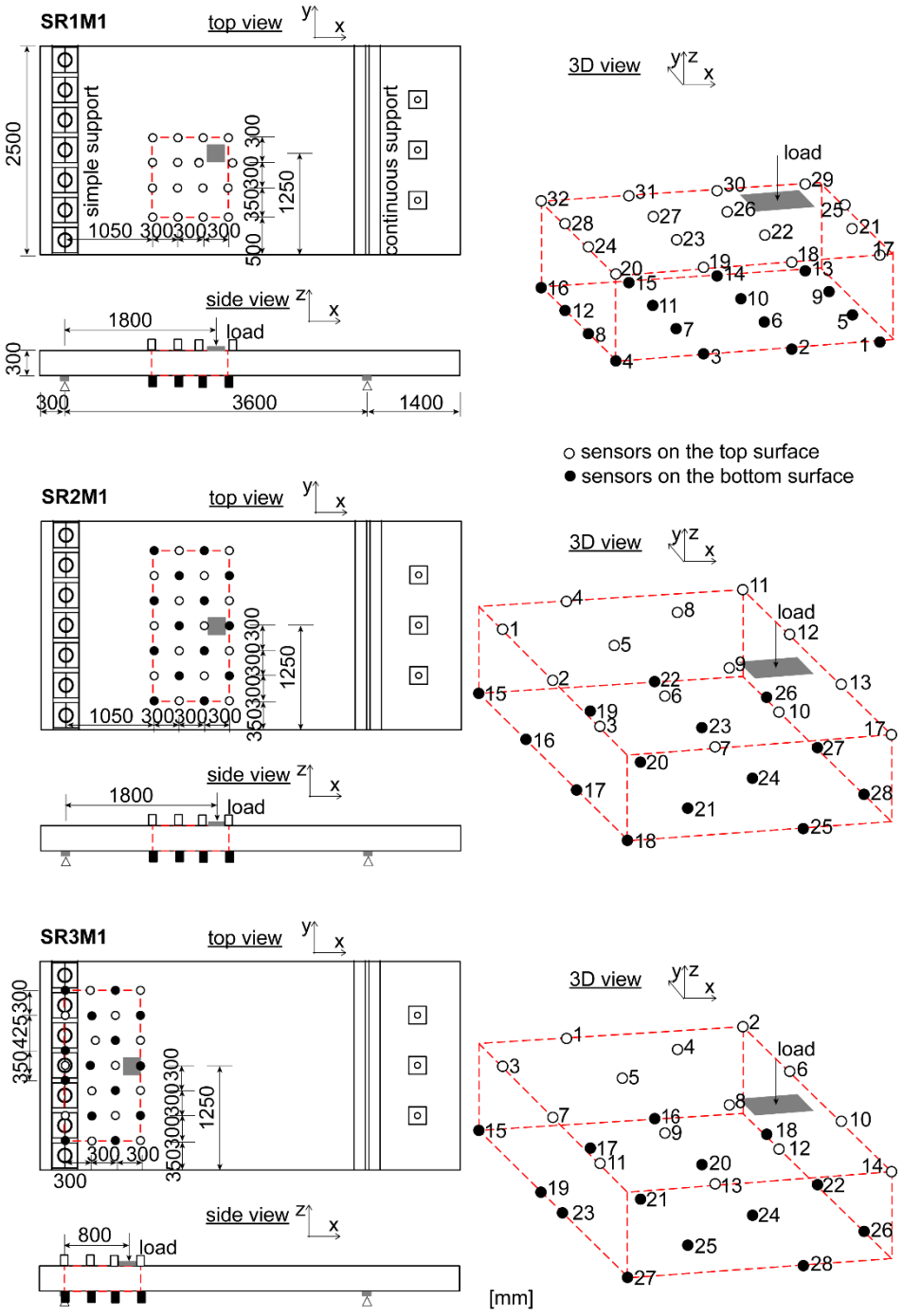

Figure 5.16 AE sensor layout in the slab tests.

5.4.5 Acoustic emission results using conventional methods

This section reports the AE source localization results using the conventional method. As reviewed in Chapter 4, the conventional method uses first arrival times, sensor locations and wave speed to estimate the source location. In our tests, the first arrival times were automatically selected by the AEwin software embedded in the MISTRAS system, with a fixed threshold of 45 dB. The sensor locations were known. The wave speed was estimated in the preliminary test in Section 5.4.3. Grid search method was used with grid point spacing of 10 mm in each direction.

For beam tests, due to small dimension in width (y) direction compared to length (x) and height (z), we assumed a plain stress condition. Crack pattern variation in y direction was neglected. Therefore, we applied a 2D source localization in x-z plane. For slab tests, a 3D source localization was applied.

A special consideration in this dissertation is that we did not use all the received signals from one AE event. The signals received by farther sensors were more attenuated, which may lead to larger arrival time picking error, thus larger localization error. Therefore, we only used the signals from sensors that were within 1 m from the closest sensor. Moreover, a previous study has shown that localization results outside the sensor enclosed zone were not accurate (Zhang 2017). Therefore, those AE events were not considered. Another calibration is that after an AE event was located, we estimated its source amplitude according to the received signal amplitude and the wave attenuation after propagating from the source to the sensor. Based on the estimated source amplitude, we only considered events with source amplitude over a predefined threshold. The reason and details of this calibration are presented in Section 6.2.1.

Figure 5.17 shows the estimated locations of AE events until failure (without unloading parts) of the beam tests. Due to source localization error, AE can only roughly find crack pattern. The crack pattern was especially not clear at location where more than one crack presented between two sensors, e.g. in the bottom with secondary cracks.

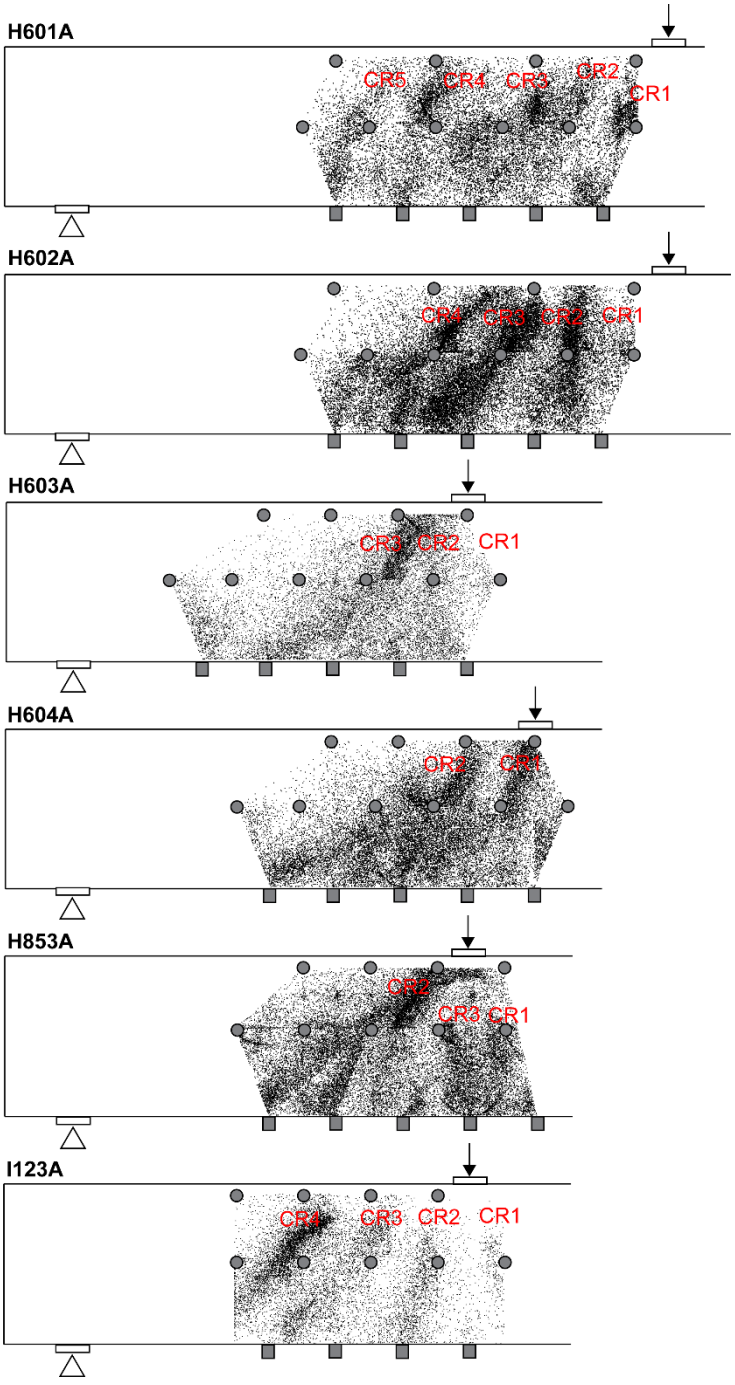

Figure 5.17 Located AE events until failure (excluding unloading parts) of the beam tests.

Figure 5.18 shows the located AE events until failure (AE events during unloading are not included) of the slab tests. Compared to the beam tests, the source localization error in the slab tests was significantly larger. This can be explained by the presence of multiple cracks between two sensors in slab tests (Figure 5.13). The effect of presence of cracks will be further discussed in Chapter 6.

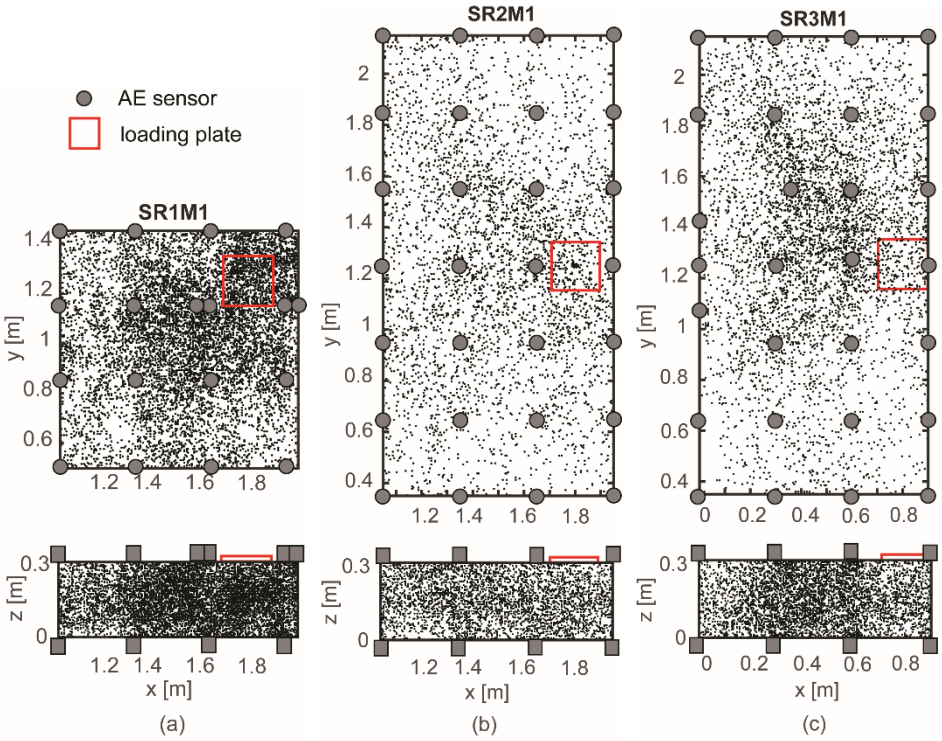

Figure 5.18 Located AE events until failure (excluding unloading parts) of the slab tests.

The obtained AE signals and estimated source locations are the AE data base for this dissertation. The data base are used in the later chapters to develop new AE methods and AE-based failure indicator of reinforced concrete structures.

Chapter 6 Probability density field of acoustic emission events

6.1 Introduction

The traditional source localization procedure (described in Chapter 4) can be influenced by various uncertainties including the presence of cracks, arrival time picking error, sensor layout etc. These uncertainties would result in erroneous estimated source locations. Many studies aim to reduce the source localization error as reviewed in Chapter 4. However, the error cannot be entirely removed. This chapter approaches the problem from another perspective by making use of the properties of the error.

We first study the properties of source localization error using simulations (Section 6.2). A probability density function of source localization error is found. Based on the function, we estimate the probability of the location of an AE event (Section 6.3). With more AE events occurring, by simply adding up the probability density field of each AE event, we are able to get the probability density field of all AE events. The integration of the probability densities over a certain space range and time period describes the probability of the total number of AE events falling in that space range within that time period. This method is named as the probability density field of AE events (pdAE field). The new method is demonstrated in one beam test and one slab test (Section 6.4). The resultant probability density field shows clear crack patterns and a close relationship with the crack width.

6.2 Study of source localization error

Traditional source localization method (described in Chapter 4) estimates the source location assuming a constant wave speed distribution and a direct wave travel path from the source to the receiver. But these assumptions are not always true in concrete. When a crack presents between the source and the receiver, wave propagation from the source to the receiver will be influenced. Moreover, the picked arrival times may not be accurate, due to the limit of arrival time picking technique. And sensor layout can also influence the source localization.

With the above influential factors, the estimated source location may not be the actual one. This dissertation defines the source localization error as the relative location between the estimated and actual source locations

$$\boldsymbol{\Delta} = \mathbf{x}_{\mathrm{S}} - \mathbf{x}_{\mathrm{g}} \tag{6.1}$$

where $\mathbf{x}_{\mathrm{S}}$ is the actual source location and $\mathbf{x}_{\mathrm{g}}$ is the estimated source location.

The magnitude of source localization error $\|\boldsymbol{\Delta}\|$ is the Euclidean distance between the two locations

$$\|\boldsymbol{\Delta}\| = \sqrt{\sum_{i=1}^{k} \Delta_i^2}, k \in \{1,2,3\} \tag{6.2}$$

where k is the dimension of the measuring zone which could be 1D, 2D or 3D and Δ_i is the error component in the i^{th} direction.

This section first discusses the influential factors on source localization (Section 6.2.1). Then considering the influential factors, we simulate the localization process to study the localization error (Section 6.2.2). Based on the simulation, we find the properties of source localization error (Section 6.2.3).

6.2.1 Influential factors on source localization

This section discusses the influential factors on source localization, which are presence of cracks, arrival time picking error and sensor layout.

Presence of a crack

The AE signals experience extraordinary complications when propagating through an existing crack. Since AE source localization in this dissertation only uses the first arrival of the signals, we limit our study to the influence of presence of crack on the first arrivals in terms of wave speed and peak amplitude. We simplify that the first arrivals come from two paths: (i) the direct wave path, where the waves are delayed and attenuated when going through the crack or (ii) the tip-diffracted wave path, where the wave propagation direction is changed by the crack tip, shown in Figure 6.1.

For the direct waves, the influence of a crack was studied previously (Pahlavan, Zhang et al. 2018). Experiments were carried out on multiple cracks with width in range of 0.05-3 mm. At the time of test, the cracks were relaxed. A crack delayed the arrival time by 5-20 μs, depending on the angle between wave propagating direction and the crack. A crack reduced the peak amplitude by -10 dB to -50 dB, depending on the crack width.

Based on this observation, the simulation in Section 6.2.2 assumes that wave speed in the crack band follows an elliptical distribution (giving a 5-μs-delay in the direction parallel to the crack and a 20-μs-delay orthogonal). And we take an attenuation of -10 dB as the influence of a crack. This attenuation from crack is combined with material attenuation and geometric spreading loss, to obtain the complete attenuation of the direct waves.

For the tip-diffracted waves, the simulation assumes that the crack tip only changes the wave travel direction. Other influences on wave speed and amplitude are neglected. The arrival time and the amplitude of the tip-diffracted waves are estimated considering a travel distance of the wave path (ii) in Figure 6.1.

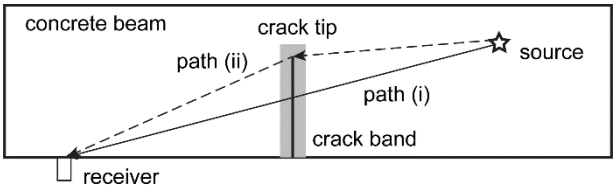

Figure 6.1: Wave propagation in existing concrete structures with a crack between the source and the sensor

Arrival time picking error

Fixed threshold method has been widely applied, especially in commercialized monitoring systems (MISTRAS 2011). Though this method is not the most advanced and accurate one, to simulate the practical conditions, we evaluate the arrival time picking error of fixed threshold method.

The arrival time picking error is evaluated using the 29,232 signals from shear test I123A (described in Chapter 5). In the test, the fixed threshold value was set at 45 dB (which was 17.8 mV considering a pre-amplification of 40 dB and a reference voltage of 1 μV). The picked arrival time was compared to the actual one. The actual arrival time was determined using akaike information criterion (AIC) automatically (Kurz, Grosse et al. 2005). Though the AIC results were also not actual ones, this method has proven to be substantially more accurate than the fixed threshold method (Schechinger and Vogel 2007). Figure 6.2a exemplifies the results from the fixed threshold method and AIC. The arrival time picking error is estimated as:

$$\Delta t = t_{\text{threshold}} - t_{\text{AIC}} \tag{6.3}$$

where $t_{\text{threshold}}$ is the arrival time determined by the fixed threshold method and t_{AIC} is the arrival time determined by AIC.

Figure 6.2b shows the statistical distribution of the arrival time picking errors of the total 29,232 signals. The values were most positive, which means the fixed threshold picked the first arrivals later than the real times. Although unable to demonstrate the goodness of fit, we assume that the (positive) picking error followed a half-normal distribution with a zero mean and a standard deviation of 10.5 μs. This distribution of arrival time picking error is used in the simulation in Section 6.2.2.

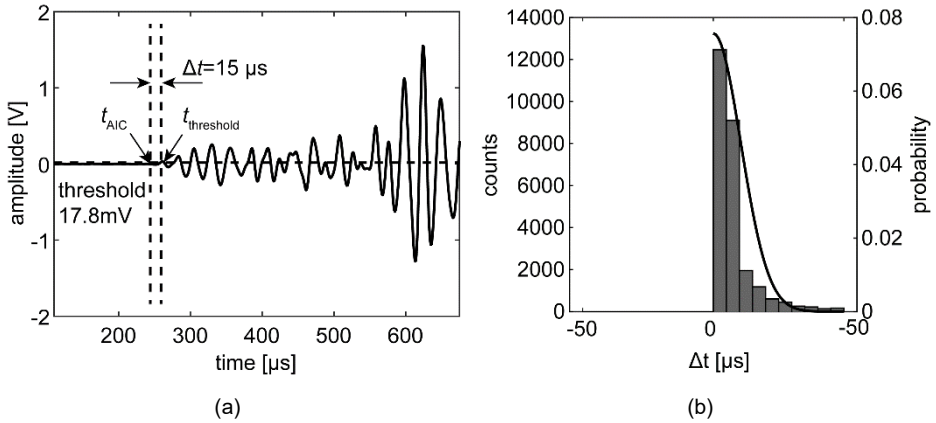

Figure 6.2 Arrival time picking error using fixed threshold method compared to AIC results: (a) an example and (b) the statistical distribution from 29,232 signals.

Sensor layout

Sensor layout influences the source localization due to wave attenuation. The effects would be (1) large source localization error or (2) missing of AE events. These two effects are discussed separately below.

For an AE source, the signals received by the farther sensor have larger attenuation. When after attenuation, the direct waves could not be detected, the first arrival will be picked at a later part of the signal (which could be other wave modes, diffractions or reflections). Using these arrival times would generate larger source localization error.

To reduce this effect, we need to limit the sensor-to-source distance, to ensure that the direct waves can be detected. According to the measurement of wave attenuation in Chapter 5, the sensor-to-source distance has to be within 1 m in the presented experiments in this thesis. Since the source location is not pre-known, we use the sensor that first detects the signal as a reference for source location. Therefore, for an AE event, only the sensors that are within 1 m to the one that first detects the signal are used for localization (not only in the experiments in Section 5.4.5 but also in the simulations in Section 6.2.2).

The other effect, missing of an AE event, occurs when not enough number of sensors can receive the direct waves. The required minimum number of sensors are three for 2D localization and four for 3D.

When the third/fourth closest sensor cannot receive the signal, the farther sensors cannot receive due to more attenuation. Here we assume that the attenuation only depends on the sensor-to-source distance. We would then have not enough number of sensors. Therefore, the signal amplitude received at the third/fourth closest sensor determines whether an AE event can be located in 2D/3D.

Figure 6.3 exemplifies a 2D sensor layout with three sensors. The threshold value at each sensor is 45 dB. Supposing that an AE event is at location p_1, the decisive sensor is the third closest sensor to the source, which is R_3 with distance of d_{13}. Considering the attenuation function f of distance d, to ensure the signal can be received by R_3 after attenuation, the source amplitude is required to be larger than $45 + f(d_{13})$. At another location p_2, the third closest sensor is of d_{23} distance ($d_{23} < d_{13}$), the required source amplitude is $45 + f(d_{23})$, which is smaller than $45 + f(d_{13})$. This means that at location p_2, AE events of a smaller amplitude can be located. The sensor layout is more sensitive to AE events at location p_2 than p_1.

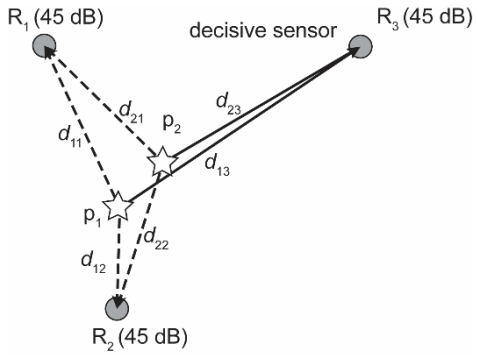

Figure 6.3 Illustration of the decisive sensor in 2D source localization.

We use the required source amplitude to evaluate the sensitivity of a sensor layout to AE events at a location. The required source amplitude at a location is calculated as the sensor threshold level plus the wave attenuation from the studied location to the decisive sensor, which is third (for 2D) and fourth (for 3D) closest sensor. The sensor layout is more sensitive to AE events at locations with a smaller required source amplitude.

Figure 6.4 shows the required source amplitude at every possible source location in a 2D layout. The threshold at each sensor is 45 dB and the attenuation function takes the one measured in Chapter 5. We find a lower required source amplitude in the centre of a sensor grid than on the edge (71 dB and 82 dB respectively). This means that AE events with amplitude in range of 71-82 dB can only be located when they occur in the centre of a sensor grid. This sensor layout turns out to be more sensitive to AE events in the centre of a sensor grid.

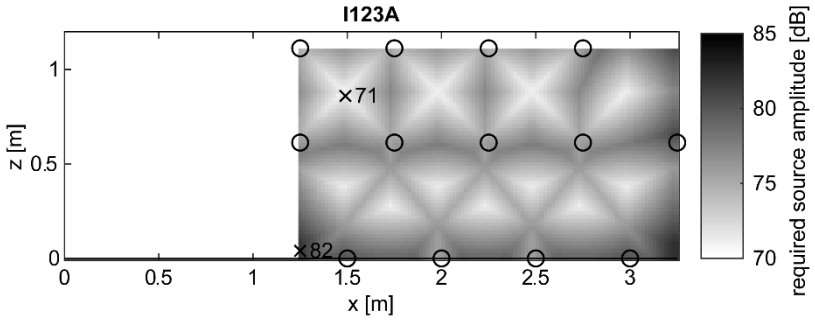

Figure 6.4 Distribution of the required source amplitude for localization in test I123A.

To reduce this effect, we set up a source amplitude threshold that only AE events with the source amplitude over this threshold are counted. The threshold is taken as the highest value in the distribution of required source amplitude in the measuring zone. When an AE event is localized, we first estimate its source amplitude according to the received signal amplitude and the wave attenuation after propagating from the source to the receiver. If the estimated source amplitude is over the pre-set threshold, the AE event is counted. In this way, the required source amplitude in the whole measuring zone is unified, giving a same sensitivity to AE events at different locations. This calibration is not only applied in the experiments in Section 5.4.5 but also simulations in Section 6.2.2.

6.2.2 Simulation of source localization process in a concrete beam with a flexural crack

Considering the above influential factors, a reliable evaluation of source localization error requires a large quantity of measurements, which is costly and labour-intensive. A more practical solution is to simulate the AE source localization process considering the influential factors. By simulating a large number of tests, we study the properties of source localization error.

A concrete beam with a flexural crack is modelled (Figure 6.5). The dimensions of the beam is 3000 mm × 400 mm × 400 mm. The wave speed of the first arrivals in the sound concrete is assumed to be 4100 m/s, and the material attenuation factor is 20 dB/m for signals with central frequency of 60 kHz. The crack is a typical flexural crack with a surface crack width of 0.05 mm which propagates from the bottom of the beam. The variation of the crack surface at aggregate level is neglected resulting in a plain surface being perpendicular to the longitudinal direction of the beam. The influence of the crack on wave propagation is included as described in Section 6.2.1. When the direct waves cannot be received, the diffracted waves by the crack tip are taken.

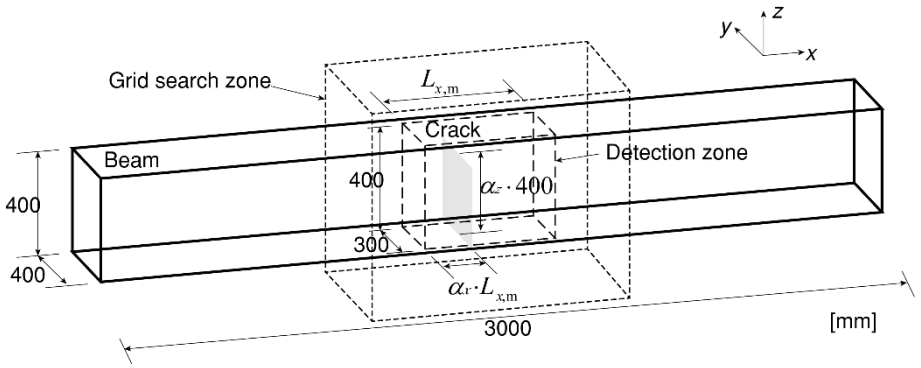

Figure 6.5 Beam configuration in the simulations

Four AE sensors with central frequency of 60 kHz are applied on the surface of the beam around the crack. Sensors are arranged in eight different sensor layouts, which are categorized into four groups: in 3D, vertically 2D, horizontally 2D, and 1D (Figure 6.6). The 2D sensor layouts (Group 2 and 3) are included to simulate the practical cases when only one surface is accessible. Sensor layout of 1D (Group 4) is included to simulate slender structures where only 1D measurement is necessary. The detection zone is defined as the sensor covering zone, which are in a volume, a plane, or a line, when the sensor layout is 3D, 2D or 1D respectively (indicated by dashed lines in Figure 6.6).

In this model, the variables are maximum sensor spacing $L_{x,max}$, crack position in x direction, and crack height (indicated in Figure 6.5):

$$\begin{aligned} l_{x,cr} &= \alpha_x \cdot L_{x,m} \\ l_{z,cr} &= \alpha_z \cdot L_{z,m} \end{aligned} \tag{6.4}$$

where $l_{x,cr}$ is the distance from the left edge of the detection zone to the middle of the crack profile in x direction, $l_{z,cr}$ is the distance from the crack bottom to the tip in z direction, $L_{x,m}$ is the maximum sensor spacing in x direction, $L_{z,m}$ is the maximum sensor spacing in z direction, α_x and α_z are the crack position factors, evaluating the relative crack positions compared to the dimensions of the detection zone in x and z directions.

The variable maximum sensor spacing $L_{x,m}$ changes from 300 mm to 1500 mm. The crack position factors α_x and α_z each varies from 0 to 1. These variables result in 24 independent models (listed in Table 6.1).

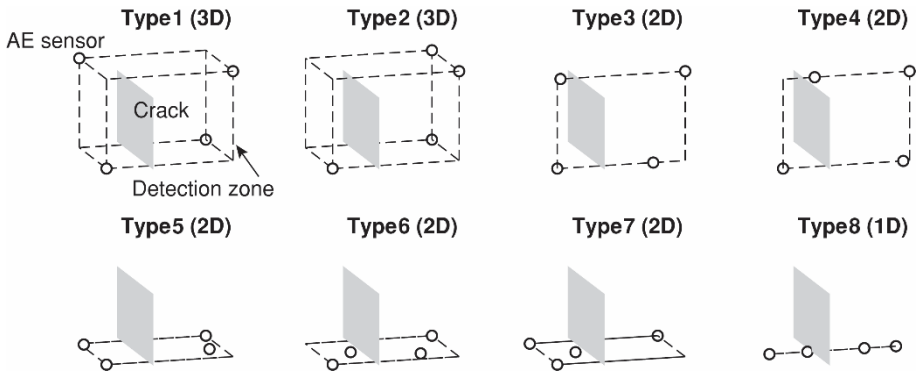

Figure 6.6 Sensor layouts in the simulations

In each model, we define a total number of 308 (11 × 4 × 7) source locations uniformly distributed in the detection zone (as illustrated in Figure 6.7). At each source location, a pulse with amplitude of 100 dB is generated in turn.

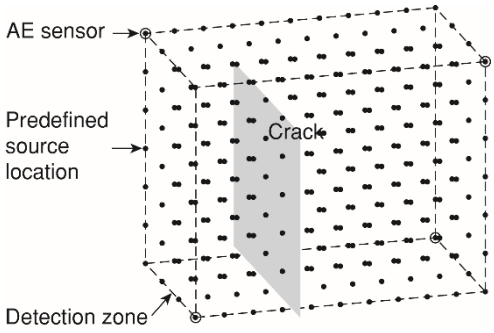

Figure 6.7 Predefined source locations in the simulations

From each source to a sensor, the arrival time is the summation of wave propagation time in sound concrete, delay from the presence of crack and arrival time picking error. The first one is calculated as the travel path distance divided by the wave speed. And the latter two are as quantified in Section 6.2.1.

Based on the obtained arrival times, grid search method is used to estimate the source location. The grid searching zone is $2\Delta L_{x,max}$ × 600 mm × 800 mm with a grid size of 10 mm. The source location is first estimated in 3D, and then projected to the detection zone. This means that for 2D and 1D sensor layouts, only the location components within the 2D plane and 1D line are considered. We get the localization error as the relative location between the (projected) estimated location and the predefined location according to Equation (6.1).

We repeat the localization procedure for 200 times, by considering the arrival time error as a random value from the statistical distribution obtained in Section 6.2.1. In the end, a

total number of 11,827,200 (24 × 8 × 308 × 200) independent simulated tests are generated (including 24 models, 8 sensor layouts, 308 predefined source locations and 200 random arrival time picking errors).

Table 6.1 Model configurations and the error properties

Model	$L_{x,m}$ [mm]	α_x [-]	α_z [-]	σ of error component [mm]	95 percentile error magnitude [mm]		
					3D	2D	1D
1	300	0.33	0.8	55	153	134	107
2	500	0.13	0.8	53	147	129	103
3	500	0.17	0.8	53	147	129	103
4	500	0.20	0.8	50	139	121	97
5	500	0.25	0.8	53	147	129	103
6	500	0.33	0.8	54	150	131	105
7	500	0.40	0.8	52	144	126	101
8	500	0.50	0.8	51	142	124	99
9	500	0.60	0.8	52	144	126	101
10	500	0.67	0.8	55	153	134	107
11	500	0.75	0.8	58	161	141	112
12	500	0.80	0.8	53	147	129	103
13	500	0.83	0.8	56	155	136	109
14	500	0.88	0.8	57	158	138	111
15	500	0	0	39	108	94	75
16	500	0.33	0.1	42	116	102	81
17	500	0.33	0.2	46	128	112	89
18	500	0.33	0.4	50	139	121	97
19	500	0.33	0.6	52	144	126	101
20	500	0.33	1	55	153	134	107
21	800	0.33	0.8	53	147	129	103
22	1000	0.33	0.8	52	144	126	101
23	1200	0.33	0.8	54	150	131	105
24	1500	0.33	0.8	67	185	163	130

* In each configuration, eight types of sensor layouts are tested. The error properties consider all the layouts.

6.2.3 Statistical properties of source localization error

Chi distribution of source localization error magnitude

As stated in Equation (6.2), the error magnitude is the Euclidean distance between the estimated and actual source locations. To describe the error magnitude, we use chi distribution which is defined as a distribution of the Euclidean distance of the random variables from the origin (Abell, Braselton et al. 1999). An assumption is that the error component in each direction Δ_i has to follow a normal distribution, with zero mean and standard deviation σ.

We use a same normal distribution for all $\{\Delta_1,\cdots,\Delta_k\}$ ignoring the possible anisotropic distribution of the source localization error in concrete structures. The anisotropy could come from the alignment of cracks between the source and the sensors, or from different sensor spacing in different directions. Since this anisotropy is hard to be quantified and

may vary from case to case, for a general case, this dissertation assumes an isotropic source localization error.

Under this assumption, we can determine the probabilistic density function of the source localization error $\mathbf{\Delta} = (\Delta_1,\cdots,\Delta_k)^T$ as:

$$f(\mathbf{\Delta}) = \frac{1}{\left(\sqrt{2\pi}\right)^k}\frac{1}{\sigma^k}e^{-\|\mathbf{\Delta}\|^2/2\sigma^2}, k \in \{1,2,3\} \tag{6.5}$$

For 1D source localization, the scalar-valued error $\mathbf{\Delta} = \Delta_1$ follows a normal distribution with mean zero and standard deviation σ. For 2D and 3D source localization, the error $\mathbf{\Delta}$ follows a multivariate normal distribution with uncorrelated error components Δ_i, with mean zero and the same standard deviation σ.

Then we derive the chi distribution of the source localization error magnitude $\|\mathbf{\Delta}\|$. We start from the standard chi distribution:

$$\chi(x,k) = \frac{x^{k-1}e^{-x^2/2}}{2^{k/2-1}\Gamma\left(\frac{k}{2}\right)}, x \geq 0, k \in \{1,2,3\} \tag{6.6}$$

where $\Gamma(k/2)$ is gamma function with $\Gamma(1/2) = \pi^{1/2}$, $\Gamma(1) = 1$ and $\Gamma(3/2) = \pi^{1/2}/2$ and $x = \sqrt{\sum_{i=1}^{k} y_i^2}$ where y_i independently follows a standard normal distribution (mean 0 and standard deviation 1).

In our case of source localization, the error component $\Delta_i = y_i\,\sigma$. Therefore, x is related to the error magnitude $\|\mathbf{\Delta}\|$ as:

$$x = \sqrt{\sum_{i=1}^{k} y_i^2} = \sqrt{\sum_{i=1}^{k}\left(\frac{\Delta_i}{\sigma}\right)^2} = \frac{1}{\sigma}\sqrt{\sum_{i=1}^{k}\Delta_i^2} = \frac{\|\mathbf{\Delta}\|}{\sigma}, k \in \{1,2,3\} \tag{6.7}$$

Then the standard chi distribution of x can be transformed into the distribution of error magnitude $\|\mathbf{\Delta}\|$:

$$g(\|\mathbf{\Delta}\|,k) = \chi(x,k)\frac{\partial x(\|\mathbf{\Delta}\|)}{\partial\|\mathbf{\Delta}\|} = \frac{\chi(x,k)}{\sigma}, k \in \{1,2,3\} \tag{6.8}$$

which is written as:

$$g(\|\mathbf{\Delta}\|,k) = \frac{\|\Delta\|^{k-1}\,e^{-\|\mathbf{\Delta}\|^2/(2\sigma^2)}}{2^{k/2-1}\Gamma\left(\frac{k}{2}\right)}\frac{1}{\sigma^k}, k \in \{1,2,3\} \tag{6.9}$$

For 1D source localization, $k = 1$, the chi distribution is also known as half-normal distribution; for 2D source localization, $k = 2$ leads to a Rayleigh distribution; for 3D source localization, the chi distribution with $k = 3$ is Maxwell-Boltzmann distribution (Figure 6.8). For the same standard deviation of the error component σ, a higher degree of freedom k gives a larger expected value of error magnitude.

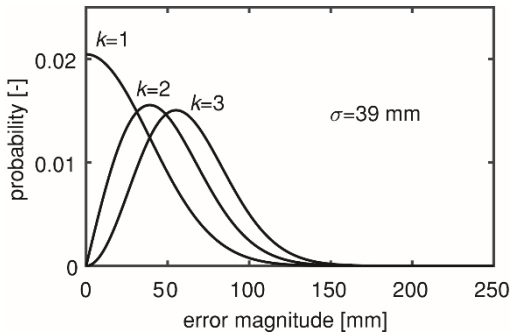

Figure 6.8 Probability distribution of error magnitude for $k = \{1,2,3\}$, with $\sigma = 39$ mm.

Calibration of the distribution using simulated results

Figure 6.9 shows the counts of the error magnitudes from Model 15 where no crack is present. The results in the eight sensor layouts are shown, with the 95 percentile error magnitude marked. The value of 95 percentile errors reach 165 mm, 156 mm and 90 mm for 3D, 2D and 1D respectively.

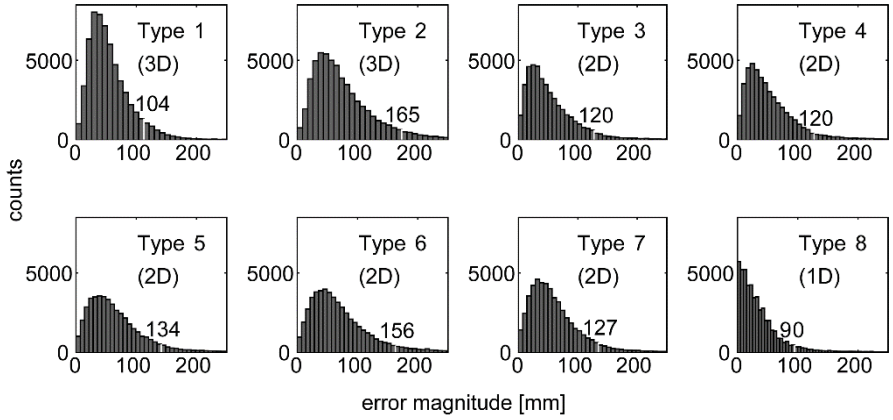

Figure 6.9 Counts of the error magnitude in the eight sensor layouts when no crack is present, with the 95 percentile error magnitude marked. Type 1-2 are 3D layouts, Type 3-7 are 2D layouts and Type 8 is a 1D layout. All sensor layouts have a maximum sensor spacing of 500 mm.

The next step is to find σ for the chi distribution of the error magnitude. We normalize the counts of error magnitude in Figure 6.9 by scaling the vertical axes. Then we calculate

the residual between the normalized data and the probability density function of chi distribution in each sensor layout. Considering the residuals in all the sensor layouts, we find the best-fit σ value. Here the 3D layout has two cases, 2D layout has five cases and 1D layout has one case. Since five of the eight cases are 2D layouts, it is likely that the found σ is more fitted into 2D cases. Therefore, we take different weight factors: the two 3D layouts each has a weight factor of 0.5 (=1/2), the five 2D layouts each has a weight factor of 0.2 (=1/5), and the one 1D layout has a weight factor of 1. The best-fit σ considers the weighted sum of residuals in all sensor layouts.

Figure 6.10 shows the normalized data and the fitted curves based on all the sensor layouts, with the 95 percentile error magnitudes marked. The standard deviation of error component σ is found to be 39 mm. The goodness of fit is hard to be improved since we assume a constant parameter σ for every sensor layout type. This thesis neglects the effect from sensor layout types as long as they have same maximum sensor spacing.

We use the same approach to obtain the error properties in other models with different sensor spacings, crack positions and crack heights. The results are listed in Table 6.1.

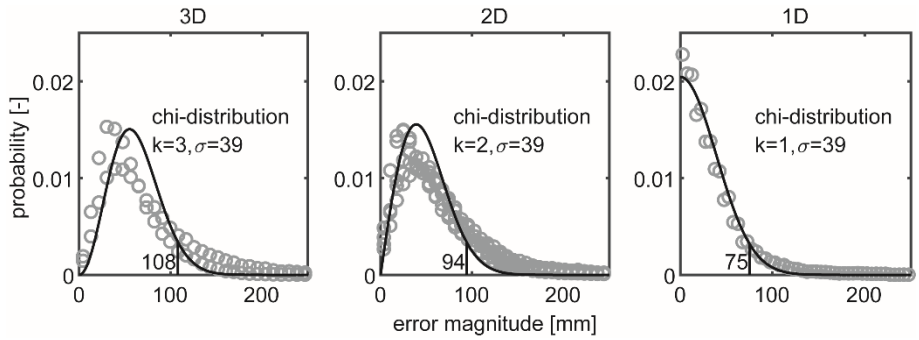

Figure 6.10 Probability distribution of the error magnitude when no crack is present, with the 95 percentile error magnitude marked.

In Models 6, 15-20, the crack height factor α_z is the variable, ranging from 0 to 1. Figure 6.11a shows the relationship between the error property σ and the crack height factor α_z. With increasing crack height, σ increases from 39 mm to 55 mm. The maximum value is obtained when the crack cuts through the measurement volume. Figure 6.11b explains this observation. We define a free zone, where the direct ray paths from sources to the receivers do not go through the crack. For sources in this free zone, the source localization is not influenced by presence of the crack. For sources outside the free zone, at least one of the direct ray paths will go through the crack. The crack will delay the arrival time, resulting in large source localization error. When the crack height increases, the volume of free zone is reduced. More percentage of sources will be located with the influence from the crack, giving larger overall source localization error. This explains why the standard deviation of the error component σ increased with crack height.

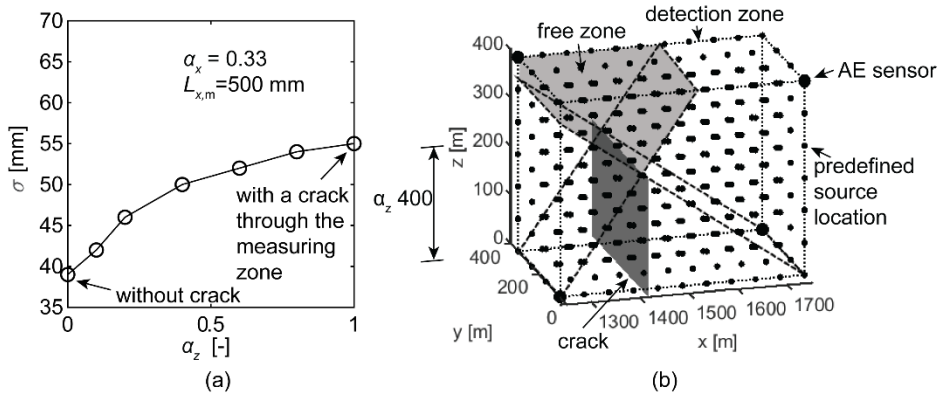

Figure 6.11 (a) Standard deviation of the error component in conditions with different crack heights, and (b) illustration of the free zone in source localization with a crack

In Models 1, 16, 21-24, the variable is the maximum sensor spacing $L_{x,\mathrm{m}}$ changing from 300 mm to 1500 mm. Figure 6.12a shows the relationship between the error property σ and the maximum sensor spacing $L_{x,\mathrm{m}}$. When the maximum sensor spacing is within 1200 mm, it hardly influences the localization error. At sensor spacing of 1500 mm, the localization error enormously increases. This is due to the fact that direct waves through the crack could not be detected when the sensors are 1 m away from the actual source, but tip-diffracted waves are received instead. Tip-diffracted waves introduce larger time delays and consequently increase the errors. This observation suggests that the localization error property is independent of the maximum sensor spacing when the spacing is within the distance that the direct waves can be detected.

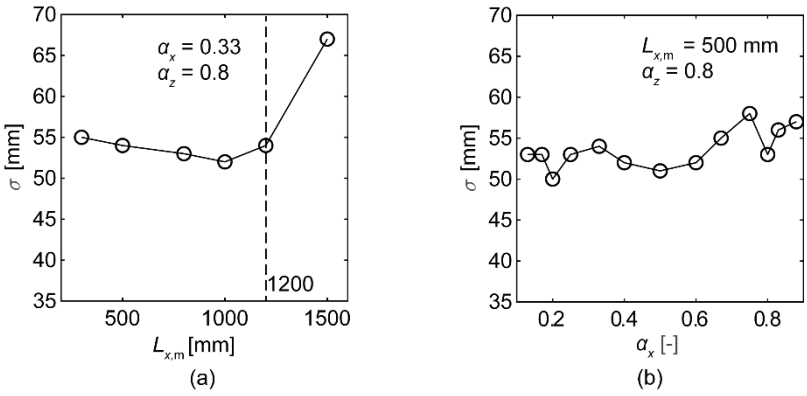

Figure 6.12 Standard deviation of error component in conditions of (a) different maximum sensor spacings and (b) different crack positions in *x* direction.

In Models 2-14, the variable is the sensor position in *x* direction. Figure 6.12b shows the relationship between the error property σ and the sensor position factor α_x. The localization error is independent of the crack position in *x* direction.

The above results apply to the real conditions that first the sensor spacing should be designed that the direct waves can be detected by sufficient number of sensors. In our case, the maximum sensor spacing is found to be 1200 mm. Within this sensor spacing, (1) when no crack is present, one can take the localization error properties obtained in Model 15 (σ = 39 mm), (2) when a crack presents, one can take the error properties obtained in Models 6,16-20 depending on the estimated crack height, and (3) when the presence of crack is unknown, one can take the error properties obtained in Model 20 considering the worst scenario that a crack cuts through the sensor grid (σ = 55 mm).

6.3 Probability density field of acoustic emission events

In literature, many algorithms have been developed to reduce the source localization error, including using akaike information criterion (AIC) to more accurately pick the arrival time (Kurz, Grosse et al. 2005) and using variable wave speed models to simulate uncertainty of concrete material properties (Pahlavan, Paulissen et al. 2014, Gollob 2017). However, these advanced algorithms often lead to longer computational time which is not suitable for real-time monitoring, and the source localization error cannot be entirely removed.

This section considers the source location as a variable. Based on the properties of localization error, obtained in the previous section, we propose a new method to estimate the probability of the source location.

6.3.1 Derivation of probability density field of acoustic emission events

Based on Equation (6.5), with the estimated source location as the origin, we are able to create the probability density field of source location as:

$$f\left(\mathbf{x},\mathbf{x}_{\mathrm{g}}\right)=\frac{1}{\left(\sqrt{2\pi}\right)^{k}}\frac{1}{\sigma^{k}}e^{-\left\|\mathbf{x}-\mathbf{x}_{\mathrm{g}}\right\|^{2}/2\sigma^{2}},k\in\{1,2,3\} \tag{6.10}$$

where $\mathbf{x}_{\mathrm{g}}$ is the estimated source location, $\mathbf{x}$ is a random point in the space of k dimensions. This function describes the probability density of the source location at $\mathbf{x}$, when the estimated location is $\mathbf{x}_{\mathrm{g}}$. The integration of probability densities over the whole space equals to 1.

Here an infinite space is considered. However, source localization in concrete structures is clearly bounded by the dimension of the concrete structure itself and the measuring zone inside it. This dissertation neglects the effect from assuming an infinite space of the source location.

When more AE events occur during monitoring, the probability density field of each event can be added, resulting in a probability density field of multiple AE events. For all

AE events that occur in the measuring time and space range, the probability density field is calculated as:

$$p_{\mathrm{A}}(\mathbf{x}) = \sum_{a\in\mathbf{A}} f\left(\mathbf{x}, \mathbf{x}_{\mathrm{g},a}\right) = \sum_{a\in\mathbf{A}} \frac{1}{\left(\sqrt{2\pi}\right)^{k}} \frac{1}{\sigma^{k}} e^{-\left\|\mathbf{x}-\mathbf{x}_{\mathrm{g},a}\right\|^{2}/2\sigma^{2}}, k \in \{1,2,3\} \tag{6.11}$$

where $\mathbf{A}$ is a set of all AE events that occurred in the measuring time and space range, $\mathbf{x}_{\mathrm{g},a}$ is the estimated location of event a, and other parameters are defined as before.

This method is called probability density field of AE events (pdAE field). Figure 6.13 illustrates the procedure. The required variables/inputs are the arrival times $\mathbf{t}_{\mathrm{r}}$, the sensor locations $\mathbf{x}_{\mathrm{r}}$, the wave speed c and the standard deviation of the error component σ. The first three inputs are required for a deterministic source localization, and the last one is needed additionally for the probabilistic approach. The Matlab code to realize this method is provided in Appendix B.

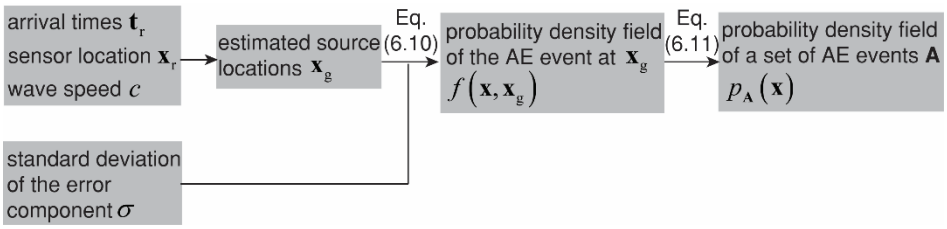

Figure 6.13 Derivation of probability density field of AE events.

6.3.2 Physical explanation of probability density field of acoustic emission events

A more specific description of 'probability density of AE events' is 'probability density of the location of AE events'. The random variable is 'the location of AE events'. Same as any other variable, its probability density at a point can be interpreted as a relative likelihood that the AE events would locate at that point. In other words, the absolute likelihood of AE events to locate exactly at one point is 0. Comparing the probability density at two different points can indicate how much more likely it is that the AE events would locate at one point compared to the other. For example, Figure 6.14a shows the probability density field of (location of) AE event a_1. Due to source localization error, this event can be estimated at any point in the space with different likelihood. The probability densities at two points p_1 and p_2 are 75.32 /m^2 and 12.76 /m^2 respectively. This indicates that the AE event more likely locates at p_1 than at p_2, which makes sense that p_1 is closer to the actual location than p_2.

More precisely, probability density of (the location of) AE events can be used to estimate the probability of AE events falling in a particular space range. The particular space range can be decided freely by the user depending on the purpose of the measurements. For

example, when the flexural zone is of more interest, the user could select the flexural zone and calculate the probability in that zone. The probability is calculated by the integral of probability densities over that space range (which is the volume under the probability density field within that space range). In the same example shown in Figure 6.14a, the probability of AE event a_1 located in the area (enclosed by the black frame) is calculated as 0.82. The integral over the whole space is 1.

Figure 6.14b shows the probability density field of three AE events at a_1, a_2 and a_3, by cumulating the field of every event. Therefore, the probability density at the same point p_1 increases to 125.27 /m2, and the probability of AE event within the same area (enclosed by the black frame) increases to 1.85. This means that the likelihood that AE events are at point p_1 or within the black frame increases when more AE events occur. The integral over the whole space is the number of AE events (which is 3 in our example).

From the above analysis, probability density of (location of) AE events at any point is determined by the source localization error, the number and the locations of AE events. Based on the probability density, one can estimate the relative likelihood of AE events located at any point, and estimate the probability of AE events located within a certain space range. Using probability density field of (location of) AE events is a novel method to quantify AE distribution including uncertainties. In this dissertation, the simplified term 'probability density field of AE events' or 'pdAE field' is used.

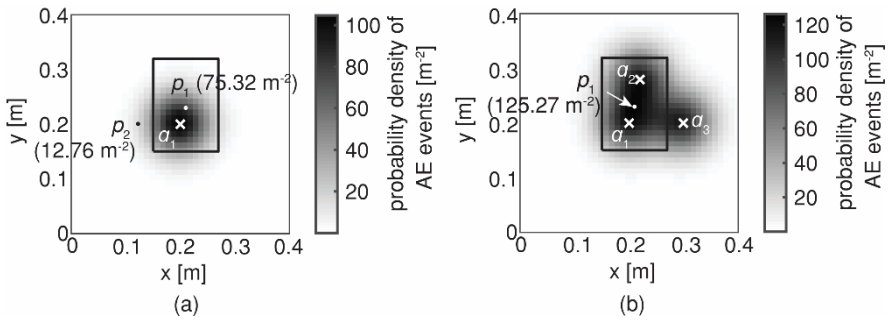

Figure 6.14 Illustration of probability density field of (a) one AE event and (b) multiple AE events.

6.4 Demonstration of the method in experiments

This section demonstrates the pdAE field in shear tests of a beam and a slab. The beam test I123A and slab test SR1M1 are taken.

The source locations have been estimated as shown in Chapter 5. In this section, we process the estimated source locations using the new method pdAE field.

We need to determine the source localization error property σ. For the beam test, the sensor layout was designed as only one crack formed in a sensor grid. During cracking, no other cracks lay between the source and the receiver. The condition was in line with

the simulation Model 15 in Table 6.1, where the crack height factor $\alpha_z = 0$ and the sensor spacing $L_{x,\mathrm{m}} = 500$ mm. Therefore, we take the value $\sigma = 39$ mm. For the slab test, multiple cracks formed in a sensor grid. Here we apply the value $\sigma = 55$ mm from Model 1 in Table 6.1, where $\alpha_z = 0.8$ and $L_{x,\mathrm{m}} = 300$ mm..

Then we construct the pdAE field from Equation (6.11). The pdAE is evaluated at predefined grid points in the measuring zone. We take a grid size of 20 mm.

Figure 6.15 shows the results in the beam test from 0 until 200 kN (excluding the AE events during unloading).

- Plot (a) shows the estimated locations of AE events by the grid search method. We detect two cracks CR1 and CR2. Due to the source localization error, the results are scattered.
- Plot (b) shows the pdAE field for one AE event. We can find that the likelihood is little at locations farther than 0.09 mm (which is the 95 percentile error).
- Plot (c) shows the pdAE field for all AE events. Cracks are more clearly detected (even the secondary crack near CR2 can be distinguished).
- Plot (d) compares the pdAE and the crack width (obtained from DIC) at points p_1-p_7 along CR2. We find a close relationship between the pdAE and the crack width, especially for points p_1-p_4. This relationship is further studied in Chapter 8.

The probability density field can be updated in real time when new AE events occur. In the demonstration, for a single AE event, the total computational time including calculation and visualization is around 0.12 s. This is a significant reduction compared to the more complex probabilistic methods (which is around 50 s per AE event (Schumacher, Straub et al. 2012)).

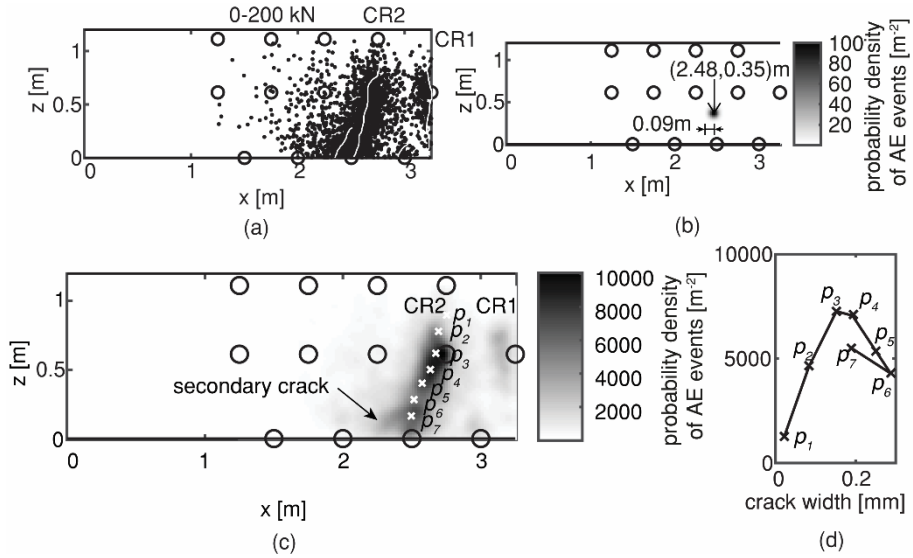

Figure 6.15 From 0 to 200 kN (excluding AE events during unloading) in test I123A: (a) estimated source locations with marked actual crack patterns, (b) the pdAE field of one AE event, (c) the pdAE field of all AE events and (d) relationship between pdAE and local crack width at points p_1-p_7.

The phAE field in the slab test is in 3D. Figure 6.16 shows the sectional results from 0 to the maximum load 1125 kN (excluding AE events during unloading). Compared to the raw data in Figure 5.18 in Chapter 5, the cracking area is more clearly distinguished. From the vertical sections at different locations in *y* direction, we find that the section closer to the loading plate was more damaged. Comparing the two horizontal sections at different height, we can find that cracks tended to concentrate to the loading plate when approaching the top section (where was the compressive zone).

To provide a 3D internal view, we plot the results in voxels (Figure 6.17). The voxel size is 20 mm × 20 mm × 20 mm. The voxel is plotted in different colors according to the pdAE value. The voxel is plotted in red, where the pdAE is over the ½ of the maximum pdAE. The voxel is plotted in yellow, where the pdAE is in range (¼, ½) of the maximum pdAE. The voxel is not plotted, where the pdAE is below ¼ of the maximum pdAE. The maximum pdAE in the detection zone is found to be 71,827 m^{-3}. At 400 kN (plot a), AE events most occurred under the loading plate where the bending moment was the largest. This indicates the flexural cracking. At 1125 kN (which was close to failure, plot b), we can find a shape of punching cone under the loading plate. The slab failed in punching.

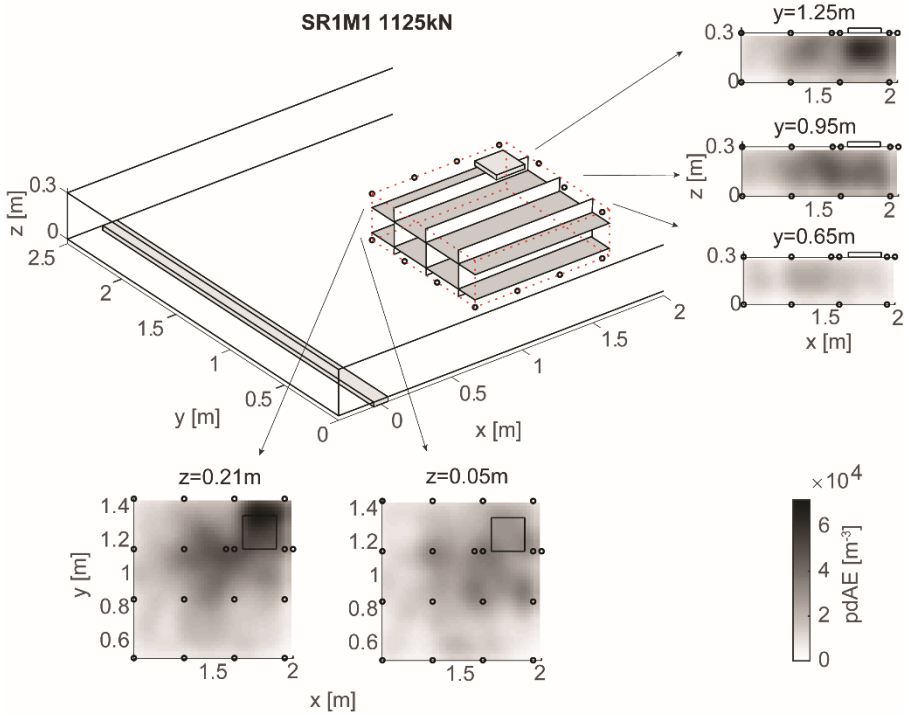

Figure 6.16 pdAE field at sections, considering AE events until failure (excluding AE events during unloading) in slab test SR1M1.

Compared to the beam tests, the crack patterns in the slab tests are less recognizable by the pdAE field. This is due to larger source localization error in slab tests. The 95 percentile error reached 153 mm according to the simulation Model 1 which is similar to the slab tests. This error magnitude was comparable or even larger than the crack spacing in the slabs, leading to less able to distinguish two cracks in the slabs using the pdAE field.

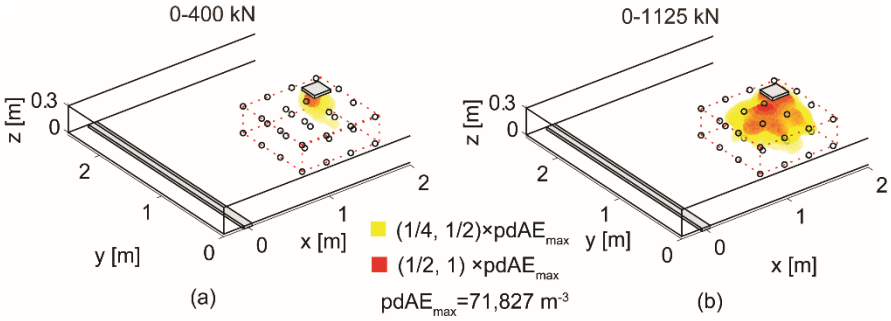

Figure 6.17 3D voxel plot of the pdAE (a) until 400 kN and (b) until failure (both without unloading parts) in slab test SR1M1.

The above demonstration shows the benefits of using pdAE field. Firstly the crack pattern can be more clearly distinguished after considering the source localization error in a probabilistic manner. Secondly pdAE field quantifies the spatial distribution of AE events reasonably by including the source localization error. Thirdly the pdAE is found closely related to the crack width at crack locations. This shows the possibility of using the pdAE to quantify the crack width, which will be discussed in Chapter 8. Fourthly the calculation of pdAE is computationally efficient, which serves for a real-time monitoring.

To implement the probability density field of AE events in practice, some remarks are addressed:

- When designing the sensor spacing, two aspects need to be considered. Firstly the sensor spacing should allow the direct waves being detected by sufficient number of sensors after attenuation. Here a preliminary measurement on wave attenuation is needed. Secondly the sensor spacing is suggested to be smaller than the expected crack spacing. In this way, it is likely that only the crack which generates AE sources is present between two sensors and no other cracks are present between the source and the receiver. This consideration limits the influence from presence of crack.
- This dissertation uses the grid search method to estimate the source locations. Other localization methods can also be used, such as those considering a variable velocity distribution (Gollob 2017). A different localization method may provide different source localization errors. Therefore, the standard deviation of error component σ needs to be adjusted correspondingly.
- The influential factor i.e., the arrival time picking error, need to be updated if different arrival time picking methods are used. Once the arrival time picking error is determined for a specific test setup, it is suggested to run the simulation to get the standard deviation of the error component.
- For the studies that only require the crack patterns, one can directly use the source localization error properties proposed in this paper, without running the simulations.
- For real-time monitoring, the probability density field of AE events can be updated at every new AE event or in a certain time interval according to the users' need.

6.5 Conclusion

Source localization in concrete structures is influenced by many uncertainties including presence of crack, arrival time picking error and sensor layout. The consequence is that the estimated source location is not the actual one, and the distance between the two locations is defined as source localization error. This chapter proposed a simple probabilistic method that is able to consider the source localization error in a systematic manner. We first evaluated the properties of source localization error using simulations. A total

number of 11,827,200 simulated tests were conducted. From the simulation, we used a probability density function to describe the source localization error. We further constructed a probability density field of the location of an AE event, where the integration of probability densities over a certain space range indicates the probability of AE events located in that space range. When dealing with more AE events, the probability density field is updated by adding up the field of each AE event. The output of this method is called probability density field of AE events (pdAE field).

Then we demonstrated the pdAE field in tests of reinforced concrete beam (2D member) and slab (3D member). In both demonstrations, pdAE can more clearly distinguish the crack patterns compared to the traditional source localization method. And the value of pdAE is found closely related to the crack width at local positions. This shows the possibility of using the pdAE to quantify the crack width, which will be discussed in Chapter 8. Moreover, the calculation of pdAE is computationally efficient, which serves for real-time monitoring.

We use this method in the rest of this dissertation to identify the crack location and quantify the AE events spatial distribution.

Chapter 7 Acoustic emission source classification criterion for concrete structures based on signal parameters

7.1 Introduction

Acoustic emission (AE) signals from different types of sources in concrete (i.e. tensile cracking and friction) have different features. By distinguishing these features, we can classify the source type. In Chapter 4, we have reviewed the available source classification techniques, including parameter-based method and signal-based method. Signal-based methods usually take longer computational time, thus are not widely applied in real-time monitoring.

Parameter-based methods use signal parameters to describe the features. However, the signal parameters are influenced by wave propagation from the source to the receiver, which may lead to false source classification results, especially for monitoring large concrete structures. In literature, the influence of wave propagation on signal parameters were mostly evaluated using simulations (Aggelis, Shiotani et al. 2011, Polyzos, Papacharalampopoulos et al. 2011, Zhang 2017), which simplified the wave propagation in real concrete structures. The influence of wave propagation on the AE signal parameters in large-scale concrete structures is not available yet in literature.

This chapter first introduces the two types of AE sources in concrete cracking (Section 7.2). Then we experimentally study the behaviour of signal parameters from the two source types (Section 7.3). The studied signal parameters include the RA value, average frequency, peak frequency, frequency centroid, and partial power. To reduce the influence of wave propagation, the signals that were received at the closest sensor to the source are used (with a distance less than 0.3 m). Then by comparing to the signals that were received at farther sensors to the source (with a distance up to 1.5 m), we evaluate the influence of wave travel distance on signal parameters (Section 7.4). Based on the evaluation, we propose a new source classification criterion using peak frequency or partial power and suggest a sensor layout that is suitable for source classification in concrete structures with realistic dimensions. The new source classification criterion is also validated in another type of concrete structure, the reinforced concrete slab (Section 7.5). The new criterion classifies the source type in a reliable and efficient way.

7.2 Two types of acoustic emission sources in concrete structures

As reviewed in Section 4.2.5, source classification in concrete mainly distinguishes two types of sources, i.e. tensile cracking and friction. Concrete cracking (both flexural and shear cracking) are a combination of tensile cracking and friction, with more friction at shear cracking due to more shear displacement (Zarate Garnica 2018). Figure 7.1 shows the combination of tensile cracking and friction at a local crack profile.

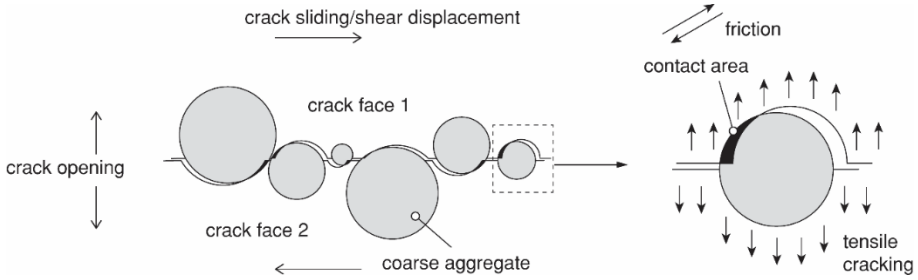

Figure 7.1 Illustration of tensile cracking and friction at local crack profile

Due to different crack kinematics, these two types of AE sources generate signals with different features. One feature is the slope of the signal ascending part, which is evaluated by RA value: the ratio between rise time and peak amplitude. The other feature is the signal frequency, which can be evaluated by parameters peak frequency, frequency centroid and partial power. Figure 7.2 shows the typical received signals from tensile cracking and friction obtained in test I123A. Signals from friction have larger slope (smaller RA value) and more energy in the lower frequency components. This behaviour has been observed in many other experiments not only in concrete but also other cement-based materials (Shiotani, Ohtsu et al. 2001, Shiotani, Bisschop et al. 2003). RILEM technical committee suggest to use RA value and average frequency to distinguish signals from tensile cracking and friction (Ohtsu 2010).

But these two features can be significantly influenced by the wave propagation. With longer wave travel distance, the rise time will increase between the P-wave and the peak amplitude (which could be S-wave or combination of other wave modes), while the peak amplitude will reduce due to wave attenuation, resulting in larger RA value. Therefore it is hard to determine whether variation of RA value is due to different source types or wave travel distances. The same effect is also on the signal frequency that longer wave travel distance will cause more attenuation in high frequency components, resulting in lower frequency in the received signals. The effect of wave propagation may mislead the distinguish of signals from tensile cracking and friction using RA value and average frequency.

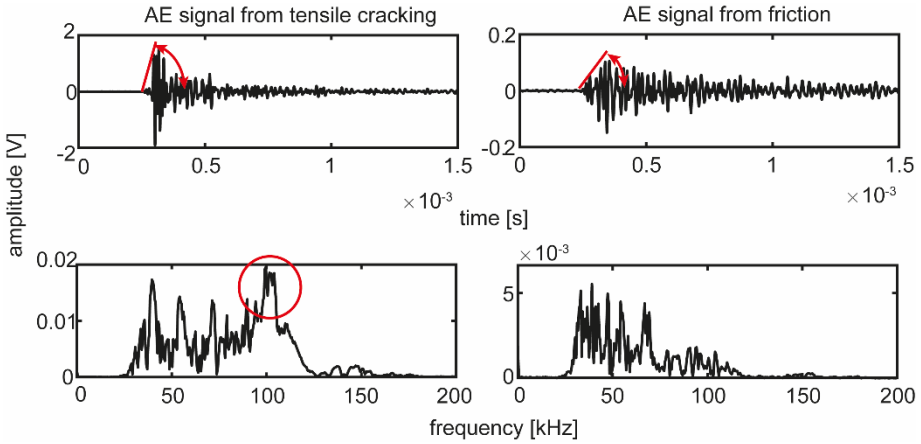

Figure 7.2 Typical AE signals from tensile cracking and friction obtained in test I123A.

7.3 Behaviour of signal parameters from the two source types

We study the signal parameter behaviour from the two source types using the signals in test I123A. Based on the estimated source location, AE events around the flexural crack CR2 are selected typically for tensile cracking (Figure 7.3a), and AE events around the shear crack CR4 are selected for friction (Figure 7.3b). Note that the estimated locations are scattered around the real crack location, which is due to source localization error. The source localization error can reach 0.09 m when no crack is between source and sensor (according to Chapter 6). Consequently, the calculated wave travel distance from source to sensor can have an error of ± 0.09 m. We neglect the error of the calculated wave travel distance. In total, 337 AE events are selected for tensile cracking and 1342 AE events for friction.

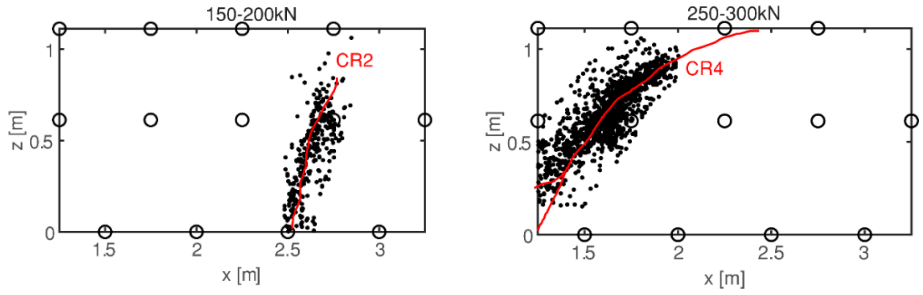

Figure 7.3 Selection of typical AE events for (a) tensile cracking (around flexural crack CR2 at load 150-200kN), and (b) friction (around shear crack CR4 at load 250-300kN).

For each AE event, the signal that was received by the closest sensor is used. This minimizes the influence of wave propagation on the received signals. Around 80% of these

signals had a wave travel distance less than 0.3 m (the other 20% were within 0.5 m). We assume that this wave travel distance did not significantly influence the signal parameters, thus the received signals can represent the signal source.

Figure 7.4 compares the distribution of signal parameters from typical AE events for tensile cracking (a) and friction (b). The main observations are listed below.

- The RA values (a.1 and b.1): the distributions are similar in the two types of sources, both having most events with RA values lower than 0.2 ms/V.
- The average frequency (a.2 and b.2): the modal bins are 60-70 kHz and 50-60 kHz in tensile cracking and friction respectively.
- The peak frequency (a.3 and b.3): the modal bins are 90-100 kHz and 30-40 kHz in tensile cracking and friction respectively. We could conclude that AE events with peak frequency around 100 kHz were from tensile cracking, and 40 kHz from friction.
- The frequency centroid (a.4 and b.4): the modal bins are 80-100 kHz and 70-80 kHz in tensile cracking and friction respectively.
- The partial power (a.5 and b.5) is calculated as the percentage of frequencies above 70 kHz. The boundary of 70 kHz is selected in the middle of the two possible peak frequencies (40 kHz and 100 kHz). Though partial power is more evenly distributed, we find that more signals have partial power over 0.5 in tensile cracking, and below 0.5 in friction. This indicates that signals from tensile cracking had larger amount of energy in high frequency components (>70 kHz).

The comparison shows that the RA value cannot distinguish signals from tensile cracking and friction. The frequency-related parameters turn out to be reliable. Among them, the peak frequency shows a more significant difference between signals from tensile cracking and friction (which are 100 kHz and 40 kHz respectively).

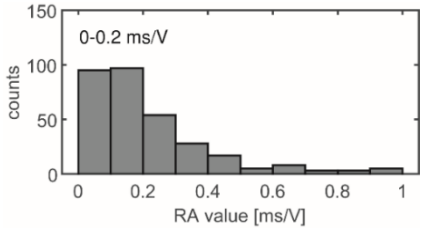

(a.1)

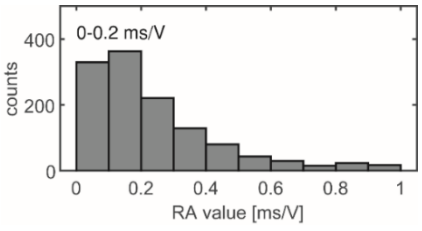

(b.1)

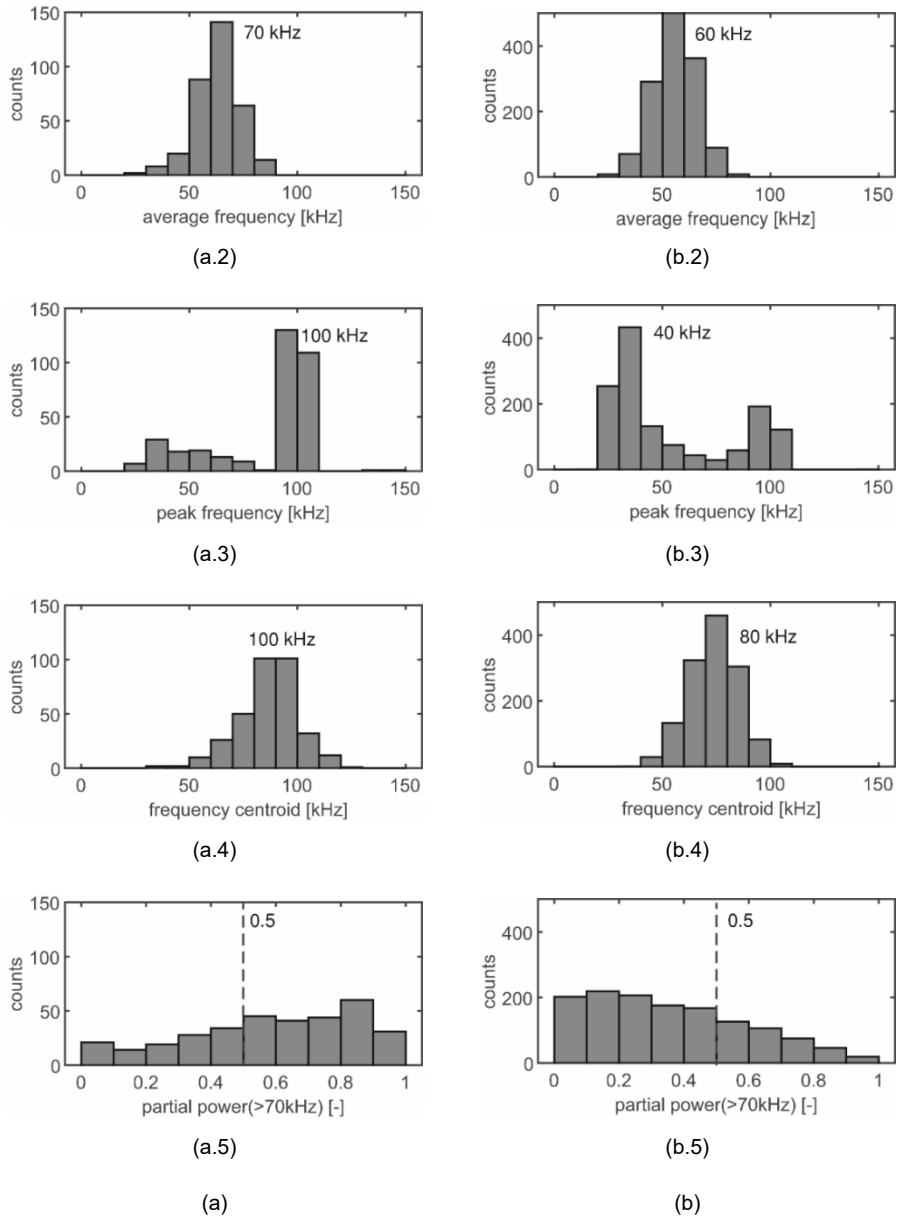

Figure 7.4 Distribution of the parameters from signals received by the closest sensors in (a) tensile cracking and (b) friction, with (a.1) (b.1) RA value, (a.2) (b.2) average frequency, (a.3) (b.3) peak frequency, (a.4) (b.4) frequency centroid, (a.5) (b.5) partial power (>70kHz).

7.4 Influence of wave travel distance on signal parameters

To study the influence of wave travel distance on the signal parameters, we use all the recorded signals where the wave travel distance varies from 0.05 m to 1.5 m.

Figure 7.5 exemplifies the behaviour of signal parameters after different travel distances. The signals were originally from the same AE event (located at x = 2.5 m, z = 0.15 m), but received at different distances to the source, i.e. 0.15 m, 0.51 m and 0.88 m (by sensors AE2, AE6 and AE8 respectively). No crack was between the sensors and the signal source at the time of measurement. Therefore, the behaviour of signal parameter is mainly due to different wave travel distances. The signal parameters are marked in the graph. In the waveform in time domain (top row of plots): the peak amplitude reduces and arrives later after longer wave travel distance, resulting in an increase of RA values from 0.03 ms/V to 0.62 ms/V; the average frequency decreases from 69 kHz to 51 kHz. In the frequency spectrum (bottom row of plots): after traveling 0.15 m, high frequency components (>70 kHz) still have a large percentage of energy, giving large peak frequency, frequency centroid and partial power; after traveling 0.51 m, the energy in high frequency components (> 70 kHz) significantly reduces, but the energy in low frequency components remains; after traveling 0.88 m, the energy in low frequency components also reduces.

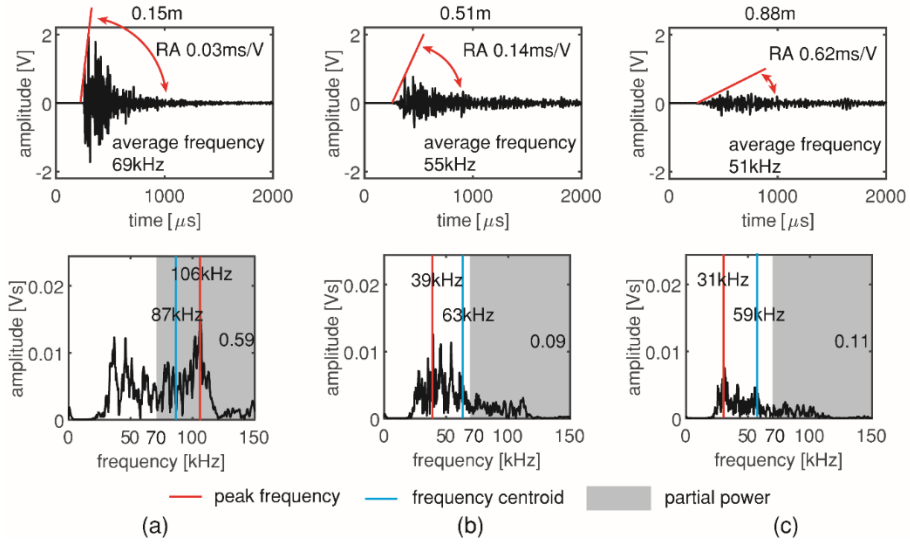

Figure 7.5 Signals from an AE event (x = 2.5 m, z = 0.15 m) received at different distances: (a) 0.15 m, (b) 0.51 m and (c) 0.88 m.

We find that high and low frequency components attenuate differently, which influences the frequency-based parameters. To study the different attenuation in high and low frequency components, we separate the frequency components above and below 70 kHz by applying a high-pass filter and a low-pass filter (Figure 7.6a). Then the amount of energy in the filtered signals are calculated (which is the area under the signal envelop in Vμs). Next we calculate the change of energy at different distances in dB, comparing to the energy of the closest signal (which is set as the reference). We use signals from AE events from CR2 in test I123A as examples. Figure 7.6b and c show the energy changes of the

filtered signals by high pass filter and low pass filter respectively. The high frequency components attenuate more during wave propagation, which meets our expectation.

In the above examples, the signal parameters change with increasing wave travel distance in the following manner: increasing RA value and decreasing frequency-related parameters (i.e. average frequency, peak frequency, frequency centroid and partial power of high frequency components).

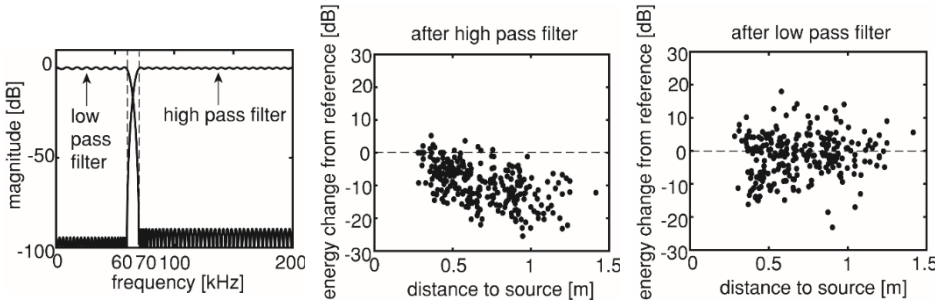

Figure 7.6 (a) High-pass filter and low-pass filter, energy changes of the filtered signals by (b) high pass filter and (c) low pass filter.

Including all the recorded signals from CR2 and CR4, Figure 7.7 shows the distribution of signal parameters varying with the wave travel distance. We compare the results from tensile cracking (a) and friction (b):

- The RA value (a.1 and b.1): the modal bin increases with wave travel distance in both tensile cracking and friction. No clear difference is found between signals from tensile cracking and friction.
- The average frequency (a.2 and b.2): the modal bin reduces from 60-70 kHz to 50-60 kHz after around 0.5 m in tensile cracking. After 0.5 m, the average frequency in signals from tensile cracking and friction are comparable.
- The peak frequency (a.3 and b.3): the modal bin in tensile cracking reduces from 90-100 kHz to 30-40 kHz after 0.5 m. In friction, the modal bin remains 30-40 kHz.
- The frequency centroid (a.4 and b.4): the modal bin gradually reduces with wave travel distance in both tensile cracking and friction. In tensile cracking, the modal bin reduces from 90-100 kHz to 60-70 kHz after a wave travel distance of 0.5 m. In friction, the reduction is not that significant, from 80-90 kHz to 60-70 kHz.

- The partial power (>70 kHz) (a.5 and b.5): the modal bin reduces with wave travel distance in both tensile cracking and friction. But, in tensile cracking, the modal bin was initially above 0.5. In friction, the value is always below 0.5.

We find that 0.5 m is a critical wave travel distance. After 0.5 m, high frequency components significantly attenuate and are not dominant anymore, even in signals from tensile cracking. As a result, signals from tensile cracking may be falsely distinguished as signals from friction. Therefore, the first requirement for source classification is to use signals that are within 0.5 m to the source. The value of 0.5 m depends on the distance within which the high frequency components can dominate, thus may vary with different materials.

Among all the parameters, the peak frequency is the one showing a significant difference between tensile cracking (around 100 kHz) and friction (around 40 kHz). We can define a boundary of 70 kHz considering the possible scatterings of peak frequency. When the peak frequency is larger than 70 kHz (which represents the cases where the frequency component around 100 kHz is dominant), the signal is from tensile cracking. Otherwise, the signal is from friction. The partial power may also be used, by determining whether the energy in high frequency components (>70 kHz) is more than that in low frequency components. But the other two parameters i.e., average frequency and frequency centroid, 'averaged' the high and low frequency components, indicating less difference between tensile cracking and friction. This adds difficulty in defining a clear boundary to separate the signals from the two types of sources using average frequency or frequency centroid.

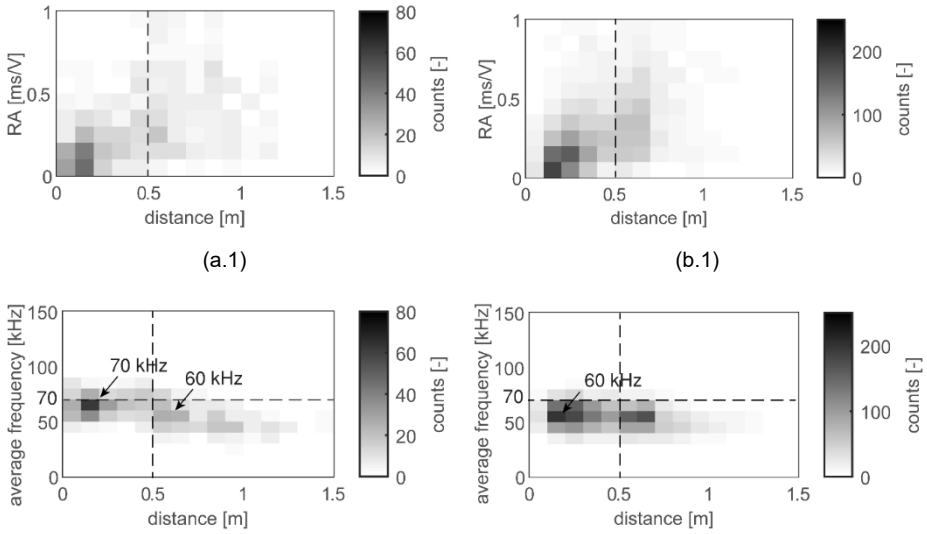

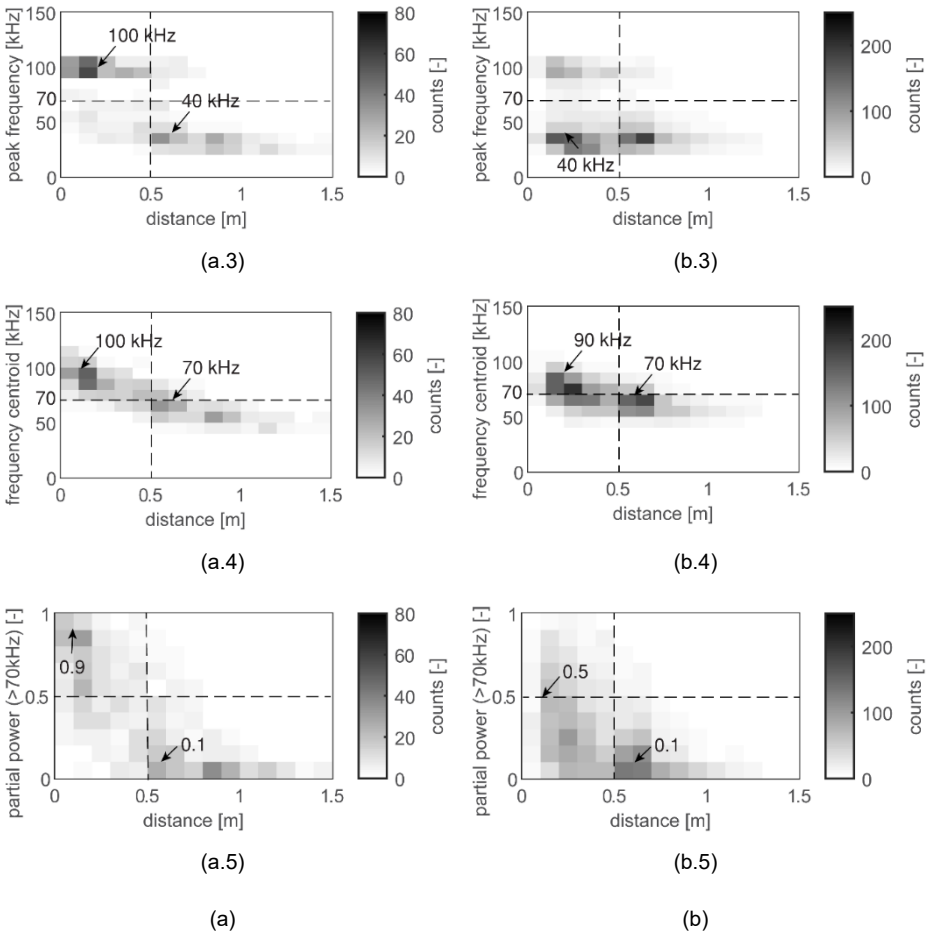

Figure 7.7 Distribution of the parameters of all the signals, varying with wave travel distance, in AE events (a) for tensile cracking and (b) friction, with (a.1) (b.1) RA value, (a.2) (b.2) average frequency, (a.3) (b.3) peak frequency, (a.4) (b.4) frequency centroid, (a.5) (b.5) partial power.

Therefore, we suggest a new criterion for source classification: the signals with peak frequency larger than 70 kHz or partial power (>70 kHz) larger than 0.5 are considered from tensile cracking; otherwise, the signals are from friction. A requirement is that the source and receiver distance should be within 0.5 m. The conformance of the source classification using the two parameters i.e., peak frequency and partial power, are evaluated in the following section.

7.5 Validation of the new criterion

In this section, we validate the source classification criterion on other cracks of the same beam and a different type of concrete structure i.e., the reinforced concrete slab SR1M1.

7.5.1 Validation on other cracks of the same beam

Figure 7.8a - c show the source classification results using peak frequency from first cracking to failure of the beam I123A (only considering the loading part when cracks open). The red dots are AE events classified as friction and the blue dots are tensile cracking.

- At 150-200 kN (plot a), only flexural cracks CR1 and CR2 formed. More AE events are classified as tensile cracking.
- At 200-250 kN (plot b), the shear crack CR3 formed. At upper part of CR3, more AE events are classified as tensile cracking, while at bottom part, more AE events as friction. This is expected as the secondary crack in the bottom was more inclined with larger shear displacement, generating more friction between two crack faces.
- At 250-300 kN (plot c), the shear crack CR4 formed. The shear crack CR4 generated a large amount of AE events of friction. Moreover, the existing crack CR3 also had many AE events of friction. This means that both CR3 and CR4 had larger crack sliding (or shear displacement) when close to shear failure (at 300 kN). The classification results are in line with the shear failure models that near failure, the critical crack would have a large shear displacement (Yang, den Uijl et al. 2016).
- Plot d shows the ratio of the number of AE events classified as friction to the total number of AE, varying with the load levels. With increasing load, the ratio of friction within each load increment increases. This is due to the formation of new shear cracks and the sliding between crack surfaces of the existing cracks. The source classification criterion performs well in all the cracks of the reinforced concrete beam during the whole loading process.

The above results are obtained using peak frequency. Using the other parameter partial power may provide different results in some cases. An example signal is provided in Figure 7.9. The signal has a peak frequency at 105 kHz which is larger than 70 kHz, thus is classified as from tensile cracking. However, since the peak is very narrow, the energy in the frequency range of over 70 kHz is still not large. This results in a partial power (>70 kHz) of only 0.41 which is lower than 0.5. Consequently, the signal is classified as friction by partial power. Therefore, a further study to check the differences between the two criteria are made below.

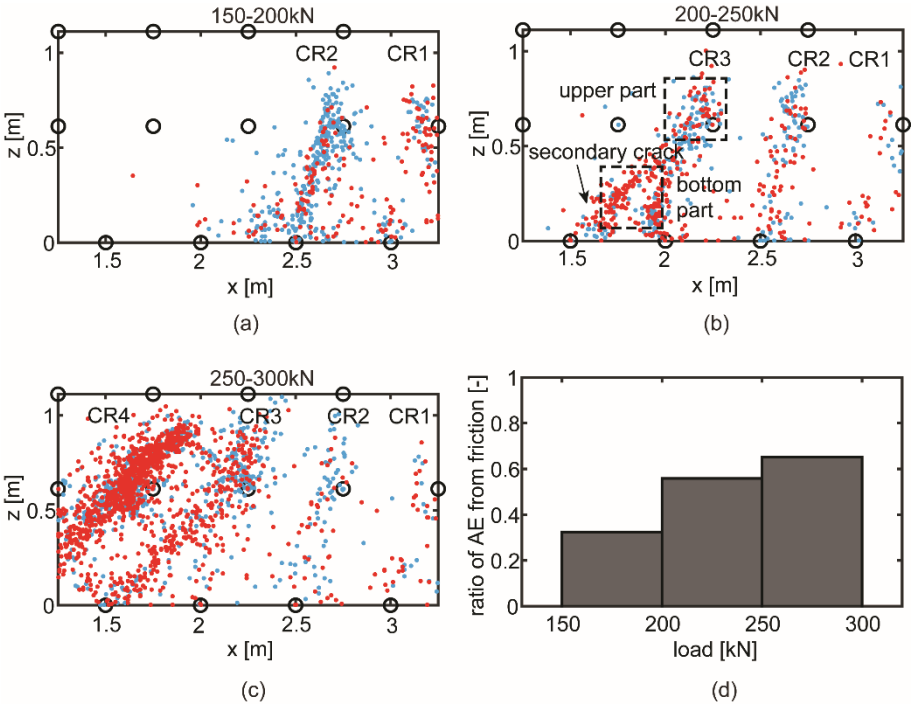

Figure 7.8 Source classification using peak frequency in the beam: (a) at 150-200 kN, (b) at 200-250 kN, (c) at 250-300 kN, and (d) ratio of number of AE events as friction at different load ranges. (Blue dots are AE events classified as tensile cracking, and red dots are as friction.)

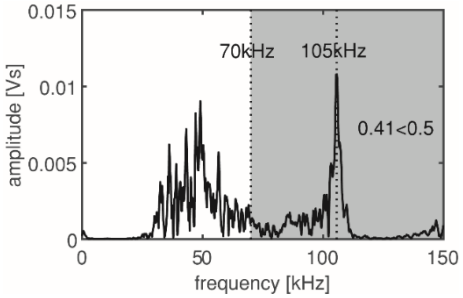

Figure 7.9: Frequency spectrum of a typical signal that was sorted as from tensile cracking by peak frequency (105 kHz>70 kHz), but friction by partial power (0.41<0.5).

Table 7.1 counts the signals that, according to the two parameters, have matching and contrary source classification results. The number of signals that result in matching source classification from the two parameters are greyed out in the table. The percentages of matching classification are 87%, 89% and 91% in the three load increments respectively. Around 10% of the signals result in contrary classification. This thesis considers the two parameters equivalent. Without further mentioning, we use peak frequency by default in the study presented below. Combining the two parameters might improve the classification results, but is out of the scope of this dissertation.

Table 7.1 Comparison of source classification results using peak frequency and partial power (>70 kHz)

Load increment	150-200 kN		200-250 kN		250-300 kN	
Peak frequency / Partial power	Tensile cracking	Friction	Tensile cracking	Friction	Tensile cracking	Friction
Tensile cracking	311	17	232	17	555	57
Friction	54	158	52	342	127	1219
Matching classification*	87%		89%		91%	

*The percentage of signals that had matching source classification results according to peak frequency and partial power (>70 kHz). The number of signals that had matching results from the two parameters is greyed out.

7.5.2 Validation on a reinforced concrete slab test

We evaluate the proposed source classification criterion in the slab test SR1M1.

Comparing to the beam, the slab is much wider. Therefore, the crack distribution cannot be simplified as a 2D case as in the beam. We use 3D source localization, which brings larger source localization error compared to 2D (Zhang, Pahlavan et al. 2020). Moreover, the slab has smaller crack spacing than the sensor spacing (according to crack pattern in Chapter 5). Consequently, more than one crack is present between two sensors, which also increases the source localization error. The localization error would result in an unclear located crack pattern, but will limitedly influence the classification results.

Figure 7.10 shows the source classification results using the new criterion in the slab test SR1M1. Plot a shows the ratio of number of AE events classified as friction to the total AE events within each load increment (every 50 kN). The first crack opened at 150 kN. Afterwards, the ratio of AE events from friction increased with loading. This meets our expectation that more shear displacement occurred with increasing load, which generated more AE events of friction. We also observe a relatively larger ratio of AE events from friction before 150 kN. These events are around the loading plate from the source localization results (Figure 7.10b). They could come from the friction between the loading plate and the structural surface during the setting of contact.

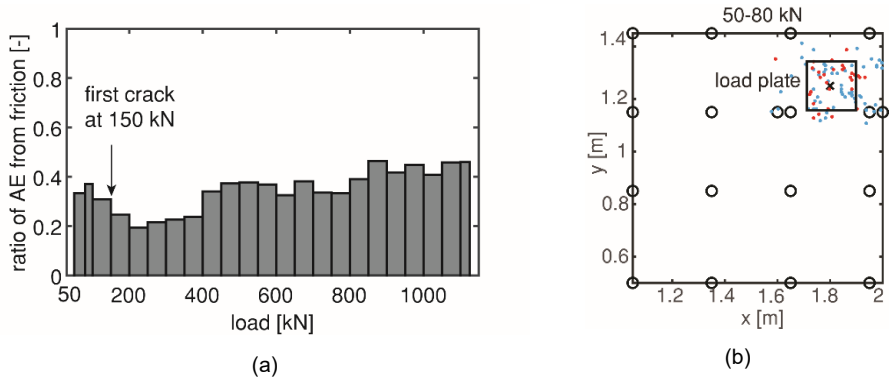

Figure 7.10: Source classification results using peak frequency in slab test SR1M1: (a) ratio of number of AE events from friction at different load increments and (b) at 50-80 kN (blue dots are AE events classified as tensile cracking, and red dots are classified as friction).

We also validate if the distance limit of 0.5 m in the source classification criterion can be applied in the slab test. AE events from the first cracking is used, which is not influenced by any crack between source and receiver. Figure 7.11 shows the distribution of the two parameters, varying with the distance. We find a clear difference of peak frequency after 0.5 m: the modal bin reduces from 90-100 kHz to 30-40 kHz. The modal bin of partial power also reduces to values lower than 0.5 after 0.5 m.

The above results prove the applicability of the proposed source classification criterion in the reinforced concrete slab.

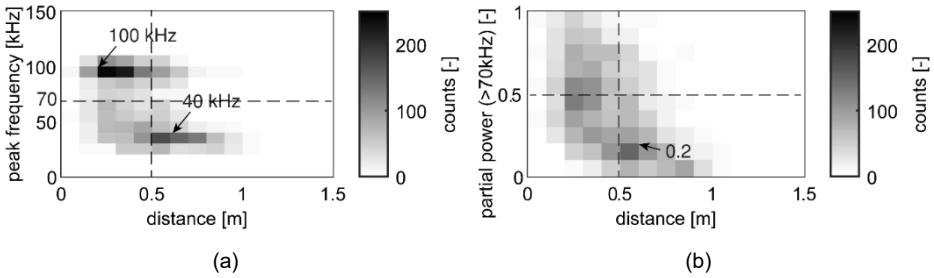

Figure 7.11 Influence of wave travel distance on the signal parameters in the slab test: (a) peak frequency, and (b) partial power (>70 kHz)

7.6 Discussion and recommendation

When using the new classification method, an important assumption is that the signal received by the closest sensor is representative of the source signal. However, these signals are still attenuated. The attenuation would result in lower frequency in the received signal. Therefore, for signals from friction, it is hard to determine to which extent the observed lower frequency is from the original source signal features or signal attenuation.

A possible solution is to further reduce the distance of the closest sensor to limit the influence from attenuation. For now, irrespective to the reason of lower frequency of received signals from friction, the proposed criterion can be used.

We should also consider the influence from sensor frequency response. Though the sensor operating frequency covers the two frequency components 40 kHz and 100 kHz (ASTM E1106-86 1997), the sensitivity at 40 kHz can be 5 dB more than that at 100 kHz (MISTRAS 2008), which is around 1.7 times larger. In this case, applying a factor of 0.6 (1/1.7) to the amplitude at 40 kHz may be more reasonable to determine the peak frequency. The same applies to the partial power calculation, a factor from the sensor frequency response should be multiplied to the amplitude of each frequency component in the received signal. When another type of sensor is used, it is suggested to modify this factor according to the sensor frequency response. It is a benefit of the proposed criterion that it can be calibrated for the sensor type.

Further study can consider the calibration of the frequency spectrum according to the sensor frequency response. Moreover, the proposed criterion also needs to be verified in other types of concrete. For example, deteriorated concrete will influence the coupling effect and further attenuate the signal, which will eventually influence the criterion.

7.7 Conclusion

This chapter first experimentally evaluated the available signal parameters for source classification in full-scale concrete structures, including RA value, average frequency, peak frequency, frequency centroid and partial power. The performances of these parameters with short travel distances (< 0.3 m) and long travel distances (up to 1.5 m) were studied. We found that the RA value, recommended by RILEM AE standard, is strongly influenced by wave attenuation, thus is not reliable for source classification in large concrete structural members with limited sensors. Among the other frequency-related parameters, peak frequency and partial power can provide a clear boundary between signals from two types of sources. Therefore, they were used to develop the new source classification criterion: in case the peak frequency is over 70 kHz, or the partial power (>70 kHz) is larger than 0.5, the signal is identified as from tensile cracking; otherwise, the signal is from friction. In a real test, we suggest that only the signal received by the closest sensor should be used, and the distance should be within 0.5 m. This distance limit suggests that the sensor spacing for a reliable source classification should be smaller than 1 m. The proposed source classification criterion was validated by AE signals from other cracks of the same concrete beam and from a concrete slab test.

The new source classification criterion has great potential in real-time AE monitoring. Using the selected signal parameters saves computational time compared to more sophistic classification using waveforms or even artificial intelligence-based methods, and provides more reliable results than traditional signal parameters for source classification.

Chapter 8 Relationship between acoustic emission events and crack kinematics

8.1 Introduction

As reviewed in Chapter 2, a challenge of using AE to identify concrete cracking is quantification of the crack width. Many studies have found that the number of AE events increase with crack width. But the relationship varies among different tests and has not been well explained. Moreover, the quantification is influenced by the limitation of current AE methods e.g. errors of source localization.

In this chapter, we explore the relationship between AE events and crack kinematics using the newly developed AE method, probability density of AE events (pdAE), and the DIC technique. We use the DIC to track the crack pattern and measure the local crack kinematics (including crack width change and shear displacement). This information is then compared with the pdAE at any location along the crack. This approach helps us to reveal the relationship between AE events and crack width locally.

Section 8.2 introduces the method to relate the pdAE and the crack kinematics measured from the experiments. The experiments were carried out in cyclic loading (Chapter 5). In each cycle, cracks were opened and closed during the loading and unloading process. Crack opening and closure have different mechanisms and different pdAE may be obtained accordingly. Therefore, the relationship between the pdAE and the crack kinematics during the crack opening and closure are discussed separately in Section 8.3 and Section 8.4. We explain the physical background of the obtained relationships from the experiments. Section 8.5 further studies the influence of number of load cycles and loading speed on the relationships.

8.2 Preparation of acoustic emission events and crack kinematics data

This section introduces the method to relate the AE and the DIC data in tests. We use tests H601A, H602A, H603A, H604A and I123A introduced in Chapter 5. During the tests, both AE and DIC measurements were performed (as outlined in Section 5.2.2). DIC measured the crack pattern from one side of the specimen in the x-z plane. We manually select 10 locations along every crack from the tip to the bottom (as exemplified in Figure 8.1a). Those locations are selected to cover the whole crack. At every location, we calculate the crack kinematics including crack width change and shear displacement. In this way, the local crack kinematics along the cracks are studied.

Unlike DIC which measured from surface, AE signals were from the whole cross section of the beam. Since the beam width (y) is small compared to its length (x) and height (z), we locate AE events in the x-z plane and obtain a 2D probability density field of AE events (pdAE field), as exemplified in Figure 8.1b. The field reflects the crack pattern in the x-z plane. At a certain height, the local peak of pdAE indicates the average centre of

the crack across the beam width. For example, at the height z = 0.82 m (marked in Figure 8.1b), the pdAE distribution has five local peaks which correspond to the centres of the five cracks CR1-CR5 (shown in Figure 8.1c).

We should note that the locations from DIC are not exactly at the local peaks of pdAE. Figure 8.1b marks the locations from DIC on the pdAE field using the black '×'. For an example at x = 2.75 m, z = 0.82 m (point a, highlighted as the red '×'), the local peak of pdAE is actually at x = 2.71 m, as shown in Figure 8.1c. A deviation of 0.04 m is found. This difference could come from the AE source localization errors or the variation of the crack patterns in the width direction since DIC measured from one surface and the pdAE measured the whole volume. We consider this variation by using the location of the nearest local peak of pdAE at a same height (z) as the correspondence to the location from DIC.

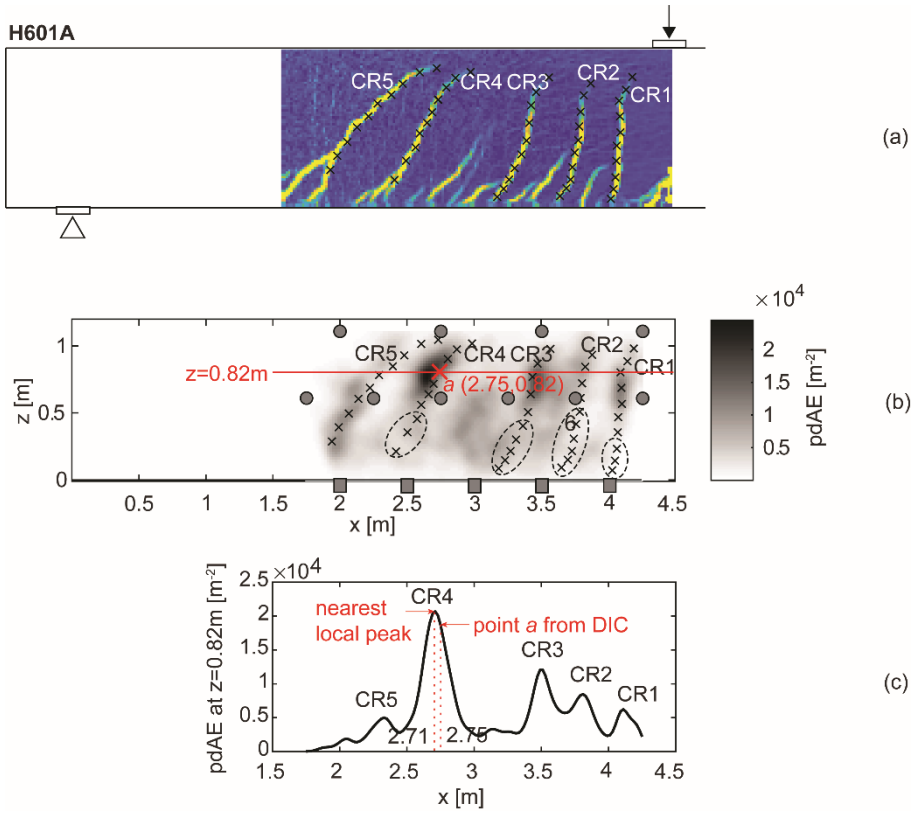

Figure 8.1 Calibration of the crack patterns detected by DIC and AE in test H601A: (a) DIC crack pattern, where 10 selected locations along each crack are marked, (b) pdAE field, with selected locations from DIC projected, and (c) pdAE distribution at z = 0.82 m, where the nearest local peak is used to find the corresponding location.

We compare the crack kinematics from DIC and the pdAE at the selected locations, but some locations are excluded which are generally in two regions. One region is around the longitudinal reinforcement where distributed secondary cracks are present. The crack spacing there is significantly smaller than the typical distance between source and receiver, leading to larger AE source localization error (as discussed in Chapter 6). Therefore, in this region, the crack pattern could not be clearly recognized by the pdAE field. The locations where pdAE could not clearly identify the crack patterns are circled in Figure 8.1b. The other region is the edge of AE measuring zone. When calculating the pdAE, an infinite space is assumed, which is not valid at the edge. Without clarifying the effect of assuming an infinite space at the edge, this dissertation excludes the points that are within 0.09 m to the edge (which takes the 95 percentile localization error from the simulation in Chapter 6).

After these adjustments, Figure 8.2 shows the locations where the pdAE and the crack kinematics from DIC are related. They are numbered from the crack tip to the bottom. The black '×' indicates the locations marked from DIC, and the white '+' shows the corresponding locations in the pdAE field.

In all the tests except for H602A, the specimens were under cyclic loading (which has been introduced in Chapter 5). During loading and unloading, cracks opened and closed respectively. Crack width and shear displacement increased during crack opening and decreased during closure. AE events were generated in both processes. We collect and analyse the AE and DIC data obtained during loading and unloading separately.

Figure 8.3 shows a schematic cyclic loading, where the path of loading and unloading are marked in red and blue respectively. During loading, the pdAE considers the cumulative AE events from the start of test (which is marked in the figure). Correspondingly, the crack kinematics in the same part of loading path is considered. When multiple unloading paths present (three paths present in the example), for each unloading path, the pdAE considers the cumulative AE events from the start of unloading in that path (marked in the figure). And accordingly the crack kinematics is calculated.

In the following sections, we will discuss the relationships between the pdAE and the crack kinematics at the selected locations along the cracks (as shown in Figure 8.2) in the loading and unloading paths.

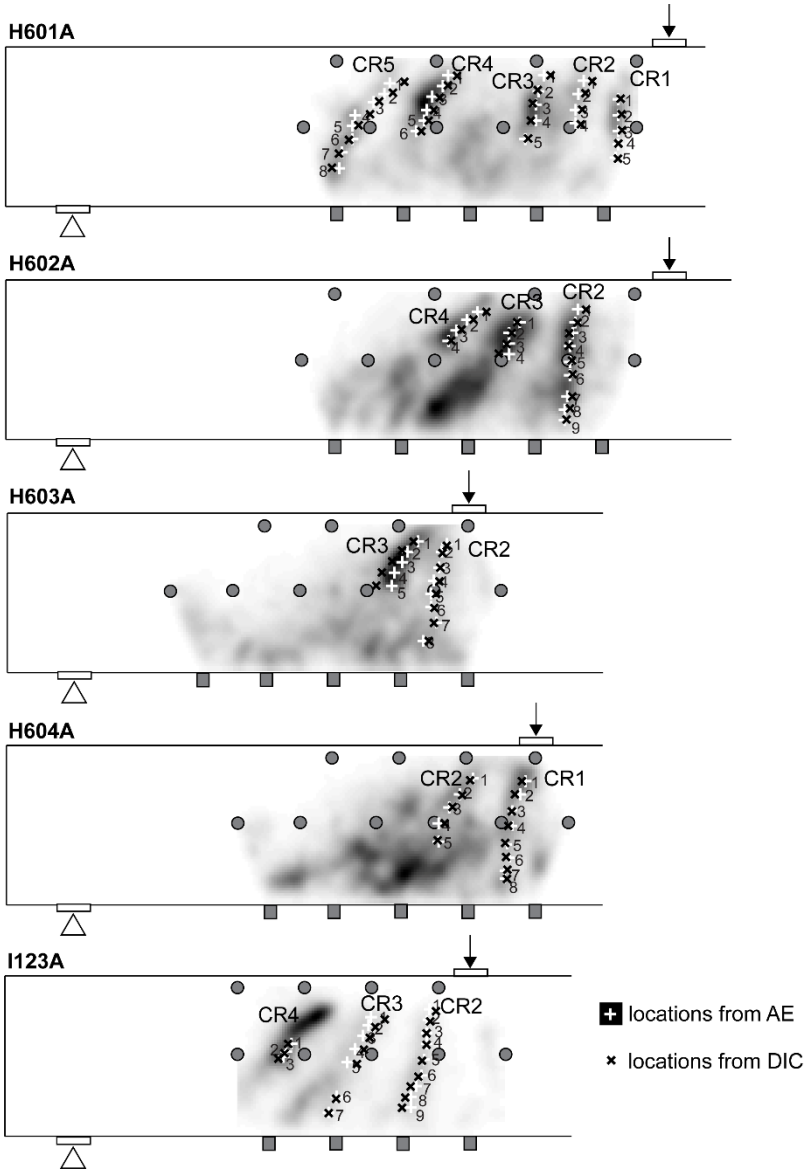

Figure 8.2 The selected locations after calibration, which are numbered from the crack tip. The 'x' marker shows the location from DIC, and the '+' marker shows the corresponding location from AE.

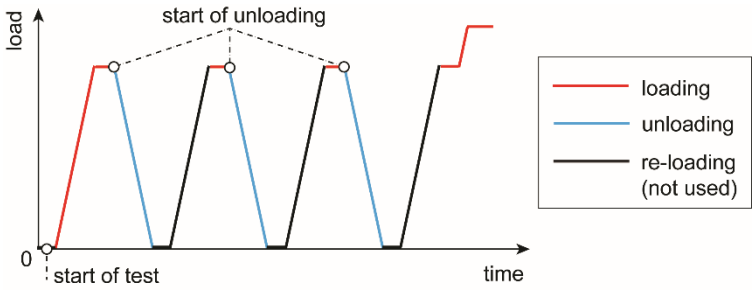

Figure 8.3 A schematic cyclic loading history with one loading path and three unloading paths, to indicate the data organization during loading and unloading.

8.3 Relationship between acoustic emission events and crack kinematics during crack opening

Using the method explained in Section 8.2, Figure 8.4 shows the relationship between the pdAE and the crack width during loading at the local positions in all the tests in Figure 8.2. A dotted line shows the change of the pdAE and the crack width at a location with increasing load. For clarity, only the value at the maximum load level is marked as a solid dot. Different lines indicate the relationships at different locations.

The obtained pdAE-crack width relationships are categorized into three groups, coloured as red, yellow and green in Figure 8.4a. With a same crack width, the pdAE is the largest in the red group, and the smallest in the green group. The three groups are divided by two curves: $p_1 = 15000 \cdot \arctan(5w)$ and $p_2 = 7500 \cdot \arctan(5w)$, where w is the crack width and p is the pdAE. For every relationship (the dotted line), the values of the pdAE and the crack width at the maximum load level (the solid dot) determines to which group the relationship belongs. Figure 8.4b exemplifies the group determination at one location. The pdAE and crack width at the maximum load are denoted as p_{max} and w_{max} respectively. The p_{max} divided by $\arctan(5w_{max})$ is 17,365 which is over 15,000, therefore, the relationship is sorted into the red group. The other relationships are categorized in the same manner.

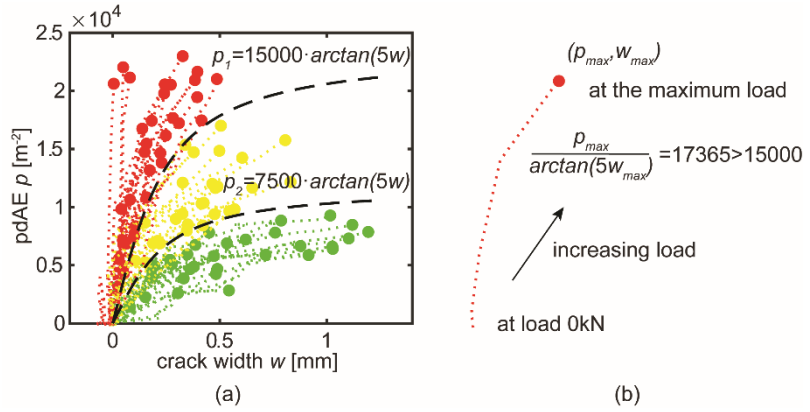

Figure 8.4 Relationships between pdAE and crack width during loading: (a) at all the selected locations in Figure 8.2 and categorized into three groups: red, yellow and green, and (b) an example showing the decision of the group.

Figure 8.5 marks the locations along the cracks where the three groups of relationships are found. The colour corresponds to the group colour. We can find that the locations with green group relationships are at cross sections with larger bending moment over shear force ratio and at the bottom part of a cross section (the tensile zone). The locations with red group relationships are closer to the compressive zone of a cross section. The locations of the yellow group are between the green and the red groups. This turns out to be a more general observation: the relationship between the pdAE and the crack width depends on the location of the measurement. Typically, with the same crack width, more AE events are expected at locations in the compressive zone than in the tensile zone.

The dependency of the pdAE-crack width relationship to the location of measurement can be explained by the crack opening history. Figure 8.6a shows the crack opening history (development of crack width and shear displacement during loading) obtained from DIC at all the locations in Figure 8.2. A dotted line shows the crack opening history at one location. For clarity, only the crack width and shear displacement at the maximum load level is marked as a solid dot. According to the group that this location belongs to, the colour of the line corresponds to the group colour. Generally, in the red group, a larger shear displacement occurs at a small crack width. While in the green group, the crack first opens wider, and slides gradually afterwards. Some locations in the red group are found having negative crack width in the beginning. These locations are mostly in the compressive zone, and were under compression before crack tip reaching the location.

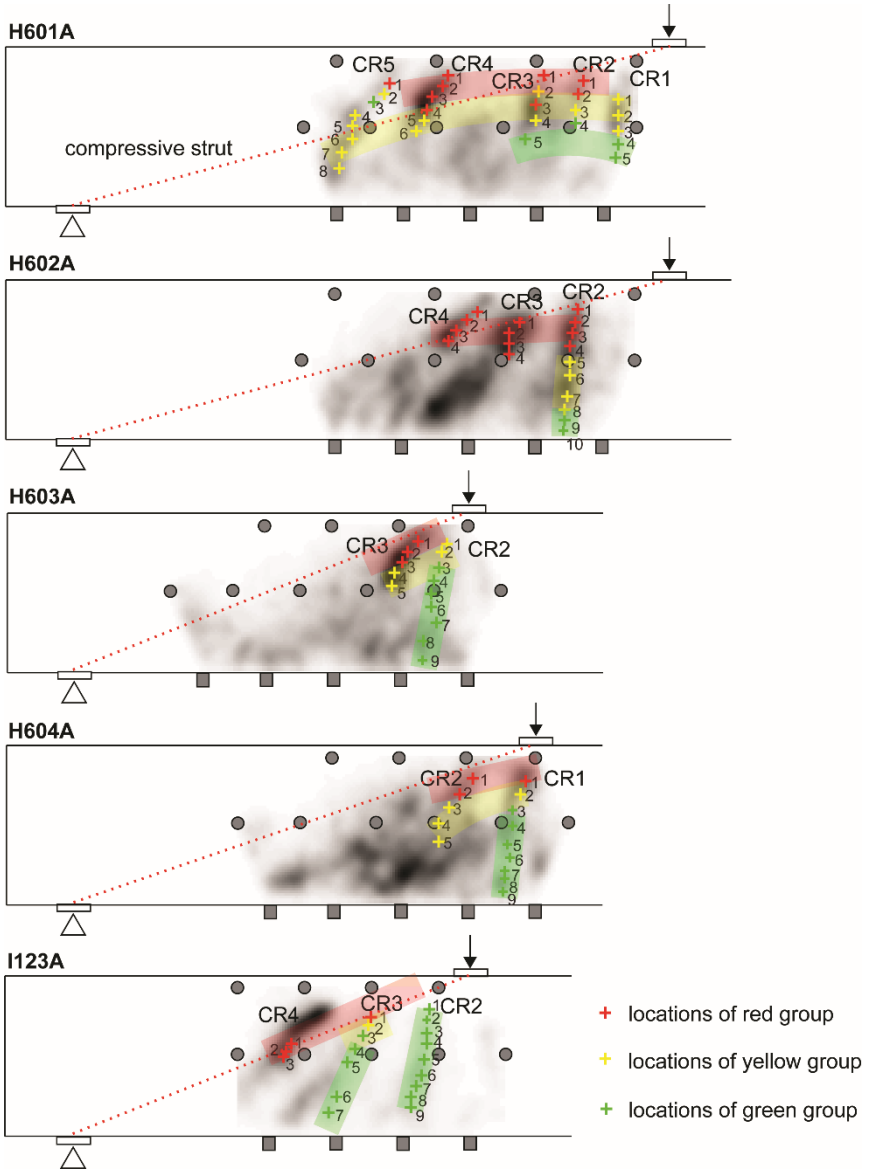

Figure 8.5 The locations of the three groups, with the compressive strut marked.

When the crack first slides at a small crack width (the condition of red group), the two crack faces are more in contact, leading to more AE events from friction. When the crack first opens wide (the condition of green group), the contact area between two crack faces is reduced. The sliding afterwards would generate less friction, thus less AE events. Figure 8.6b picks up three locations, where similar crack width and shear displacement are found at the maximum load level, but significantly different pdAE are obtained. The pdAE at the maximum load at these three locations are given in the plot. Tracing back

their crack opening history, we can find that at the location from red group, more sliding first occurs at smaller crack width. Therefore, the amount of AE events is not only related to the absolute crack width as usually stated in the literatures (Ohtsu, Uchida et al. 2002, Yang 2016), but depends on the crack opening history.

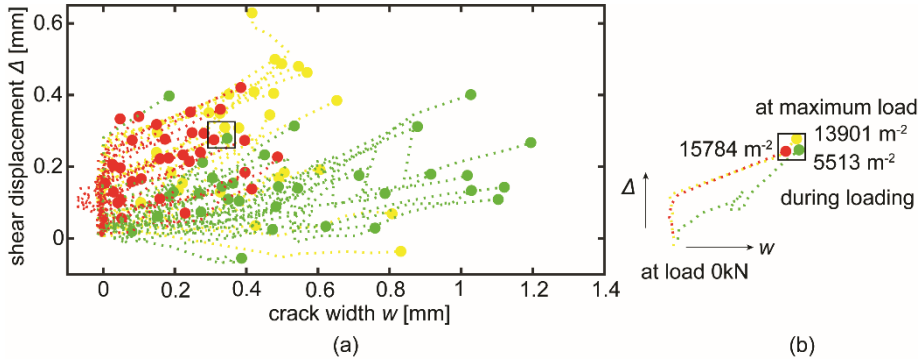

Figure 8.6 Crack opening history during loading: (a) at all the locations of the three groups and (b) at one example from each group. The colour corresponds to the group colour.

We idealize the relationships between the pdAE and the crack width in Figure 8.7. Two extreme conditions are illustrated, corresponding to the green and the red groups in Figure 8.4-Figure 8.6. Plot a shows the relationships between the pdAE and the crack width. Plot b shows the corresponding crack opening history. Plot c shows the locations where these relationships are found in a beam.

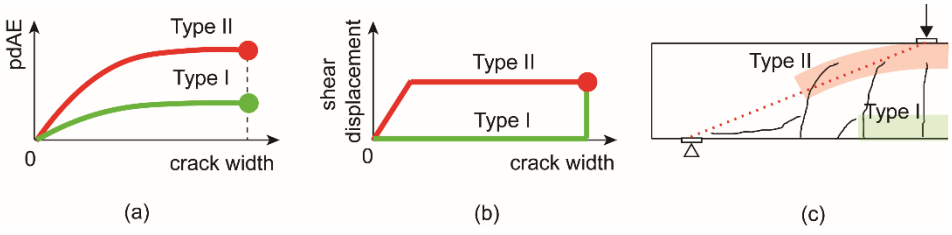

Figure 8.7 Illustration of crack opening history Type I and Type II: (a) locations, (b) crack opening history, (c) relationship between pdAE and crack width.

In Type I crack opening history, the crack firstly opens in the perpendicular direction of the crack path with limited sliding (corresponding to the green group). The pdAE increases with the crack width first and then stabilises. The stabilisation means limited increase of pdAE, which indicates that the two crack faces make little contact, generating limited AE events. This type of cracking normally occurs in the tensile zone. The other extreme condition is defined as Type II crack opening history (corresponding to the red group). The crack faces slide at small crack width, resulting in significantly increasing of pdAE in the beginning. Afterwards, the further opening would hardly increase pdAE. This type of crack opening history normally occurs in the compressive zone.

According to Chapter 7, AE events from concrete cracking can be categorized as AE from tensile cracking and friction between crack faces. We assume that the amount of AE events from tensile cracking is more related to the material property, thus independent of the crack opening history. The different pdAE-crack width relationship in Type I and Type II crack opening history is assumed mainly due to the AE events from friction, which is related to the contact area between two crack faces. As stated before, compared to Type I, Type II has shear displacement at smaller crack width, when the two crack faces are more in contact. More contact area results in more AE events from friction. Therefore, a potential mechanical model can be built to describe the pdAE – crack width relationship, based on the contact area between two crack faces during crack opening. To build such a mechanical model is outside the scope of this dissertation but suggested as a promising future research.

This section revealed the relationship between the pdAE and the crack width during crack opening. At a cracking location, the pdAE increases with the crack width and stabilizes until the two crack faces open to a certain width and do not contact. This relationship varies with different cracking locations in a beam, and eventually depends on the crack opening history. We discussed two types of crack opening history Type I and II, their commen locations in a beam and the resulting relationships between the pdAE and the crack width.

8.4 Relationship between acoustic emission events and crack kinematics during crack closure

The relationship during crack closure is studied using test I123A. In this test, we loaded the beam in cycles and at each load level, three load cycles were applied (Figure 8.8a). In the first load cycle, the beam was unloaded stepwise. During first unloading from 250 kN and 300 kN (marked out in Figure 8.8a), at every step when the load was held, DIC measurement was carried out. We use DIC to track the change of the crack width in the unloading process.

Figure 8.8b and c show the two unloading paths and the incremental increase of AE events. These AE events are from the whole measuring zone, which describe the closure of CR2 and CR3 when unloading from 250 kN and the closure of CR2-CR4 when unloading from 300 kN. The numbering of the cracks can be found in Figure 8.5. In both unloading paths, we observe limited increase of AE events in the beginning. Until the load is reduced to a certain level, AE events start to increase. With further unloading, more increase of AE events is found. This could be related to the increase of contact area between two crack faces during unloading (as illustrated in Figure 8.9). In the beginning of unloading, the crack has the maximum crack width and the two crack faces are hardly in contact, therefore, hardly any AE event is generated between the two crack faces. We call this ‘free closure stage’ without crack faces contact. With unloading, the two faces

get closer until they contact each other, when AE events start to increase. Further closure reduces the crack width and increases the contact area between two crack faces. We suppose that more contact area leads to more increase of AE events.

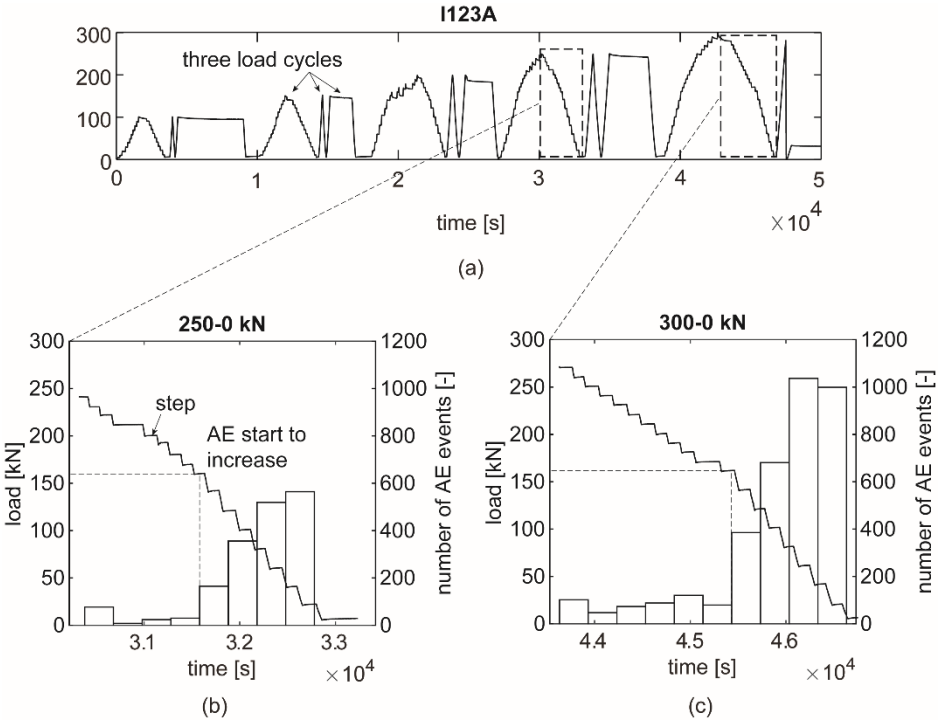

Figure 8.8 (a) The studied unloading paths in test I123A, and incremental increase of AE events during unloading paths: (b) from 250 kN and (c) from 300 kN.

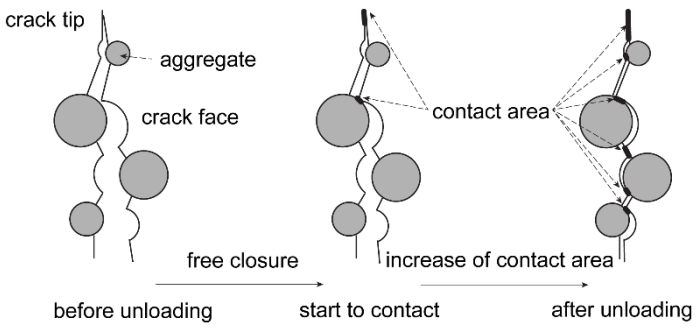

Figure 8.9 Illustration of crack closure process: before unloading, the crack is widely opened without contact between two faces; the faces start to contact at a certain crack width; the contact area increases until fully unloaded.

After discussing the evolution of AE events during unloading in the whole measuring zone, we study the relationship between the pdAE and the crack width at local points

along a crack. As described in Section 8.2, the pdAE counts for the cumulative amount of AE events locally from the start of unloading of a given load cycle. The crack width is calculated in the corresponding unloading path. Figure 8.10 shows the relationship between the pdAE and the crack width during unloading from 250 kN and 300 kN. The relationship is obtained at the selected locations along the cracks CR2 and CR3. The locations are indicated in Figure 8.2. Every line shows the relationship at one location. The location number is shown next to the line. For clarity, we only mark the pdAE and the crack width before unloading, at the start of AE events and after unloading (by the dots):

- Before unloading, the crack width is the maximum (denoted as w_m).
- During unloading, the crack closes and AE events start to occur when the crack width reduces to w_0. The start of AE is determined by setting a threshold of 105 m^{-2}, which is the pdAE value when only one AE event occurs at the location.
- After unloading, the crack width cannot reduce to zero due to many factors such as rough crack surface, leaving a residual crack width, denoted as w_r.

When the maximum crack width w_m before unloading is large (for example points 7 and 8 in Figure 8.10a), the crack first freely closes without the two faces contacting each other. At this stage, limited AE events are generated. The crack width that the two faces start to contact is related to the mismatch of the two crack faces. When the two crack faces are perfectly matched, they start to contact when fully closed (ideally at crack width 0). In most cases in concrete, the two crack faces are locally not matched due to various reasons such as local damage of concrete faces. In the case of mismatch, the two crack faces start to contact at a certain crack width, which is called mismatch width and denoted as w_{mis}.

Figure 8.11 shows a model of mismatch, where shear displacement is not considered and the variation of crack profile in the width (y) direction is neglected. The mismatch width is the distance between the peaks of the crack surface. The actual shape of crack surfaces vary but is within the mismatch width.

For the cases that the maximum crack width is larger than the mismatch width ($w_m > w_{mis}$), AE does not increase until the crack closes to the mismatch width. For the cases that the maximum crack width is within the mismatch width ($w_m \leq w_{mis}$), AE start to increase in the beginning of crack closure. Therefore, the crack width that AE events start is determined by the minimum of the maximum crack width and the mismatch width ($w_0 = \min\{w_m, w_{mis}\}$).

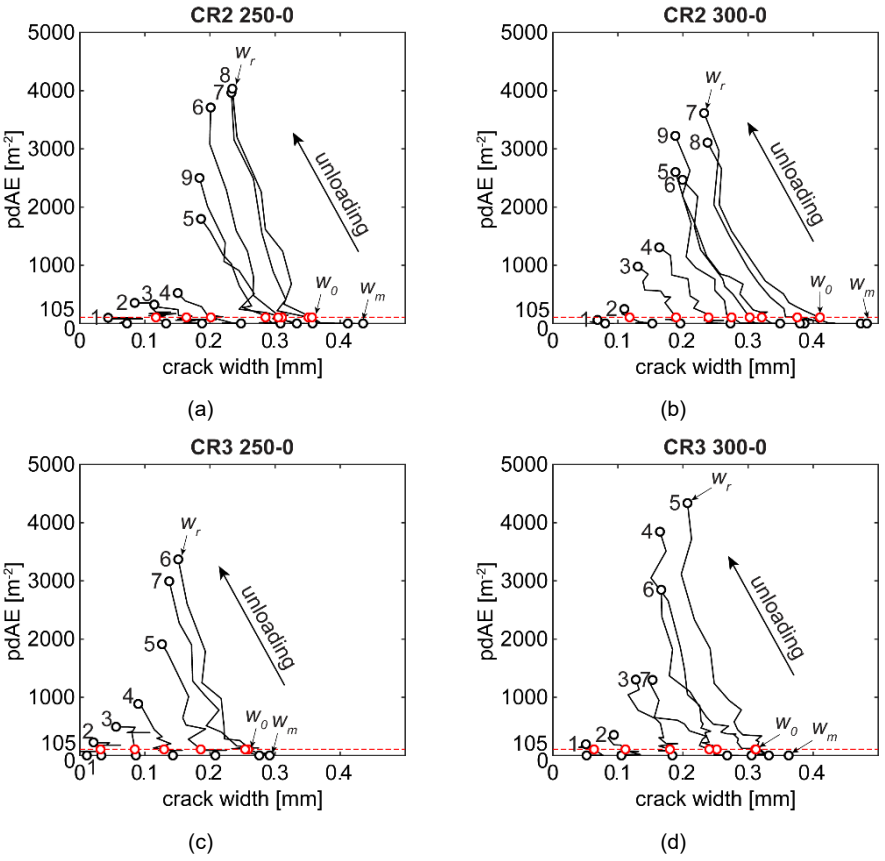

Figure 8.10 Relationship between the pdAE and the crack width during crack closure in test I123A: (a) at points along CR2 at 250-0 kN, (b) at points along CR2 at 300-0 kN, (c) at points along CR3 at 250-0 kN and (d) at points along CR3 at 300-0 kN. The point number follows that in Figure 8.2.

We can estimate the mismatch width from the experimental results (Figure 8.10a-d). The w_0 is observed mostly smaller than 0.4 mm, while w_m can be larger. Therefore, the mismatch width can be estimated as around 0.4 mm. We assume a constant mismatch width w_{mis} = 0.4 mm in our experiment.

In the model of the mismatch in Figure 8.11, by normalizing the beam width to 1, the overlap of the mismatch regions at crack width w is w_{mis}-w. Assuming the increase of pdAE is proportional to the overlap of mismatch region, we estimate the cumulative pdAE from the start of unloading as:

$$p(w) = p_0 + \int_{w_0}^{w} -\alpha\left(w_{mis} - w\right)dw = p_0 + \frac{\alpha}{2}\left[\left(w_{mis} - w\right)^2 - \left(w_{mis} - w_0\right)^2\right], w \le w_0 \quad (8.1)$$

where w_{mis} is the mismatch width of the crack face, w_{mis}-w is the overlap width of the mismatch region at crack width w, α is a constant describing the proportional relationship between the increase of pdAE and the overlap, w_0 is the crack width at the onset of pdAE, p_0 is the threshold on determining onset of pdAE. This formula does not include the free closure stage $w > w_0$, when the pdAE is limited.

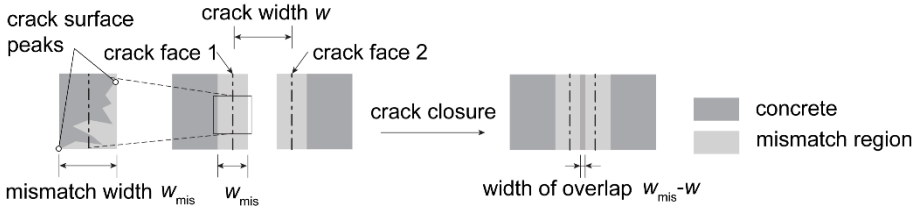

Figure 8.11 Illustration of crack face mismatch.

The pdAE-crack width relationships in Figure 8.10 were found along CR2 and CR3 in test I123A, which are flexural cracks with limited shear displacement. Therefore, we neglect the influence of shear displacement, and fit the relationships found along CR2 and CR3 into Equation (8.1). Figure 8.12a exemplifies the curve fitting at points 5 and 8 along CR2 (unloading from 250 kN). The black line shows the measured relationship and the red solid line shows the fitted curve for $w \leq w_0$. A larger α is found at point 8 than at point 5. Figure 8.12b shows the parameter α for all the relationships. We find that α increases with w_0. The relationship between α and w_0 appears independent to the crack profile (CR2 or CR3) or the maximum load (250 kN or 300 kN).

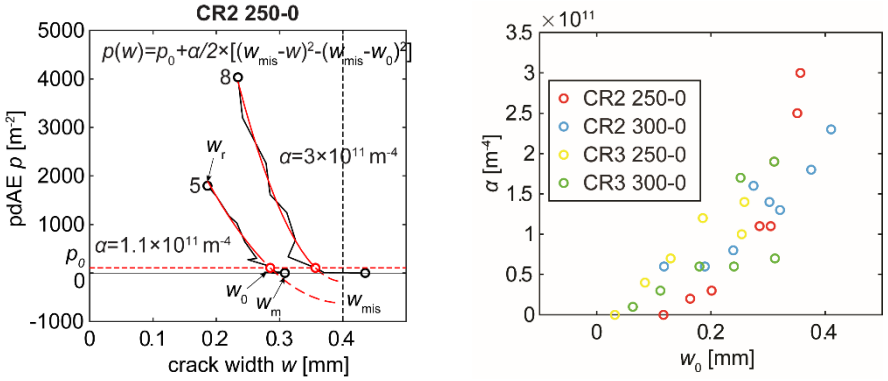

Figure 8.12 Curve fitting to find the parameter α: (a) at points 5 and 8 along CR1 (250-0 kN) as examples, (b) the fitted parameter α at all points (unloading from 250 kN and 300 kN), related to w_0.

The relationship between α and w_0 cannot be explained by the model in Figure 8.11. One of the reasons is that shear displacement is not considered in the model but exists in actual

cracking even for flexural cracking. Shear displacement would influence the contact between two crack faces in the mismatch zone. As a phenomenological observation, we propose that the parameter α is proportionally related to w_0.

Figure 8.13 idealizes the relationship between the pdAE and the crack width during crack closure of a flexural crack (with limited shear displacement). The model of crack face mismatch is used (illustrated in Figure 8.11), where a constant crack face mismatch w_{mis} is assumed and no shear displacement is considered. When the maximum crack width is larger than the mismatch width, a free closure stage presents (at location *i*). AE events start after the crack width reduces to the mismatch width. When the maximum crack width is within the mismatch width, AE events start in the beginning of unloading (at location *j*).

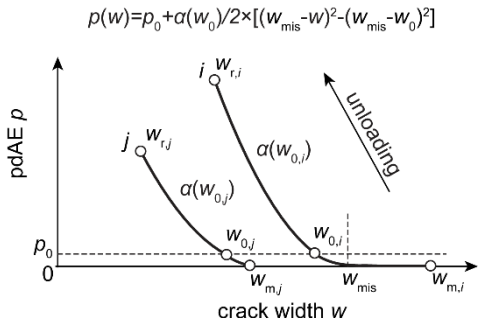

Figure 8.13 Illustration of the relationship between the pdAE and the crack width during crack closure of a flexural crack.

The proposed solution of the pdAE-crack width relationship suits for the condition without shear displacement. For the cases with shear displacement, a model based on the contact area is more relevant. With more contact area during crack closure, more AE events will be generated. Therefore, this mechanical model could be unified with the model for crack opening process, which is also based on the contact area between the two crack faces (according to Section 8.3).

This section revealed the relationship between the AE events and the crack width during the closure of flexural cracks. AE events start to occur when the crack closes to a certain width that the two faces are in contact. This certain crack width is related to the mismatch of the two crack faces. When the crack width further reduces, the overlap of the mismatch region increases, leading to more increase of AE events (pdAE). We proposed a model of mismatch to describe the relationship between the pdAE and the crack width during the closure of flexural cracks.

8.5 Influence of number of load cycles and loading speed on the relationships

The relationships between the pdAE and the crack kinematics were found using the measurement results during the first load cycle in the loading protocol. This means that the detected cracks were newly opened. However, the cracks in a real structure, especially those structures that have to carry traffic load may have been opened and closed for many times during the structural service life. The continuous friction between the crack faces will smoothen the surface, leading to less AE events with increasing load cycles. The value of pdAE will reduce and the obtained relationships based on the measurement of first load cycles may not be applicable.

This section studies the influence of the number of load cycles and loading speed on the relationship between the pdAE and the crack kinematics. Test H603A is used in which 75 repeated load cycles (numbered by L1-75) were applied and afterwards 5 more load cycles (L76-80) were applied with increasing loading speed. The loading speed increases from 0.02 mm/s in L76 to 0.64 mm/s in L80. The loading history can be found in Chapter 5. In L1 and L76-80, we measured the crack width and shear displacement with DIC when the specimen was fully loaded and unloaded in the cycle. Figure 8.14 shows the relevant load cycles and DIC measurements in the test.

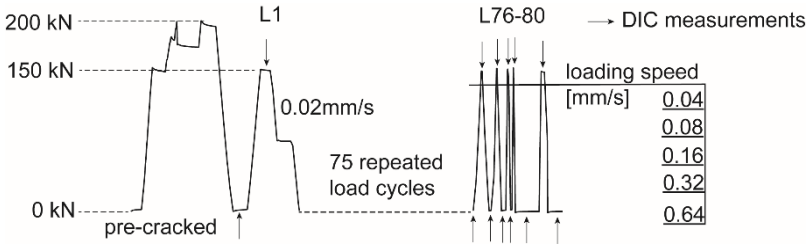

Figure 8.14 The relevant load cycles and DIC measurements in test H603A.

Before applying the repeated load cycles, the beam had been loaded up to 200 kN and two cracks CR1 and CR2 had been formed. The location of the cracks can be found in Figure 5.9. CR2 is within the measuring zone, therefore, we study the influence of the number of load cycles and loading speed on opening and closure of CR2.

Figure 8.15 shows the crack kinematics (including the crack width and the shear displacement) at the selected locations along CR2 during loading of L1 and L76-80. The selected locations can be found in Figure 8.2 (points 1-8 along CR2 in test H603A). After 75 load cycles, the crack kinematics were almost the same as those in L1, with a difference less than 0.02 mm. And the crack kinematics in L76-80 (with different loading speed) were also comparable. Therefore, we can neglect the influence of the number of load cycles and loading speed on the crack kinematics.

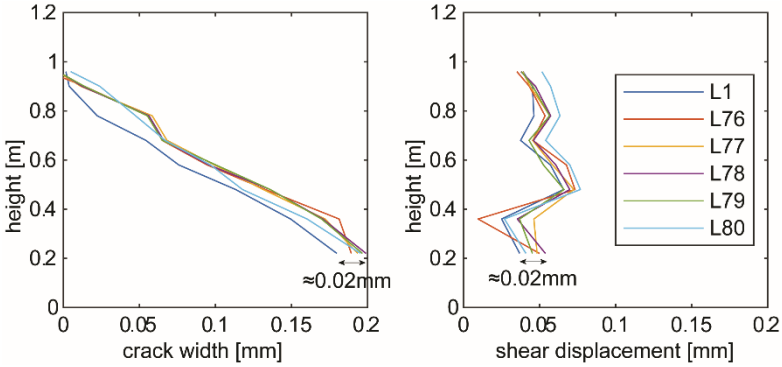

Figure 8.15 Influence of the number of load cycles and the loading speed on the crack width and the shear displacement during loading.

Figure 8.16 shows the summation of the pdAE at the selected locations along CR2 during loading and unloading of L1-80. A significant drop of the pdAE was found in the load cycle L2. This load cycle is actually the third time that CR2 was opened and closed, considering the previous load cycle of 200 kN before L1 when the crack newly formed. So in the first three cycles since the crack forms, the pdAE significantly reduces in both loading and unloading process.

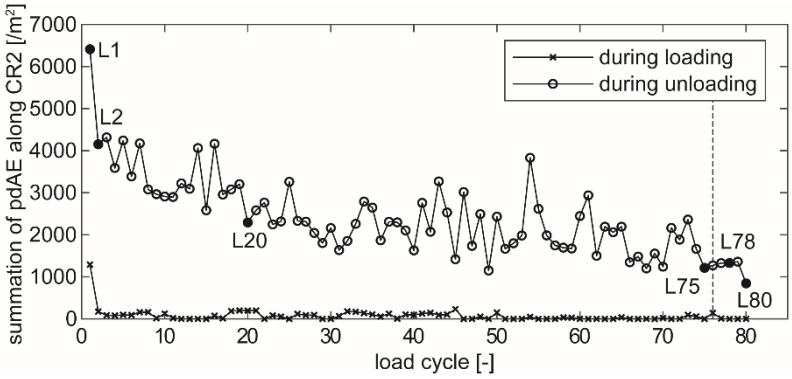

Figure 8.16 Influence of number of load cycle and loading speed on the pdAE from loading and unloading.

After L2, the pdAE during loading reduced to almost zero, indicating limited AE events in the reopening. The pdAE during unloading gradually reduced and stabilized after around L20. The remaining pdAE during unloading could come from the contact of the two crack faces after closure. Here one can also assume a linear relationship between the pdAE and the load cycles after L2. To confirm a relationship, more load cycles than 80 are needed.

After L75, the influence of number of load cycles on the pdAE during unloading was insignificant. Therefore, the pdAE at L76-80 could reflect the influence of loading speed.

Within the tested range, the loading speed had limited influence on value of pdAE during unloading.

Figure 8.17 shows the pdAE field during unloading of L1, L2, L20, L75, L78 and L80. Despite that the pdAE during unloading reduces with number of load cycles, the crack pattern can still be recognized. This observation suggests that one can use AE events from crack closure to find the location of existing cracks. In this case, only applying a relatively-low load onto a structure is sufficient to reopen the existing cracks. The benefit is that applying a low load level would not further damage the structure.

Regarding the magnitude of the low load level to reopen the existing cracks, in the experiment, we applied load level of 150 kN, which is smaller than the needed load to first open CR2. For a real bridge, it worth testing if the normal traffic load is sufficient.

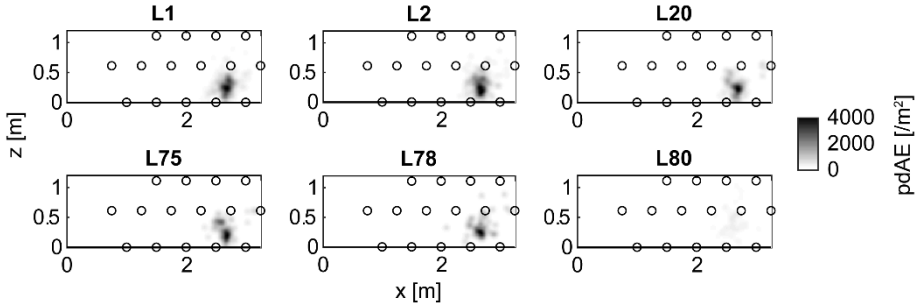

Figure 8.17 The pdAE field during unloading of L1, 2, 20, 75, 78 and 80.

For the future research, it would be interesting to study the influence of number of load cycles and loading speed not only on the pdAE but also on the signal features. A presumption is that with more load cycles, the crack surfaces would be more smoothened, leading to less AE events from friction. AE events from friction have lower peak frequency according to Chapter 7. Therefore, possibly with increasing number of load cycles, the number of AE events from friction reduces, resulting in higher peak frequency in the acquired signals. This presumption has not been checked in this dissertation due to the resource and time limit.

This section evaluated the influence of the number of load cycles and loading speed on the pdAE and the crack kinematics during crack opening and closure. More load cycles in the history reduce the pdAE from both crack reopening and closure. Therefore, we are unable to quantify the crack width of a structure that may have been loaded and unloaded for many times in the absolute sense. Nevertheless, the pattern of the existing cracks can still be recognized by locating AE events during reloading and unloading of a structure. And we have found limited influence of the loading speed on the pdAE and the crack kinematics within the tested range.

8.6 Conclusion

This chapter revealed the relationship between AE events and crack kinematics during crack opening and closure based on the experiments. We also explained the physical background of the experimental results. During crack opening, the pdAE increases with the crack width and stabilizes until the two crack faces open to a certain width and do not contact. This relationship depends on the crack opening history. When the crack first opens widely then slides (defined as crack opening history Type I), less amount of AE events are generated due to less contact between crack faces at the shear displacement. This type often occurs in the tensile zone of a beam. When the crack starts shear displacement at a small crack width (defined as crack opening history Type II), due to more contact between crack faces, more AE events are generated. This type is often found in the compressive zone of a beam.

Regarding the relationship between AE events and crack kinematics during crack closure, we only studied the closure of flexural cracks where shear displacement was limited. We found that AE events do not occur until the crack width reduces to a certain value that the two crack faces contact. This value is related to the mismatch of the two crack faces. Afterwards, further reduction of crack width leads to more contact, generating more increase of AE events.

We found that the amount of AE events during opening or closure is highly related to the contact area between the two crack faces. Therefore, a possible mechanical model could be built to describe the relationships, based on the contact area during crack opening or closure. To build such a model is outside the scope of this dissertation but suggested it as topic for future research.

We also found that the pdAE-crack kinematics relationships during crack opening and closure are also influenced by the number of load cycles in the history. More load cycles reduce the pdAE from both crack reopening and closure. Therefore, we are unable to quantify the crack kinematics using pdAE of a structure that may have been loaded and unloaded for many times in the absolute sense. Nevertheless, the pattern of the existing cracks can still be recognized by locating AE events during reloading and unloading of a structure. This suggests a method of using a relatively-low load level to reopen and close the existing cracks. By locating the AE events from crack closure, we can find the location of existing cracks.

The results of this chapter provide a better understanding of the acquired AE events from concrete crack opening and closure. Compared to the literatures, we are able to quantify and explain the relationships with a clear physical background. The insights from this chapter also contribute to the development of AE-based indicators of failure of concrete structures in Chapter 9.

Chapter 9 Acoustic emission-based indicators of shear failure of concrete structures without shear reinforcement

9.1 Introduction

In Chapter 2, we reviewed the shear failure mechanisms and the available theoretical models in literatures. The shear capacity is found related to the integrity of compressive strut. If the compressive strut is not damaged by the flexural shear crack, the structure has a significantly higher bearing capacity and fails due to the crushing of the compressive strut (which is called shear compression failure). If the compressive strut is damaged by the flexural shear crack, the structure fails with a much lower capacity (which is called flexural shear failure). Therefore, we suggest using the integrity of compressive strut to indicate the shear failure.

This chapter first evaluates the integrity of compressive strut using the probability density of AE events (pdAE) (Section 9.2). The pdAE is calculated using the method in Chapter 6. Then, based on the evaluation of the compressive strut integrity, we develop a traffic light system which indicates shear failure at different levels (Section 9.3). We also explain the physical meaning of the indicators, with the help of the insights from Chapter 7 and 8. The traffic light system is validated using the shear tests of reinforced concrete beams. And the robustness of the system is studied. Then we extend the system from reinforced concrete beams to slabs (Section 9.4). The extension is validated using the shear tests of reinforced concrete slabs.

9.2 Evaluation of the integrity of compressive strut using acoustic emission

9.2.1 Determination of the compressive strut region

To evaluate the integrity of compressive strut, this section first determines the region of strut according to the strut and tie model. For beams under concentrated load, a strut forms between load and support. The shape of the strut could be like a bottle (Figure 9.1a) that the force is applied over a small area and the resulting stresses disperse as they flow through the member (Schlaich 1991). In design, the strut is usually idealized as a prismatic strut (Figure 9.1b). The width of a prismatic compressive strut is determined by the loading plate dimension and the effective concrete tension height. According to Eurocode (CEN 2004), the effective concrete tension height for specimen under bending is:

$$h_{\mathrm{c,eff}} = \min\left\{\left(h - x_{\mathrm{c}}\right)/3, 2.5\left(h - d_{\mathrm{e}}\right)\right\} \tag{9.1}$$

where h is the height of cross section, x_{c} is the compressive zone height $x_{\mathrm{c}} = d_{\mathrm{e}} - s_{cr}$ where s_{cr} is the crack height that the flexural crack stablizes (calculated by Equation 2.1) and d_{e}. is the effective height of cross section.

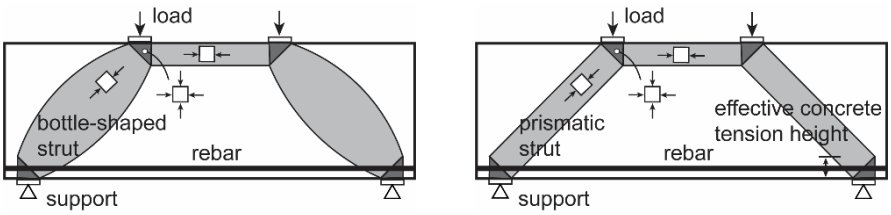

Figure 9.1 Estimated compressive strut in beams under concentrated loads: (a) bottle-shaped and (b) prismatic strut, reproduced from (Muttoni, Schwartz et al. 1996)

One shall note that the real compressive force transfer path at the failure of a structure is not necessarily the same as predefined by the strut. When the estimated strut is damaged, there is a possibility that the compressive force can be carried by the surrounding concrete. This also reflects that the strut and tie model is based on a lower-bound approximation of the actual load bearing mechanism (Nielsen and Hoang 2016). Damage of compressive strut does not always lead to structural failure. Therefore, deviation of the predefined region of compressive strut is acceptable.

9.2.2 Acoustic emission events in compressive strut during loading

We evaluate the integrity of compressive strut using the maximum pdAE in the region of the strut. The pdAE field is calculated as outlined in Chapter 6. At every load level, the pdAE considers the cumulative AE events from the start of the test (0 kN, uncracked) and excludes those during unloading if the beam is loaded in cycles. According to Chapter 8, the pdAE in the compressive zone increases with the crack width following the relationship of the crack opening Type II (Figure 8.7a). Therefore, the maximum pdAE in the region of compressive strut corresponds to the maximum crack width in that region. We can use the maximum pdAE to evaluate the damage level of compressive strut.

Figure 9.2 exemplifies the evaluation in test I123A. Plot (a) shows the determined region of strut according to Section 9.2.1, which is a prismatic strut from the load to the support. Only the part covered by AE sensors is studied. The crack pattern at failure is also marked there. Plot (b) shows the maximum pdAE in the strut region with increasing load. The AE events during unloading are excluded. To compare with the development of the crack pattern, plot (c) shows the evolution of the pdAE field with the increase of load levels:

- At 180 kN, the first flexural crack in the detection zone formed (CR2). CR2 did not reach the compressive strut, thus generating limited pdAE in the strut.
- At 230 kN, CR3 formed, whose tip was close to the compressive strut. We found a slight increase of the maximum pdAE in the strut.
- At 250 kN and 260 kN, CR3 further propagated into the compressive strut, resulting in a larger maximum pdAE in the strut.

- At 290 kN, the inclined part of CR4 developed, which heavily damaged the compressive strut. A significant increase of the maximum pdAE in the strut was found at the inclined part of CR4. CR4 was the critical flexural shear crack that led to the flexural shear failure (at 300 kN).

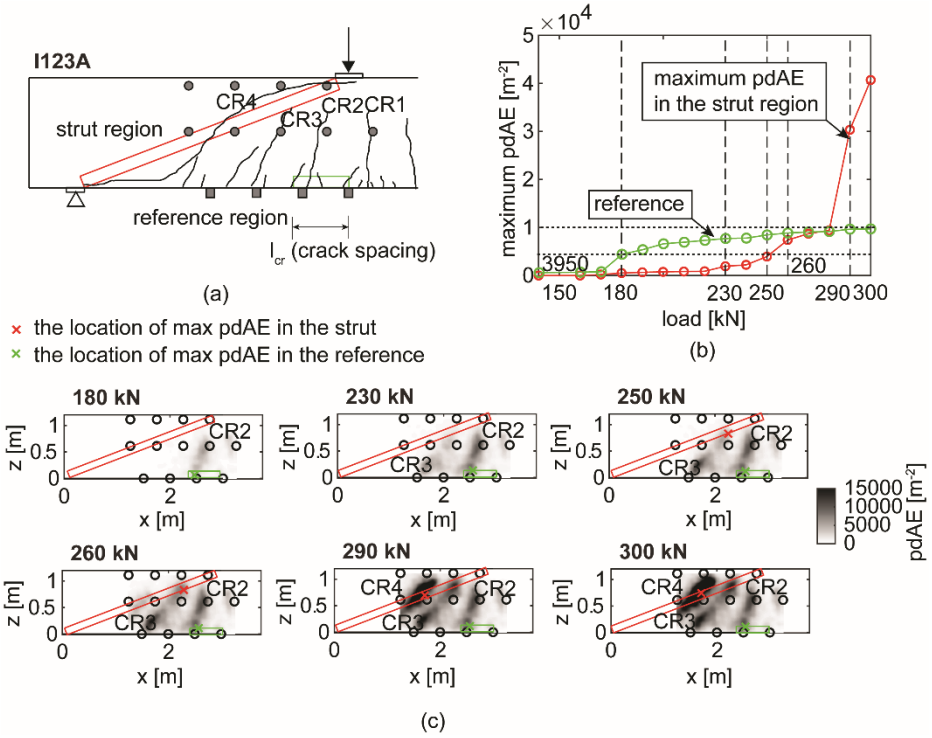

Figure 9.2 Evaluation of compressive strut integrity using the maximum pdAE in I123A: (a) region of compressive strut and the reference region, (b) maximum pdAE in the strut region and the reference with increasing load, (c) pdAE field at the selected load levels, with the locations of the maximum pdAE in the strut and reference marked.

This experimental observation confirms that the maximum pdAE in the strut region can reflect the cracking condition in the compressive strut and is related to the shear failure of the structure.

9.2.3 Acoustic emission damage indication of compressive strut

The maximum pdAE is found promising to indicate the integrity of the compressive strut. However, the value of the maximum pdAE depends on the material property, structural type and AE setup, thus may differ among tests. To improve the applicability to different tests, we evaluate the maximum pdAE in the strut using an AE reference.

We select the AE reference as the maximum pdAE in the tension chord of the same structure (shown in Figure 9.2a). The region has a height of the effective concrete tension

chord and a length of one times the estimated flexural crack spacing (Equation 2.2). We use the crack spacing to ensure at least one flexural crack can be covered by the region. Since the region is in tension, the pdAE there increases with the crack width following the relationship of the crack opening Type I according to Chapter 8 (Figure 8.7a). Therefore, the maximum pdAE in the reference region corresponds to the maximum crack width of a flexural crack in that region.

The reasons of selecting this reference are

- For reinforced concrete members without shear reinforcement under regular loading conditions, the tensile chord with the maximum bending moment will always crack first. The reference region is usually cracked before compressive strut.
- Taking the reference from the same structure avoids the influence from the uncertainties of the structural type, material property, AE setup and environmental noise.
- The reference is taken near the surface of the structure, where the crack pattern can be easily calibrated by observations or other displacement measurements.
- The pdAE in the reference region mainly come from the flexural cracking. Other mechanisms, like bond slip or yielding of reinforcement, are found limitedly influencing the obtained pdAE for structures with limited reinforcement compared to the large bulk of concrete.

The limited influence of other mechanisms to the AE reference can be proven by the experimental results in Chapter 8:Figure 8.4. The green group includes the pdAE-crack width relationships at locations in tension that can be near or far from the reinforcement. But, we do not observe significantly different pdAE. This could indicate that the influence of other mechanisms like bond slip or steel yielding can be neglected, comparing to the large amount of pdAE from flexural cracking.

Figure 9.2b exemplifies the performance of AE reference with increasing load in test I123A. We observe the start of the reference (with pdAE of 3950 m^{-3}) at 180 kN. This was the load level when CR2 first opened. Afterwards, the reference increased and stabilized at around 10,000 m^{-3}. This met our expectation that further crack opening generated limited AE events, because the crack faces hardly contacted.

By comparing the maximum pdAE in the strut to the AE reference, we evaluate the integrity of the compressive strut. We use test I123A as an example (Figure 9.2b).

- When the maximum pdAE in the strut first exceeds a certain value, the strut region starts to crack. This value is taken as the maximum pdAE at the start of AE reference, which describes the formation of a flexural crack. We call this

value 'the threshold of crack initiation'. In the presented test, the threshold value was 3950 m^{-3} (Figure 9.2b). The maximum pdAE in the strut exceeded this threshold at 260 kN, which indicates the first cracking in the strut. Though the strut was firstly cracked at 250 kN according to the crack development in Figure 9.2c, a variation of 10 kN was acceptable compared to the load magnitude.

- When the maximum pdAE in the strut exceeds that in the reference region at a same load level, the strut is more heavily damaged by the flexural shear cracking. More shear displacement is generated, leading to more AE events from friction. In the presented test, the maximum pdAE in the strut exceeds that in the reference at 290 kN when the critical flexural shear cracking CR4 forms (Figure 9.2c). We compare the percentage of AE events from friction obtained in the strut at critical flexural shear cracking to that in the reference at flexural cracking (Figure 9.3). At the critical flexural shear cracking, the percentage of AE from friction was significantly larger. This indicates more shear displacement in the strut near failure.

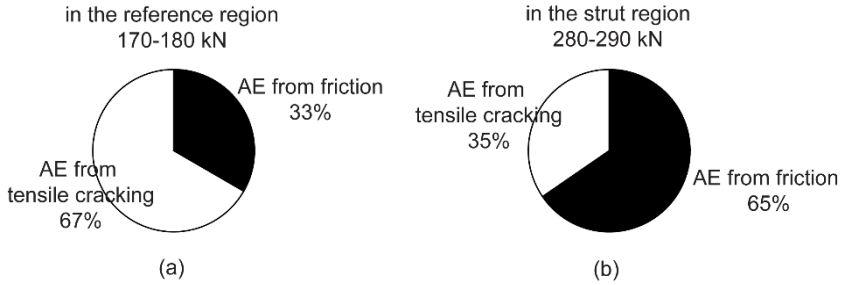

Figure 9.3 Percentage of AE events from friction in test I123A: (a) at the flexural cracking in the reference region at 170-180 kN and (b) at the critical flexural shear cracking in the strut at 280-290 kN.

It should be noted that when comparing the pdAE in the strut to that in the reference, one should not compare the crack width. Though the maximum pdAE in each region corresponds to the maximum crack width, the pdAE-crack width relationships are different in the two regions, following Type I in the reference region and Type II in the strut, according to Chapter 8:Figure 8.7. The pdAE increases more in Type II at a same crack width. This means that when obtaining a same pdAE, the strut region usually has a smaller crack width than the reference region.

For concrete structures with unreinforced compressive strut, e.g. beams without shear reinforcement in our tests, the main bearing mechnism is strongly related to the capacity of the compressive strut. But because the strut is not reinforced, it suffers from brittle failure. AE is sensitive to concrete cracking, thus promising to indicate brittle failure before the failure occurs.

This section proposed a method to indicate the brittle failure of the strut using the pdAE. The maximum pdAE in the strut was used, which corresponded to the maximum crack width in the same region. An AE reference was taken from the same structure in the tension chord. By comparing the maximum pdAE in the strut to the reference, we evaluated the integrity of compressive strut.

9.3 Development of a traffic light system for shear failure based on compressive strut integrity

Based on the evaluation of the integrity of the compressive strut, this section proposes a traffic light system for reinforced concrete members that may have brittle failure relating to the failure of the unreinforced strut. Then we validate the proposed traffic light system in the six shear tests of reinforced concrete beams. And the robustness of the system is studied.

9.3.1 A traffic light system for shear failure indication

From the evaluation of compressive strut integrity, we can identify three levels of structural conditions. A concept of 'traffic light system' is implemented to describe the three levels (Figure 9.4).

- Green-light criterion: the start of AE reference. This criterion indicates the formation of flexural cracks in the reference region. The start of AE reference is determined when a significant increase of AE reference is observed in a load step, comparing to the previous slight increase due to microcracking (Figure 9.4b). The value of AE reference at this criterion can be used as a threshold of crack initiation in the strut.
- Yellow-light criterion: the maximum pdAE in the strut region exceeding the threshold of crack initiation obtained from the green-light criterion. This criterion indicates the first cracking in the compressive strut.
- Red-light criterion: the maximum pdAE in the strut region exceeding that in the reference region at a same load level. This criterion is usually observed at the critical flexural shear cracking in the strut, where large shear displacement occurs at relatively small crack width, leading to more AE events from friction. The red-light criterion, which indicates the inclined critical cracking in the strut, is close to shear failure of the structure.

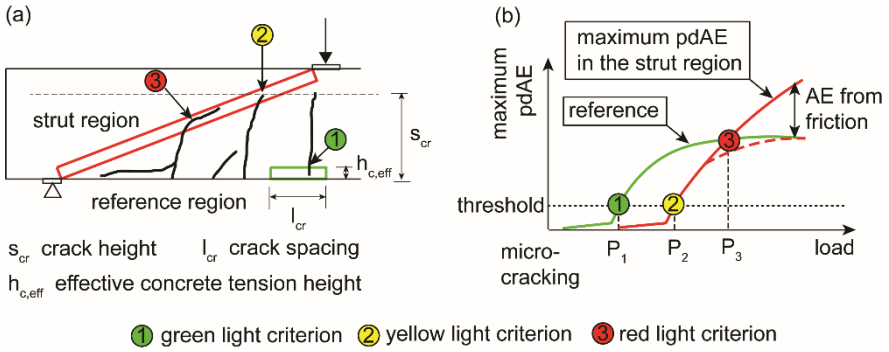

Figure 9.4 The traffic light system for shear failure indication: (a) cracking behaviour at the criteria and (b) determination of the criteria by comparing the maximum pdAE in the strut and the reference region.

In the traffic light system, we compare the maximum pdAE in the strut to that in the reference region. The comparison evaluates the integrity of the compressive strut, which is related to the structural shear failure. But it should be noted that, in the evaluation, the crack width cannot be compared in the strut and the reference region (which is also mentioned in Section 9.2.3). According to Chapter 8, due to different crack opening histories, the pdAE-crack width relationship follows Type I in the reference region and Type II in the compressive strut. When obtaining same amount of pdAE in the two regions, the crack width in the strut is usually smaller than that in the reference region.

9.3.2 Validation with shear tests of reinforced concrete beams

Figure 9.5 shows the traffic light criteria in the six shear tests of reinforced concrete beams. The plots on the right-hand side show the determination of the three criteria per test. The plots on the left-hand side show the corresponding cracking behaviour in the strut and reference region. The cracking behaviour at the criteria generally meets our descriptions in Section 9.3.1. For tests failed in shear compression (H603A, H604A and H853A), the critical flexural shear crack reaches the strut but does not propagate across it, thus the remaining strut provides additional shear capacity (which are greyed out in the figure).

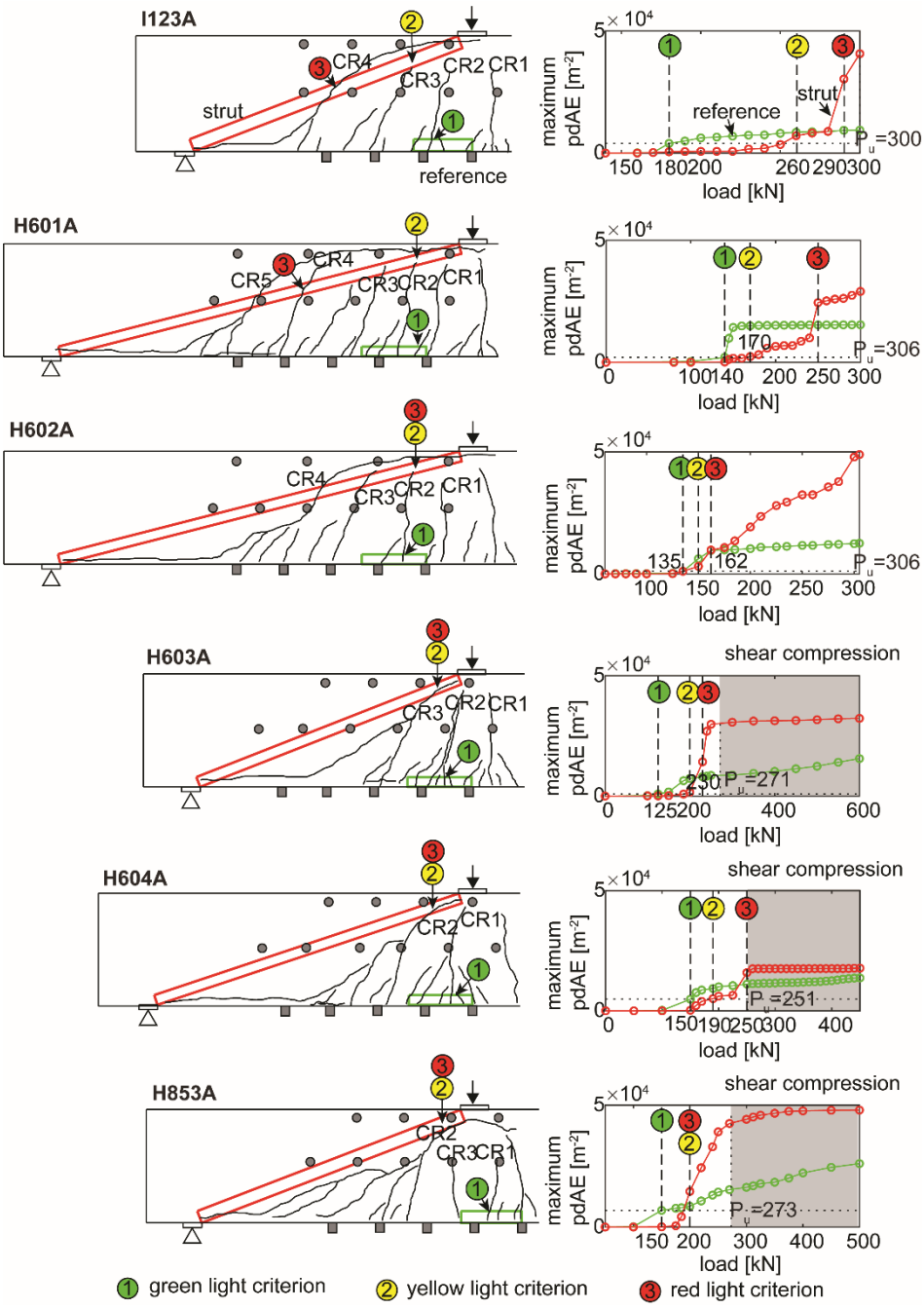

Figure 9.5 The traffic-light criteria in the beam tests, with the plots on the right the determination of the criteria, and the plots on the left the corresponding cracking behaviour.

Table 9.1 lists the load ratio which is the load level at reaching a criterion divided by the load level at critical flexural shear cracking (which is defined as the ultimate shear capacity of a structural member P_u). The P_u can be found in Table 5.3. In some tests, the beam failed in shear compression, resulting the maximum load level (P_m) larger than P_u. We consider the ultimate shear capacity P_u critical, since it is not always known beforehand whether the compressive strut can carry additional force after critical flexural shear cracking. Moreover, for moving traffic load on a bridge, it is hard to ensure a complete compressive strut at any loading position. P_1, P_2 and P_3 are the load level where green-light, yellow-light and red-light criteria are fulfilled respectively. The ratio between shear span a_s (distance between the centre of load and support) and effective height of cross section d_e is also listed.

Table 9.1 Load ratio at the three criteria in the beam tests

Beam test	a_s/d_e [-]	P_1/P_u (green-light)	P_2/P_u (yellow-light)	P_3/P_u (red-light)
I123A	2,61	0,6	0,87	0,93
H601A	3,89	0,46	0,56	0,82
H602A	3,89	0,44	0,49	0,53
H603A	2,59	0,46	0,74	0,85
H604A	3,02	0,6	0,76	0,99
H853A	2,61	0,55	0,73	0,73

The green-light criterion indicates a safe condition, with the load ratio less than 60%. This is reasonable as only flexural cracks form at this stage. The yellow-light criterion is fulfilled at load ratio in range of 49%-87%. Within the presented tests, the load ratio at yellow-light follows a certain relationship with the shear span to depth ratio (Figure 9.6). With a larger shear span to depth ratio, the load ratio at yellow-light reduces. The red-light criterion indicates a very dangerous situation for flexural shear failure, with load level reaching around 99% of the ultimate shear capacity.

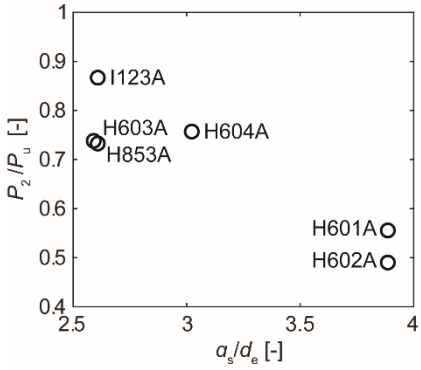

Figure 9.6 Relationship between load ratio at the yellow-light criterion and shear span to depth ratio.

9.3.3 Robustness of the traffic light system

In the traffic light system, an important parameter is the maximum pdAE. Based on the maximum pdAE in the strut and the reference region, we determine the criteria for shear failure. However, the value of the maximum pdAE can be influenced by uncertainties in concrete structures like the local crack profile variation.

The local crack profiles are in various angles to the crack opening direction. In the traffic light system, the pdAE in the reference region evaluates the formation of a flexural crack, which opens perpendicular to the crack direction (Figure 9.7). Therefore, we use the pdAE-crack width relationship of Type I according to Chapter 8. But irrespective to the global crack direction, locally, the crack profile direction may not be perpendicular to the opening direction (Figure 9.7). In this case, we may have larger local shear displacement at a small crack width, which generates more AE events from friction, giving larger pdAE. The same condition can happen to the pdAE in the strut.

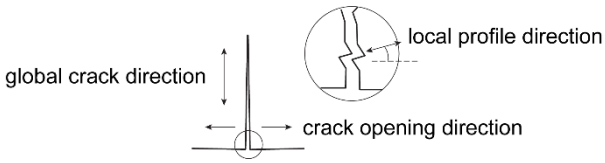

Figure 9.7 Illustrated directions of crack opening, global crack pattern and local crack profile.

We evaluate the influence of variation of local crack profile using the studied tests. In Chapter 8:Figure 8.4, the pdAE-crack width relationships were sorted into green, yellow and red groups. The green group corresponded to crack opening Type I that mostly occurred in the tensile zone, and the red group corresponded to Type II that occured in the compressive zone. In each group, the pdAE-crack width relationships were found at various locations in the relative zone. At those locations, the angles of local crack profile differed. Therefore, we estimate the influence of angle variation from the scattering of the pdAE in each group. The scatterings in green and red groups reflect the influence on the pdAE in the reference and the strut region respectively.

The scattering is described by the standard deviation of pdAE at a given crack width. Figure 9.8 shows the distribution and standard deviation at several selected crack widths in a range of 0.2 – 0.8 mm. For Type I, we take the mean of standard deviations at these crack widths which is 1171 m^{-2}, denoted as σ_I. For Type II, we take the standard deviation at crack width 0.2 mm which is 3160 m^{-2}, denoted as σ_{II}. The standard deviation at other crack widths is not considered for Type II due to shortage of data.

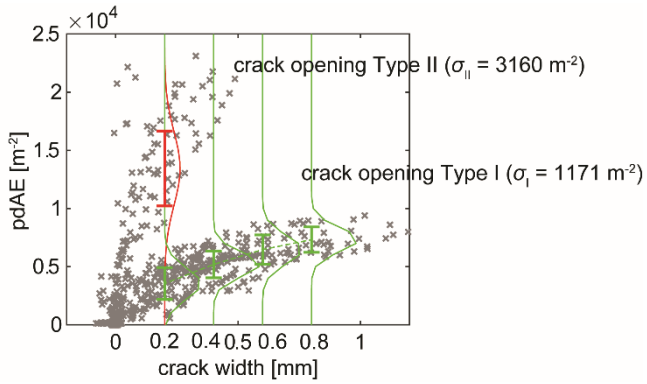

Figure 9.8 Distribution of the pdAE at some selected crack widths.

The scattering of the pdAE will influence the determination of the criteria. Figure 9.9 exemplifies the influence in test I123A. Plot (a) shows the criteria without considering scattering of the measurement. Plot (b) shows one possible situation in which we overestimate one σ_I in the reference (+ 1171 m^{-2}) and underestimate one σ_{II} in the strut (- 3160 m^{-2}). In this case, the yellow-light criterion is reached at a higher load level (from 260 kN to 280 kN). Plot (c) considers the other possible situation that we underestimate one σ_I in the reference (-1171 m^{-2}) and overestimate one σ_{II} in the strut (+3160 m^{-2}). In this case, the yellow-light and red-light criteria are reached at a lower load level.

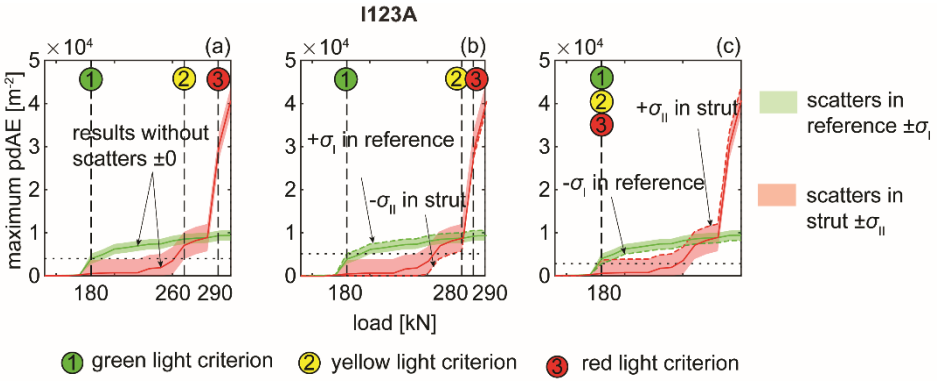

Figure 9.9 Influence of scattering on traffic light criteria in test I123A: (a) without scattering, (b) overestimating an σ_I in the reference and underestimating an σ_{II} in the strut, and (c) underestimating an σ_I in the reference and overestimating an σ_{II} in the strut.

Using the same method, Table 9.2 calculates the load ratios when the three criteria are fulfilled in all the tests, considering the variations. The load levels that are influenced by the variation are denoted as P'_1, P'_2 and P'_3 for green-light, yellow-light and red-light criteria respectively. The influences on green-light criterion are limited, with the load ratio increasing from 0.46 to 0.55 at the maximum (in test H603A). The influences on

red-light criterion are acceptable which most are to the safe side. The influences on yellow-light criterion are acceptable except for test H604A. There the corresponding load ratio increases from 0.76 to 0.99, which is unsafe.

Table 9.2 Load ratio at the traffic light criteria in beam tests, influenced by the variation of the crack pattern.

	Green-light criterion		Yellow-light criterion		Red-light criterion	
Beam test	P_1/P_u	P'_1/P_u	P_2/P_u	P'_2/P_u	P_3/P_u	P'_3/P_u
I123A	0.6	0.6	0.87	0.6-0.93	0.93	0.6-0.97
H601A	0.46	0.46	0.56	0.47-0.65	0.82	0.82
H602A	0.44	0.44-0.49	0.44	0.49-0.53	0.53	0.49-0.65
H603A	0.46	0.46-0.55	0.74	0.68-0.85	0.85	0.85
H604A	0.6	0.6	0.76	0.64-0.99	0.99	0.76-0.99
H853A	0.55	0.55	0.73	0.68-0.73	0.73	0.68-0.73

Other uncertainties like the spatial variation of concrete quality may also influence the pdAE and the criteria. Generally, at locations with lower concrete quality, AE signals are more attenuated, leading to less detected AE events. The study of influence of other uncertainties requires dedicated tests, which is out of the scope of this dissertation.

9.4 Extension of the traffic light system to reinforced concrete slabs

This section extends the traffic light system, which was developed from shear tests of beams, to shear tests of slabs. The shear tests of beams have 2D plain stress conditions where the stresses perpendicular to the *x*-*z* plane (in the *y* direction) are assumed zero. This leads to comparable inner and surface crack patterns in the *y* direction. But the shear tests of slabs have 3D stress conditions. The inner crack patterns differ from the surface. We need to monitor the cracking behaviour in 3D. So a 3D pdAE field will be generated. Moreover, according to the 3D stress distribution in slabs, the strut and reference regions need to be adjusted. This section uses tests SR2M1 and SR3M1 (introduced in Chapter 5) to develop a 3D traffic light system for reinforced concrete slabs.

9.4.1 Application of the traffic light system in concrete slabs

This section directly applies the traffic light system obtained and validated from beam tests to the slab tests, considering the slab as a wide beam member. We first need to determine the compressive strut and reference region in the slab. The slab was loaded by a point load. The compressive strut region is determined as direct paths from the point load to the support (Figure 9.10). In reality, the strut region may not be the estimated one. But as discussed in Section 9.2.1, deviation of the strut region is accepted as the strut and tie model is based on the lower-bound theorem. The reference region is selected in the tension zone under the load. From the bottom of the slab, the reference region has a height

of effective concrete tension height $h_{c,eff}$ and a length of one estimated flexural crack spacing l_{cr} (as shown in Figure 9.10).

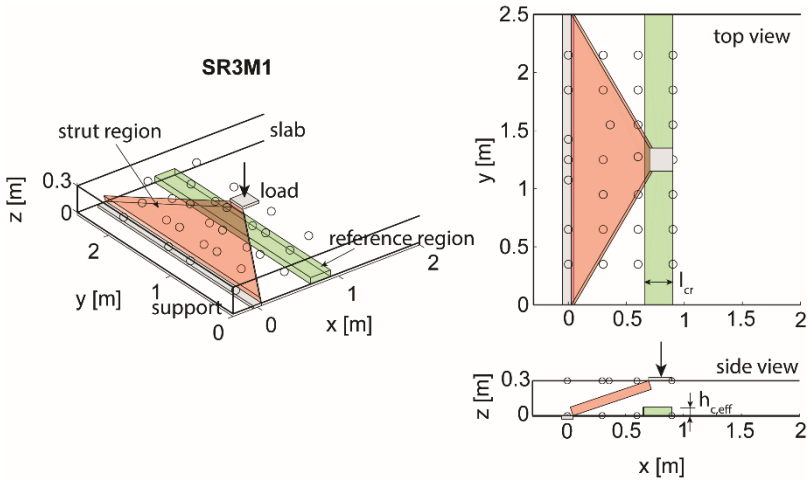

Figure 9.10 Region of compressive strut and reference in slab test SR3M1.

The slab was loaded in cycles (as shown in Chapter 5). At every load level, we calculate the 3D pdAE field considering the cumulative AE events from the start of test (0 kN) and excluding those events during unloading. Then we find the maximum pdAE in the strut and reference region. Similar to the beam tests, we use the maximum pdAE in the strut, evaluated by that in the reference region, to indicate the damage level of compressive strut.

Figure 9.11 shows the maximum pdAE in the strut and reference region with increasing load in tests SR2M1 and SR3M1. In SR2M1, the green-light and yellow-light criteria reached at 100 kN and 200 kN respectively. However, the red-light criterion was not reached: the maximum pdAE in the strut region did not get higher than that of the reference region. This means that the strut was not damaged by the critical shear crack and still had sufficient bearing capacity. This is in line with the observation during the test and the other measurements that the slab did not have shear failure but flexure failure. In SR3M1, the green-light, yellow-light and red-light criteria were reached respectively at 100 kN, 300 kN and 550 kN. After the red-light criterion was reached, the slab could carry additional 590 kN of load before shear failure. Since SR3M1 failed in shear, in the following study, we use it as an example.

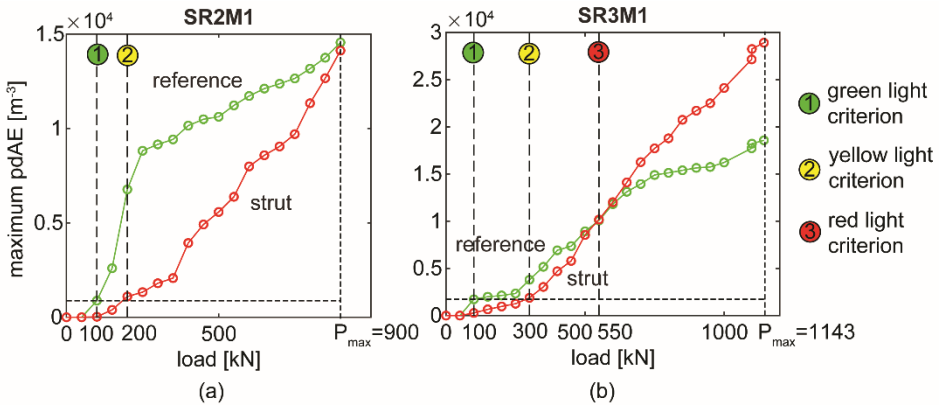

Figure 9.11 Traffic light criteria in slab tests: (a) SR2M1 and (b) SR3M1.

Figure 9.12 shows the cracking behaviour at the traffic light criteria in slab test SR3M1. Plot (a) shows the locations where the maximum pdAE was found at the three criteria. They were all close to the loading plate in the width direction. Plot (b) shows the pdAE field in the *x*-*z* plane at the y = 1.42 m when the green-light criterion was reached. The maximum pdAE in the reference (marked by green '×') comes from the flexural cracking under the loading plate. Plot (c) is the pdAE field at the yellow-light criterion. The location of the maximum pdAE (marked by the yellow '×') shows the first crack reaching the compressive strut. Plot (d) is the pdAE field when the red-light criterion was reached. We find another crack developed into the compressive strut region and generated the maximum pdAE (marked by the red '×').

From the above analysis, we can find that the green-light and yellow-light criteria in slab tests represent the same phenomena as in beam tests, which were flexural cracking and first cracking in the strut respectively. But the red light criterion has a different meaning for the strut failure. In beam tests, the compressive strut is 2D. When a local point failed to carry shear force, the whole strut failed, leading to structural failure (Figure 9.13a). In slab tests, the compressive strut is 3D. Failure of one local point in the width direction did not lead to failure of the whole strut. The compression force can be transferred by the surrounding concrete in the strut (Figure 9.13b). The redistribution of the stresses has been tested and validated in literature (Yang 2014). The redistribution provided extra load bearing capacity. Therefore, reaching the red-light criterion locally in a slab does not mean failure of the strut, nor the failure of the whole structure.

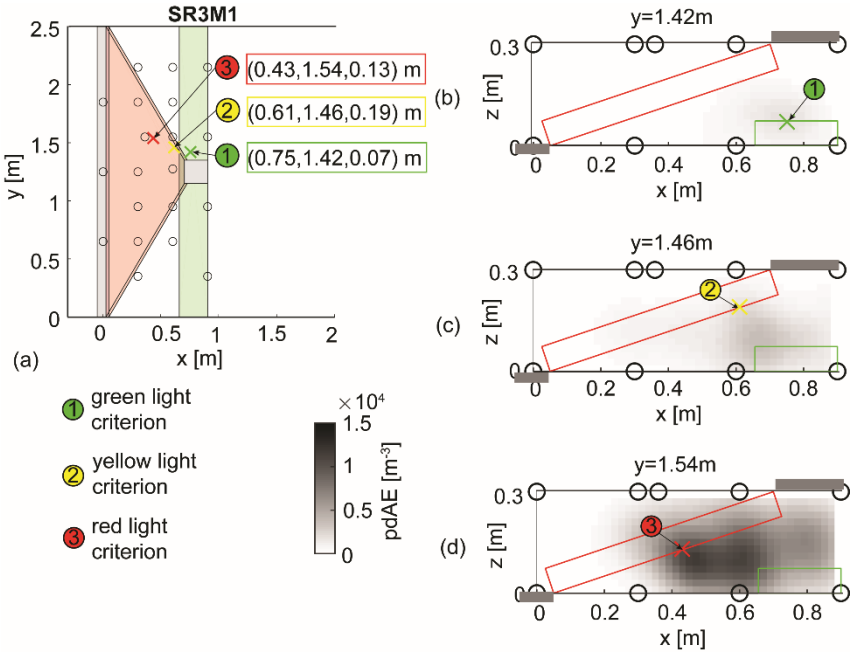

Figure 9.12 Cracking behaviour at the traffic light criteria in slab test SR3M1: (a) locations of the three criteria, (b) pdAE field at y = 1.42 m when the green-light criterion is reached, (c) pdAE field at y = 1.46 m when the yellow-light criterion is reached and (d) pdAE field at y = 1.54 m when the red-light criterion is reached.

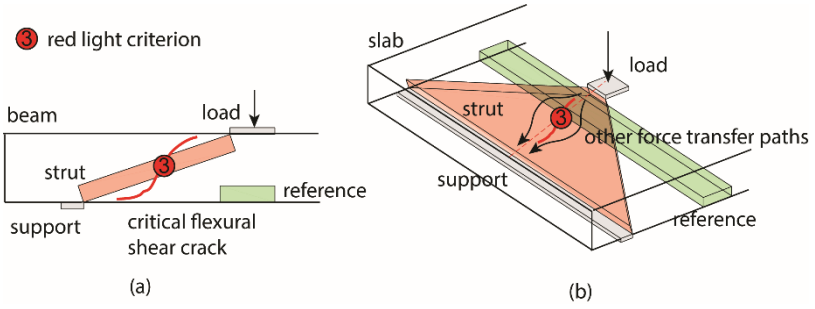

Figure 9.13 Comparison of the red-light criterion in (a) beam tests and (b) slab tests.

9.4.2 Shear failure indicator for concrete slabs based on the traffic light system

The former example shows that the red-light criterion only indicates a local failure in the wide compressive strut in a slab. The remaining part of the strut in the width direction can still provide additional bearing capacity. Only when a larger percentage of the total width of the strut is damaged, one may expect the loss of the bearing capacity of the whole system.

Figure 9.14 shows the locations in the strut where the red-light criterion was reached at 750 kN in test SR3M1. At these locations, we assume that the bearing capacity of the strut deteriorated. In the test of SR3M1, the deteriorated strut area in the *x*-*y* plane is indicated in Figure 9.14, it is mostly on one side of the beam in the width direction.

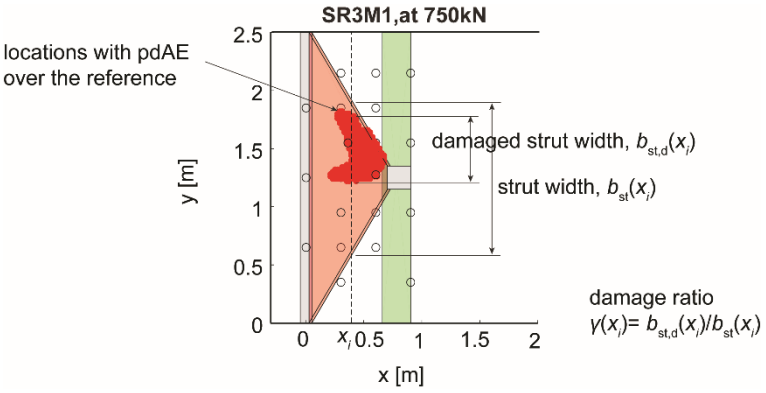

Figure 9.14 Locations in the strut where the red-light criterion was reached in test SR3M1 at load level 750 kN.

We consider that the deteriorated strut area could not carry compression force. At every cross section of the strut perpendicular to the *x* direction (at x_i), the width of the deterioration is $b_{st,d}(x_i)$, (noted in Figure 9.14), which is called 'damaged width'. Then considering the total width of the strut $b_{st}(x_i)$, we calculate the ratio that fails to carry compression force at cross section x_i as:

$$\gamma(x_i) = \frac{b_{st,d}(x_i)}{b_{st}(x_i)} \tag{9.2}$$

where x_i is the location of cross section perpendicular to the *x* direction, b_{st} is the width of compressive strut, $b_{st,d}$ is the damaged width of the compressive strut and γ which is the ratio between $b_{st,d}$ and b_{st} is defined as 'damage ratio'.

Figure 9.15 shows the damage ratio at cross sections perpendicular to the *x* direction at different load levels. The positions of support and loading plate in *x* direction are greyed out. With increasing loads, the damage ratio increased. The distribution of damage ratio at load level of 750 kN is highlighted in red as an example. At 750 kN, the maximum damage ratio was 0.51. This means that half of the strut could not carry compression force. The maximum damage ratio was found near the loading plate. It was not the closest location to the loading plate, maybe because the concrete under the load is in multi-axle compression with higher strength.

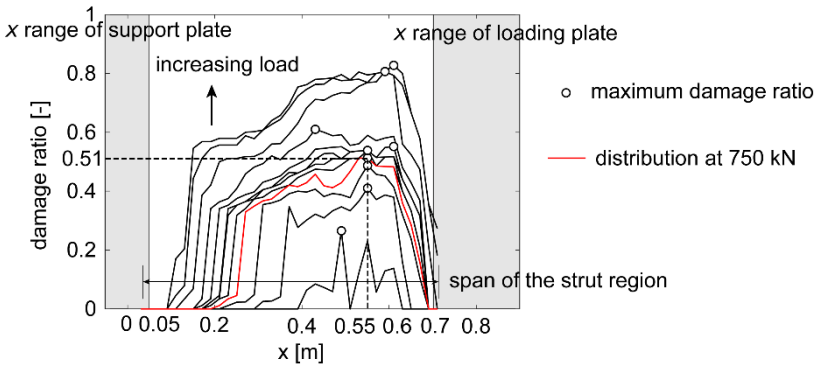

Figure 9.15 Distribution of the damage ratio at different load levels in test SR3M1.

We take the maximum damage ratio to represent the damage level of the strut at a given load level. Figure 9.16 shows the maximum damage ratio with respect to the applied load level in test SR3M1. The original red-light criterion is also plotted for comparision.

At the original red-light criterion (at 550 kN), the maximum pdAE in the strut first exceeded that in the reference. According to the previous study, only one local point in the width direction reached this criterion (shown in Figure 9.12a). Until 750 kN, half of the strut width reached the red-light criterion and failed to transfer compression force. Afterwards, the maximum damage ratio kept stable, only increased slightly. When the load reached 1000 kN, the maximum damage ratio significantly increased. The original red-light criterion, the fail of half strut width, and the significant increase of damage ratio near failure respectively indicated around 48%, 66% and 87% of the maximum load.

By considering the damage distribution in the width direction of the strut, we introduced a modified shear failure indicator to account the deterioration of the strut in the width direction. The indicator was based on red-light criterion, and calculated the ratio of the strut width that fails to carry compression force, which was called damage ratio. The maximum damage ratio along the strut determined the damage level of the strut at a load level. In the presented test, when the maximum damage ratio reached 0.5, which meant half of the compressive strut in the width direction could not carry compression force, the load was around 66% of the shear capacity. When the maximum damage ratio was near 1, almost the whole compressive strut could not carry force, which was close to shear failure. More tests are needed to validate the relationship between the maximum damage ratio and the load margin to shear failure.

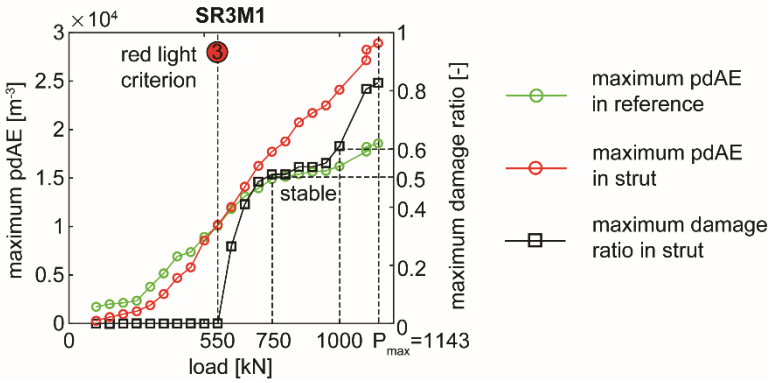

Figure 9.16 Maximum failed width percentage with increasing load, compared to the original red light criterion in test SR3M1.

Moreover, the traffic light system can also be extended to other loading conditions. Under a certain loading condition, the regions of the compressive strut and tension chord can be determined according to stress distribution (Muttoni, Schwartz et al. 1996). Then a same methodology can be used: comparing the maximum pdAE in the strut to that in the reference, to indicate the integrity of compressive strut which is closely related to the shear failure of the structure. Some modifications may be needed as what we have done for extension to slabs, but the general concept is valuable for other applications.

9.5 Conclusion

This chapter developed AE-based indicators for shear failure of reinforced concrete structures without shear reinforcement. For this type of structure, the compressive strut is unreinforced, thus suffers from brittle failure. Failure of the strut would lead to the shear failure of the structure. Therefore, evaluation of the integrity of compressive strut is important.

To evaluate the integrity of compressive strut, we used the maximum pdAE in the strut, evaluated by the maximum pdAE in the reference. The selection of strut and reference region was according to the strut and tie model: a prismatic compressive strut was assumed between the load and the support; and a reference region was selected within the tension chord where the flexural cracks form.

Based on the evaluation of compressive strut integrity, we developed a traffic light system which can indicate three levels of structural damages against shear: the green-light criterion was reached when only flexural cracks formed; the yellow-light criterion was reached when the compressive strut was first cracked; the red-light criterion indicated that critical flexural shear crack propagated across/along the strut, which was close to shear failure. In the presented shear tests on RC beams, the green-light criterion was reached earlier than 60% of the shear capacity. The yellow-light criterion was fulfilled at load

ratio in range of 49%-87%, related to the shear span to depth ratio. The red-light criterion indicates a very dangerous situation for flexural shear failure, with load level reaching around 99% of the shear capacity. We also studied the robustness of the traffic light system to the variation of local crack profile. In the presented tests, the influence on the three criteria was acceptable.

Then we extended the traffic light system from the 2D members to 3D members. For reinforced concrete slabs, the cracking behaviour was monitored by a 3D pdAE field. And the compressive strut was wide compared to that in beams. Considering the strut bearing capacity in the width direction, we modified the shear failure indicator for slabs. The modified indicator was based on red-light criterion, and calculated the ratio of the strut width that fails to transfer compression force. This ratio was defined as damage ratio. The maximum damage ratio along the strut determined the damage level of the strut at a load level. In the presented test, when the maximum damage level reached 0.5, which meant half of the compressive strut could not carry force in the width direction, the load was around 66% of the shear capacity. When the maximum damage level was near 1, which meant almost all the strut width could not carry force, the structure was close to shear failure.

Moreover, the developed traffic light system can also be used for different loading conditions. Under a certain loading condition, the region of compressive strut and reference can be determined according to the stress distribution. Then a same methodology can be used: comparing the maximum pdAE in the strut to that in the reference, to indicate the integrity of compressive strut which is closely related to the shear failure of the structure. The extension to different loading conditions is not included in the dissertation due to time and resource limit.

We can identify four benefits of using the traffic light system:

- Firstly the system has a strong physical background of shear failure mechanism. The integrity of compressive strut is evaluated, which is closely related to shear failure of the structure.
- Secondly the system indicates three different levels of structural damages against shear. The user can decide the relevant criterion according to their needs. Further discussion on users' action on reaching a certain criterion is presented in the next Chapter 10.
- Thirdly the system is applicable to different types of structures, loading conditions, material properties and AE setups.
- Fourthly the system can automatically calculate the indicators and determine if the criteria are fulfilled. Since the calculation is computationally efficient, the

traffic light system can work for real-time monitoring. This is especially beneficial for load testing. Further discussion is provided in Chapter 10.

The AE-based traffic light system contributes to the field of indicating shear failure of concrete structures. This chapter provides the theoretical development, experimental validations, robustness analysis and extension from 2D to 3D members. Due to its strong physical background, different levels of criteria, applicability and computational efficiency, the system is suggested for the future application.

Chapter 10 Guidance on implementing acoustic emission-based indicators in load testing

10.1 Introduction

In the previous chapter, we have developed an AE-based indicator for shear failure of concrete structures without shear reinforcement. To implement the indicator in practice in a load testing, this chapter provides guidance to the user. The guidance covers a complete procedure comprising a preliminary survey, the design of a loading protocol and sensor layout, the execution of AE monitoring and real-time data analysis, and the decision making when pre-defined criteria are reached.

The guidance first suggests a preliminary survey to acquire necessary information relating to the design of the load test and the monitoring system. Such survey includes review of available documentation, visual inspection and measurement of the wave propagation properties (Section 10.2). Then we discuss the design of loading protocol including load levels and position in a load test considering the need from AE-based indicators (Section 10.3). Section 10.4 discusses the design of AE sensor layout, which includes the determination of the measuring zone and the positions of the sensors. We also provide a method to evaluate the sensor layouts from the perspective of source localization efficiency. Section 10.5 recommends on the execution of AE monitoring and real-time data analysis. Execution of AE monitoring includes the sensor installation and the system setup. Real-time data analysis focuses on instant output of AE-based indicators. When the indicators reach the pre-defined criteria, Section 10.6 suggests corresponding actions according to the users' need.

10.2 Preliminary survey

The first step of the preliminary survey is to review the available documentation of the target structure. The relevant information includes the geometry of the structure, the design of reinforcement, the mechanical properties of the structure (concrete and steel classes), the original design calculation, structural assessment reports and previous maintenances records. Other useful information could be the inspection results of the deterioration condition of the structure in the past. Though the deterioration condition may have been changed from the time of documentation, the record in the history can update our knowledge to improve the design of the new test and serve as a reference.

The next step is visual inspection. Attention is given to the structural surface condition and the environment condition. The access to the bridge surface is needed for instrumentation. Moreover, any delamination, carbonation or presence of crack at the structural surface would influence the AE monitoring. Sensors should be installed at undamaged and smooth surfaces. Besides, the observed damages on the surface can be used by structural engineers to determine the critical element to be monitored. Regarding the environmental conditions, AE sensors should be protected against high moisture conditions like rain or flood and should be away from running traffic.

Besides the review of documentation and the visual inspection, one should always measure the wave propagation properties including wave speed and attenuation before AE monitoring. The wave speed is needed to estimate the AE event location (source localization), and the wave attenuation is needed to determine the maximum sensor spacing (which will be discussed in Section 10.4.2).

The technique to measure the wave propagation properties is ultrasonic pulse velocity, the basic principle of which is introduced in Chapter 3. A stepwise explanation of how to apply this technique is referred to the preliminary test discussed in Chapter 5. An array of sensors is used, with one sending a signal and the others receiving (Figure 5.14). By comparing the arrival times and amplitudes of signals received at different locations, the wave speed and attenuation can be estimated. Here the measured amplitude is mostly from surface wave. One need to calibrate the attenuation for P-wave. Details have been introduced in Chapter 5. In literatures, the wave speed and attenuation can also be measured using pencil lead testing which has a similar background (Felux 2017).

10.3 Design of loading protocol

A comprehensive design of loading protocol should consider the objective of the load test, the requirements of AE monitoring and other measurements during the test (Lantsoght, van der Veen et al. 2017). This section focuses on the requirement of AE monitoring on the loading protocol, or more specifically, the adjustments needed for the AE-based indicator.

For reinforced concrete beams or slabs without shear reinforcement, under vertical traffic load, this dissertation considers the failure mode shear. Therefore, the loading protocol is designed for a shear test. Load design for other failure modes like flexure is not discussed.

According to the commonly applied practices in a proof load test, the load is usually applied in cycles and at a fixed position (Figure 10.1a). Unlike the load testing that requires at least three repeated cycles at a certain load level, the AE-based indicator only uses the first load cycle, as marked by red lines in Figure 10.1b. This is to limit the influence of the number of repeated load cycles on the pdAE value (according to Chapter 8).

In a load cycle, when first reaching a higher load level, the load has to be increased with small steps to enable a good control of load execution. At every step, the load is hold for a while to allow the calculation of the AE-based indicator, which enables a near real-time analysis. The load holding time depends on the calculation time, thus is related to the data size obtained in the step. In the experiment SR3M1 in this dissertation, the holding time should be larger than 2 minutes (which will be explained in Section 10.5). During unloading, AE events are mostly from crack closure which can be used to identify the location of existing cracks (Chapter 8). The conditions of using AE during unloading are discussed in Section 10.6.

Regarding the load level of a cycle, the design in load testing can be applied for the AE-based indicator (Figure 10.1b). A low load level is needed to check the monitoring system. No new crack is expected at this stage. Afterwards, the AE-based indicator has no specific requirement on the load level of a cycle. The user can take the design from the shear test (for example, the load levels 2-4 in Figure 10.1b).

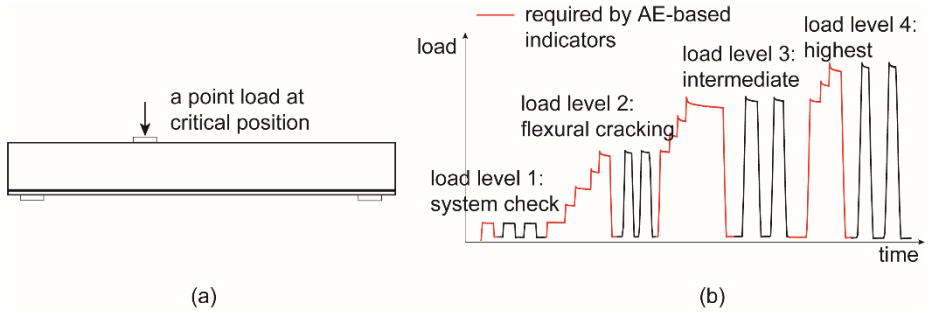

Figure 10.1 Design of loading protocol for implementing AE-based failure indicators: (a) a point load at shear-critical position and (b) cyclic loading with different load levels.

10.4 Design of sensor layout

This section introduces the design of sensor layout for implementing the AE-based failure indicator. Firstly a specific measuring zone needs to be determined to obtain the AE-based indicator. Secondly the sensor spacing needs to be limited to provide reliable source localization and classification results (Chapters 6 and 7). Even within the required sensor spacing, the layout of the sensors can still influence the monitoring results, especially the source localization efficiency. Therefore, we provide a method to evaluate the source localization efficiency of a sensor layout. With this method, the sensor layout can be refined.

10.4.1 Determination of measuring zones

According to Chapter 9, the AE-based failure indicator uses the strut and tie modelling of the structure and thus requires monitoring AE events in the region of the strut and part of the tie.

The region of compressive strut depends on the structural type and the load condition (Chapter 9). Figure 10.2 illustrates the strut of a beam and a slab with a point load. When monitoring a relatively small structure with sufficient sensors, one can install sensors to cover the whole strut region. When the number of sensors is limited or the size of the structure is large, the measuring zone in the strut can be reduced. In our tests, the yellow-light and red-light criteria were often reached in the region closer to the loading point. This is due to the larger bending moment in that region. Therefore, the measuring zone in the strut can be reduced, for example, to half in the longitudinal direction (measuring zone 2 in Figure 10.2).

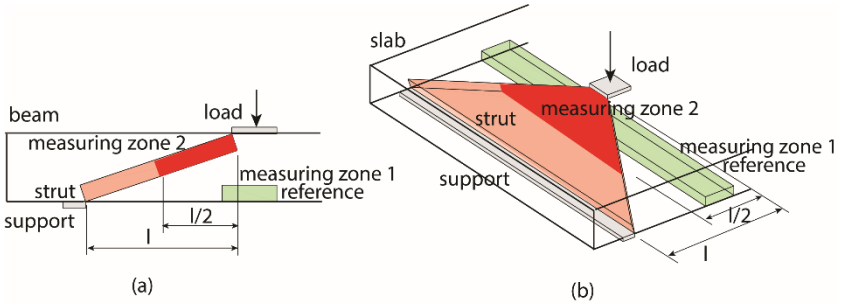

Figure 10.2 Determination of measuring zones: (a) in beam tests and (b) in slab tests.

The measuring zone 1 (in Figure 10.2) should cover the region of reference, which is part of the tie where flexural cracks form. We propose that the length of the region is one times the estimated crack spacing (Equation 2.2) which covers at least one major flexural crack. In conventional strut and tie analysis, the height of the tie is typically not considered. However, in an AE analysis the cracking of the concrete in the tensile tie is our focus, thus we need to define the height of the tensile tie as well. We propose that the height of the region is the effective concrete tension height (Equation 9.1). Preferably the measuring zone 1 should be around the cross section with the maximum bending moment, to detect the first flexural cracking. But in condition that the cross section with the maximum bending moment is not accessible or has already been cracked, other part of the member that will be cracked in flexure is also acceptable. The indicator is not working when no new flexural crack forms in the measuring zone 1.

The two measuring zones should be enclosed by the sensors since AE source localization outside the sensor enclosed zone is not accurate (Chapter 6). The sensors cannot enclose the measuring zone when the member is covered by other materials, such as the asphalt layer typically on the top surface of concrete bridges. In this case, holes can be drilled at the designated sensor location, and be filled back after the measurement.

10.4.2 Sensor spacing

Due to the wave attenuation from the source to the sensor, the sensor spacing should be within a limit to provide reliable source localization and classification results (Chapters 6 and 7).

The attenuation property should be measured in a preliminary survey as suggested in Section 10.2. In the experiments in this dissertation, the amplitude of P-wave attenuated around 55 dB after 1 m. The first arrival of a wave is usually the P-wave that directly travels from the source to the receiver, which is referred as direct wave and used for source localization (Chapter 6). When the amplitude of the source signal is 100 dB and the noise level is 45 dB, the direct wave could not be detected after 1 m. In this case, the

sensor spacing should be within 1 m to ensure that sufficient sensors can receive the direct waves for source localization.

For source classification, the closest sensor should be within 0.5 m from the source according to Chapter 7. The value 0.5 m was determined considering the attenuation of high frequency components (over 70 kHz) of the wave. After 0.5 m, the high frequency component was insignificant. For the source classification method proposed in this dissertation, which is related to the frequency component, the closest sensor should be within 0.5 m from the potential source location. This means that the sensor spacing should be within 1 m.

Considering both requirements from source localization and classification, the maximum sensor spacing is determined as 1 m in our experiments. For other applications, the maximum sensor spacing needs to be adjusted according to the wave attenuation properties and the signal and the noise level, following the same approach as above.

10.4.3 Evaluation of sensor layouts

Even with a determined sensor spacing, various sensor layouts are possible in the measuring zone. This section provides a method to evaluate the sensor layout optimized for the source localization.

Source localization requires at least three sensors (for 2D) or four sensors (for 3D) that can receive the direct waves from the source. Supposing that the wave attenuation is only related to the wave travel distance, when the $3^{rd}/4^{th}$ closest sensor could not receive the signal, the farther sensors could not receive either. We would then not have a sufficient number of sensors. Therefore, the signal amplitude at the $3^{rd}/4^{th}$ closest sensor determines whether an AE event can be located in 2D/3D. The $3^{rd}/4^{th}$ closest sensor is defined as the decisive sensor for localization.

As illustrated in Figure 6.3, for a possible source location p_1, the decisive sensor and its distance d_1 to the source can be calculated. Supposing that the wave attenuation function $f(d)$ in decibels is measured from the preliminary test and the threshold value at the sensor is A_0 in decibels, the source amplitude is required to be over $A_0 + f(d_1)$ so that the signal can be detected by the decisive sensor after attenuation, and the event can be located. Therefore, the required source amplitude for location p_1 is $A_0 + f(d_1)$. For another location p_2 in the same sensor layout, the distance to the decisive sensor changes to d_2 which is smaller. Consequently, attenuation by this shorter travel distance $f(d_2)$ is less, resulting in a lower required source amplitude $A_0 + f(d_2)$. This means that the source at location p_2 with lower amplitude can already be located. The AE sensor layout is more sensitive to AE events at location p_2 than at location p_1.

Therefore, we use the required source amplitude to evaluate the sensitivity of a sensor layout to AE events at a location. The required source amplitude at a location is calculated

as the sensor threshold level plus the wave attenuation from the studied location to the decisive sensor, which is 3rd (for 2D) and 4th (for 3D) closest sensor. The sensor layout is more sensitive to AE events at locations with smaller required source amplitude.

Figure 10.3a shows the requried source amplitude at every possible source location in a 2D layout. The threshold at each sensor is 45 dB and the attenuation function takes the one measured in Chapter 5. We find a lower value in the centre of a sensor grid than on the edge (71 dB and 82 dB respectively). This sensor layout is more sensitive to AE events in the centre of a sensor grid.

To equally count the AE events at any location, we set up a unified source amplitude threshold, which is taken as the highest value of required source amplitude within the measuring zone. For a localized AE event, one should first estimate its source amplitude according to the received signal amplitude and the wave attenuation from the source to the receiver. If the source amplitude is over the pre-defined threshold, the AE event is counted. In this way, AE events at different locations are counted under a same requirement of the source amplitude.

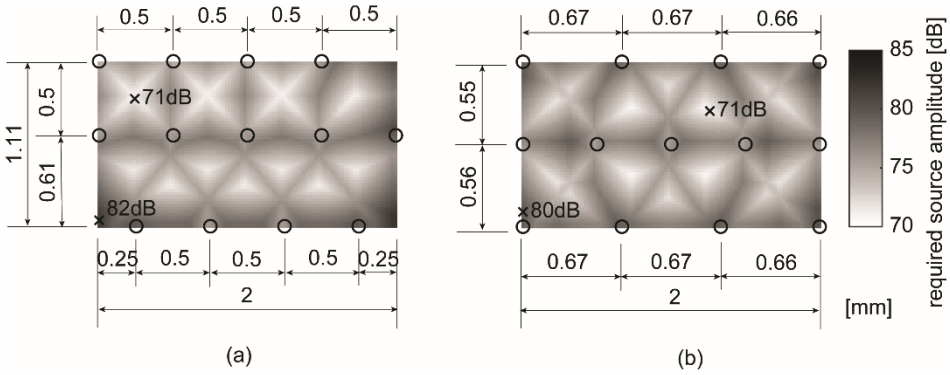

Figure 10.3 Evaluation of sensor layout in test I123A: (a) before and (b) after adjustment.

But the above calibration discards some located AE events which could have been used. In the presented example in Figure 10.3a, the threshold is set as 82 dB which is the largest value in the distribution. AE events with amplitude lower than 82 dB are all wasted. A better sensor layout should have a lower threshold, thus discarding less AE events. An improvement is made in Figure 10.3b, where the sensors are more evenly distributed in the measuring zone, resulting in the largest value to be reduced to 80 dB. The threshold for source amplitude reduces from 82 dB to 80 dB. This means that more AE events can be kept. To lower the source amplitude threshold, further improvement to the sensor layout may be possible but is not studied in this dissertation.

10.5 Acoustic emission monitoring and real-time data analysis

Execution of AE monitoring includes sensor installation and system setup. Sensors can be installed using a steel holder as introduced in Chapter 5: Figure 5.5a. Vacuum greases, propylene glycol or electrical compound can be used as couplant between sensor surface and structure surface (Theobald, Zeqiri et al. 2008). The sensor and the coupling need to be checked using pencil lead testing next to each sensor. At least three times of pencil lead break are needed for each sensor. The averaged peak amplitude of the received signals was required to be over 90 dB in our experiments. To improve the coupling effect, the concrete surface needs to be smoothed and cleaned, and the voids should be filled between sensor and concrete surface. Small voids can be filled by couplant. Applying the couplant a few hours ahead of the test allows couplant penetrating the surface, which fills the small voids better. We have observed significant improvement on coupling effect in our tests by applying 24 hours before testing.

To set up the AE system, an important parameter is the threshold of recording signal. This threshold should be over the noise level. To acquire the noise level, the system starts to acquire signals from environment before applying any load. The acquisition can be stopped until a constant noise is detected. In our lab condition, the noise level was found below 40 dB. On site, the noise level depends on the environmental condition. Other system setups can follow the user manual provided by the data acquisition system (MISTRAS 2011). The setups of the experiments in this dissertation can be found in Chapter 5 as a reference.

Then load testing can be started. A real-time data analysis is needed during testing. The steps of the real-time data process algorithm developed for the AE-based indicator are explained as following. Firstly the data acquisition system records the signals and extracts the signal parameters. Then the obtained signal parameters are read every e.g., 60 seconds from the data acquisition system. This time interval can be adjusted according to the amount of data generated during monitoring. Afterwards, the exported data are inputted into an external program which calculates the pdAE field and the AE-based indicator according to the methods provided in this dissertation. In our experiments, we used Mistras system to acquire and record the signals, an embedded software AEwin to extract signal parameters, a software Noesis to export the data continuously and a software Matlab to calculate the indicators. In our test, for data file of size 20.4 MB in DTA format (which is a file generated and stored on the hard disk of AE system (MISTRAS 2011)), the time delay was 131.4 s, among which 60 s was from the time interval of data exportation and 71.4 s was from the calculation of the AE-based indicator. The calculation time can be improved by using faster programming language like C/C++.

The near real-time data analysis (with a time delay of around 2 min) is accepted for load testing of concrete structures. The time delay requires a load holding time at every load

step as described in Section 10.3. During this load holding time, other measurements can also be performed like taking photos for DIC or marking the cracks from the structural surface.

10.6 Decision making at acoustic emission criteria

In Chapter 9, we developed the AE-based failure indicator for reinforced concrete members without shear reinforcement. We first briefly review the physical background of the indicators, which helps the users to understand the suggested decision making.

In reinforced concrete members, AE-based indicators show three damage levels: when the green-light criterion is reached, the flexural crack forms in the reference region; when the yellow-light criterion is reached, the strut is first cracked; when the red-light criterion is reached, the strut is significantly deteriorated by the flexural shear crack. For beams, the whole strut fails, leading to structural failure. But for slabs, due to the wide strut, other parts of the strut in the width direction can still transfer the force, providing extra shear capacity after the red-light criterion. To consider the contribution from strut width, we developed another parameter based on the red-light criterion, which is damage ratio of the strut. This parameter evaluates the ratio of the strut width that exceeds the red-light criterion. The damage ratio is near 1 when the whole strut fails, which is close to shear failure.

Table 10.1 summarizes the physical background of the AE-based indicator and the possible corresponding actions of the users. At each criterion, the load level compared to the shear capacity is given below. The values are observed from this dissertation which are provided only as a reference.

- For beams, at green-light criterion, the load was less than 60% of the shear capacity; at yellow-light criterion, the load was 49%-87% of the shear capacity, depending on the ratio between shear span (distance between the centre of the load and the closer support) and beam height; at red-light criterion, the structure was very close to failure, reaching 99% of the capacity.
- For slabs, when the damage ratio reaches 0.5, the load was around 66% of the shear capacity; when the damage ratio was near 1, the structure was very close to shear failure.

When the user prefers not to further damage the structure in a load testing, we suggest applying a small load level and using AE events during unloading. According to Chapter 8, AE events during unloading can be used to locate the existing cracks. The crack distribution can determine which criteria have been reached in the past. When the crack only presents in the reference region, the structure was at green-light criterion in its loading history. When the crack reaches the strut, but no inclined cracks, the structure was at yellow-light criterion. When a large amount of AE events were found in the strut at an

inclined crack, red-light criterion has been reached before. For reinforced concrete slabs, the damage ratio of the strut can also be calculated according to the crack distribution in the strut. Afterwards, corresponding actions can be taken according to Table 10.1.

The guidance on implementing the AE system includes preliminary survey, design of loading protocol, design of sensor layout, execution of AE monitoring, real-time data analysis and decision making at AE criteria. Figure 10.4 shows the steps that the users should take to implement the AE system in load testing.

Table 10.1 Decision making based on AE-based failure indicators, considering user need and structural type.

User objective	Structural type	AE-based indicator	Physical behaviour	Corresponding actions
Estimate the cracking load	RC beams & slabs	Green-light criterion	Cracking in the reference region	Stop loading; Can repair the cracks.
Load the structure to the most, but keep safety against shear failure	RC beams	Yellow-light criterion	Cracking in the strut	Stop loading; Can keep the structure, but under lower load; Can maintain the structure to prolong the service life.
	RC slabs	Damage ratio of 0.5	Half of the strut width deteriorated	
Approach the actual shear capacity, but avoid collapsing of structure	RC beams	Red-light criterion	Cracking in the strut that significantly reduces the bearing capacity	Take safety measures for a collapse; Stop loading immediately; Replace or repair the structure
	RC slabs	Damage ratio near 1	Almost the whole strut width deteriorated	

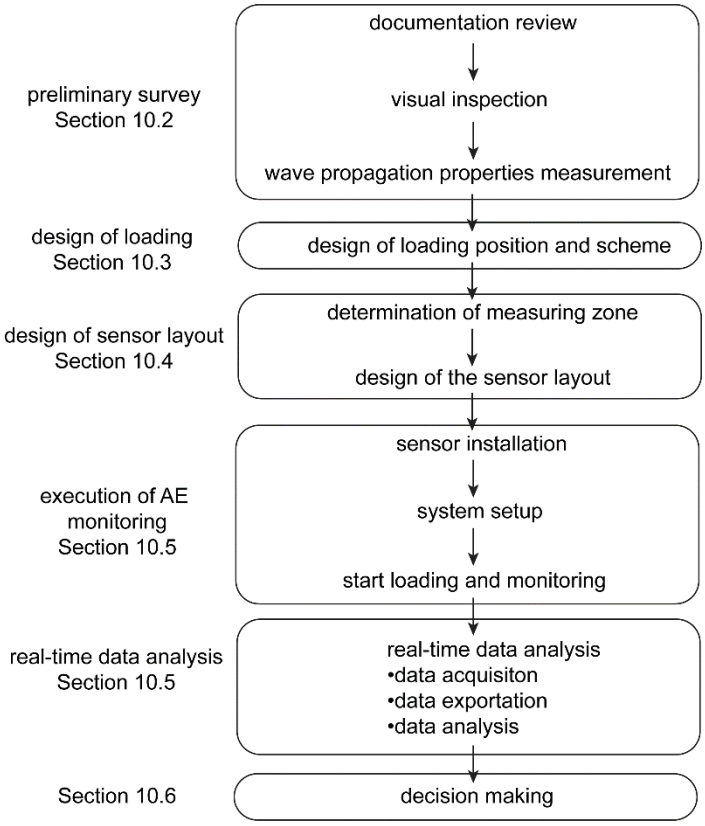

Figure 10.4 Steps that the user should take to implement the AE system.

Chapter 11 Conclusions and recommendations

11.1 Conclusions

As stated in Chapter 1, the goal of this dissertation was to develop an AE system to indicate shear failure of reinforced concrete structures without shear reinforcement. To reach this goal, several research questions were raised, which are repeated here:

Q1: What are the properties of source localization error, considering various uncertainties in the localization process?

Q2: How can we improve the AE source localization results, considering the localization error?

Q3: How can we classify the types of AE sources in concrete in an efficient and reliable way?

Q4: What is the relationship between AE events and crack kinematics?

Q5: How can we indicate possible shear failure of concrete member at early stage using AE?

Q6: How can we apply the AE-based indicators of shear failure in load testing of concrete structures?

To answer these questions, literature reviews and experiments have been performed. Chapters 2-4 were literature reviews on shear failure mechanisms, various monitoring techniques and the AE technique. The knowledge from literature inspired the following chapters to answer the research questions. The experiments that have been used in this dissertation were collected and introduced in Chapter 5.

With the literature insights and experimental results, the dissertation developed a probabilistic AE method for source location identification (Chapter 6, Q1 and Q2) and a source classification criterion (Chapter 7, Q3), explored the relationship between AE events and crack kinematics (Chapter 8, Q4), and established a set of AE-based failure indicators for reinforced concrete structures (Chapter 9, Q5). Then Chapter 10 provided a guidance on implementing the indicators (Q6). The following subsections describe these contributions in more detail.

11.1.1 A probabilistic acoustic emission method to identify source locations in concrete structures

Chapter 6 presented a probabilistic AE source localization method, with the output probability density field of AE events or pdAE field. The pdAE estimates the probability of the location of AE events, considering the source localization error due to inevitable uncertainties in the localization process. In this method, the properties of source localization error are important parameters which were determined from simulated tests. The integral

of pdAE over a certain space range and time period indicates the total amount of AE events in that space range and time period.

We calculated the pdAE field in the presented experiments in this dissertation. In the demonstrations, many benefits of using the pdAE field were found. Firstly the source localization errors are included by using a probability density function. Secondly the pdAE field provides a clearer crack pattern compared to the conventional source localization. Thirdly the value of pdAE at a location is closely related to the crack width (which is further studied in Chapter 8). Moreover, this method is time efficient, thus is suitable for real-time monitoring.

This probabilistic AE source localization method addressed research questions Q1 and Q2 and has been adapted as a tool to identify the damage locations in this dissertation.

11.1.2 A source classification criterion based on signal parameters

Chapter 7 presented a new source classification criterion to distinguish signals from concrete tensile cracking and friction between two crack faces. Firstly we experimentally evaluated the performance of various signal parameters in source classification, including RA value, average frequency, peak frequency, frequency centroid and partial power. We found that the RA value, recommended by RILEM AE standard, was strongly influenced by the wave attenuation, thus was not reliable for classification in large concrete structural members. In the study we observed that peak frequency and partial power provided a clear boundary between signals from different types of sources. Therefore, we proposed the following classification criterion: a signal with peak frequency over 70 kHz, or partial power (>70 kHz) larger than 0.5 is identified as from tensile cracking; otherwise, the signal is from friction.

We suggested to use the signal received by the closest sensor to reduce the influence of wave propagation. The distance between the closest sensor and the source should be less than 0.5 m.

The new criterion substantially improves the applicability and reliability of source classification. Firstly the criterion can be calculated in real time by commercially available AE software like AEwin. The computational time is much less compared to the waveform-based methods or the artificial intelligence-based methods. Secondly the new criterion is more reliable against the influence of wave propagation. Lastly compared to the traditional methods, the new criterion provides a clearer and more consistent boundary between signals from the two types of sources.

The new AE source classification criterion addressed research question Q3 and was used to classify the source type of tensile cracking or friction in the dissertation.

11.1.3 Relationships between acoustic emission events and crack kinematics

Chapter 8 revealed the relationship between AE events and local crack kinematics. The kinematics included the crack width change and shear displacement. The amount of AE events at a location was evaluated by the pdAE (using the method in Chapter 6). The pdAE-crack kinematics relationships during loading and unloading were studied separately, accordingly different observations and conclusions were obtained.

During loading, AE events are mostly from the opening of concrete cracks. The pdAE increases with crack width, but the relationship is strongly related to the crack opening history. We idealized two extreme conditions of crack opening history and corresponding pdAE-crack width relationship. In reality, the observations should be between the two extreme conditions. In Type I, the crack first opens in the perpendicular direction of the crack path without sliding. The pdAE increases with the crack width and then stabilizes. The limited increase of pdAE afterwards is due to limited contact between two crack faces when the crack opens to a certain crack width. This type of crack opening history mostly occurs in the tensile zone. In Type II, the crack faces slide already from the beginning at a small crack width, where the contact area between crack faces are large. The large contact area at shear displacement results in significant increase of pdAE. This type of crack opening history mostly occurs in the tip of an inclined crack in the compressive zone.

During unloading, AE events are mostly from the closure of concrete cracks. AE events start to accumulate when the crack width reduces to a certain value that the two crack faces are in contact. With further crack closure, the contact area between the two crack faces increases, resulting in more increase of AE events (pdAE). We proposed a simplified model to explain the relationship between pdAE and crack width during crack closure.

The above-described relationships were found from the first load cycle when the crack was newly opened. However, in practice, a crack may have been opened and closed for many times in the service history of the structure. We found that more load cycles would reduce the number of AE events within the same load increment, thus influence the relationship between pdAE and crack kinematics. We also evaluated the influence of loading speed to the relationships, and concluded that the influence was limited within the tested range.

The new understanding of relationship between AE events and crack kinematics addressed research question Q4 and provided insights into developing AE-based failure indicators in this dissertation.

11.1.4 Acoustic emission-based failure indicators for reinforced concrete structures without shear reinforcement

We noted the importance of the integrity of the compressive strut to the shear capacity from the literature review in Chapter 2. Based on this notion, Chapter 9 evaluated the damage level of compressive strut. The maximum pdAE in the strut was proposed as an indicator, which corresponded to the maximum cracking damage in that region (according to Chapter 8). We also proposed to use the maximum pdAE in the flexural zone as a reference within the structure. The maximum pdAE in the strut was compared to the reference. From the comparison, we suggested three levels of structural damage: the flexural cracking (green-light criterion), the initiation of cracking in the strut (yellow-light criterion) and the formation of critical flexural shear crack in the strut (red-light criterion). This is called the traffic light system for structural failure indication.

The proposed system was validated with shear tests of reinforced concrete beams. In the validation, at green-light criterion, the load reached up to 60% of the capacity. At yellow-light criterion, the load reached 49%-87%, depending on the shear span and beam depth ratio. At red-light criterion, the load reached up to 99% of the capacity. The robustness of the traffic light system was also evaluated considering the variation of crack patterns in practice.

The traffic light system has also been extended from 2D members (concrete beams) to 3D members (concrete slabs). Slabs revealed extra shear capacity after the red-light criterion, because of the redistribution of the load in the undamaged strut of the slab in the width direction. Therefore, we used the damage ratio of the strut in the width direction to indicate shear failure of slabs. A damage ratio of 0.5 means that half of the strut width cannot carry compressive force, which corresponded to 66% of the capacity in the presented tests. A damage ratio close to 1 means that almost the whole strut fails and no redistribution in the width direction is possible, which is close to shear failure.

For users of the AE indicator, Chapter 10 provided a guidance on its implementation, including the preliminary survey, load design, sensor layout design, execution of AE monitoring and real-time data analysis and decision making based on the traffic light criteria.

The developed AE system and the guidance on its implementation addressed research questions Q5 and Q6 respectively. We meet our goal to use AE to indicate shear failure of reinforced concrete structures without shear reinforcement.

11.2 Recommendations

This section lists some topics that are closely related to this dissertation and recommended for the future research.

11.2.1 Nature of acoustic emission in concrete cracking

In Chapter 8, we distinguished two types of AE sources in concrete cracking, which are tensile cracking and friction between two crack faces. AE events from tensile cracking are most likely related to the release of kinetic energy at local snapback according to Chapter 4. AE events from friction can be related to the contact area of the two crack faces according to Chapter 8. Though not classified, we found that the total AE increased more when the contact area was large. Therefore, one can possibly explain the nature of AE in concrete cracking from two aspects: the kinetic energy from tensile cracking and the kinetic energy from friction at contact area between the two crack faces.

One needs to first classify the obtained AE events into two groups from tensile cracking and friction using the source classification method. Then the pdAE of each group needs to be calculated. For a certain crack, one would then have the information of pdAE of tensile cracking, pdAE of friction and the complete crack kinematics from DIC.

The pdAE of tensile cracking will be compared to the kinetic energy from tensile cracking. The kinetic energy can be estimated by simulating a tensile cracking process of the measured crack at macro scale level. The pdAE of friction will be compared to the kinetic energy from friction at contact area between two crack surfaces. The friction at the contact area can be estimated using a contact area-based physical model that describes the shear behaviour along a crack. A typical physical model is the aggregate interlocking model proposed by Walraven (Walraven 1981). In this way, one can explain the nature of obtained AE events with a physical background. A strong assumption in this proposed methodology is that the process of tensile cracking and friction can be decoupled.

11.2.2 Design of sensor layout

In Chapter 6, we studied the factors that influences the source localization accuracy. They were the arrival time picking error, presence of crack and sensor spacing. We found that even with the same sensor spacing, the positions of the sensors would influence the error properties. For example, sensor layout Type 1 and 2 in Chapter 6 have same sensor spacing, but Type 2 resulted in larger localization error (Figure 6.9). The reason of the larger error could be the sensor distribution in the measuring zone. To study the influence of sensor distributions, more sensor layouts need to be included in the simulations.

In Chapter 10, we proposed a method to evaluate the sensor layout in terms of source localization efficiency, which shows that the minimum source amplitude that can be located is related to the sensor positions. In the presented examples in Chapter 10, a more evenly distributed sensor layout can locate more AE events (Figure 10.3). Combining the evaluation of source localization accuracy and efficiency, an optimum sensor positioning strategy is expected.

11.2.3 Improvement of the probability density field of acoustic emission events

In Chapter 6, when calculated the pdAE field, we assumed that the source localization error property is the same in all directions. This assumption applies when no crack presents between source and receiver and the sources are far from the edges of the member. The wave propagation to every direction is not influenced by presence of crack or the edges of the member, thus the error property in each direction can be assumed same. A more accurate estimation of pdAE should account for the anisotropic error properties influenced by the presence of crack and the geometries of the member. To ensure that no crack presents between source and receiver, we designed the sensor spacing to be smaller than the crack spacing so that only one crack formed between two adjacent sensors. However, in practice, this assumption cannot always apply, even with limited sensor spacing. For example, in the presented tests, secondary cracks formed near the major cracks in the bottom part of the beam, leading to two or more cracks between two adjacent sensors. We observed larger source localization errors in the region with secondary cracks. The error properties need to be updated with evolution of cracks.

According to our previous study (Pahlavan, Zhang et al. 2018), a crack between source and receiver has an anisotropic effect on the wave propagation: the arrival times delayed more in the direction perpendicular to the crack than that parallel to the crack. This will lead to anisotropic error properties. The error components in directions perpendicular and parallel to the crack can be studied using the same simulations in the dissertation.

To apply the anisotropic error properties which are related to the crack direction, one needs to know the direction of the crack between source and receiver. This information can be obtained by AE source localization or DIC. In the cases that the crack direction cannot be (accurately) measured, one can combine with the finite element modelling approach to estimate the direction of the crack. Considering the estimated crack path, one can apply the anisotropic error properties from the simulations. And the probability density function of location of AE events can be updated.

11.2.4 Improvement of the source classification criterion

In Chapter 7, we developed a source classification criterion based on peak frequency or partial power observed in the experiments. However, the experiments used the same type of concrete and sensor. Further validations on other types of concrete and sensors are needed for a wider application. Moreover, the criterion was from the frequency spectrum of the received signal, which is influenced by the sensor frequency response. For example, R6I type sensor is more sensitive to signals of 40 kHz than signals at 100 kHz (MISTRAS 2008). The response to the former frequency component is around 1.7 times larger than the latter. To compensate the different sensitivities, one can applying a factor of 0.6 (1/1.7) to the amplitude at 40 kHz. The same applies to other frequency components.

The determination of the peak frequency or partial power has to be adjusted according to the sensor frequency responses. In this way, the criterion is independent of the sensor frequency response.

11.2.5 Extension of the acoustic emission system to other practical conditions

In Chapter 9, we developed a set of AE-based shear failure indicators and evaluated their robustness considering various uncertainties. However, the experiments were carried out in lab conditions, which means that many uncertainties in practice could not be well represented such as the variation of concrete strength, the poor sensor coupling due to surface deterioration, change of environmental conditions etc. To evaluate the influence of the uncertainties in practice and validate the indicators ultimately, a demonstration in real concrete structures is suggested.

Since we found that the indicator (the yellow-light criterion) depends on the shear span and depth ratio in the beam tests, it worth to check if the dependence gets stable with more tests.

Moreover, the indicators can also be extended to other structural types and loading conditions when the structural failure is dependent on the brittle failure of a compressive strut in concrete.

In Chapter 10, we provided a general guidance on implementing the AE-based failure indicators in load testing. This could be extended to long-term monitoring of real structures. Many additional considerations are then needed. For examples, with moving traffic in a long-term monitoring, the regions of strut and tie cannot be accurately determined; sensors need to be well protected, like using embedded sensors smart aggregates; a remote monitoring is needed; and the influence of weather changes needs to be calibrated.

Notations

Roman upper case

$\mathbf{A}$	A set of AE events that occur in the measuring time and space ranges
A (or A_{dB})	Peak amplitude of AE signal in decibels
ΔA_1	Geometric spreading loss during wave propagation
ΔA_2	Material attenuation during wave propagation
E	Dynamic elastic modulus
H	Historic index, and $H(t)$ is the historic index at time t
J	Empirical constant defined in severity index
K	Empirical constant defined in historic index
$L_{x,\mathrm{m}}$	Maximum sensor spacing in x direction
$L_{z,\mathrm{m}}$	Maximum sensor spacing in z direction
N_{e}	Number of acoustic emission events
N_{h}	Number of acoustic emission hits
N_{r}	Total number of sensors
P_{g}	Total number of grid points in the grid search method
P_{m}	Maximum load when the structure fails
P_{u}	Ultimate load when critical flexural shear crack forms
S_{O}	Signal strength, and $S_{\mathrm{O},i}$ is the signal strength of the hit i
S_r	Severity index

Roman lower case

a	Empirical constant defined in b-value analysis
a_{s}	Shear span, which is the distance between the centre of load and support
b	Empirical constant defined in b-value analysis
b_{st}	Width of the compressive strut in the specimen width (y) direction
$b_{\mathrm{st,d}}$	Deteriorated width of the compressive strut in the specimen width (y) direction
c_{P}	Speed of P-waves
c_{R}	Speed of R-waves
c_{S}	Speed of S-waves
d	Wave travel distance
d_{e}	Effective cross section height
$f_{\mathrm{c,cube}}$	Concrete cubic strength
f_{yk}	Reinforcement characteristic yield strength
h	Height of the cross section
$h_{\mathrm{c,eff}}$	Effective concrete tension height
k	Dimension of the AE measuring zone
k_{c}	Inclination of stress line to distribute localized load/deformation to the whole section
l_{cr}	Mean crack spacing along the reinforcement

$l_{x,\mathrm{cr}}$	Distance from the left edge of the measuring zone to the middle of the crack profile in x direction
$l_{z,\mathrm{cr}}$	Distance from the crack bottom to the tip in z direction
n_e	Elastic modulus ratio between steel and concrete
p	Probability density of AE events (pdAE)
r	Source sphere radius
s_cr	Height of the crack after it is stabilized
t	Signal time
$\mathbf{t}_\mathrm{r}$	Signal arrival times, and $t_{\mathrm{r},i}$ is the arrival time at sensor i
t_S	Estimated source time
$t_\mathrm{threshold}$	Arrival time determined by fixed threshold method
t_AIC	Arrival time determined by akaike information criterion (AIC)
Δt	Arrival time picking error
w	Crack width
w_m	Maximum crack width before unloading
w_r	Residual crack width after unloading
w_R	Width of mismatch region at crack faces
w_0	Crack width at onset of pdAE during crack closure
$\mathbf{x}$	Location of a random point in the measuring zone
x_c	Compressive zone height of a cross section
$\mathbf{x}_{\mathrm{g},p}$	Location of grid point p
$\mathbf{x}_\mathrm{g}$	Estimated source location
$\mathbf{x}_\mathrm{r}$	Sensor location, and $\mathbf{x}_{\mathrm{r},i}$ is the location of sensor i
$\mathbf{x}_\mathrm{S}$	Actual source location

Greek upper case

$\boldsymbol{\Delta}$	Source localization error vector, and Δ_i is the error component in the i^{th} direction

Greek lower case

α	Material attenuation factor (except in Chapter 8, describing the proportional relationship between increase of pdAE and mismatch region)
α_c	Crack position factor in longitudinal direction of the beam
α_x	Crack position factor in x direction
α_z	Crack position factor in z direction
γ	Damage ratio of compressive strut width
ρ	Mass density
ρ_s	Reinforcement ratio
υ	Dynamic Poisson's ratio
σ	Standard deviation of source localization error
σ_I	Standard deviation of pdAE for crack opening type I
σ_II	Standard deviation of pdAE for crack opening type II

Appendix A

This appendix shows the crack kinematics and the pdAE at the local points along the selected cracks. The results are used to find the relationship between the pdAE and the crack kinematics during loading in Chapter 8.

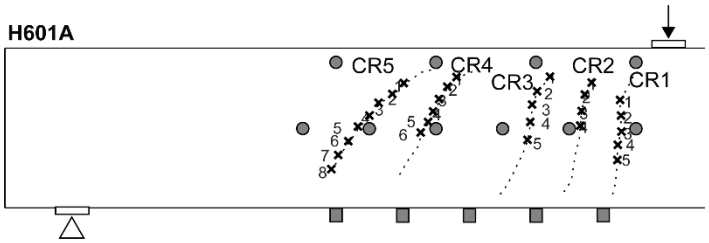

Figure 11.1 Selected local positions along cracks CR1-5 in H601A.

Table A.1 Crack kinematics (w, Δ) and pdAE (p) at local positions in H601A.

Load [kN]			100	140	145	150	160	200	250	300
CR1	w [mm]	1	-0.01	-0.01	0.00	0.04	0.10	0.16	0.16	0.21
		2	-0.01	-0.01	0.04	0.13	0.20	0.22	0.25	0.33
		3	-0.01	0.00	0.08	0.18	0.26	0.29	0.34	0.43
		4	-0.01	0.00	0.12	0.24	0.31	0.35	0.41	0.49
		5	-0.01	0.00	0.15	0.29	0.36	0.39	0.46	0.54
	Δ [mm]	1	0.01	0.03	0.04	0.07	0.09	0.10	0.12	0.13
		2	0.01	0.02	0.03	0.06	0.08	0.10	0.12	0.13
		3	0.01	0.02	0.01	0.01	0.03	0.03	0.03	0.04
		4	0.01	0.02	0.04	0.08	0.11	0.11	0.13	0.14
		5	0.01	0.02	0.04	0.07	0.09	0.10	0.12	0.14
	p [m^{-2}]	1	0.00	2.69	675.20	3312.30	5330.05	6174.33	6494.62	6533.97
		2	0.00	29.49	4667.71	8760.72	10076.17	10510.81	10661.73	10813.84
		3	0.00	154.16	6282.83	8507.62	9028.87	9337.92	9587.75	9687.63
		4	0.00	10.09	2367.53	3667.64	4180.55	4237.34	4294.62	4369.11
		5	0.00	1.77	1541.69	2429.20	2646.98	2647.41	2649.49	2649.73
CR2	w [mm]	1	-0.01	-0.01	0.00	-0.01	-0.01	0.01	0.02	0.03
		2	-0.01	-0.01	0.00	-0.01	-0.01	0.06	0.08	0.11
		3	-0.01	-0.01	-0.01	-0.01	0.00	0.13	0.17	0.19
		4	-0.01	-0.01	-0.01	-0.01	0.00	0.22	0.23	0.28
	Δ [mm]	1	0.01	0.02	0.05	0.09	0.11	0.11	0.11	0.13
		2	0.01	0.03	0.05	0.09	0.11	0.13	0.14	0.17
		3	0.01	0.03	0.03	0.08	0.09	0.14	0.16	0.18
		4	0.01	0.03	0.05	0.08	0.10	0.16	0.18	0.21
	p [m^{-2}]	1	0.00	0.00	204.48	342.09	372.83	3716.57	4427.40	4944.78
		2	0.00	0.00	143.02	203.33	240.26	5418.50	6854.72	7868.87
		3	0.00	0.67	156.97	216.62	456.30	4836.79	6112.71	6571.70
		4	0.00	82.28	583.81	654.55	854.25	3609.64	4513.00	4766.89
CR3	w [mm]	1	-0.01	-0.01	-0.01	-0.01	-0.01	-0.01	0.00	0.03
		2	-0.01	-0.01	0.00	-0.01	-0.01	-0.01	0.11	0.15
		3	0.00	0.00	0.00	0.00	0.00	0.00	0.21	0.25
		4	0.00	0.00	-0.01	-0.01	-0.01	-0.02	0.29	0.34
		5	0.00	0.00	0.00	0.00	0.00	-0.01	0.38	0.45

Appendix A

Load [kN]			100	140	145	150	160	200	250	300
CR3	Δ [mm]	1	0.01	0.03	0.05	0.08	0.11	0.16	0.18	0.21
		2	0.01	0.03	0.05	0.09	0.10	0.15	0.20	0.24
		3	0.01	0.03	0.05	0.08	0.10	0.14	0.25	0.29
		4	0.01	0.03	0.05	0.09	0.10	0.15	0.26	0.31
		5	0.01	0.03	0.04	0.08	0.10	0.14	0.20	0.23
	p [m^{-2}]	1	0.00	0.03	59.76	60.00	106.90	375.85	2345.43	3050.78
		2	0.00	73.47	486.96	572.99	725.49	1270.62	6367.53	7498.40
		3	0.00	35.41	221.14	433.22	771.97	1587.26	12420.59	14306.30
		4	0.00	27.32	153.51	281.02	553.08	2032.86	13283.40	13901.18
		5	0.00	0.00	140.83	339.18	523.03	2198.15	6851.93	7357.74
CR4	w [mm]	1	0.00	-0.01	0.00	0.00	0.00	0.00	0.02	0.10
		2	0.00	-0.01	0.00	0.00	0.00	-0.01	0.01	0.15
		3	0.00	-0.01	0.00	-0.01	-0.01	-0.01	0.07	0.24
		4	-0.01	-0.01	0.00	0.00	0.00	-0.01	0.13	0.33
		5	0.00	-0.02	0.00	-0.01	0.01	0.00	0.17	0.38
		6	0.00	0.00	0.00	0.00	0.00	0.01	0.24	0.42
	Δ [mm]	1	0.01	0.03	0.05	0.09	0.12	0.17	0.26	0.34
		2	0.02	0.03	0.05	0.10	0.13	0.17	0.24	0.32
		3	0.01	0.03	0.05	0.09	0.10	0.14	0.24	0.35
		4	0.01	0.03	0.06	0.09	0.11	0.17	0.26	0.36
		5	0.02	0.03	0.06	0.10	0.12	0.19	0.21	0.31
		6	0.01	0.04	0.05	0.08	0.11	0.16	0.27	0.41
	p [m^{-2}]	1	0.00	0.00	17.98	17.98	18.68	42.10	1621.64	6840.54
		2	0.00	0.00	50.40	50.40	107.08	155.30	4764.50	14050.53
		3	0.00	0.00	0.28	0.35	3.84	43.23	11700.50	18877.43
		4	0.00	0.04	12.90	22.59	22.62	41.54	15283.57	20888.11
		5	0.00	9.26	66.72	112.36	113.20	154.59	9937.03	13349.17
		6	0.00	3.15	140.18	264.22	264.26	388.03	4718.13	7994.15
CR5	w [mm]	1	0.00	-0.01	0.01	-0.01	0.00	0.00	0.01	0.05
		2	0.00	-0.01	0.00	-0.01	-0.01	-0.01	0.03	0.15
		3	0.00	0.00	-0.01	0.00	-0.01	0.00	0.00	0.18
		4	0.00	-0.01	0.00	-0.02	-0.02	-0.01	0.00	0.30
		5	0.00	0.00	0.00	0.00	0.00	-0.01	0.01	0.35
		6	0.00	0.00	0.00	0.00	0.00	0.00	0.01	0.48
		7	0.00	-0.01	-0.01	-0.01	-0.02	-0.01	0.01	0.55
		8	0.00	0.00	-0.01	-0.01	-0.01	-0.01	0.02	0.57
	Δ [mm]	1	0.02	0.04	0.05	0.09	0.11	0.15	0.26	0.33
		2	0.02	0.03	0.06	0.10	0.11	0.17	0.25	0.30
		3	0.01	0.04	0.06	0.10	0.11	0.18	0.28	0.40
		4	0.01	0.03	0.07	0.10	0.12	0.17	0.28	0.35
		5	0.01	0.03	0.05	0.09	0.12	0.14	0.26	0.40
		6	0.01	0.03	0.06	0.09	0.13	0.17	0.28	0.40
		7	0.01	0.03	0.05	0.09	0.11	0.16	0.27	0.48
		8	0.01	0.03	0.06	0.10	0.11	0.16	0.28	0.46
	p [m^{-2}]	1	0.00	0.00	0.00	0.00	0.00	0.00	225.79	4497.62
		2	0.00	0.00	0.00	0.00	0.00	0.00	263.17	4954.12
		3	0.00	0.00	0.00	0.00	0.00	0.00	55.13	3803.84
		4	0.00	0.00	0.06	0.06	0.06	0.07	24.07	8139.52
		5	0.00	0.19	2.34	2.57	2.57	2.62	123.57	7869.45
		6	0.00	1.76	3.85	70.91	70.91	71.02	256.60	8240.39
		7	0.00	17.91	65.24	71.82	71.82	99.13	415.09	8660.84
		8	0.00	0.00	1.40	1.43	1.43	11.87	1469.15	9105.55

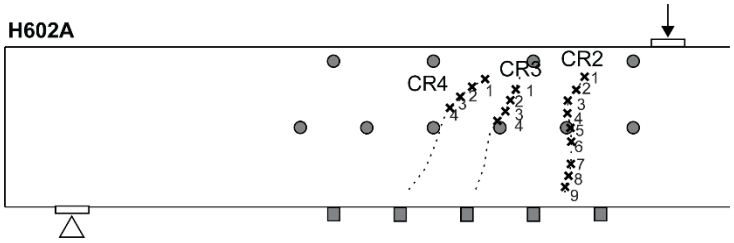

Figure 11.2 Selected local positions along cracks CR2-4 in H602A

Table A.2 Crack kinematics (w, Δ) and pdAE (p) at local positions in H602A.

Load [kN]			100	150	162	175	200	225	250	275	305
CR2	w [mm]	1	0.00	0.00	0.00	0.00	0.01	0.02	0.03	0.03	0.04
		2	0.00	0.00	0.04	0.06	0.07	0.09	0.11	0.14	0.16
		3	0.00	0.00	0.12	0.14	0.16	0.17	0.21	0.23	0.24
		4	0.00	0.01	0.21	0.23	0.28	0.33	0.34	0.39	0.42
		5	0.00	0.00	0.27	0.30	0.34	0.38	0.41	0.46	0.51
		6	0.00	0.00	0.34	0.37	0.42	0.45	0.51	0.55	0.61
		7	0.00	0.01	0.45	0.50	0.55	0.62	0.67	0.74	0.81
		8	0.00	0.01	0.45	0.50	0.55	0.61	0.68	0.75	0.83
		9	0.00	0.00	0.35	0.40	0.43	0.47	0.53	0.58	0.62
	Δ [mm]	1	0.01	0.04	0.05	0.04	0.06	0.08	0.09	0.11	0.10
		2	0.00	0.05	0.05	0.04	0.06	0.09	0.09	0.10	0.11
		3	0.01	0.05	0.09	0.09	0.12	0.17	0.17	0.20	0.21
		4	0.01	0.03	0.04	0.04	0.06	0.11	0.11	0.13	0.14
		5	0.01	0.04	0.06	0.06	0.09	0.12	0.15	0.17	0.18
		6	0.00	0.04	0.08	0.08	0.12	0.13	0.16	0.19	0.19
		7	0.01	0.04	0.01	0.01	0.03	0.04	0.06	0.07	0.07
		8	0.00	0.04	-0.04	-0.05	-0.04	-0.04	-0.04	-0.04	-0.04
		9	0.01	0.04	0.03	0.02	0.04	0.04	0.03	0.03	0.03
	p [m^{-2}]	1	0.00	515.13	2994.26	3534.30	4399.89	5430.39	6172.50	7589.64	8805.10
		2	0.00	1881.26	6275.74	7255.51	8720.16	10076.03	10640.86	12208.99	14322.33
		3	0.00	3261.68	8266.03	9312.66	11130.81	13592.76	14354.87	15899.51	17752.68
		4	0.00	5298.18	9912.05	10344.51	11315.87	13295.41	13815.24	14587.38	15893.36
		5	0.00	6724.55	11520.84	11812.41	12355.72	13068.13	13402.12	14197.72	15169.97
		6	0.00	6974.42	10742.27	10947.36	11673.83	12012.04	12301.50	12913.38	13435.39
		7	0.02	7251.62	10792.02	11220.27	11549.03	12389.27	12814.50	13645.65	14385.90
		8	4.13	5749.14	8586.76	8845.76	9505.59	10068.48	10322.75	10980.26	11319.04
		9	5.82	3306.41	4472.39	4693.92	5488.59	5905.17	6030.35	6471.44	6809.10
CR3	w [mm]	1	0.00	-0.01	0.00	0.01	0.04	0.07	0.13	0.14	0.18
		2	0.00	0.00	0.01	0.03	0.10	0.15	0.22	0.24	0.27
		3	0.00	0.00	0.01	0.07	0.17	0.24	0.32	0.35	0.40
		4	0.00	0.00	0.05	0.13	0.26	0.33	0.43	0.47	0.49

Appendix A

Load [kN]			100	150	162	175	200	225	250	275	305
CR3	Δ [mm]	1	0.01	0.05	0.10	0.09	0.12	0.15	0.19	0.20	0.22
		2	0.01	0.05	0.09	0.09	0.12	0.17	0.20	0.22	0.24
		3	0.01	0.05	0.10	0.09	0.10	0.12	0.12	0.16	0.18
		4	0.01	0.05	0.10	0.08	0.11	0.16	0.18	0.20	0.23
	p [m^{-2}]	1	0.00	528.10	864.03	2238.30	6502.37	10742.23	13156.87	15109.24	15994.13
		2	0.00	275.44	1982.46	6704.42	12864.42	16226.45	17818.53	18406.09	19230.13
		3	0.00	66.90	2055.06	7200.18	12165.63	16268.95	17697.00	18656.98	19664.66
		4	0.00	191.66	3368.73	8234.31	12133.22	15144.68	17307.66	18148.49	19147.82
CR4	w [mm]	1	0.00	0.00	0.01	0.03	0.02	0.03	0.03	0.04	0.08
		2	0.00	0.01	0.01	0.01	0.01	0.03	0.03	0.03	0.17
		3	0.00	-0.01	0.00	0.01	0.01	0.01	0.00	0.06	0.28
		4	-0.01	-0.01	-0.01	-0.02	-0.01	-0.01	0.02	0.12	0.38
	Δ [mm]	1	0.01	0.06	0.11	0.14	0.17	0.21	0.24	0.25	0.27
		2	0.01	0.06	0.09	0.13	0.16	0.20	0.22	0.24	0.28
		3	0.01	0.05	0.09	0.12	0.16	0.19	0.22	0.24	0.29
		4	0.01	0.06	0.11	0.14	0.18	0.23	0.25	0.31	0.42
	p [m^{-2}]	1	0.00	281.74	432.98	747.88	1319.32	1625.14	1999.51	3364.42	9608.64
		2	0.00	270.56	385.88	579.73	989.74	1113.49	2031.44	5309.11	11486.76
		3	0.00	31.20	184.93	634.72	699.54	832.38	2705.57	9504.75	15784.53
		4	0.00	59.95	426.61	964.50	1143.57	1307.34	5424.06	12631.81	18953.79

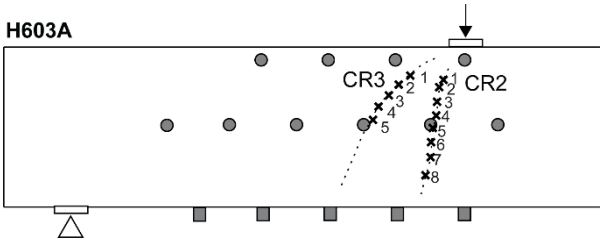

Figure 11.3 Selected local positions along cracks CR2-3 in H603A.

Table A.3 Crack kinematics (w, Δ) and pdAE (p) at local positions in H603A.

Load [kN]			150	185	199	200	230	250	270	300	350	400	450	500	550
CR2	w [mm]	1	0.00	0.00	0.03	0.03	0.10	0.13	0.10	0.12	0.13	0.13	0.15	0.17	0.22
		2	0.01	0.01	0.05	0.07	0.18	0.19	0.15	0.19	0.20	0.22	0.26	0.29	0.35
		3	0.01	0.07	0.13	0.14	0.26	0.27	0.24	0.28	0.32	0.37	0.40	0.45	0.53
		4	0.01	0.13	0.21	0.23	0.38	0.38	0.34	0.39	0.45	0.48	0.55	0.60	0.71
		5	0.01	0.19	0.28	0.31	0.46	0.48	0.42	0.50	0.55	0.62	0.67	0.75	0.88
		6	0.00	0.25	0.32	0.34	0.51	0.52	0.49	0.57	0.64	0.71	0.80	0.87	1.03
		7	0.01	0.32	0.41	0.44	0.55	0.59	0.53	0.62	0.71	0.78	0.85	0.95	1.10
		8	0.00	0.38	0.43	0.47	0.52	0.56	0.52	0.62	0.69	0.77	0.85	0.96	1.12
	Δ [mm]	1	0.03	0.06	0.07	0.08	0.08	0.07	0.05	0.06	0.07	0.11	0.13	0.15	0.15
		2	0.03	0.06	0.08	0.10	0.14	0.16	0.11	0.11	0.13	0.17	0.21	0.23	0.28
		3	0.03	0.06	0.10	0.12	0.18	0.18	0.11	0.14	0.16	0.19	0.23	0.26	0.31
		4	0.03	0.04	0.07	0.08	0.09	0.11	0.05	0.05	0.08	0.09	0.12	0.15	0.18
		5	0.03	0.08	0.13	0.13	0.17	0.18	0.12	0.13	0.17	0.19	0.22	0.26	0.31
		6	0.03	0.11	0.16	0.18	0.22	0.23	0.15	0.18	0.22	0.25	0.30	0.35	0.40
		7	0.03	0.04	0.07	0.08	0.07	0.08	0.02	0.02	0.03	0.04	0.07	0.09	0.11
		8	0.03	0.08	0.10	0.12	0.09	0.08	0.04	0.04	0.05	0.09	0.10	0.12	0.14
	p [m^{-2}]	1	232.14	1214.49	2021.53	2316.28	3142.66	4338.95	4602.89	4873.23	4880.60	5066.79	5075.36	5089.64	5754.52
		2	376.10	1690.84	2370.06	2750.14	3482.45	4503.57	4635.16	4834.09	4850.48	4965.13	4966.00	4983.66	5513.31
		3	286.39	2710.93	3355.99	3961.02	4738.06	4926.18	4928.03	5092.39	5124.21	5139.30	5139.36	5141.90	5385.33
		4	360.05	2636.35	3272.51	3622.15	4089.66	4324.27	4324.52	4342.98	4394.89	4481.52	4518.99	4569.24	4682.63
		5	444.69	3261.39	3586.58	3873.57	4330.09	4603.09	4603.10	4603.18	4665.67	4798.82	4944.84	4976.83	5440.11
		6	930.76	3631.41	3932.84	4281.25	4498.64	4574.28	4575.04	4575.55	4672.49	4855.36	4959.52	5056.69	5508.63
		7	1572.70	4361.52	4498.37	4819.71	5122.79	5173.53	5357.83	5455.03	5572.87	5777.78	5823.92	5897.12	6222.73
		8	1320.03	3641.62	3884.70	4037.64	4075.11	4128.17	4639.74	4757.33	5249.12	5456.89	5594.19	5707.85	6309.47
CR3	w [mm]	1	0.00	0.00	-0.01	-0.02	-0.02	0.22	1.50	2.12	2.47	2.80	3.16	3.55	4.12
		2	-0.01	-0.01	-0.02	-0.01	0.01	0.31	1.66	2.33	2.70	3.08	3.44	3.87	4.51
		3	0.00	-0.01	-0.01	0.00	0.07	0.40	2.03	2.80	3.22	3.68	4.13	4.63	5.38
		4	0.00	0.00	0.00	0.01	0.16	0.50	1.93	2.62	3.01	3.40	3.80	4.24	4.93
		5	0.00	0.00	0.00	0.01	0.23	0.65	2.15	1.63	1.75	1.82	1.74	1.71	1.71

Appendix A

Load [kN]			150	185	199	200	230	250	270	300	350	400	450	500	550
CR3	Δ [mm]	1	0.05	0.09	0.10	0.13	0.16	0.23	0.71	1.06	1.25	1.48	1.69	1.96	2.30
		2	0.05	0.08	0.09	0.13	0.15	0.28	1.03	1.52	1.80	2.10	2.38	2.72	3.18
		3	0.04	0.09	0.10	0.12	0.14	0.27	1.07	1.57	1.84	2.13	2.44	2.79	3.24
		4	0.05	0.10	0.11	0.13	0.21	0.49	1.82	2.64	3.10	3.57	4.02	4.55	5.33
		5	0.05	0.10	0.11	0.14	0.18	0.38	1.39	0.92	0.99	1.09	1.18	1.33	1.48
	p [m^{-2}]	1	4.23	46.28	105.28	105.37	3100.09	1202 9.67	1265 5.32	1274 4.28	1280 5.69	1299 7.61	1310 4.34	1327 1.05	1366 0.90
		2	146.54	434.35	591.52	596.70	7973.81	1381 9.88	1453 0.51	1492 5.33	1508 1.15	1569 7.09	1576 7.65	1590 6.90	1599 6.76
		3	347.81	1067.16	1351.62	1456.02	7728.88	1455 5.26	1606 7.86	1688 9.83	1703 9.35	1787 1.00	1795 5.92	1809 5.76	1818 5.04
		4	854.10	1585.73	1905.43	1953.94	6664.78	1210 8.25	1276 6.20	1353 8.71	1359 6.13	1368 8.37	1410 9.03	1497 7.27	1620 8.73
		5	468.33	1607.70	1734.20	1803.76	5449.34	9419.74	1055 3.06	1126 2.06	1126 3.36	1133 7.21	1183 0.23	1320 7.50	1550 7.61

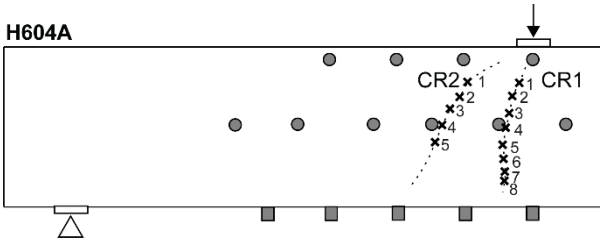

Figure 11.4 Selected local positions along cracks CR1-2 in H604A.

Table A4 Crack kinematics (w, Δ) and pdAE (p) at local positions in H604A.

Load [kN]			150	160	173	190	200	225	250	267	333	400	450
CR1	w [mm]	1	0.00	0.08	0.10	0.14	0.15	0.17	0.20	0.17	0.21	0.21	0.23
		2	0.02	0.20	0.23	0.28	0.30	0.35	0.38	0.37	0.42	0.46	0.49
		3	0.09	0.34	0.40	0.45	0.51	0.58	0.62	0.56	0.64	0.75	0.79
		4	0.12	0.44	0.53	0.59	0.64	0.73	0.77	0.72	0.84	0.97	1.02
		5	0.19	0.54	0.64	0.70	0.75	0.82	0.87	0.84	0.99	1.13	1.19
		6	0.23	0.52	0.58	0.61	0.63	0.69	0.74	0.73	0.85	0.97	1.03
		7	0.24	0.47	0.50	0.53	0.56	0.59	0.65	0.64	0.74	0.86	0.92
		8	0.23	0.38	0.42	0.43	0.47	0.50	0.54	0.53	0.60	0.71	0.76
	Δ [mm]	1	0.01	0.02	0.05	0.08	0.10	0.11	0.13	0.03	0.05	0.05	0.07
		2	0.01	0.07	0.11	0.15	0.18	0.23	0.24	0.11	0.13	0.17	0.17
		3	-0.01	0.04	0.08	0.13	0.15	0.20	0.21	0.09	0.10	0.11	0.13
		4	0.02	0.06	0.12	0.17	0.19	0.24	0.26	0.12	0.14	0.16	0.18
		5	0.03	0.12	0.17	0.23	0.25	0.31	0.33	0.16	0.21	0.25	0.27
		6	0.01	0.06	0.10	0.12	0.15	0.19	0.20	0.05	0.10	0.10	0.13
		7	0.02	0.09	0.12	0.15	0.16	0.21	0.23	0.09	0.14	0.15	0.18
		8	-0.01	0.01	0.04	0.06	0.07	0.11	0.11	-0.01	0.01	0.01	0.03
	p [m^{-2}]	1	171.09	2250.94	2982.52	3686.93	4566.37	6384.48	6796.13	7634.12	8490.60	9849.47	11084.43
		2	1833.78	3762.52	4517.07	5449.96	5929.94	6724.65	7225.39	7562.06	7832.81	8276.03	8688.79
		3	3041.62	4589.99	5295.46	6210.25	6458.55	6794.03	6952.58	7022.80	7068.68	7316.20	7338.86
		4	3597.44	4771.59	5070.22	5422.72	6039.14	6415.56	6459.58	6474.59	6574.44	6684.17	6978.90
		5	2861.95	3823.91	4515.36	5122.07	5358.60	5704.00	5841.77	5849.80	6127.81	6442.06	6686.16
		6	1683.50	2668.75	3009.90	3621.62	4112.49	4376.25	4663.87	4665.57	4944.61	5240.54	5468.22
		7	2144.16	2446.35	2640.51	3024.12	3274.32	4385.00	4494.57	4624.51	4752.37	4937.47	5060.06
		8	2640.42	3274.00	3575.07	3966.60	4246.62	5567.54	5788.00	5870.30	5998.50	6061.21	6316.24

Appendix A

Load [kN]			150	160	173	190	200	225	250	267	333	400	450
CR2	w (mm)	1	0.01	0.00	-0.01	0.00	-0.01	0.00	0.05	2.72	3.37	4.08	4.55
		2	0.00	-0.01	-0.01	-0.02	-0.02	0.02	0.16	3.79	4.70	5.69	6.37
		3	0.00	0.00	-0.01	0.01	-0.01	0.11	0.26	0.52	0.46	0.42	0.42
		4	0.00	0.00	-0.02	0.00	-0.02	0.19	0.35	0.35	0.33	0.32	0.33
		5	0.00	-0.01	-0.01	-0.02	-0.01	0.27	0.42	0.42	0.43	0.45	0.47
	Δ [mm]	1	0.02	0.06	0.10	0.14	0.17	0.19	0.20	3.30	4.19	5.24	6.07
		2	0.03	0.07	0.11	0.16	0.16	0.19	0.22	2.78	3.55	4.45	5.17
		3	0.03	0.08	0.11	0.16	0.18	0.22	0.27	0.52	0.57	0.59	0.63
		4	0.03	0.09	0.11	0.14	0.17	0.22	0.29	0.25	0.29	0.33	0.35
		5	0.03	0.09	0.12	0.15	0.16	0.22	0.29	0.24	0.28	0.32	0.34
	p [m^{-2}]	1	1.71	107.03	380.39	576.27	662.35	1253.20	5913.17	6874.97	6875.02	6908.74	6918.42
		2	13.78	134.50	607.84	1011.10	1034.77	4433.51	8779.11	9287.86	9293.04	9316.71	9400.53
		3	43.51	358.57	1136.19	1579.23	1661.06	6473.08	8345.31	8573.63	8575.39	8663.30	8821.93
		4	29.80	1018.27	1927.52	2700.40	3632.39	5756.55	7619.12	8143.41	8143.81	8162.52	8289.81
		5	62.51	848.75	2591.43	3576.28	4279.45	7444.29	9089.55	9484.64	9560.32	9786.32	9951.45

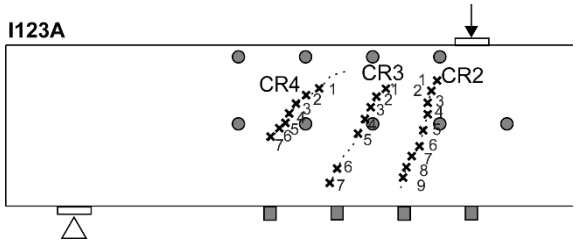

Figure 11.5 Selected local positions along cracks CR2-4 in I123A.

Table A.5 Crack kinematics (w, Δ) and pdAE (p) at local positions in I123A.

Load [kN]			180	190	200	210	220	230	240	250	260	270	280	290	300
CR2	w [mm]	1	0.01	0.00	0.01	0.07	0.02	0.07	0.06	0.07	0.07	0.07	0.08	0.08	0.08
		2	0.01	0.02	0.03	0.11	0.07	0.12	0.12	0.13	0.14	0.13	0.15	0.15	0.15
		3	0.02	0.06	0.09	0.16	0.12	0.18	0.17	0.19	0.19	0.19	0.20	0.20	0.20
		4	0.05	0.11	0.13	0.22	0.20	0.23	0.24	0.25	0.25	0.26	0.26	0.28	0.27
		5	0.10	0.15	0.17	0.29	0.27	0.30	0.31	0.31	0.32	0.32	0.33	0.34	0.35
		6	0.13	0.16	0.19	0.32	0.30	0.32	0.34	0.33	0.36	0.36	0.36	0.37	0.39
		7	0.17	0.22	0.26	0.38	0.36	0.40	0.41	0.41	0.42	0.44	0.44	0.46	0.47
		8	0.17	0.24	0.28	0.39	0.38	0.41	0.43	0.44	0.45	0.45	0.47	0.48	0.48
		9	0.18	0.23	0.24	0.32	0.30	0.34	0.33	0.36	0.35	0.34	0.37	0.37	0.38
	Δ [mm]	1	0.04	0.04	0.04	-0.01	0.00	0.00	0.01	0.01	0.00	0.01	0.01	0.02	0.02
		2	0.03	0.04	0.04	0.01	0.03	0.03	0.04	0.04	0.04	0.04	0.04	0.05	0.06
		3	0.04	0.06	0.06	0.06	0.09	0.09	0.10	0.09	0.10	0.11	0.11	0.11	0.13
		4	0.04	0.04	0.04	0.02	0.04	0.04	0.05	0.04	0.05	0.05	0.05	0.05	0.07
		5	0.04	0.06	0.06	0.05	0.07	0.06	0.07	0.07	0.08	0.09	0.09	0.09	0.11
		6	-0.01	-0.02	-0.02	-0.07	-0.06	-0.06	-0.05	-0.07	-0.06	-0.05	-0.07	-0.07	-0.06
		7	0.01	0.02	0.01	0.01	0.02	0.02	0.02	0.01	0.02	0.03	0.02	0.02	0.02
		8	0.05	0.05	0.04	0.06	0.06	0.06	0.07	0.07	0.07	0.08	0.08	0.08	0.09
		9	0.06	0.05	0.06	0.07	0.07	0.06	0.07	0.07	0.09	0.08	0.09	0.09	0.10
	p [m^{-2}]	1	172	322	371	468	625	662	662	844	872	967	1080	1113	1256
		2	357	552	883	910	1081	1165	1165	1324	1558	1621	1740	1765	1948
		3	632	1412	2741	2832	2974	3170	3187	3592	3846	3874	3949	4244	4348
		4	957	1724	3096	3128	3386	3579	3739	4022	4176	4267	4275	4378	4491
		5	1742	2337	3848	3851	3969	4018	4086	4344	4786	4820	4976	5159	5210
		6	2419	3490	4662	4730	4867	4886	4903	5156	5471	5613	5692	5812	5819
		7	2262	3225	4286	4339	4637	4642	4646	4750	4907	4996	5025	5044	5100
		8	1434	2162	2904	2921	3098	3102	3104	3303	3447	3456	3586	3657	3722
		9	1721	2555	3266	3306	3586	3676	3686	3841	3975	4026	4080	4216	4228
CR3	w [mm]	1	0.01	0.01	0.00	0.02	-0.02	0.01	0.01	0.01	0.01	0.00	0.03	0.06	0.05
		2	0.01	0.00	0.00	0.02	-0.01	0.03	0.03	0.03	0.06	0.06	0.10	0.11	0.11
		3	0.00	0.00	0.00	0.02	0.00	0.07	0.07	0.09	0.12	0.11	0.16	0.17	0.18
		4	0.00	0.00	0.01	0.06	0.04	0.11	0.13	0.14	0.18	0.18	0.24	0.26	0.27
		5	0.00	0.00	0.00	0.11	0.10	0.18	0.20	0.21	0.25	0.27	0.32	0.34	0.36
		6	0.00	0.00	0.00	0.22	0.21	0.28	0.28	0.29	0.32	0.31	0.33	0.33	0.33
		7	0.02	0.01	0.02	0.22	0.22	0.26	0.26	0.28	0.27	0.29	0.29	0.30	0.31
	Δ [mm]	1	0.04	0.06	0.07	0.03	0.04	0.04	0.05	0.04	0.04	0.05	0.05	0.05	0.06
		2	0.05	0.07	0.07	0.04	0.05	0.03	0.05	0.07	0.08	0.08	0.09	0.10	0.10
		3	0.05	0.06	0.06	0.04	0.06	0.05	0.06	0.08	0.10	0.08	0.11	0.10	0.12
		4	0.05	0.05	0.06	0.04	0.06	0.06	0.07	0.07	0.08	0.08	0.09	0.10	0.13
		5	0.06	0.06	0.07	0.06	0.07	0.08	0.10	0.09	0.11	0.12	0.14	0.14	0.15
		6	0.05	0.07	0.08	0.09	0.10	0.11	0.11	0.13	0.13	0.13	0.14	0.14	0.14
		7	0.06	0.07	0.07	0.12	0.12	0.14	0.13	0.15	0.16	0.16	0.16	0.16	0.17

Load [kN]			180	190	200	210	220	230	240	250	260	270	280	290	300
CR3	p [m^{-2}]	1	137	138	138	138	156	613	649	980	2076	2446	2667	3553	3896
		2	19	27	27	27	124	985	1021	1787	2975	3424	3692	4583	4871
		3	0	4	4	10	346	943	1167	2316	2941	3358	3514	4275	4485
		4	3	22	102	373	672	1632	2021	2869	3369	3763	3810	4386	4463
		5	44	178	184	547	1206	2505	2526	2650	3232	3757	3908	4280	4314
		6	28	114	124	459	773	1403	1614	2105	2589	2637	2912	3252	3265
		7	46	68	184	828	1102	1513	1652	1897	1953	2019	2060	2292	2292
CR4	w [mm]	1	-0.01	-0.02	-0.01	-0.04	-0.07	-0.05	-0.05	-0.05	-0.06	-0.06	-0.04	-0.06	-0.05
		2	-0.01	-0.02	-0.02	-0.04	-0.08	-0.06	-0.06	-0.05	-0.06	-0.07	-0.07	-0.05	-0.05
		3	0.00	-0.02	-0.01	-0.04	-0.07	-0.06	-0.05	-0.05	-0.05	-0.06	-0.05	-0.04	-0.03
		4	-0.02	-0.01	-0.01	-0.04	-0.07	-0.06	-0.06	-0.04	-0.05	-0.06	-0.03	-0.01	0.01
		5	0.00	-0.01	-0.01	-0.03	-0.06	-0.04	-0.05	-0.04	-0.05	-0.05	0.03	0.04	0.05
		6	-0.01	-0.01	-0.01	-0.04	-0.08	-0.05	-0.05	-0.05	-0.07	-0.06	0.04	0.05	0.08
		7	0.00	-0.01	-0.01	-0.03	-0.07	-0.05	-0.04	-0.03	-0.04	-0.06	0.08	0.11	0.14
	Δ [mm]	1	0.05	0.06	0.07	0.06	0.08	0.08	0.10	0.11	0.10	0.11	0.12	0.14	0.13
		2	0.06	0.06	0.07	0.06	0.07	0.09	0.10	0.10	0.11	0.12	0.13	0.13	0.12
		3	0.06	0.07	0.07	0.08	0.08	0.10	0.11	0.10	0.12	0.12	0.12	0.12	0.15
		4	0.05	0.07	0.07	0.08	0.09	0.09	0.11	0.10	0.12	0.11	0.13	0.16	0.15
		5	0.06	0.06	0.07	0.09	0.09	0.10	0.11	0.11	0.12	0.12	0.12	0.11	0.11
		6	0.06	0.07	0.08	0.10	0.11	0.12	0.13	0.12	0.14	0.14	0.14	0.14	0.16
		7	0.06	0.06	0.08	0.10	0.11	0.12	0.13	0.12	0.14	0.14	0.14	0.16	0.16
	p [m^{-2}]	1	64.20	64.20	64.20	64.20	64.20	143.92	143.92	143.92	151.62	151.63	151.63	11853.27	25972.85
		2	125.97	125.97	125.97	125.97	125.97	247.32	247.32	247.41	320.41	329.96	342.35	15889.21	24597.85
		3	2.84	2.84	2.84	2.84	2.85	186.30	186.30	197.50	406.20	566.25	662.76	17106.04	22571.10
		4	48.37	48.37	48.37	48.37	58.31	140.39	140.39	161.09	1251.66	1422.55	1451.20	13116.51	16537.54
		5	130.50	130.50	130.50	130.50	164.32	167.86	167.86	195.92	1375.59	2168.37	2310.41	13997.88	18197.49
		6	105.95	105.95	105.95	105.95	122.00	125.18	125.18	133.96	1997.84	3212.31	3391.95	14112.65	17307.58
		7	32.18	32.18	32.29	32.29	34.85	101.91	101.91	109.35	1599.87	2501.95	2554.71	10600.42	13294.85

Appendix B

This appendix includes the Matlab code that realizes the pdAE field method. The code starts with grid search method to estimate the source location. Then using the estimated source, the code calculates the probability density field of AE events. Other codes related to this dissertation can be found in https://gitlab.tudelft.nl/fzhang9/fengqiao-zhang-phd-project.

Part I: grid search method

The inputs are arrival times, sensor locations, wave speed

The outputs are source locations

The code is:

```
%% define the grid mesh that covers the sensor enclosed zone
% Sensor.x is an array of x coordinates of all sensors
% Sensor.y is an array of y coordinates of all sensors
% Sensor.z is an array of z coordinates of all sensors
gd  = 20; % [mm] define the spacing between grid points
gx  = (min(Sensor.x)-gd/2:gd:max(Sensor.x)+gd/2);
gy  = (min(Sensor.y)-gd/2:gd:max(Sensor.y)+gd/2);
gz  = (min(Sensor.z)-gd/2:gd:max(Sensor.z)+gd/2);
n   = length(gx)*length(gy)*length(gz);
sz  = [length(gx),length(gy),length(gz)];
[GX,GY,GZ] = ind2sub(sz,1:n);
Grid.x  = gx(GX); % an array of x of all grids
Grid.y  = gy(GY); % an array of y of all grids
Grid.z  = gz(GZ); % an array of z of all grids

%% calculate the distance between each grid point and each sensor
dgs  = sqrt((Sensor.x-Grid.x).^2+(Sensor.y-Grid.y).^2+(Sensor.z-
Grid.z).^2); % a matrix includes the distance between each grid
point and each sensor, every row is the distance between a sensor
to all the grid points.

%% calculate the source locations
function [res,idmin] = AE_src_loc_v4(dgs,t,cp)
% The input variables are:
% dgs—the matrix of the distance between each sensor and each
grid point in [mm]
% t—the array of arrival times at sensors of one AE event in [s]
% cp—the wave speed in [m/s]
% The output variables are:
% r—an array of the residuals between estimated distance differ-
ence and the actual distance difference at all grid points, which
is the value of r in Equation (4.9) in [mm]
% idmin—the grid point that has the minimum residual which is se-
lected as the source location
```

```
d         = cp.*t*1000;  % [mm]
[ns,ng]   = size(dgs);
r         = zeros(1,ng);
for ii = 1: ns-1
    for jj = ii+1:ns
        ri  = sqrt((dgs(ii,:)-dgs(jj,:)-(d(ii)-d(jj))).^2);
        r   = r+ri;
    end
end
[~,idmin]  = min(r); % the grid point with the minimum residual
end
sloc  = [Grid.x(idmin) Grid.y(idmin) Grid.z(idmin)]; % the esti-
mated source location
```

Part II: pdAE field method

The inputs are source locations and standard deviation of localization error component.

The output is the probability density field of AE events.

The code is:

```
%% define the error properties
mu = [0 0 0]; % [mm] an array of mean value of localization error
in x, y and z directions
sg = 55; % [mm] an array of standard deviation of localization
error in x, y and z directions
Sigma = [sg 0 0; 0 sg 0;0 0 sg].^2;

%% define the discrete points in the pdAE field
igd  = 25; %[mm] point spacing
igx  = min(Sensor.x)+igd/2:igd:max(Sensor.x)-igd/2;
igy  = min(Sensor.y)+igd/2:igd:max(Sensor.y)-igd/2;
igz  = min(Sensor.z)+igd/2:igd:max(Sensor.z)-igd/2;
in   = length(igx)*length(igy)*length(igz);
isz  = [length(igx),length(igy),length(igz)];
[iGX,iGY,iGZ] = ind2sub(isz,1:in);

iGrid.x  = igx(iGX); % an array of x of all points
iGrid.y  = igy(iGY); % an array of y of all points
iGrid.z  = igz(iGZ); % an array of z of all points
iGrid.sz = isz;

%% calculate probability density field for each source
% The input variable is the source location sloc from Part I.
% Here the sloc can be a matrix that include locations of
% multiple AE events. Every row is the coordinates of
% one AE event.

prob  = zeros(size(sloc,1),length(iGrid.x)); % create the matrix
that includes the pdAE field of each AE event. Every row is the
pdAE field of one AE event.
for jj = 1:size(sloc,1)
```

```
    % calculate the relevant position of each image grid point
    % and each located event
    rloc  = [iGrid.x'-loc(jj,1) iGrid.y'-loc(jj,2) iGrid.z'-
loc(jj,3)];
    % calculate the pdAE at each grid point
    pb    = mvnpdf(rloc,mu,Sigma);
    prob(jj,:)  = pb';
end
% for multiple AE events, the pdAE field adds up.
probsum  = cumsum(prob); % the cumulative pdAE field of multiple
AE events.
```

Reference

AASHTO (2018). The manual for bridge evaluation. Washington, DC, USA, AASHTO.

Abdelrahman, M. (2013). Assessment of Damage in Concrete Structures Using Acoustic Emission, Master thesis, University of South Carolina.

Abell, M. L. L., J. P. Braselton, J. A. Rafter and J. A. Rafter (1999). Statistics with Mathematica, Elsevier Science.

Achenbach, J. (2012). Wave propagation in elastic solids, Elsevier.

ACI-ASCE Committee 426 (1973). "The Shear Strength of Reinforced Concrete Members." Journal of the Structural Division, ASCE **99**(6): 1091-1187.

ACI-ASCE Committee 445 (1998). "Recent Approaches to Shear Design of Structural Concrete." Journal of Structural Engineering, ASCE **124**(12): 1375-1417.

ACI Committee 437 (2013). Code requirenments for Load Testing of Existing Concrete Structures (ACI 437.2M-13) and Commentary. Farmington Hills, MI, American Concrete Institute.

Aggelis, D. G. (2011). "Classification of cracking mode in concrete by acoustic emission parameters." Mechanics Research Communications **38**(3): 153-157.

Aggelis, D. G., T. Shiotani, A. Papacharalampopoulos and D. Polyzos (2011). "The influence of propagation path on elastic waves as measured by acoustic emission parameters." Structural Health Monitoring **11**(3): 359-366.

Aggelis, D. G., D. V. Soulioti, E. A. Gatselou, N. M. Barkoula and T. E. Matikas (2013). "Monitoring of the mechanical behavior of concrete with chemically treated steel fibers by acoustic emission." Construction and Building Materials **48**: 1255-1260.

ASTM E976-15 (2015). Standard Guide for Determining the Reproducibility of Acoustic Emission Sensor Response. West Conshohocken, PA, USA, ASTM.

ASTM E1106-86 (1997). Standard Method for Primary Calibration of Acoustic Emission Sensors. West Conshohocken, PA, USA, ASTM.

Barat, V., Y. Borodin and A. Kuzmin (2010). "Intelligent Acoustic Emission Signal Filtering Methods." Journal of Acoustic Emission **28**.

Barbara, G., Ś. Grzegorz, T. Wiesław and K. Aleksandra (2012). Application of the acoustic emission (AE) method to bridge testing and diagnostics comparison of procedures. Proceedings of the IEEE 2012 Prognostics and System Health Management Conference (PHM-2012 Beijing).

Bayane, I. and E. Brühwiler (2020). "Structural condition assessment of reinforced-concrete bridges based on acoustic emission and strain measurements." Journal of Civil Structural Health Monitoring **10**(5): 1037-1055.

Bedford, A. and D. Drumheller (1994). Introduction to Elastic Wave Propagation, Wiley.

Benedetti, M. D. and A. Nanni (2014). "Acoustic Emission Intensity Analysis for In Situ Evaluation of Reinforced Concrete Slabs." Journal of Materials in Civil Engineering **26**(1): 6-13.

Benitez, K., E. O. L. Lantsoght and Y. Yang (2018). Development of a Stop Criterion for Load Tests based on the Critical Shear Displacement Theory. International Association for Life-Cycle Civil Engineering (IALCCE), Gent, Belgium.

Bormann, P., B. Engdahl and R. Kind (2012). Seismic Wave Propagation and Earth models. New Manual of Seismological Observatory Practice 2 (NMSOP2). P. Bormann, GFZ German Research Centre for Geosciences.

CARP (1987). Recommended practice for acoustic emission of fiberglass reinforced plastic resin (RP) tanks/vessels, Composites Institute Society of the Plastics Industry New York.

Carpinteri, A., M. Corrado and G. Lacidogna (2013). "Heterogeneous materials in compression: Correlations between absorbed, released and acoustic emission energies." Engineering Failure Analysis **33**: 236-250.

Carpinteri, A., G. Lacidogna, M. Corrado and E. Di Battista (2016). "Cracking and crackling in concrete-like materials: A dynamic energy balance." Engineering Fracture Mechanics **155**: 130-144.

Carter, G. and J. Ferrie (1979). "A coherence and cross spectral estimation program." Programs for digital signal processing: 1-2.3.

CEN (2003). Eurocode 1: Actions on structures - Part 2: Traffic loads on bridges. EN 1991-2:2003 (E). Brussels, Belgium, Comité Européen de Normalisation.

CEN (2004). Eurocode 2: Design of Concrete Structures - Part 1-1: General Rules and Rules for Buildings. EN 1992-1-1:2004 (E). Brussels, Belgium, Comité Européen de Normalisation.

Chai, H. K., S. Momoki, Y. Kobayashi, D. G. Aggelis and T. Shiotani (2011). "Tomographic reconstruction for concrete using attenuation of ultrasound." Ndt & E International **44**(2): 206-215.

Chana, P. S. (1987). "Investigation of the mechanism of shear failure of reinforced concrete beams." Magazine of Concrete Research **39**(141): 196-204.

Chang, P. C. and S. C. Liu (2003). "Recent Research in Nondestructive Evaluation of Civil Infrastructures." Journal of Materials in Civil Engineering **15**(3): 298-304.

Chateau, C., L. Gélébart, M. Bornert, J. Crépin, E. Boller, C. Sauder and W. Ludwig (2011). "In situ X-ray microtomography characterization of damage in SiCf/SiC minicomposites." Composites Science and Technology **71**(6): 916-924.

Cheng, H., F. Zhang, Y. Yang and C. B. M. Blom (2022). Monitoring of Repaired Concrete Floor in the Maastunnel Using Smart Aggregates. 11th International Conference on Bridge Maintenance, Safety and Management (IABMAS), Barcelona, Spain.

Choi, H., G. Palacios, J. S. Popovics and S. H. Chao (2018). "Monitoring Damage in Concrete Columns Using Ultrasonic Tomography." ACI Structural Journal **115**(2): 545-558.

Christenson, J. (2019). Chapter Three - Sensors and Transducers. Handbook of Biomechatronics. J. Segil, Academic Press**:** 61-93.

Clark, M. R., D. M. McCann and M. C. Forde (2003). "Application of infrared thermography to the non-destructive testing of concrete and masonry bridges." NDT & E International **36**(4): 265-275.

Classen, M. (2020). "Shear Crack Propagation Theory (SCPT) – The mechanical solution to the riddle of shear in RC members without shear reinforcement." Engineering Structures **210**: 110207.

Collins, M. (1978). "Towards a Rational Theory for RC Members in Shear." Journal of the Structural Division **104**: 649-666.

Colombo, I. S., I. G. Main and M. C. Forde (2003). "Assessing Damage of Reinforced Concrete Beam Using "b-value" Analysis of Acoustic Emission Signals." Journal of Materials in Civil Engineering **15**(3): 280-286.

Colombo, S., M. Forde, I. Main, J. Halliday and M. Shigeishi (2005). "AE energy analysis on concrete bridge beams." Materials and Structures **38**: 851-856.

Colombo, S., M. C. Forde, I. G. Main and M. Shigeishi (2005). "Predicting the ultimate bending capacity of concrete beams from the "relaxation ratio" analysis of AE signals." Construction and Building Materials **19**(10): 746-754.

Deng, L. and C. Cai (2007). "Applications of fiber optic sensors in civil engineering." Structural Engineering and Mechanics **25**: 577-596.

Deutscher Ausschuss für Stahlbeton (2000). DAtStb-Guideline: Load Tests on Concrete Structures (in German) DAfStb-Richtlinie : Belastungsversuche an Betonbauwerken. Berlin, Germany, DAfStb.

Dryver R. Huston, R. L. W. I. I. M. M. D. and P. Mauricio (2021). "Acoustic Emission Monitoring of Prestressed Girders during Fabrication and Transport." ACI Structural Journal **118**(2).

Farhidzadeh, A., E. Dehghan-Niri, S. Salamone, B. Luna and A. Whittaker (2013). "Monitoring Crack Propagation in Reinforced Concrete Shear Walls by Acoustic Emission." Journal of Structural Engineering **139**(12): 04013010.

Farhidzadeh, A., S. Salamone, B. Luna and A. Whittaker (2013). "Acoustic emission monitoring of a reinforced concrete shear wall by b-value–based outlier analysis." Structural Health Monitoring **12**(1): 3-13.

Felux, M. W. (2017). "Acoustic emission monitoring on bridges under regular operating conditions." IBK Bericht. Zürich, Switzerland, ETH Zürich, Institut für Baustatik und Konstruktion (IBK).

fib (2003). Monitoring and safety evalutation of eixisting cocrete structures, Elsener and Böhni.

Fowler, T., J. Blessing, P. Conlisk and T. Swanson (1989). "The MONPAC system." Journal of Acoustic Emission **Volume 8**: 1.

Fowler, T. J. (1986). Experience with Acoustic Emission Monitoring of Chemical Process Industry Vessels. 8th International Acoustic Emission Symposium, Tokyo, Japan.

Gambarova, P. G. (1981). "On Aggregate Interlock Mechanism in Reinforced Concrete Plates with Extensive Cracking." IABSE reports of the working commissions **34**.

Gaydecki, P., F. M. Burdekin, W. Damaj and D. John (1992). "The propagation and attenuation of medium-frequency ultrasonic waves in concrete: a signal analytical approach." Measurement Science and Technology **3**: 126-134.

Golaski, L., P. Gebski and K. Ono (2002). "Diagnostics of reinforced concrete bridges by acoustic emission." Journal of acoustic emission **20**(2002): 83-89.

Gollob, S. (2017). Source localization of acoustic emissions using multi-segment paths based on a heterogeneous velocity model in structural concrete, PhD thesis, ETH Zürich.

Griffith, A. A. (1921). "The Phenomena of Rupture and Flow in Solids." Philosophical Transactions of the Royal Society of London. Series A, Containing Papers of a Mathematical or Physical Character **221**: 163-198.

Grosse, C. and M. Ohtsu (2008). Acoustic emission testing: Basics for Research-Applications in Civil Engineering.

Guo, H., G. Xiao, N. Mrad and J. Yao (2011). "Fiber Optic Sensors for Structural Health Monitoring of Air Platforms." Sensors **11**(4): 3687-3705.

Gutenberg, B. and C. Ritcher (1954). Seismicity of the earth and associated phenomena. Princeton (NJ), Princeton University Press.

Hashimoto, K., T. Shiotani, T. Nishida and T. Miyagawa (2017). "Application of Elastic-Wave Tomography to Repair Inspection in Deteriorated Concrete Structures." Journal of Disaster Research **12**(3): 496-505.

Hillerborg, A., M. Modéer and P. E. Petersson (1976). "Analysis of crack formation and crack growth in concrete by means of fracture mechanics and finite elements." Cement and Concrete Research **6**(6): 773-781.

Hoffmann, K. (1979). Practical hints for the installation of strain gages. Darmstadt, Hottinger Baldwin Messetechinik HBM.

Hoffmann, K. (1989). An introduction to measurements using strain gages, Hottinger Baldwin Messtechnik Darmstadt.

Hordijk, D. A. (1992). "Tensile and tensile fatigue behaviour of concrete; experiments, modelling and analyses." Heron **37**(1): 1-79.

Hordijk, D. A. (1993). Local approach to fatigue of concrete, PhD thesis, Delft University of Technology.

Huber, P., T. Huber and J. Kollegger (2016). "Investigation of the shear behavior of RC beams on the basis of measured crack kinematics." Engineering Structures **113**: 41-58.

Jones, E. (2015). Documentation for Matlab-based DIC code. Urbana-Champaign: University of Illinois.

Jost, M. and R. Herrmann (1989). "A Student's Guide to and Review of Moment Tensor." Seismol. Res. Lett. **2**.

Kaiser, J. (1950). Untersuchungen über das Auftreten von Geräuschen beim Zugversuch, PhD thesis, Technische Hochschule München.

Kani, G. N. J. (1964). "The Riddle of Shear Failure and its Solution." ACI Journal Proceedings **61**(4).

Kashif Ur Rehman, S., Z. Ibrahim, S. A. Memon and M. Jameel (2016). "Nondestructive test methods for concrete bridges: A review." Construction and Building Materials **107**: 58-86.

Kundu, T. (2014). "Acoustic source localization." Ultrasonics **54**(1): 25-38.

Kurz, J. H., C. U. Grosse and H.-W. Reinhardt (2005). "Strategies for reliable automatic onset time picking of acoustic emissions and of ultrasound signals in concrete." Ultrasonics **43**(7): 538-546.

Lacidogna, G., F. Accornero and A. Carpinteri (2019). "Influence of snap-back instabilities on Acoustic Emission damage monitoring." Engineering Fracture Mechanics **210**: 3-12.

Landis, E. N. and L. Baillon (2002). "Experiments to relate acoustic emission energy to fracture energy of concrete." Journal of Engineering Mechanics **128**(6): 698-702.

Lantsoght, E., C. van der Veen, A. de Boer and D. A. Hordijk (2017). "Proof load testing of reinforced concrete slab bridges in the Netherlands." Structural Concrete **18**(4): 597-606.

Lantsoght, E. O. L. (2017). "Development of a stop criterion for shear based on aggregate interlock." Stevin Report **25.5-17-09**. Delft, the Netherlands, Delft University of Technology.

Lantsoght, E. O. L., R. T. Koekkoek, D. Hordijk and A. de Boer (2018). "Towards standardisation of proof load testing: pilot test on viaduct Zijlweg." Structure and Infrastructure Engineering **14**(3): 365-380.

Lantsoght, E. O. L., C. van der Veen, J. Walraven and A. de Boer (2013). "Recommendations for the shear assessment of reinforced concrete slab bridges from experiments." Structural Engineering International **23**(4): 418-426.

Lee, B. H., Y. H. Kim, K. S. Park, J. B. Eom, M. J. Kim, B. S. Rho and H. Y. Choi (2012). "Interferometric Fiber Optic Sensors." Sensors **12**(3): 2467-2486.

Leonhardt, F. and R. Walther (1962). "Shear Tests on Beams With and Without Shear Reinforcement." Deutscher Ausschuss für Stahlbeton **No 151**: 83.

Li, B. and K. Maekawa (1987). Contact density model for cracks in concrete. International Association for Bridge and Structural Engineering (IABSE), Delft, the Netherlands.

Livitsanos, G., N. Shetty, E. Verstrynge, M. Wevers, D. Hemelrijck and D. Aggelis (2020). "Numerical simulation of elastic wave propagation in masonry compared with acoustic emission experimental results." Archives of Civil and Mechanical Engineering **20**.

MacGregor, J. G., M. A. Sozen and C. P. Siess (1960). "Strength and Behavior of Prestressed Concrete Beams with Web Reinforcement." Civil Engineering Studies SRS-201, University of Illinois at Urbana-Champaign.

Mari, A., A. Cladera, J. Bairán, E. Oller and C. Ribas (2014). "Shear-flexural strength mechanical model for the design and assessment of reinforced concrete beams subjected to point or distributed loads." Frontiers of Structural and Civil Engineering **8**: 337–353.

Martin, J. and M. C. Forde (1995). "Influence of concrete age and mix design on impulse hammer spectrum and compression wave velocity." Construction and Building Materials **9**(4): p. 245-255.

McCann, D. M. and M. C. Forde (2001). "Review of NDT methods in the assessment of concrete and masonry structures." NDT & E International **34**(2): 71-84.

MISTRAS (2008). "R6I-AST Sensor." Product Data Sheet. Princeton Junction, NJ 08550, MISTRAS Group Inc.

MISTRAS (2008). "WD Sensor." Product Data Sheet. Princeton Junction, NJ 08550, MISTRAS Group Inc.

MISTRAS (2010). "SENSOR HIGHWAY II-SMART MONITOR USER'S MANUAL Rev 0." Princeton Junction, New Jersey, USA, Products & Systems Division, MISTRAS Group Inc.

MISTRAS (2011). "AEwin SOFTWARE, Installation, Operation and User's Reference Manual." Princeton Junction, NJ, USA, Products & Systems Division.

MOLYKOTE (2018). "MOLYKOTE 4 Electrical Insulating Compound." Product Data Sheet, DuPont de Nemours, Inc.

Mörsch, E. (1909). Der Einsenbetonbau (Published in English as: Concrete-Steel Construction), Engineering News Publishing Co.

Muttoni, A. and M. Fernández Ruiz (2008) "Shear strength of members without transverse reinforcement as function of critical shear crack width." **105, No 2**, 163-172-163-172.

Muttoni, A., J. Schwartz and B. Thürlimann (1996). Design of concrete structures with stress fields, Springer Science & Business Media.

Nagataki, S., T. Okamoto, T. Ayata and S. Yuyama (1991). Classification of Crack Pattern developed in Reinforced Concrete Members by Acoustic Emission. Proc. Sym. NDE in Civil Engineering, JSCE.

Nair, A. and C. S. Cai (2010). "Acoustic emission monitoring of bridges: Review and case studies." Engineering Structures **32**(6): 1704-1714.

Nielsen, M. P. and L. C. Hoang (2016). Limit Analysis and Concrete Plasticity, CRC Press.

Ogilvy, J. A. and J. A. G. Temple (1983). "Diffraction of elastic waves by cracks: application to time-of-flight inspection." Ultrasonics **21**(6): 259-269.

Ohtsu, M. (2010). "Recommendation of RILEM TC 212-ACD: Acoustic emission and related NDE techniques for crack detection and damage evaluation in concrete: Measurement method for acoustic emission signals in concrete." Materials and Structures **43**(9): 1177-1181.

Ohtsu, M. (2010). "Recommendation of RILEM TC 212-ACD: Acoustic emission and related NDE techniques for crack detection and damage evaluation in concrete: Test method for classification of active cracks in concrete structures by acoustic emission." Materials and Structures **43**(9): 1187-1189.

Ohtsu, M. (2010). "Recommendation of RILEM TC 212-ACD: Acoustic emission and related NDE techniques for crack detection and damage evaluation in concrete: Test method for damage qualification of reinforced concrete beams by acoustic emission." Materials and Structures **43**(9): 1183-1186.

Ohtsu, M., T. Okamoto and S. Yuyama (1998). "Moment tensor analysis of acoustic emission for cracking mechanisms in concrete." Structural Journal **95**(2): 87-95.

Ohtsu, M., M. Shigeishi, H. Iwase and W. Koyanagit (1991). "Determination of crack location, type and orientation ina concrete structures by acoustic emission." Magazine of Concrete Research **43**(155): 127-134.

Ohtsu, M., M. Uchida, T. Okamoto and S. Yuyama (2002). "Damage assessment of reinforced concrete beams qualified by acoustic emission." ACI Structural Journal **99**(4): 411-417.

Ono, K. (1997). "Acoustic emission." Encyclopedia of acoustics **68**: 797-809.

Otsuka, K. and H. Date (2000). "Fracture process zone in concrete tension specimen." Engineering Fracture Mechanics **65**(2): 111-131.

Owino, J. O. and L. J. Jacobs (1999). "Attenuation Measurements in Cement-Based Materials Using Laser Ultrasonics." Journal of Engineering Mechanics **125**(6): 637-647.

Pahlavan, L., F. Zhang, G. Blacquière, Y. Yang and D. Hordijk (2018). "Interaction of ultrasonic waves with partially-closed cracks in concrete structures." Construction and Building Materials **167**: 899-906.

Pahlavan, P. L., J. Paulissen, R. Pijpers, H. Hakkesteegt and R. Jansen (2014). Acoustic emission health monitoring of steel bridges. EWSHM-7th European Workshop on Structural Health Monitoring, Nantes, France.

Paulay, T., R. Park and M. H. Phillips (1974). "Horizontal Construction Joints in Cast-In-Place Reinforced Concrete." ACI Symposium Publication **42**: 599-616.

Philippidis, T. P. and D. G. Aggelis (2005). "Experimental study of wave dispersion and attenuation in concrete." Ultrasonics **43**(7): 584-595.

Polyzos, D., A. Papacharalampopoulos, T. Shiotani and D. G. Aggelis (2011). "Dependence of AE parameters on the propagation distance." Journal of Acoustic Emission **29**: 57+.

Prasad, B. K. R. and R. V. Sagar (2008). "Relationship between AE Energy and Fracture Energy of Plain Concrete Beams: Experimental Study." Journal of Materials in Civil Engineering **20**(3): 212-220.

Pruijssers, A. F. (1986). "Shear resistance of beams based on the effective shear depth." Stevin Report **5-86-1**. Delft, the Netherlands, Delft University of Technology.

Reineck, K.-H. (1991). "Ultimate shear force of structural concrete members Without Transverse Reinforcement Derived From a Mechanical Model (SP-885)." ACI Structural Journal **88**(5).

Ridge, A. and P. Ziehl (2006). "Evaluation of stengthened reinforced concrete beams: Cyclic load test and acoustic emission methods." ACI Structural Journal **103**: 832-841.

Rüsch, H. (1959). "Physical Problems in the Testing of Concrete (Physikalische Fragen der Betonprufung)." Zement-Kalk-Gips **12**(I): 1-9.

Sammonds, P. R., P. G. Meredith, S. A. F. Murrell and I. G. Main (1994). Modelling the damage evolution in rock containing pore fluid by acoustic emission. Rock Mechanics in Petroleum Engineering.

Schechinger, B. and T. Vogel (2007). "Acoustic emission for monitoring a reinforced concrete beam subject to four-point-bending." Construction and Building Materials **21**(3): 483-490.

Schlaich, J. (1991). "Design and detailing of structural concrete using strut-and-tie models." The Structural Engineer **69**(6): 113-125.

Schreurs, P. J. G. (2012). Fracture Mechanics. Eindhoven, the Netherlands.

Schubert, F. (2004). "Basic principles of acoustic emission tomography." Journal of Acoustic Emission **22**(1): 147-158.

Schumacher, T., C. C. Higgins and S. C. Lovejoy (2011). "Estimating Operating Load Conditions on Reinforced Concrete Highway Bridges with b-value Analysis from Acoustic Emission Monitoring." Structural Health Monitoring **10**(1): 17-32.

Schumacher, T., D. Straub and C. Higgins (2012). "Toward a probabilistic acoustic emission source location algorithm: A Bayesian approach." Journal of Sound and Vibration **331**(19): 4233-4245.

Shigeishi, M. and M. Ohtsu (2001). "Acoustic emission moment tensor analysis: development for crack identification in concrete materials." Construction and Building Materials **15**(5): 311-319.

Shiotani, T., D. G. Aggelis and O. Makishima (2009). "Global Monitoring of Large Concrete Structures Using Acoustic Emission and Ultrasonic Techniques: Case Study." Journal of Bridge Engineering **14**(3): 188-192.

Shiotani, T., J. Bisschop and J. G. M. Van Mier (2003). "Temporal and spatial development of drying shrinkage cracking in cement-based materials." Engineering Fracture Mechanics **70**(12): 1509-1525.

Shiotani, T., K. Fujii, T. Aoki and K. Amou (1994). "Evaluation of progressive failure using AE sources and improved b-value on slope model tests." Progress in Acoustic Emission **7**: 529-534.

Shiotani, T., X. Luo, H. Haya and M. Ohtsu (2007). Damage Quantification for Concrete Structures by Improved b-value Analysis of Acoustic Emissioin. Earthquakes and Acoustic Emission: Selected Papers from the 11th International Conference on Fracture, Turin, Italy, March 20-25, 2005, CRC Press.

Shiotani, T., M. Ohtsu and K. Ikeda (2001). "Detection and evaluation of AE waves due to rock deformation." Construction and Building Materials **15**(5): 235-246.

Shiotani, T., S. Osawa, S. Momoki and H. Ohtsu (2015). Visualization of Damage in RC Bridge Deck for Bullet Trains with AE Tomography, New York, NY, Springer New York.

Slobbe, A. T., M. Hendriks and J. Rots (2014). "Smoothing the propagation of smeared cracks." Engineering Fracture Mechanics **132**: 147-168.

Soga, K. and L. Luo (2018). "Distributed fiber optics sensors for civil engineering infrastructure sensing." Journal of Structural Integrity and Maintenance **3**(1): 1-21.

Song, G. B., H. C. Gu and Y. L. Mo (2008). "Smart aggregates: multi-functional sensors for concrete structures - a tutorial and a review." Smart Materials & Structures **17**(3).

Soutsos, M., J. Bungey, S. Millard, M. Shaw and A. Patterson (2001). "Dielectric properties of concrete and their influence on radar testing." NDT & e International **34**(6): 419-425.

Soutsos, M., B. Denys, V. Garnier, A. Gonçalves and A. Monteiro (2012). Non-Destructive Assessment of Concrete Structures: Reliability and Limits of Single and Combined Techniques**:** 119-186.

Srivastava, J. (2020). Estimation of Energy Released from Crack in Concrete using Acoustic Emission and Comparison with the Numerical Results, Master thesis, Delft University of Technology.

Su, T.-C. (2020). "Assessment of Cracking Widths in a Concrete Wall Based on TIR Radiances of Cracking." Sensors **20**(17): 4980.

Tassios, T. and E. Vintzileou (1986). "Mathematical Models for Dowel Action under Monotonic Conditions." Magazine of Concrete Research - MAG CONCR RES **38**: 13-22.

Theobald, P., B. Zeqiri and J. Avison (2008). "Couplants and their influence on AE sensor sensitivity." Journal of Acoustic Emission **26**.

Tsangouri, E., O. Remy, F. Boulpaep, S. Verbruggen, G. Livitsanos and D. G. Aggelis (2019). "Structural health assessment of prefabricated concrete elements using Acoustic Emission: Towards an optimized damage sensing tool." Construction and Building Materials **206**: 261-269.

Tue, N. V., W. Theiler and N. D. Tung (2014). "Schubverhalten von Biegebauteilen ohne Querkraftbewehrung." Beton- und Stahlbetonbau **109**(10): 666-677.

VALLEN (2021). "AMSY-6 System Description." Germany.

Van Steen, C., L. Pahlavan, M. Wevers and E. Verstrynge (2019). "Localisation and characterisation of corrosion damage in reinforced concrete by means of acoustic emission and X-ray computed tomography." Construction and Building Materials **197**: 21-29.

Van Steen, C., F. Zhang, H. Nasser, Y. Yang and E. Verstrynge (2018). On-site inspection of a reinforced concrete structure deteriorated due to corrosion by means of acoustic emission and other techniques. Conference: Structural Faults and Repair 2018 Edinburgh, Scotland.

Vecchio, F. and M. P. Collins (1986). "The modified compression-field theory for reinforced elements subjected to shear." ACI Journal **83**: 219-231.

Walraven, J. C. (1980). Aggregate Interlock, PhD thesis, Delft University of Technology.

Walraven, J. C. (1981). "Fundamental Analysis of Aggregate Interlock." ASCE J Struct Div **107**(11): 2245-2270.

Wang, S., S. Zhao and I. Al-Qadi (2019). "Real-Time Monitoring of Asphalt Concrete Pavement Density during Construction using Ground Penetrating Radar: Theory to Practice." Transportation Research Record: Journal of the Transportation Research Board **2673**(5): 329-338.

Yang, Y. (2014). Shear Behaviour of Reinforced Concrete Members without Shear Reinforcement, PhD thesis, Delft University of Technology.

Yang, Y. (2016). Acoustic emission study on 50 years old reinforced concrete beams under bending and shear tests. International Institute of Innovative Acoustic Emission (I3AE), Kyoto, Japan.

Yang, Y. (2020). "Shear behaviour of deep RC slab strips (beams) with low reinforcement ratio." Stevin Report **25.5-19-06**. Delft, the Netherlands, Delft University of Technology.

Yang, Y., J. den Uijl and J. Walraven (2016). "Critical shear displacement theory: on the way to extending the scope of shear design and assessment for members without shear reinforcement." Structural Concrete **17**(5): 790-798.

Yang, Y., D. A. Hordijk and A. de Boer (2016). Acoustic emission measurement in the proof loading of an existing bridge affected by ASR. 5th International Symposium for Life-Cycle Civil Engineering, Delft, the Netherlands.

Zararis, P. D. and G. C. Papadakis (2001). "Diagonal Shear Failure and Size Effect in RC Beams without Web Reinforcement." Journal of Structural Engineering **127**(7): 733-742.

Zarate Garnica, G. (2018). Analysis of shear transfer mechanisms in concrete members without shear reinforcement based on kinematic measurements, Master thesis, Delft University of Technology.

Zarate Garnica, G. (2021). "Measurement report of reinforced concrete slabs." Stevin Report **25.5-21-03**. Delft, the Netherlands, Delft University of Technology.

Zarate Garnica, G. I., E. O. L. Lantsoght and Y. Yang (2022). "Monitoring structural responses during load testing of reinforced concrete bridges: a review." Structure and Infrastructure Engineering: 1-23.

Zhang, F. (2017). Evaluation of Acoustic Emission Monitoring of Existing Concrete Structures, Master thesis, Delft University of Technology.

Zhang, F., L. Pahlavan and Y. Yang (2020). "Evaluation of acoustic emission source localization accuracy in concrete structures." Structural Health Monitoring **19**(6): 2063-2074.

Zhang, F., Y. Yang, K. Hashimoto and T. Shiotani (2018). A comparative study of acoustic emission tomography and digital image correlation measurement on a reinforced concrete beam. International Association for Life-Cycle Civil Engineering (IALCCE), Ghent, Belgium.

Zhang, F., G. I. Zarate Garnica, Y. Yang, E. Lantsoght and H. Sliedrecht (2020). "Monitoring Shear Behavior of Prestressed Concrete Bridge Girders Using Acoustic Emission and Digital Image Correlation." Sensors **20**(19): 5622.

Acknowledgement

This dissertation would not have been possible without the contributions of many people.

I would like to thank my promoter Max Hendriks who greatly supported my research. I thank him for arranging time to supervise me every two weeks. Every meeting with Max was thoughtful, not only due to his broad knowledge and quick mind, but also his art of listening and encouraging. I cannot outline all his respectable characters that inspire me to be a good researcher.

I would like to thank my co-promoter and supervisor Yuguang Yang who gave me endless support during my PhD. He led me into the field of acoustic emission monitoring of concrete structures. He put great effort into supervising me to complete this dissertation. He influenced me in many aspects to become an independent researcher. What influenced me the most is his pure and critical research attitude, which I should take with me always.

I would like to thank Dick Hordijk who gave me the opportunity to work in the concrete group and supported me greatly to start this research. I would like to thank Pooria Pahlavan who first taught me acoustic emission when I was doing master thesis with him.

I would like to thank Eva Lantsoght who provided useful comments to this research in the monthly meeting. She offered valuable feedbacks on the content of this dissertation. More than the research content, she inspired me an effective management of PhD project.

I would like to thank Gabriela Zarate Garnica who was closely involved in this research project. The study of reinforced concrete slabs and the use of digital image correlation would not have been succeeded without her strong support.

I would like to thank Sonja Fennis, Tomoki Shiotani and Els Verstrynge who offered helpful feedbacks on the content of this dissertation. Their views improved the dissertation from the aspects of both the fundamentals and the applications.

I would like to thank Jakub Pawlowicz and Albert Bosman who helped prepare the experiments in Stevin 2 laboratory which are important for this dissertation.

Indirectly-related to the content of this dissertation, I would like to thank my families and friends who made my journey of PhD enjoyable and full of love. Without mentioning all the names, I would like to specially thank my boyfriend Lichao Wu who always accompanies, supports and cheers me up, my father who gives me unconditional love and support, and my mother who left me the gifts of courage, happiness and other abilities.

It also worth mention that most of my PhD was conducted under a special condition: the COVID-19 pandemic. For more than two years I was working from home alone. This was difficult time but precious. The difficulty accelerated the growth of my internal power,

which is important not only for finalizing this dissertation but dealing with the future challenges.

About the author

Fengqiao Zhang was born in Tangshan, Hebei, China on January 24, 1993. She received her bachelor degree on Civil Engineering at Tongji University, Shanghai, in 2015. Afterwards she studied civil engineering in Delft University of Technology, the Netherlands, with the full scholarship from TU Delft. In 2017, she obtained the master degree and her graduation research was 'Evaluation of acoustic emission monitoring of concrete structures'. From 2017 to 2022, she was a PhD candidate in the group of concrete structures in TU Delft under the supervision of Prof.dr.ir Max Hendriks and Dr.ir. Yuguang Yang. The research topic was 'acoustic emission-based indicators of shear failure of reinforced concrete structures' which was presented in this dissertation.

By the moment of finishing this dissertation, her research interests are acoustic emission monitoring, non-destructive tests, shear behaviour of reinforced concrete structures and structural reliability analysis.